# Order formation and patterns in large scale active matter systems

## From microscopic processes to emergent phenomena

Timo Krüger

Munich 2021

# Order formation and patterns in large scale active matter systems

## From microscopic processes to emergent phenomena

Timo Krüger

A dissertation submitted

to the Faculty of Physics at the

Ludwig–Maximilians–Universität München

for the degree of

DOCTOR RERUM NATURALIUM

Munich, 23rd November 2021

# Zusammenfassung

In meiner Doktorarbeit befasse ich mich mit Ordnungsbildung und Mustern in Systemen aktiver Materie. Diese Systeme setzen sich aus einer Vielzahl einzelner, meist identischer, Konstituenten zusammen, die sich individuell fortbewegen und auf lokaler Ebene wechselwirken. Durch ein Zusammenspiel von Bewegung und Wechselwirkung auf Agentenebene kann sich aktive Materie selbst organisieren und verschiedene Arten makroskopischer Ordnung und Mustern ausbilden. Nach einer Einleitung präsentiere ich in den Kapiteln 2 bis 5 unsere Untersuchungen zu verschiedenen Aspekten dieser Phänomene, in denen wir jeweils numerische Simulationen mit anderen theoretischen Ansätzen oder mit Experimenten kombiniert haben.

**Kapitel 2 - Emergenz von koexistierenden geordneten Zuständen in Systemen aktiver Materie**
*gemeinsam mit Lorenz Huber, Ryo Suzuki, Erwin Frey und Andreas Bausch.*
In diesem Kapitel entwickeln wir eine neuartige Simulation des Actin Motility Assays, einem experimentellen Modellsystem aktiver Materie. Wir kombinieren großskalige Simulationen mit Experimenten und finden durch Kontrolle der mikroskopischen Interaktionen zwischen einzelnen Konstituenten heraus, dass geordnete Muster polarer und nematischer Symmetrien in aktiven Systemen koexistieren können. Somit zeigen wir, dass die Symmetrie der Ordnung in aktiver Materie nicht direkt durch die mikroskopische Interaktion bestimmt wird, sondern selbst eine emergente Eigenschaft ist. Die Inhalte dieses Kapitels wurden in [1] veröffentlicht.

**Kapitel 3 - Mikrophasenseparation in aktiven Filamentsystemen wird durch zyklische Dynamik der Clustergröße und -ordnung aufrechterhalten**
*gemeinsam mit Lorenz Huber und Erwin Frey.*
In diesem Kapitel untersuchen wir den Entstehungsprozess und die Aufrechterhaltung polarer mikrophasenseparierter Muster in aktiven Systemen. In agentenbasierten Simulationen identifizieren wir Teilchencluster verschiedener Ordnung und Größe und messen die Ströme zwischen diesen. Auf Grundlage dieser Austauschprozesse entwickeln wir ein kinetisches Modell, das die Ergebnisse der Simulationen reproduziert. Hierauf basierend zeigen wir, dass Ordnungsbildung durch Clusterselbstreplikation stattfindet und die Aufrechterhaltung des mikrophasenseparierten, polar geordneten Zustands das Ergebnis einer zyklischen Dynamik in der Teilchenclustergröße und -ordnung ist. Die Inhalte dieses Kapitels wurden in [2] veröffentlicht.

**Kapitel 4 - Kondensierte topologische Defekte und filamentöse Bogenauswürfe in phasengetrennten schwach wechselwirkenden nematischen aktiven Systemen**
*gemeinsam mit Ivan Maryshev und Erwin Frey.*
Wir finden in agentenbasierten Simulationen, dass auch in phasenseparierten nematischen Systemen topologisch geladene Strukturen, insbesondere $-1/2$ Defekte, entstehen können. Wir messen den Teilchenfluss durch Defekte, in deren Nähe die Dichte stark ansteigt, im Detail und bestimmen das Auftreten der Strukturen in Abhängigkeit von globaler Dichte und Persistenzlänge. Wir entwickeln ein Kontinuumsmodell, das dieselbe Phänomenologie und Parameterabhängigkeit aufweist wie die Simulationen. Anhand dieses Modells zeigen wir, dass das Auftreten der topologisch geladenen Strukturen eng mit der lateralen Bewegung von nematischen Bahnen verbunden ist.

**Kapitel 5 - Polare Strömung gleitender Mikrotubuli, gelenkt durch passive nematische Defekte**
*gemeinsam mit Alfredo Sciortino, Lukas Neumann, Ivan Maryshev, Erwin Frey und Andreas Bausch.*
In diesem Kapitel koppeln wir ein Mikrotubuli Gliding Assay an einen nematischen Flüssigkristall und zeigen, dass dadurch polar strömende Muster erzeugt werden können. Mit Hilfe einer Kombination aus numerischen Simulationen und einem heuristischen Ansatz bestätigen wir, dass alleine die Ausrichtung der einzelnen Agenten an dem nematischen Hintergrund für die Entstehung der polaren Muster verantwortlich ist. Wir zeigen, dass insbesondere die Orientierung und Struktur von $+1/2$ topologischen Defekten entscheidend für den Musterbildungsprozess ist.

# Summary

In my PhD thesis I am investigating order formation and patterns in active matter systems. These systems are composed of a large number of single, usually identical, constituents that move individually and interact at the local level. Through an interplay of motion and interaction at the agent level, active matter can self-organize and form various types of macroscopic order and patterns. After an introduction, I present in chapters 2 to 5 our investigations of various aspects of these phenomena, in each of which we have combined numerical simulations with other theoretical approaches or with experiments.

**Chapter 2 - Emergence of coexisting ordered states in active matter systems**
*with Lorenz Huber, Ryo Suzuki, Erwin Frey and Andreas Bausch.*
In this chapter, we develop a novel simulation of the actin motility assay, an experimental model system of active matter. We combine large-scale simulations with experiments and, by controlling the microscopic interactions between individual constituents, find that ordered patterns of polar and nematic symmetries can coexist in active systems. Thus, we show that the symmetry of order in active matter is not directly determined by the microscopic interaction, but is itself an emergent property. The contents of this chapter were published in [1].

**Chapter 3 - Microphase separation in active filament systems is maintained by cyclic dynamics of cluster size and order**
*with Lorenz Huber and Erwin Frey.*
In this chapter, we investigate the formation process and maintenance of polar microphase-separated patterns in active systems. In agent-based simulations, we identify particle clusters of different size and order and measure the currents between them. Based on these exchange processes, we develop a kinetic model that reproduces the results of the simulations. Based on this, we show that order formation occurs through cluster self-replication and that the maintenance of the microphase-separated, polar-ordered state is the result of a cyclic dynamics in particle cluster size and order. The contents of this chapter were published in [2].

**Chapter 4 - Condensed topological defects and filamentous arc ejections in phase-separated weak active nematics**
*with Ivan Maryshev and Erwin Frey.*
We find in agent-based simulations that topologically charged structures, in particular $-1/2$ defects, can also emerge in phase-separated nematic systems. We measure in detail the particle flux through defects in the vicinity of which the density increases sharply, and determine the occurrence of the structures as a function of global density and persistence length. We develop a continuum model that has the same phenomenology and parameter dependence as the simulations. Using this model, we show that the occurrence of the topologically charged structures is closely related to the lateral motion of nematic lanes.

**Chapter 5 - Polar flow of gliding microtubules steered by passive nematic defects**
*with Alfredo Sciortino, Lukas Neumann, Ivan Maryshev, Erwin Frey and Andreas Bausch.*
In this chapter, we couple a microtubule gliding assay to a nematic liquid crystal and show that this can generate polarly flowing patterns. Using a combination of numerical simulations and a heuristic approach, we confirm that the orientation of each agent on the nematic background alone is responsible for the generation of the polar patterns. Moreover, we show that in particular the orientation and structure of $+1/2$ topological defects is crucial for the pattern formation process.

# Contents

# 1 Introduction

## 1.1 Active matter, a definition

We want to start this thesis with a brief definition of its object of research, active matter. Commonly, this term is used for systems that are composed of individual constituents, that each has a propulsion or force-generating mechanism, and that each can interact with other individuals of the system and possibly with their environment. For some in-depth reviews on active matter, please see e.g. [3–9]. In active matter systems, there is a continuous, effective local energy input e.g., through the consumption of fuel available in the agents' environment or through the depletion of an energy store carried by each agent, rendering them inherently non-equilibrium systems.

Due to its rather inclusive definition, "active matter" is an umbrella term for an extremely wide range of different systems. An emblematic (but by no means exhaustive) list of systems naturally occurring or human-made, to which this definition can be applied with different levels of rigor, includes examples from a broad range of length scales: bacterial suspensions [10–14], driven biofilaments [1, 15–21], active colloids [22–24], shaken granular particles [25–29], cytoskeletons [30–33], insects [34–36], flocks of birds [37–41], schools of fish [42–45], and crowds of humans [46, 47]. These examples show that active matter systems are mostly biological in nature (or, if artificial, often biologically mimicked). Hence, research in this area often takes place at the interface between biology and other disciplines.

What makes active systems particularly interesting is that they often exhibit an emergent dynamical property such as collective motion and/or pattern formation (an archetypical, but now almost clichéd, example is the multitude of formations that starlings form when they fly in large groups). A strong motivation to study active systems (apart, of course, from the spark of curiosity the awe-inspiring emergent patterns cause) is that they often exhibit phenomena akin to things that are familiar from other research fields, especially physics (hence one often sees also the description "active matter physics"): For example, a drastically altered macroscopic behavior under a change of parameter –very reminding of phase transitions– or topological defects that have many similarities, but also some peculiar differences, to their equilibrium counterparts [18, 48–51].

Moreover, it seems simply natural to extend the concepts and tools of other areas of physics that often already deal with the large scale properties of many interacting

particles (e.g. statistical physics, condensed matter physics etc.) to a situation that is, like active matter, similar in some regards. This is not entirely unjustified, as some aspects of certain phenomena occurring in active matter systems have already been successfully described by theoretical frameworks that are extensions of approaches known from other fields of physics (see also section 1.3).

There are several main motivations for studying active matter. Often at the forefront is the hope for a better understanding and identification of generic principles of how living systems can organize themselves from a set of identical building blocks into a complex whole. Hence active matter physics is generally viewed as an integral part of the "physics of life". Another, more from an engineering viewpoint, motivation is that one needs a thorough understanding of the relevant self-organization processes in order to be able to construct useful active materials that are able to perform predefined tasks in an adaptive manner. Those high level points are still state of the art research questions and it is explored how active matter physics can contribute to answering those [3–9].

In this work we particularly deal with active matter physics in the context of driven filaments. In sections 1.2 and 1.3 we provide some further introduction into active matter and how to study it. We then first will, in section 1.4 and chapter 2, examine interactions in the actin motility assay, an experimental active matter model system. These we build in a large-scale computational model (that we will use throughout most of this thesis). Using our simulations and experiments in the motility assay, we show that nematic and polar structures can simultaneously coexist with a disordered background. Second, in chapter 3, we in depth characterize the formation process of polar patterns and investigate how they are maintained. Third, in chapter 4, we discover that topological defects and other topological structures can form in phase separated active nematics. Last, in chapter 5, we investigate how active particles moving on a dense passive nematic background can form polar lanes.

## 1.2 Different types of active matter

After presenting a relatively broad list of active matter systems in the last section, we will now present various classifications which can be used to categorize systems that are composed of different building blocks but have similar properties or basic requirements. This should give the reader an overview and help to contextualize the research subjects of this thesis.

One often-used category is the classification into wet or dry systems [5–7, 9]. As the name implies, in so-called wet systems, the long-range hydrodynamic coupling that arises due to the surrounding medium is of importance. This is indispensable, for example, for the description of microswimmers [52–56] or colloids [24, 57, 58].

In dry systems, on the other hand, the long-range hydrodynamic coupling is either absent or can be neglected due to strong coupling with a substrate which damps momentum. For example, in the case of shaken granular media [25–28], or actin motility assays [1, 15, 16, 19–21]. In this thesis, we will deal exclusively with dry systems and therefore use the term active matter synonymously with dry active matter in the following.

A further relevant distinction can be drawn between dilute systems and systems in which density is high and spatially uniform (often they are also called compressible and incompressible systems, respectively). In dense systems particles generally possess a strong steric exclusion and are packed at a density that is mostly saturated (and stays largely constant). Here, often phenomena like topological defects start to play an important role [48–50, 59, 60]. On the other hand, dilute systems can show marked separation into "phases" of different density (as well as symmetry) and steric interactions are mostly weak [5, 7, 61–63]. Although we mainly study systems that are dilute, we will discuss some aspects of dense systems again in chapter 4 and 5.

In dry systems the interaction mostly takes place via a combination of repulsion and alignment (see also section 1.4). One limiting case are systems in which the particles exclusively interact via repulsion and any alignment is absent [64–68] (also any effective alignment due to anisotropies in the shape of particles [69–72]). These show an interesting phenomenon called *motility induced phase separation* (MIPS), which has been studied extensively in recent years [73–76], yet is not in the scope of this thesis. Our main focus, instead, will be on systems where interactions are dominated by alignment.

While these classifications are the most relevant to contextualize this thesis, it should not go unmentioned that they are not all-encompassing. A further number of distinct cases exist which, under certain circumstances, may merit their own category.[1]

Further, a few words of caution are worth noting at this point. First, the categories above, while often unambiguous and useful, should not be understood as absolute. Under certain circumstances, the boundaries between them are blurred (e.g., the categorization into wet or dry of the actin motility assay, see [82] and chapter 2). Also, an apriori classification can, at worst, be misguiding. It is, for example, a common view that systems showing nematic or polar (see also section 1.3) patterns

---

1 To name just one particularly interesting example: in some animals, interaction has been observed to be mostly independent of nearest neighbor distances [38], which led to the development of computational model systems with so-called "topological interactions". In these, only the topological distance between agents is of importance and not the euclidean one, leading to some seemingly distinct properties such as polar order formation without phase separation into polar waves [77–79]; a finding that is still controversially discussed [80, 81].

as strictly distinct classes [4, 5, 7, 83–90]. We discuss in chapter 2 why this is most likely not justified.

## 1.3 Approaches to studying active matter

As written in the last section, in this thesis we will generally treat dry, mostly aligning, dilute active matter. Here we will try to summarize how and with which tools one can go about this endeavor in general. After this introduction, we will then proceed to present the specific agent based approach used in most parts of this thesis in section 1.4.

To bring order into the high complexity involved in a real-world active matter system, i.e., to even have a chance to identify essential features and underlying principles how it organizes, reductionist and minimal models are the first logical step to begin with. Or, to say it the other way round: even if it were possible to model the daunting complexity of, e.g., animals and how they interact among each other, it would not be clear which of the many details are essential for the organization process. Although this approach feels very natural for a physicist, one big challenge in this context is, of course, to find the right level of "reduction".

Historically, one of the first steps that were made to study active matter systems with a minimal model was the "Vicsek model", which was introduced by its namesake, Tamás Vicsek (along with several co-authors), in 1995 [91]. This publication sparked immense interest in other scientists and is considered by some as the starting point of active matter research in general [3, 7]. One of the motivations for the defining feature of this model was the observation that animals in groups tend to move as other individuals do in their vicinity [91], i.e., that they align their direction with each other. At this point, it seems appropriate to mention that Vicsek et al. were not the very first who computationally modeled animal group behavior; the Boids model [92], very famous in the field of computer graphics, and other examples [93] are even older.

Since the Vicsek model is still widely studied [7, 9, 94, 95] and because its simplicity makes it a perfect example to illustrate in a straightforward manner how one can investigate active systems with an agent based simulation, we will briefly describe it here.

In the Vicsek model, one considers $N$ active agents, each modeled as a point like particle moving on a two-dimensional plane with periodic boundary conditions. Every agent $i \in \{0, 1, ..., N-1\}$ propagates with the same constant velocity $v_0$ along its individual direction $\theta_i^t$ and is subject to some directional noise while moving. Its position at time $t$ is denoted by $\mathbf{r}_i^t$ and the following equation of motion of the
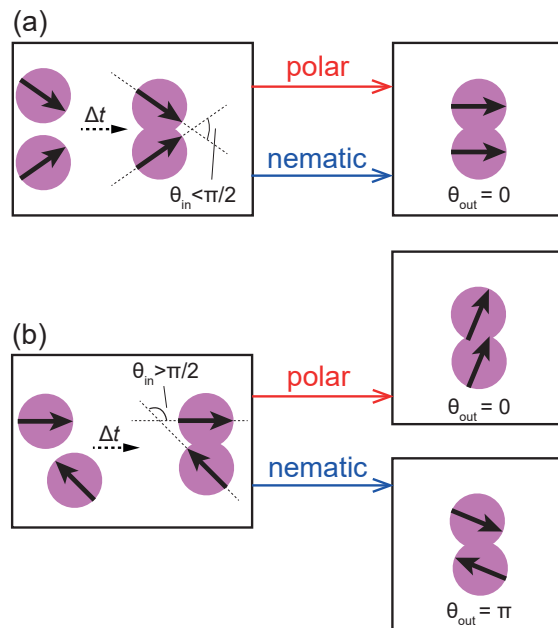
**Figure 1.1 Schematic depiction of the Vicsek Model.** Point-like particles with a certain interaction radius (colored areas) move along their orientation (indicated by the solid arrows). In every iteration of the simulation (dotted arrow), they propagate a constant step size. (**a**) If after a displacement two particles collide with an angle ($\theta_{\text{in}}$) smaller than $\frac{\pi}{2}$ [(a), left box] in both the polar and nematic case particles perfectly and instantly align their orientation [(a), right box]. (**b**) If after a displacement two particles collide with an angle lager than $\frac{\pi}{2}$ [(b), left box] in the polar case they again perfectly and instantly align their orientation [(b), right upper box] whereas in the nematic case they perfectly and instantly anti-align their orientation [(b), right lower box].

position is assumed:

$$\mathbf{r}_i^{t+\Delta t} = \mathbf{r}_i^t + v_0 \Delta t \begin{pmatrix} \cos \theta_i^{t+\Delta t} \\ \sin \theta_i^{t+\Delta t} \end{pmatrix},$$ (1.1)

where the time increment is generally chosen as $\Delta t = 1$. The orientation of a particle, $\theta_i^t$, evolves according to

$$\theta_i^{t+1} = \arg \left[ \sum_{j \in \mathcal{R}_i} e^{i\theta_j^t} \right] + \eta \xi_i^t.$$ (1.2)

Here the second term accounts for the directional noise each particle is assumed to be subject to at each iteration. The intensity of this noise is set by $\eta$, which can be fixed to values between 0 and 1; $\xi_i$ is a delta-correlated white noise ($\xi_i \in [-\pi, \pi]$).

The first part of Eq. (1.2) describes the interaction between agents. This is modeled as follows: each particle possesses a circular interaction radius, generally set to $\Delta r = 1$.[2] At every iteration the mean orientation of all particles inside the interaction radius of particle $i$ (subsumed as $\mathcal{R}_i$), is calculated (including $i$) and the direction of $i$ is perfectly aligned with the resulting mean orientation; see also Fig. 1.1. Generally, this type of interaction, i.e., an interaction where agents tend to align their directions, is called *polar*.

Despite its reductiveness, the model shows some very interesting behavior: at high noise/low density, each particle moves almost independent on a persistent random walk and the system is disordered, at low noise/high density, the system exhibits collective motion and most particles propagate in the same direction. Hence the symmetry of the system is spontaneously broken. Commonly, the degree of this alignment can be measured with the *global polar order parameter*

$$\mathcal{P}^t = \frac{1}{N} \left| \sum_{j=0}^{N-1} e^{i\theta_j^t} \right|, \tag{1.3}$$

which takes values near 0 for disordered systems and near 1 for perfectly ordered systems where all particles move in the same direction (note that this is the same as the average velocity in the case of unit and constant $v_0$).

At first it was thought that the transition between the disordered and ordered state represents a continuous phase transition [3, 7, 91]. Yet, it was discovered in 2004 that the onset of polar order in the agent-based Vicsek model is indeed not continuous but discontinuous [96] with dense polarly moving waves as the nonequilibrium steady state near the onset of order (cf. illustration in Fig 1.2(b)). Although this discovery was challenged at first [97], it was soon confirmed to be valid [85]. The continuous transition was found to be a finite size effect and only above a large enough system size polar patterns can from [7, 63, 85, 96]. It is worth noting that the patterned state is indeed micro-phase separated [63, 69, 94, 98].

Deeper in the ordered regime, i.e., at even lower noise/higher density, the system ceases to exhibit a coexistence between polar patterns and disordered background and, instead, exhibits a polarly ordered "liquid" in which the density is not phase separated [7, 63, 85, 96]. Please note that we will discuss the onset and maintenance of polar patterns in more detail in section 1.5 and chapter 3.

Additionally to the modeling of polar systems where agents always tend to align their direction while interacting, the Vicsek model was extended to cases where constituents can also anti-align their direction [86, 87, 99, 100] if the impact angle is larger than $\pi/2$. This *nematic* case in the Vicsek model is schematically depicted

---

2  It is worth to note that even with unitary $\Delta t$ and $\Delta r$, which set length- and time-scales, it was found that relatively large values of $v_0 \sim 0.5$ are still sufficient to resolve the dynamics [85].
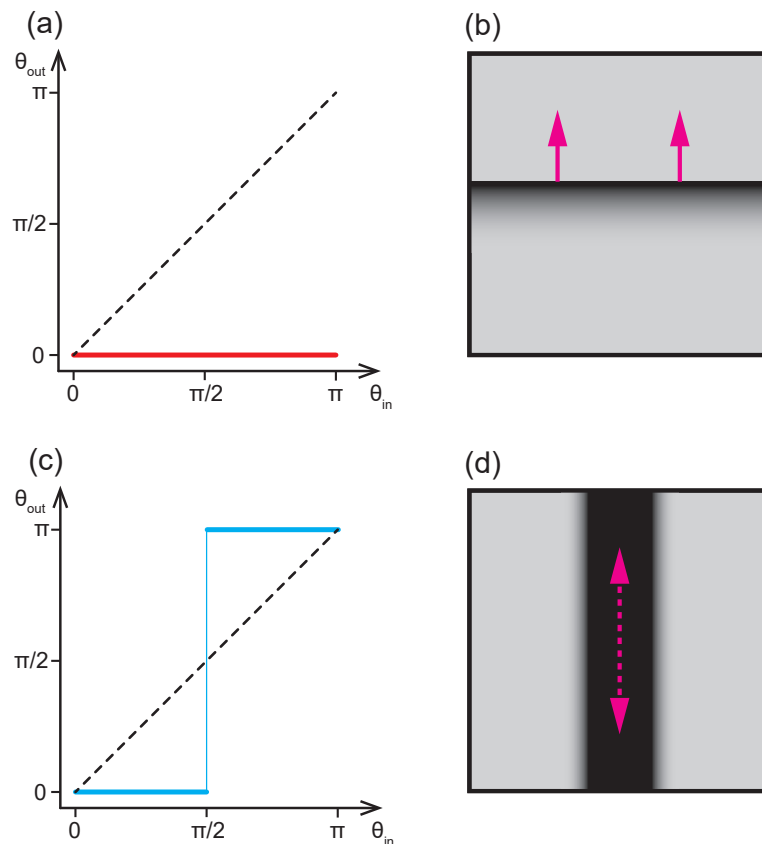
**Figure 1.2 Binary collision statistics and macroscopic patterns in the Vicsek model.** (a) and (c): Plot of the angle between the directors of two particles after an interaction, $\theta_{\text{out}}$, against the angle before the collision, $\theta_{\text{in}}$, for the polar (red line in a) and nematic case (blue line in c), respectively. The dashed line in both *binary collision statistics* corresponds to the case of no interaction. (b) and (d): Schematic depiction of the macroscopic patterns in the Vicsek model. In case of polar interacting particles, polar waves (b) form where a high-density band of ordered particles (dark black) propagates through a disordered low-density background (light grey). The direction of motion is depicted by the magenta arrows. In the case of nematic interacting particles, nematic lanes (d) form (dark black), in which particles move in both directions along the contour (magenta arrow). The lane is embedded in a disordered low-density background (light grey).

in Fig. 1.1 and e.g. models the behavior of rod-shaped particles upon collision [25, 27, 71, 86, 101–106]. Here, instead of Eq. (1.2), the interaction between agents in the Vicsek model is described as follows:

$$\theta_i^{t+1} = \arg\left[\sum_{j \in \mathcal{R}_i} \text{sign}[\cos(\theta_j^t - \theta_i^t)]e^{i\theta_j^t}\right] + \eta\xi_i^t. \tag{1.4}$$

A straightforward way to visualize the difference between polar and nematic interactions are the binary collisions statistics, as shown schematically in Fig. 1.2(a) and (c). Whereas in the polar case, the angle between two colliding particles is always zero directly after the interaction, in the nematic case, this is only true for acute incoming angles $\theta_{\text{in}}$. For obtuse angles, the outgoing angle after the interaction is always $\pi$.

A rather similar picture emerges regarding the phase separation process in this case. Also, with nematic interactions the systems exhibit order and form patterns near the onset of order, see Fig 1.2(d). As for the polar case, the ordered state seems to reflect the symmetry of the microscopic interaction [7, 86, 87, 99, 100, 105]: at high enough density/low enough noise, nematic lanes are formed, as depicted in Fig 1.2(d). Deeper in the ordered phase, there is again a nematically ordered liquid.

Again an order parameter –the *global nematic order parameter*– can be used to describe the degree of ordering in the system

$$\mathcal{N}^t = \frac{1}{N} \left| \sum_{j=0}^{N-1} e^{i2\theta_j^t} \right| . \tag{1.5}$$

The two presented cases of the Vicsek model, polar and nematic, reflect the most widely considered symmetries that order in active matter can show [4, 5, 7, 88] (see also chapter 2).

Although a number of other numerical models exist [101, 107–114], the Vicsek model, despite its simplicity, exemplifies the generally used framework: agents of a certain shape (or range of interaction) move on noisy trajectories and interact with each other. This interplay at the local level, under the right condition, can lead to the formation of collective motion and macroscopic order. For a discussion if and how the microscopic details in these simulations matter and whether the symmetry of the local interaction is always connected to the symmetry of the macroscopic patterns, please refer to section 1.4 and chapter 2.

Another approach to studying active matter is continuum models. For example, soon after the introduction of the Vicsek model, Toner and Tu developed a hydrodynamic theory [83] describing the not phase separated polar ordered state observed in the simulations and used it to show that the order is indeed truly long-ranged, although interactions have only a finite range.

Generally, these models consist out of an equation for the density, which is coupled to an order field. They can be constructed by different means. One method is to invoke symmetry arguments and collect terms that are allowed by these considerations [83, 115]. The disadvantage, in this case, is that the resulting terms contain coefficients that are not easy to connect with any microscopic details of the active matter systems the model tries to emulate.

Alternatively, one can incorporate the microscopic details of a model (often the above described polar or nematic Vicsek model), into a derivation of hydrodynamic equations via, e.g., a Fokker–Planck [116–124] or Boltzmann [84, 88, 89, 102, 125] approach. Although taking different routes, it was shown that the two mentioned methods can yield equivalent results [126]. In addition to these procedures, it is also possible to directly numerically solve the Boltzmann equation [127–129]. While these mesoscopic approaches can be better connected to the investigated systems, they still have to rely on heavy approximations like assuming that agents decorrelate between collisions or that only binary interactions are of importance. This reduces the chance to obtain any quantitative results [126].

Besides these theoretical approaches, one central pillar of active matter research is, of course, to conduct experiments. We will present and employ one experimental model system, the actin motility assay, in chapter 2 (see also section 1.4).

While this thesis has a focus on a novel agent-based simulation method (which we will motivate in section 1.4), in no case we will rely on agent-based models alone. In order to elucidate the same phenomenon resp. question from different angles, we instead always combine it with a different methodology. In chapters 2 and 5 with experiments, in chapter 3 with a kinetic model focusing on assembly and disassembly processes of clusters and in chapter 4 with a hydrodynamic model.

## 1.4 Interactions in active matter systems

As written in the last section, not only simulation models for active matter exist, but also experimental ones. One of these is the actin motility assay [15, 16, 19–21]. In essence, it relies on two main components: a surface (e.g., glass) on which heavy meromyosin motors have been attached and actin filaments that are placed on this artificially constructed "motor lawn". In the presence of ATP, motors push the filaments forward along their contour, which, driven by those continuously occurring powerstrokes, perform a persistent random walk; see schematic depiction in Fig. 1.3 (a) (and please refer to chapter 2 for a detailed description of the actin motility assay).

It was the first experiment to show polar waves [15], cf. Fig. 1.3(b), which are similar to the ones that were predicted by theoretical models (see section 1.3) and motility assays in general "are probably the best systems" [7] for the study of dry mostly aligning active matter since they are controllable and have a large number of agents.

The starting point of this thesis was the observation (made by our collaborator Ryo Suzuki in the Bausch lab) that the patterns produced in the motility assay can be altered by the addition of a depletion agent (see in-depth discussion of this mechanism in chapter 2), towards nematic lanes, see Fig. 1.4(c).

(a)                                                           (b)
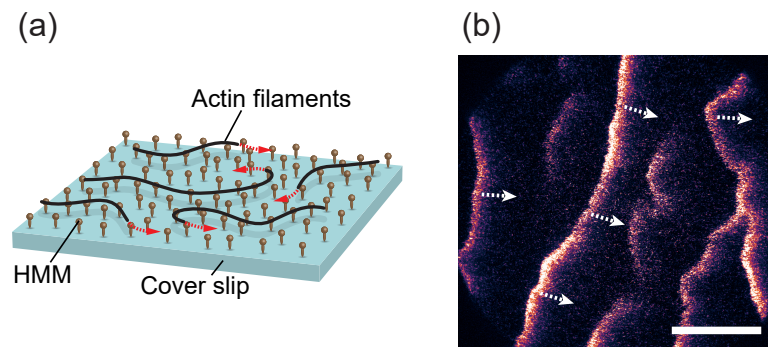


**Figure 1.3 Motility assay schematics and polar patterns.** (a) Schematic depiction of the actin motility assay. Heavy meromyosin motors (HMM) are attached to a planar glass surface. Actin filaments put on top of this "motor lawn" are pushed forward and perform a persistent random walk. (b) At high enough density of actin filaments, polar waves form on the motility assay. Scale bar: $100\mu m$. Adapted from [1].

This observation was very remarkable in light of the microscopic interactions that are observable between actin filaments. An exemplary time trace of the collision of two actin filaments, cf. Fig. 1.4(a), shows that filaments can pass over each other and that the alignment between them is only very weak. This can be further quantified by recording a binary collision statistics, see Fig. 1.4(b), for both the case in which the system exhibits polar patterns and the case of nematic lanes. The two collision statistics reveal several things. First that the interactions are indeed very weak, second that the difference between the nematic and polar case is not very pronounced, and third that the curves do not possess a clear symmetry from which one could try to unambiguously deduce the symmetry of the macroscopic patterns. These observations can be further illustrated by contrasting it with the situation in the Vicsek model, cf. Figs. 1.1 and 1.2, and can hardly be reconciled with the rather prevalent assumption that the symmetry of the order in active systems is mainly set by the symmetry of microscopic interactions [4, 5, 7, 83–90, 99]. The fact that it was already shown for the interactions measured in the polar case that, when they are incorporated into a kinetic Boltzmann approach (that has to rely on the approximations mentioned in section 1.3), can not explain the production of order [20], made this observation of a macroscopic change of patterns by a minute change of microscopic interactions even more puzzling.

Can such weak and mixed interactions solely be responsible for the observed patterns? And what would be the implications for the pattern formation process? To answer these questions, we sought to simulate the motility assay with an agent-based simulation. We aimed to account for the key features that seemed us to define the characteristic motion of the filaments and their interaction with each other. These are, first, that filaments can cross each other (i.e., they only possess a weak

(a)



(b)  (c)
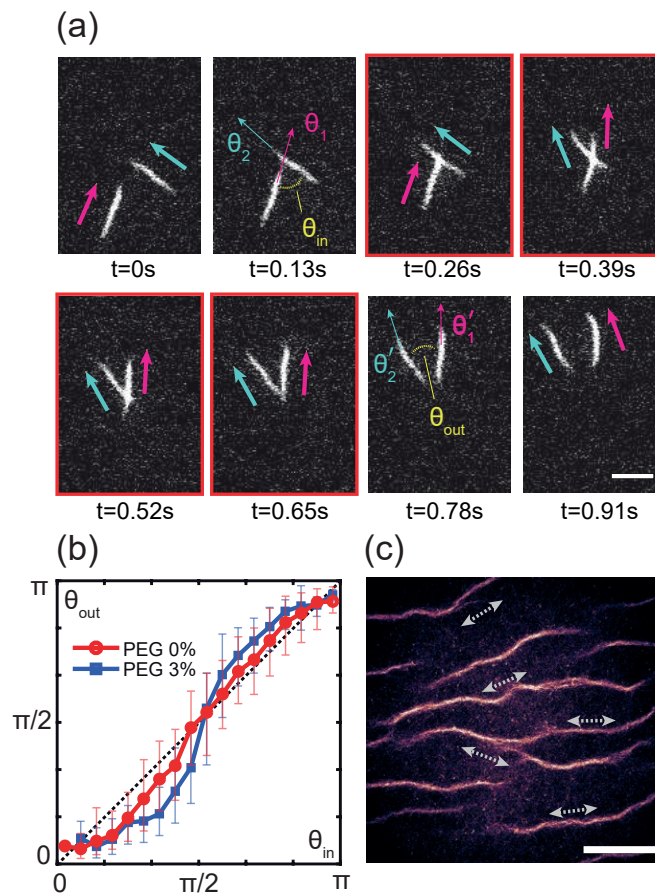


**Figure 1.4 Filament interaction in the motility assay.** (a) Time trace of the collision of two polymers. Filaments are able to cross over each other and only a slight change in the relative angle is observable. Scale bar: $2\mu m$. (b) Binary collision statistics of interacting filaments. Red curve corresponds to the motility assay without PEG. Blue curve to a system with PEG added. (c) Addition of PEG leads to the formation of nematic lanes instead of polar waves in the motility assay. Scale bar: $100\mu m$. Adapted from [1].

steric exclusion) and align only very weakly. And, second, that any perpendicular motion of the filament contour seems to be strongly suppressed due to anchoring via motors; hence a change of direction or orientation (be it random or due to interactions with other filaments) happens only at the tip of filaments, leading to the characteristic "snaking" or "trailing" motion of the polymer tails that follow the path taken by the tip; hence, noise and alignment interactions should act only on the tip and interactions should be weak and their alignment symmetry controllable. These requirements ruled out to adopt methods like the Vicsek model (see section 1.3) that is defined by strong interactions and point-like particles. But also other approaches that may seem suitable for slender particles like actin filaments, yet rely

on self-propelled rods [101, 107–110] or semiflexible polymers [112, 113, 130] that move freely and interact mainly via a steric exclusion process, which can lead to rotations and lateral movements of whole agents or even large groups of them (the characteristic polar moving agglomerations of most of these models –slightly reminiscent of "snow-plows"– seem not to be relevant for actin motility assays).
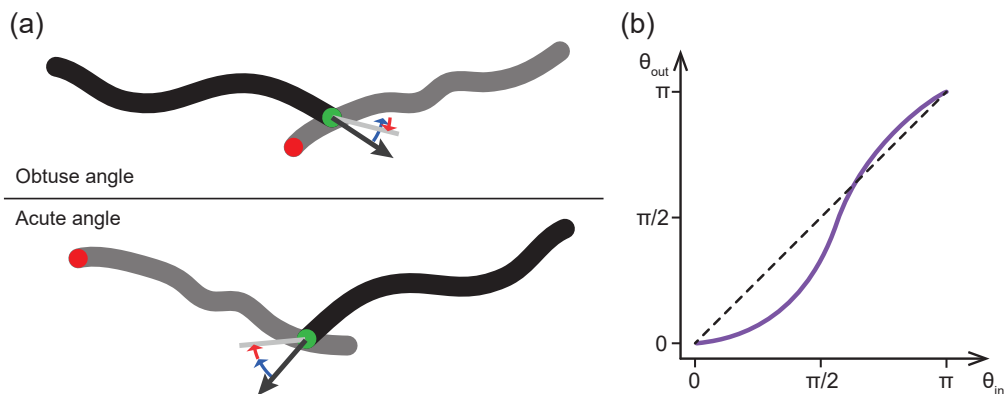


**Figure 1.5 Agent-based simulation of the motility assay.** (a) Schematic depiction of a filament (solid black with green tip) interacting with the tail of another polymer (grey with red tip). Two independently controllable alignment torques, a polar and a nematic one, act on its tip. For obtuse impact angles larger $\pi/2$ (upper panel) the nematic and polar torques (blue and red arrow) counteract each other, whereas for acute angles smaller $\pi/2$ they both align (lower panel). (b) By tuning the absolute strengths and relative ratio of the two alignment torques, the strength and symmetry of the interaction can be controlled, illustrated here by a schematic binary collision statistic of a weak and mixed interaction.

Therefore, we developed a new simulation method that met the requirements stated above. Its main function principle is outlined in Fig. 1.5 (a detailed presentation of the model and its underlying simulation algorithm can be found in chapters 2 and 3).

In chapter 2 we use this simulation method to show that the weak interactions observed in the actin motility assay seem to be indeed sufficient to account for the observed patterns. We further discover that polar and nematic patterns can simultaneously occur (together with a disordered background) at the same time in the same system, thereby forming a novel three-phase coexistence. We subsequently reproduced this observation experimentally in the actin motility assay.

This implies that the symmetry of order in active systems, other than often assumed, does not seem to be uniquely "imprinted" by the microscopic interactions, but rather to be an emergent and dynamic property. Other than in equilibrium, microscopic details seem to matter in active systems.

At this point, it may be worth noting that many aspects of our findings were already replicated by others [71, 129] (see also conclusions and outlook in chapter 6).

We designed the simulation algorithm to be as performant as possible. Thanks to this focus, we are capable to simulate large timescales on all relevant lengthscales, from single filaments to millions of polymers. Fig. 1.6 shows an exemplary simulation in the coexisting parameter regime of a system consisting of over 2 million filaments. We will further harness this power in chapter 3 and 4 of this thesis (for an outline and motivation of the research questions treated in these chapters, please refer to the next two sections).
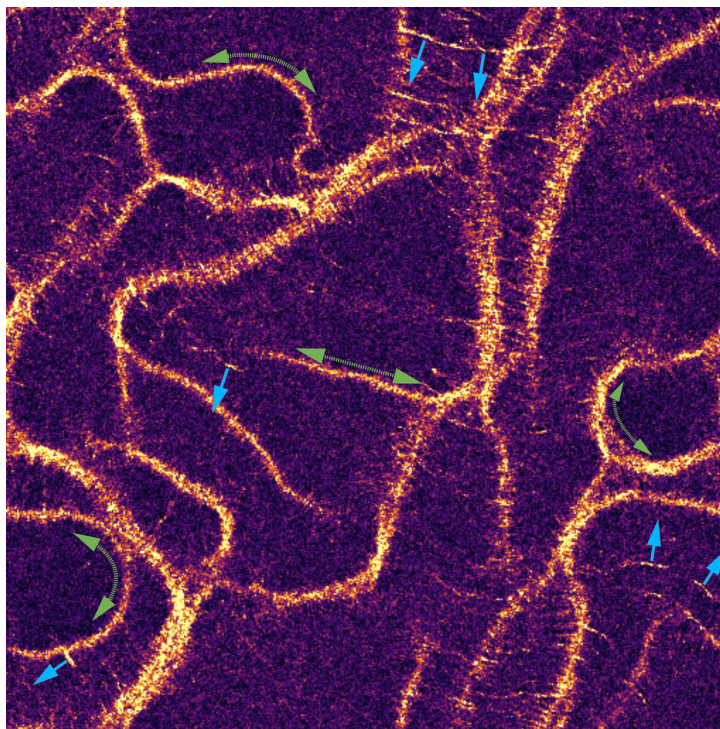


**Figure 1.6 Large-scale agent-based simulation.** Nematic lanes (some indicated by green double-headed arrows) and polar waves (some indicated by blue single-headed arrows) coexisting with a disordered background in a large-scale agent-based simulation containing 2176000 filaments. Same parameters as Fig. 2.4(C) with four times larger area.

## 1.5 Formation and maintenance of polar order

Other than the coexistence phase we presented in the last section, the parameter regimes of active matter systems in which only one single type of order or pattern can be observed have been extensively studied [5, 7, 131]. In the focus of many studies has been the macroscopically observable outcome (i.e. macroscopic patterns or global order) and how these phenomena change in dependence on parameters. More specifically (and as already touched upon in section 1.3), it is for example known that in polar flocking models the onset of order is discontinuous [84, 85, 96] and that generally the ordering process seems to be akin to a phase separation scenario [61–63]; cf. Fig. 1.7 for a pictorial illustration. In the region between disorder and the homogeneously ordered state (between the binodals), polar patterns are coexisting with a disordered background [63, 85, 96]. Near the boundaries between binodal and spinodal, the adjacent homogeneous state was found to be metastable in Vicsek and other types of models [61–63, 85]. In addition to that, the region where polar patterns can form was discovered to be indeed microphase separated [15, 63, 69, 85], which has been further investigated by means of continuum models [63, 94, 98].
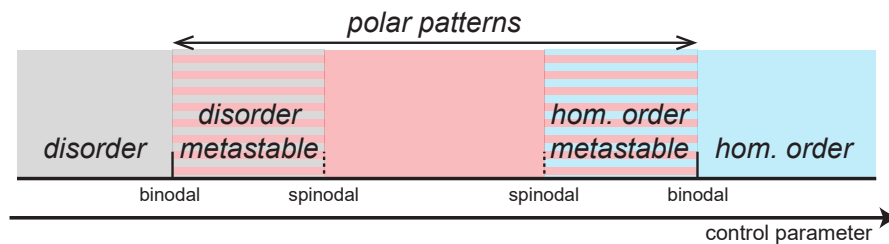


**Figure 1.7 Phase separation in polar active matter.** Schematic depiction of the prevailing phase separation picture that illustrates the behavior observed in flocking models, in dependence on a control parameter (like density or inverse noise strength). The disordered state is separated from the homogeneously ordered one (polar "liquid") by a coexistence regime in which polar patterns coexist with a disordered background. On the two borders of this regime, between the binodals and spiondals, the adjacent homogeneous phase is metastable.

Yet, the situation on the level of mesoscopic and microscopic length scales is different. The spontaneous formation of particle clusters are known to play an important role for the onset of flocking [85, 96, 132], besides this, however, the microscopic and mesoscopic processes and mechanisms that consitute the assembly pathway from a disordered to the macroscopically ordered state, and how that microphase separated ordered state is maintained, is not know.

In chapter 3 we employ our agent-based simulation –which gives us access to all length-scales, from microscopics to emergent phenomena– to investigate these processes.

A careful look at the polar structures in our system shows that they are composed of spatially separated clusters that are strongly ordered. Similar aggregations, yet disordered ones, can also be found outside patterns; cf. pictorial illustration in Fig. 1.8. To understand their role for the whole pattern formation and maintenance process we developed a tracking method to algorithmically and dynamically identify all clusters, their internal degree of order, as well as particle flows (with single agent resolution) between them. We employed this method to investigate the build-up process of order and the subsequent micro-phase separated non-equilibrium steady state; thereby identifying key exchange processes between clusters of different size and order. We further verified that these kinetic processes are indeed sufficient to explain the observed behavior by developing a kinetic model for a population of disordered and ordered clusters, which we based on these processes (reminiscent approaches have been used in previous works, yet only for a single cluster species [101, 133, 134]).

Although being space independent, this model shows the same metastability, micro-phase separation, and cyclic mass-flow dynamics as the agent-based model. This strongly indicates that micro-phase separation –and potentially also other phenomena like nematic laning or coexisting types of order (cf. section 1.3 and chapters 2 and 4)– can be understood in the framework of mesoscopic kinetic processes.
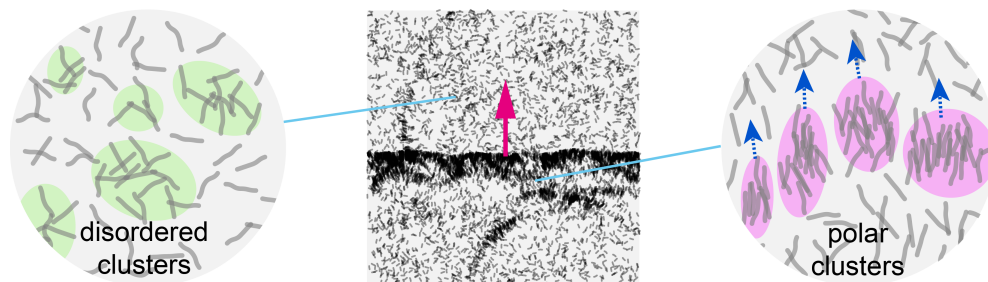


**Figure 1.8 Cluster decomposition in agent-based simulations.** The polar ordered patterns and the disordered background observed in agent-based simulations can be decomposed into clusters of different degrees of polar order. Pictorial illustration of disordered clusters in the background (left panel, green shaded) and clusters with a high degree of internal order (right panel, pink shaded) inside the patterns.

## 1.6 Topological structures in phase-separated nematic systems

Similar as for the polar case, also the phenomena in parameter regimes where only nematic patterns can be observed have been extensively studied. In these compressible active nematics, like, e.g., the nematic Vicsek model [86–88] (see also sections 1.2 and 1.3), one observes a phase separation into dense nematic lanes [cf. Fig. 1.2(d)] that are unstable with respect to bending undulations on very large length and time-scales [7, 86, 99, 100, 124, 135, 136].[3]

In parameter regimes where our agent based simulation showed nematic lanes only (i.e. for interactions that have small or no polar bias, see also chapter 2 and section 1.4), we could precisely observe this expected behaviour; cf. Fig. 1.9(a) for an example of an undulating nematic lane.
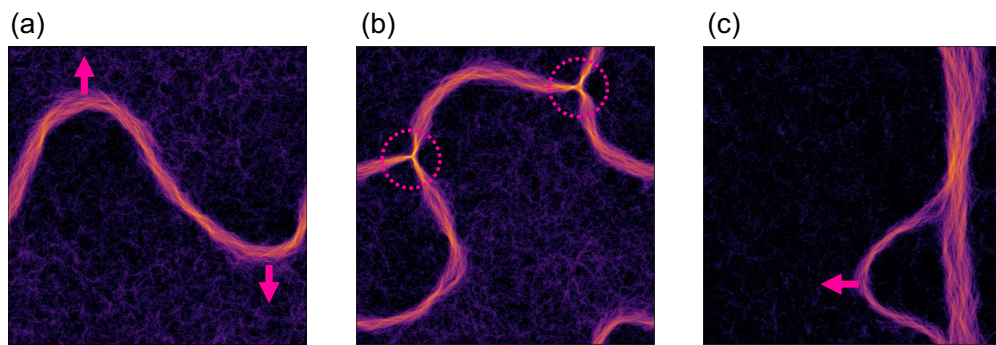


**Figure 1.9 Dynamical nematic structures.** (a) On large length and time scales nematic bands exhibit bending undulations. Magenta arrows indicate the lateral direction of motion. (b) High density $-1/2$ defects at the core of lane junctions. (c) Filamentous arc detaching from a nematic lane.

Yet, we additionally saw previously unreported structures that seem to be linked to these bending undulations. More specifically, we observed three-armed intersections of lanes, in the centers of which a $-1/2$ defect is located [Fig. 1.9(b)]. This is peculiar since defects are commonly only associated with dense, not phase-separated active nematics [18, 48–51]. Furthermore, the defects we observed are associated with a strong increase in density of the nematic phase and do not possess a $+1/2$ defect-pair, but are surrounded by a positively charged region of space. In addition to that, we observed another topologically charged structure, namely curved arcs

---

3 Under certain circumstances also another type of instability occurs where nematic lanes split up transverse to their contour [100, 136], yet the conditions in the actin motility assay –the system our agent-based simulations model– are believed to only facilitate bending undulations [100].

that detach from large nematic lanes, cf. Fig. 1.9(c), which are accompanied by a cloud of positive topological charge density on their concave side.

What causes these topological structures to emerge in a compressible active nematics? How does their formation depend on external control parameters? To answer these questions in chapter 4, we tracked particle trajectories through defect arms in detail, thereby obtaining the precise velocity and flow structure which, e.g., enabled us to exclude any MIPS-like mechanism (see section 1.2) behind these defects. We constructed a hydrodynamic model, based on previous works [124, 136], that showed the same phenomenology as the agent-based simulation and exhibited the same topologically charged structures. This model gave us access to the phase diagram structure of the occurrence of the various phenomena –the validity of which we substantiated with large-scale sweeps of the agent-based simulation– and enabled us to identify curvature-induced density fluxes as the mechanism behind both the defects and arcs.

## 1.7 Active polar currents on passive nematic patterns

Besides the self-organization of active matter systems caused by agent-agent interactions alone, as discussed in the above sections, an alternative approach to obtain patterns or order in them is to influence their dynamics externally. One general pathway to this end is the introduction of anisotropies in the space in which particles move. For example, it was shown that active particles aggregate in the vicinity of rigid boundaries [137] or that by introducing wedged-shaped obstacles into active systems, agents can be trapped and up-concentrated in targeted areas [138, 139]. Further, it was found that in systems in which interactions do not depend on the euclidean distance between agents (cf. section 1.2), randomly distributed obstacles can induce the formation of polar patterns [81]. Alternatively to a collection of isolated inhomogeneities, the behavior of active agents can be altered by embedding them in a background that is patterned as a whole. More specifically, motile agents coupled to a nematic liquid crystal exhibiting defects were shown to accumulate their density inside +1/2 defects and deplete it in -1/2 ones [140, 141]. Further, a liquid crystal pre-patterned to a bend-splay configuration was shown to funnel active particles into polar streams [142].

Recent experiments by our collaborators in the Bausch lab showed that also the behavior of microtubules in a gliding assay can be significantly altered when it is coupled to a nematic background. More specifically, microtubule embedded in a self-assembled actin nematic aligned to (and propagated along) the director of this nematic background and concentrated into dense streams in which particles move in a polar fashion into one direction (cf. Fig. 1.10(a)). Observations suggest that these streams are channeled and strongly influenced by +1/2 topological defects.

(a)



(b)
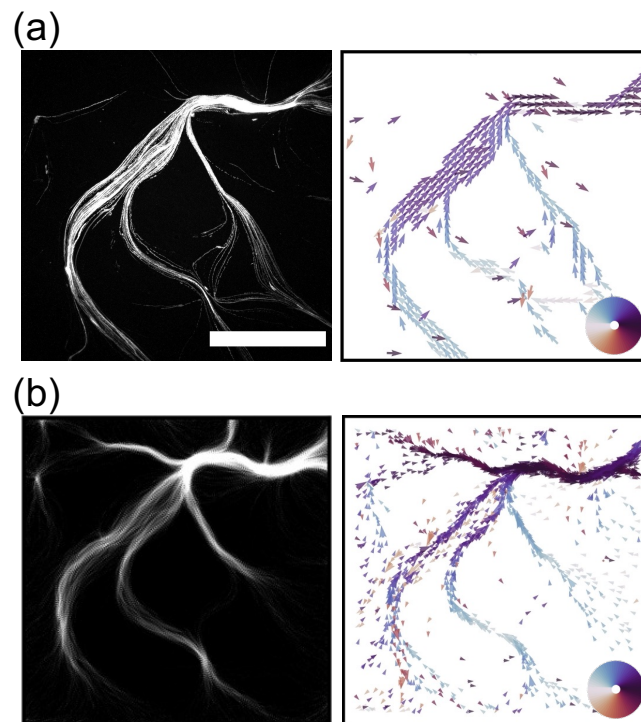


**Figure 1.10 Polar trajectories on passive nematics.** (a, left panel) Experimental trajectories of microtubules coupled to actin nematics are concentrated in dense streams. (a, right panel) Flow field of particle direction. Microtubules inside streams move in a polar fashion into the same direction. (b, left pane) Simulated particles coupled to a nematic background whose structure was extracted from the experimental actin nematic in the field of view of panel (a) show a comparable accumulation into lanes. (b, right panel) Flow field of particle direction in the simulation. Agents move in the same manner as in the experiment.

This emergence of polar patterns seemed peculiar since particle alignment to the background happens in a nematic fashion and the actin nematic background did not exhibit any intentionally induced polar symmetry. On the contrary, half-integer defects that emerged during the self-assembly process of the passive actin nematic background were located at random positions and with random orientations. Further, this effect is observable for very low microtubule concentrations, rendering inter-particle interactions unlikely to contribute to this ordering process.

Can alignment with the actin background, and hence the shape of the nematic field, be solely responsible for the formation of polar streams? To test this hypothesis in chapter 5 we developed an agent based simulation in which microtubules are represented by self propelled circular particles that can nematically align to a nematic background field with a pre-defined strength. Using nematic fields extracted from microscopy images as the background field for the simulation, we found that results

from experiments could be reproduced remarkably well. Despite its reductiveness, agents in the simulation form qualitatively similar polar streams (cf. Fig. 1.10(b)) above a certain level of alignment strength to the background. It is worth noting that these results were independent of particle-particle alignment being present or not. By simulations with artificially generated nematic fields in which defect orientations are controllable, we found that $+1/2$ defects and their orientation are indeed crucially important for the formation and direction of polar streams.

We further probed this finding with another theoretical approach in which trajectories are started near $+1/2$ defects at points that we deduce via a heuristic algorithm from the configuration of the nematic field in the vicinity of the defects. By subsequently simply following nematic field lines the same qualitative arrangement of streams is obtained as in simulations and experiments, underlining the defining role of $+1/2$ defects.

# 2 Emergence of coexisting ordered states in active matter systems

*The following chapter is based on research published in Science **361**, 255-258 (2018) [1] that I conducted together with Lorenz Huber, Ryo Suzuki, Erwin Frey and Andreas R. Bausch and to which I, together with L.H. and R.S., contributed as one of the shared first authors. Experiments were performed and designed by L.H., R.S., T.K. and A.R.B. Simulations were performed and designed by L.H., T.K. and E.F. All authors participated in interpreting the experimental and theoretical results.*

Active systems can produce a far greater variety of ordered patterns than conventional equilibrium systems. Especially, transitions between disorder and either polar- or nematically-ordered phases have been predicted and observed in two-dimensional active systems. However, coexistence between phases of different types of order has not been reported. We demonstrate the emergence of dynamic coexistence of ordered states with fluctuating nematic and polar symmetry in an actomyosin motility assay. Combining experiments with agent-based simulations, we identify sufficiently weak interactions that lack a clear alignment symmetry as a prerequisite for coexistence. Thus, the symmetry of macroscopic order becomes an emergent and dynamic property of the active system. These results provide a pathway in which living systems can express different types of order by using identical building blocks.

## 2.1 Introduction

The distinctive feature of active matter is the local supply of energy that is transduced into mechanical motion. Examples include assemblies of self-propelled colloidal particles [22–24, 143, 144], self-organising systems comprised of biopolymers and molecular motors [15–17, 145], and layers of migrating cells [146, 147]. These systems exhibit a rich phenomenology of collective phenomena and emergent properties, with features absent in passive, equilibrium systems. Self-propelled colloidal particles interacting solely by steric repulsion have been predicted [148, 149] to show phase separation into an ordered, solid-like phase with a disordered gas-like phase, similar to experimental observations [22, 23, 144]. Active systems comprised of rod-shaped particles, cytoskeletal filaments, or colloidal particles with velocity

alignment interactions show an even broader range of collective behaviour including polar clusters [15, 16, 24, 143], nematic lanes [145], and vortex patterns [17, 150], which in all cases phase-separate with a dilute isotropic, disordered background. Theoretical studies have shown that, in principle, alignment interactions can explain how these different types of orientational order and transitions between them emerge based on either agent based [86, 87, 91, 96, 99, 128, 151] or mean-field models [84, 99, 115, 118, 128, 152–155]. All these studies tacitly assume that, as in systems in thermal equilibrium, the symmetry of the observed macroscopic order is largely dictated by the symmetry of local alignment interactions. But to what degree is the symmetry of the macroscopic order constrained by the symmetry of the microscopic interactions? More broadly, can active systems depart from these constraints and express a multitude of different ordering simultaneously, as is the case for living systems like actin stress fibres and filopodia [30, 156]?

To study these fundamental questions, we employ the high-density actomyosin motility assay [Fig. 2.1(A)], which is ideally suited to address the microscopic processes that underlie pattern formation in active systems [15, 16, 19, 20, 157, 158]. By sensitively tuning the interactions between the myosin-driven filaments with a depletion agent, we are able to observe the emergence of a phase in which nematic and polar order stably coexist. The complete phase diagram is recovered from agent-based simulations of self-propelled filaments, in which weak alignment interactions quantitatively reproduce the experimentally determined microscopic collision statistics. We show that sufficiently weak interactions generically lead to dynamic coexistence of three phases (isotropic, nematic, and polar).

In the actomyosin motility assay, hydrolysis of adenosine triphosphate (ATP) enables actin filaments to actively glide over a lawn of non-processive heavy meromyosin motor proteins [157, 158]. Previous studies have shown that increasing the filament density beyond a critical value results in the emergence of polar clusters and waves [15, 16] [Fig. 2.2(A)]. These patterns are produced by collisions in which filaments may align in a polar or nematic fashion. The degree and symmetry of the alignment depends on the change in the relative orientation of the interacting filaments, $\Delta = \theta_{out} - \theta_{in}$, where $\theta_{in}$ and $\theta_{out}$ are the angles before and after a collision event, respectively [Fig. 2.1(B)]. In theoretical studies [84, 86, 87, 91, 96, 99, 115, 118, 128, 151–155] these collisions have been idealized by assuming that filaments either align in a strictly polar or strictly nematic fashion upon colliding [Fig. 2.1(C)]. However, in actual experimental active-matter systems [17, 20, 105, 145], the degree of alignment caused by a single collision event is weak, i.e. the relative change in filament orientation is small, $|\theta_{out} - \theta_{in}| \ll \pi$ [Fig. 2.1(D)]. Moreover, the resulting alignment exhibits neither perfectly nematic nor perfectly polar symmetry. Instead, depending on the collision angle $\theta_{in}$, in the motility assay there is a weak tendency to favor either alignment or anti-alignment of the filaments [Figs. 2.1(C, D)]. How then can such weak interactions without a clear alignment symmetry on
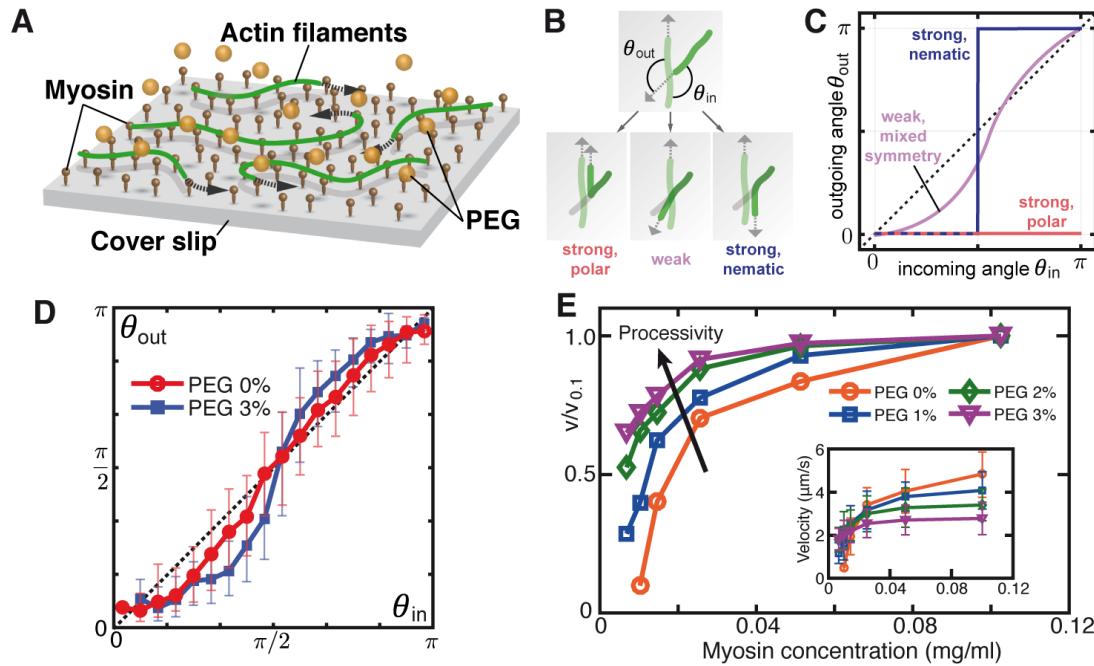
**Figure 2.1 Interactions in the actomyosin assay.** (**A**) Schematic of the actomyosin motility assay. PEG acts as a depletion agent. (**B**) Illustration of different filament collision geometries with an incoming angle $\theta_{in}$, and corresponding binary collision curves (**C**). While strong polar or nematic collision rules lead to full alignment or anti-alignment, weak collisions cause a gradual change of orientation and may exhibit both polar and nematic features (purple line). The dashed line depicts neutral collisions ($\theta_{out} = \theta_{in}$). (**D**) Binary collision statistics. Blue squares: PEG 3% (389 collisions). Red circles: no PEG (1113 collisions; data from Ref. [20]). Error bars, ± SD. (**E**) Processivity increases with PEG concentration, as indicated by the earlier saturation of normalized filament velocities as a function of motor density. $v_{0.1}$ is the velocity at $0.1\,mg/ml$ non-processive heavy meromyosin. Inset: absolute filament velocities.

a local scale lead to collective order at the system level, and what features of the local interactions determine the global symmetry of the macroscopic state?

## 2.2 Results

### 2.2.1 Nematic lanes in the motility assay

To answer this question we tuned the local interactions between the filaments, by adding polyethylene glycol (PEG, 35 kD), a depletion agent, at concentrations of up to 3% (w/v) to the assay [Fig. 2.1(D), Fig. 2.5]. The observed change in the binary collision statistics can be attributed to the excluded-volume effect of the
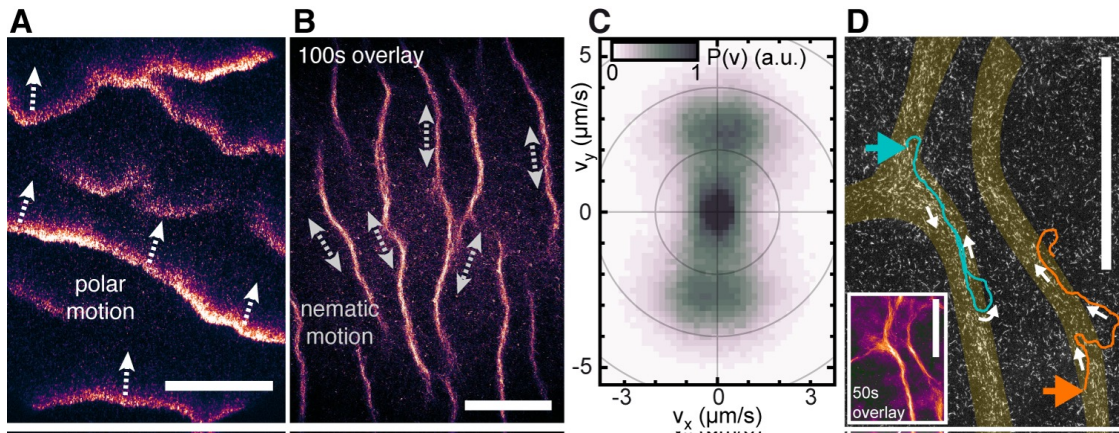
**Figure 2.2 Experimental phenomenology.** (**A**) Polar actin clusters formed in the absence of PEG, moving in the same direction as the filaments (the fraction of fluorescently labelled filaments is 1:50, monomeric actin concentration 10 $\mu M$). (**B**) Large network of high-density nematic lanes formed at a PEG concentration of 3% and 5 $\mu M$ actin. The image is an overlay covering a period of 100 $s$ to demonstrate that the structure is frozen and stable. Filaments move along the lane contours in opposite directions (labelled filament fraction is 1:60). (**C**) Probability density $P(v_x, v_y)$ of instantaneous velocities shows the preferred bi-directional motion of filaments within a lane. (**D**) Single filaments move inside lanes (bright region). Two representative trajectories are shown (turquois and orange) at 10 $\mu M$ actin and 2% PEG. Inset: overlay covering a period of 50 $s$. Polar (**A**) and nematic (**B**) motion are depicted by bi- and unidirectional arrows, respectively. Scale bars: 100 $\mu m$.

PEG molecules, which forces the filaments closer to the bottom surface covered with motors, enabling each to interact with more motors on average, with a con-comitant increase in motor processivity [Fig. 2.1(E)]. This reduces the incidence of collisions where filaments just pass over each other [145], and increases the likelihood that filaments will repel each other sterically, thus enhancing the tendency to align nematically [cf. Fig. 2.1(D)and section 2.4]. This technique enabled us to continuously modulate the symmetry of alignment interactions at the microscopic level, and probe the robustness of pattern formation in the gliding assay at high filament densities. Despite the rather minute changes in interaction characteristics caused by adding PEG at a concentration of 3% [Fig. 2.1(D)], we found that polar flocks no longer form. Instead, the moving filaments quickly, within a few minutes, self-organize into a network of "ant trails" [Fig. 2.2(B), Movie S1 in [159]]. In contrast to the unidirectional filament motion found within polar clusters, the fila-ments that form these "lanes" move bi-directionally, as do many colonial ant species [34]. Since the filaments move along these tracks in either direction with equal probability [Fig. 2.2(C), Fig. 2.6], the overall order is nematic, not polar, and stable; this is quantified by the local nematic order [Fig. 2.6(A)] and the autocorrelation

function of the filament orientations [Figs. 2.6(D,E)]. Moreover, while polar clusters propagate through the system at uniform speed, nematic lanes form static networks with branches spanning up to several 100 μm in length [Fig. 2.2(B)]. Filaments are also seen to continuously leave and enter the trails [Fig. 2.2(D), Movie S2 in [159]], such that these branches remain fixed in orientation and slowly grow and shrink at their ends [Fig. 2.6(F)]. These processes, operating on a timescale of minutes, lead to a slow reorganization of network architecture, with new branches forming (Movie S3 in [159]) while others contract (Movie S4 in [159]). Note that these networks are isotropically oriented and that no significant actin bundling was observed below 3% PEG.

### 2.2.2 Agent-based simulation

This fundamental qualitative change in macroscopic order, from propagating waves of polar order to branched networks of stable lanes within which filaments move bidirectionally, induced by relatively minor changes in interaction characteristics at the microscopic scale, is puzzling. To reveal the underlying mechanism, we developed an agent-based computational model that goes beyond simple collision rules and faithfully reproduces the experimentally observed (microscopic) binary collision statistics, and used it to predict the collective dynamics at large scales. Propelled actin filaments are modeled as discrete, slender chains of length $L$ [cf. Fig. 2.3(A), Fig. 2.7 and section 2.5]. Each filament is assumed to move at a constant speed v with the body of the filament following the tip. The direction of motion changes upon interaction with other filaments, as well as through interaction with molecular motors. When the leading segment of a given filament collides with a segment of another filament at a relative orientation $\theta$ , an alignment potential $U(\theta)$ acts upon the tip. This potential is assumed to be the sum of terms with polar and nematic symmetry, $U(\theta) \propto \phi_p \cos(\theta) + \phi_n \cos(2\theta)$, where $\phi_p$ and $\phi_n$ represent the respective mean change in orientation during a collision. We adjusted $\phi_p$ and $\phi_n$ such that the binary collision statistics of the computational model [Fig. 2.3(B)] closely resemble those observed experimentally [Fig. 2.1(D)].

Having validated the computational model at the microscopic level, we asked whether it captures the collective dynamics of the high-density actomyosin motility assay. We first performed large-scale simulations for model parameters corresponding to the absence of PEG. Starting from a random uniform distribution of filaments, we observed that high-density wave fronts of polar ordered filaments rapidly form, surrounded by disordered, low-density regions [Fig. 2.3(C), Movie S5 in [159]]. This matches the phenomenology observed in the motility assay. Next, we performed simulations in a parameter regime corresponding to 3% PEG. Again, in agreement with our experiments, we found networks of high-density nematic lanes surrounded by disordered, low-density regions [Fig. 2.3(D)], reminiscent to chaotic structures
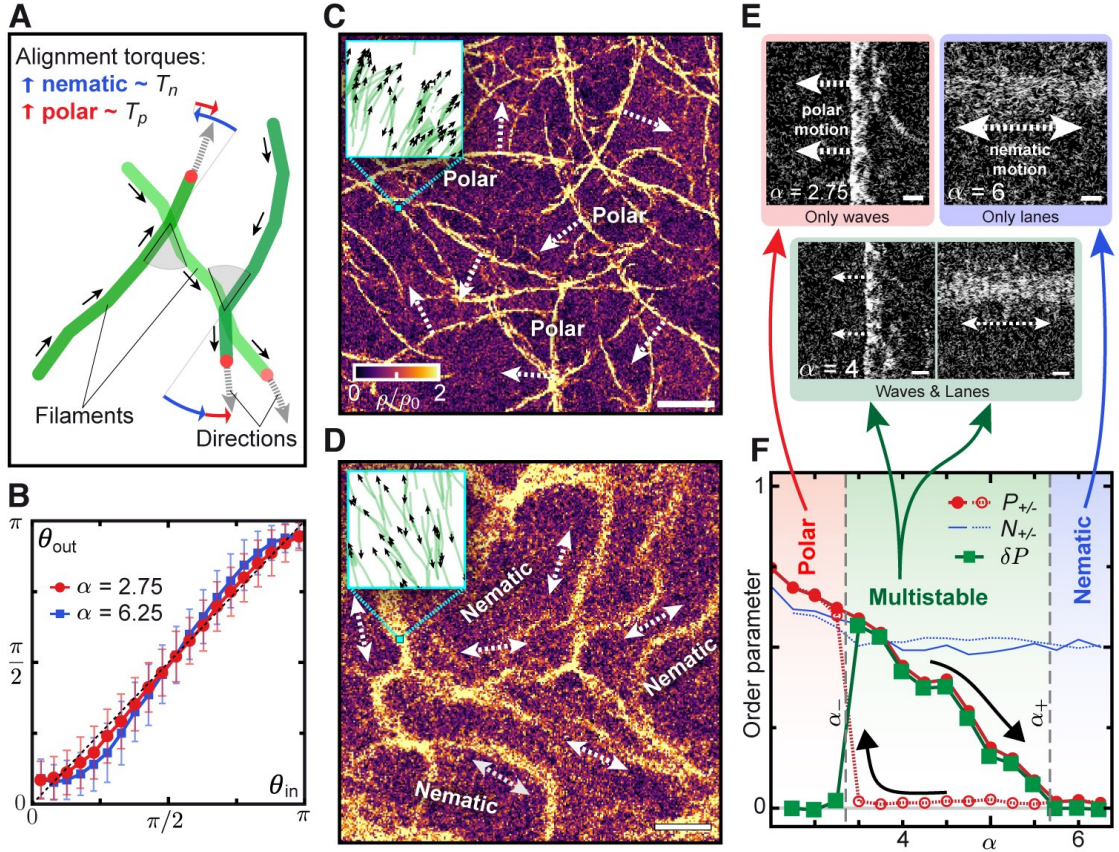
**Figure 2.3 Simulation model and phenomenology.** (**A**) Illustration of the simulation model: filaments (green) are propelled along their contour (solid black arrows). Upon collision, the orientations of tips (gray arrows) are redirected in proportion to the polar and nematic alignment strengths (red and blue arrows). (**B**) Binary collision data from simulations for two selected curves with different $\alpha$. Error bars, 1 standard deviation. (**C, D**) Emergence of (**C**) polar waves ($\alpha = 3$) and a (**D**) network of nematic lanes ($\alpha = 6.25$) in large-scale systems. Insets: filaments within a single pixel with local density $\rho$ and local polar (**C**) or nematic (**D**) order. In both panels, 544,000 filaments were simulated in a box of length $650.2L$, with a homogeneous density $\rho_0 = 1.29/L^2$. Scale bars: $100L$. Uni- and bidirectional arrows denote local polar and nematic filament motion. (**E**) Different steady states for small simulation boxes, with $\rho_0 = 1.29/L^2$: while $\alpha = 2.75$ always produces polar waves and $\alpha = 6$ always nematic lanes, at $\alpha = 4$ either waves or lanes can be obtained in different realizations. Scale bars: $10L$. (**F**) Global order parameters during a hysteresis loop in $\alpha$. Black arrows denote the direction of the loop. Regions of non-zero $\delta P$ (shaded in green) exhibit multistable behavior. For (**B-F**), $\phi_p = 2.1°$.

that were predicted for active nematics [99]. The overall network architecture changed slowly, with trails extending or retracting from their ends, and some lanes merging on longer time scales [Fig. 2.8(A), Movie S6 in [159]].

### 2.2.3 Coexistence of polar and nematic patterns

The model was then used to predict the dependence of nematic vs. polar order on the filament density $\rho_0$ and the ratio of nematic to polar alignment strength, $\alpha = \phi_n/\phi_p$. To facilitate simulations over a broad parameter range, we considered smaller systems with a box size of 81.3 $L$. We monitored the (global) polar and nematic order parameters, $P = |\langle \exp(i\theta) \rangle|$ and $N = |\langle \exp(2i\theta) \rangle|$, respectively, measured over all filaments after the dynamics had become stationary [Fig. 2.8(B)]. In initial parameter sweeps we observed that, within certain intervals of $\alpha$, simulations starting from different realizations of randomly distributed filaments, but with identical parameter sets, sometimes resulted in polar and sometimes in nematic patterns [Fig. 2.3(E), lower panel]. Similar observations were made in a Vicsek-type model, but only if strong additional memory in the particle movement is included [151]. The patterns in our simulation were stable within the simulation times and no switching between them was observed, suggesting the existence of a regime of interaction strengths in which the dynamics exhibit multistability. To probe these initial observations further, we checked for hysteresis effects in the collective dynamics [cf. Fig. 2.9 and section 2.5]. To this end, we initiated our simulations in a parameter regime in which the system shows polar waves only [$\alpha = 2.75$, Fig. 2.3(E), left panel], waited until the dynamics became stationary, and then quasi-statically increased the value of $\alpha$ (i.e. giving the system sufficient time to equilibrate between successive adjustments of $\alpha$), and monitored both nematic and polar order parameters [Fig. 2.3(F), closed symbols]. After reaching a regime in which the system gave rise to nematic lanes only [$\alpha = 6$, Fig. 2.3(E), right panel], we reduced the value of $\alpha$ quasi-statically [Fig. 2.3(F), open symbols]. While the nematic order parameter remained essentially unchanged, we observed a hysteresis loop in the polar order parameter $P$. As the relative strength of nematic to polar alignment is increased, the degree of polar order ($P_+$) gradually declines until it reaches zero at some critical value $\alpha_+$. Conversely, in the reverse direction, polar order ($P_-$) remains negligible up to a different critical value $\alpha_-$, and then suddenly jumps to a rather large value. The phase diagram in Fig. 2.4(A) was obtained using $\delta P = P_+ - P_-$ to quantify the degree of multistability.

To test these predictions, we performed experiments over a broad range of actin and PEG concentrations, and obtained a phase diagram [Fig. 2.4(B)] whose topology closely resembles that obtained from the computational model [Fig. 2.4(A)]. In particular, upon varying the strength of interaction between the filaments by changing the PEG level and thus $\alpha$, we find a broad regime of non-equilibrium steady
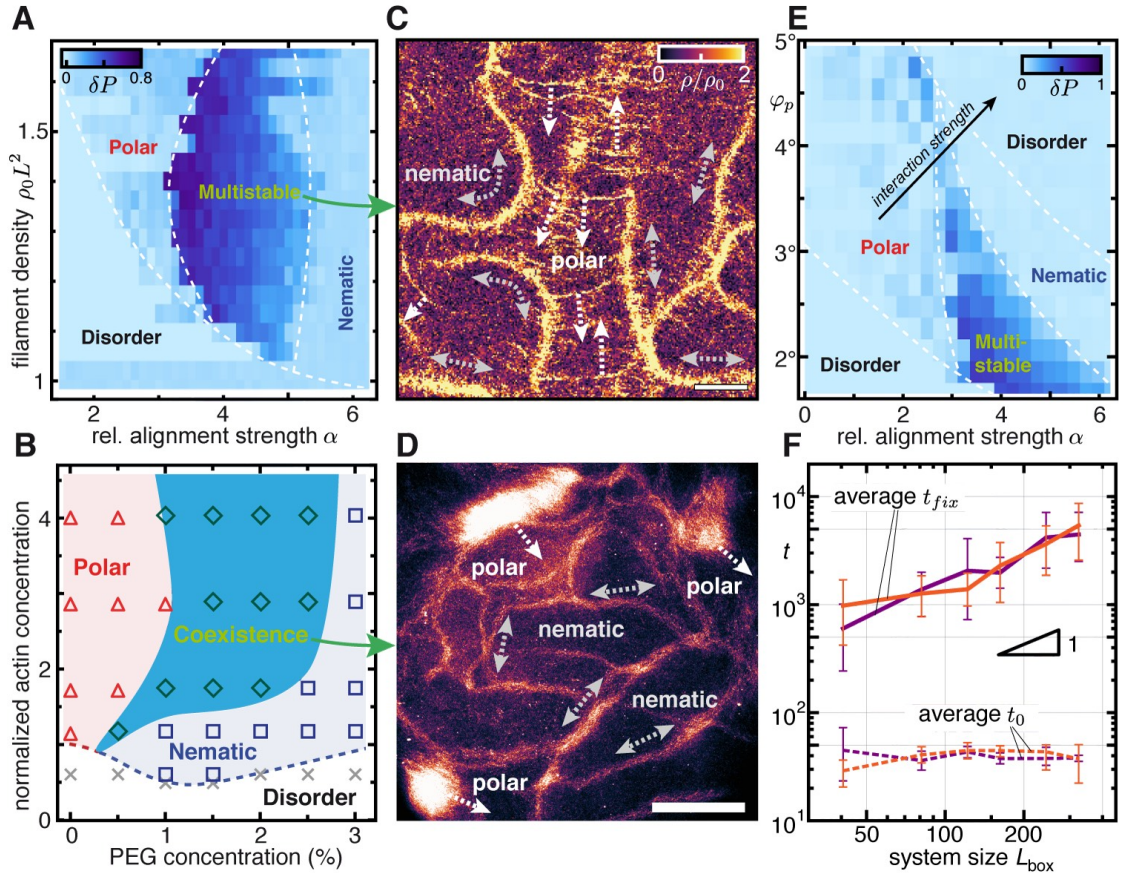
**Figure 2.4 Phase diagrams and coexisting symmetries in experiment and simulation.**
(**A**) Simulation phase diagrams for different filament densities $\rho_0$ and relative alignment strengths $\alpha$. (**B**) Experimental phase diagram of emergent patterns for varying monomeric actin and PEG concentrations. Gray crosses: disorder. Red triangles: polar clusters. Blue squares: nematic lanes. Green diamonds: coexisting polar and nematic structures. Actin concentrations were normalized with respect to the estimated critical concentration in the absence of PEG (see section 2.4 for details). (**C**) Emergence of both polar waves and nematic lanes in large-scale simulations (scale bar: $100L$) for $\alpha = 4$ and a homogeneous density $\rho_0 = 1.29/L^2$. (**D**) Coexistence of polar clusters and nematic lanes in the motility assay at 2% PEG and 5 $\mu M$ actin. Scale bar: 100 $\mu m$. (**E**) Phase diagrams for different polar alignment strengths $\phi_p$ and $\rho_0 = 1.29/L^2$. The total strength of alignment increases with both $\phi_p$ and $\alpha$. The shape of the phase diagram only slightly changes for larger system sizes [see Fig. 2.11(A)]. (**F**) Scaling analysis of time scales at two different parameter sets (orange data: $\phi_p = 2.1°$, $\alpha = 4.17$; purple data: $\phi_p = 3.3°$, $\alpha = 3.13$). The average coexistence lifetime $t_{fix}$ (solid lines) grows roughly linear with system size, while the average initial order time $t_0$ (dashed lines) remains small and constant. Averages taken over 25 simulations per size, error bars represent $15^{\text{th}}$ and $85^{\text{th}}$ percentiles (see section 2.5 and Fig. 2.11 for details). (**A,E**) Phase diagrams were obtained by hysteresis analysis in $\alpha$, white dashed lines depict the domain boundaries of the observed steady states. For (**A,C**), $\phi_p = 2.1°$.

states where polar waves and nematic lanes coexist simultaneously. Moreover, both simulations of large systems [Fig. 2.4(C), Movie S7 in [159]] and experiments [Fig. 2.4(D), Movie S8 in [159]] consistently show that the equilibrium is highly dynamic. Polar waves may invade regions containing nematic trails and thereby disrupt their network structure [Fig. 2.10(A)]. After the passage of these waves, nematic lane networks are observed to re-form locally, often close to their original positions. The formation of nematic lanes was also observed at the left and right edges of polar waves [Fig. 2.10(B), Movie S9 in [159]]. While in experiments, this coexistence remained stable during the full experiment duration [Fig. 2.10(C)], in simulations we performed a scaling analysis to probe the lifetime of coexistence $t_{fix}$ as a function of the finite system size, at different points in the multistable parameter region. We found that this lifetime grows linearly with the system size, while the time of initial pattern formation $t_0$ remains small and constant [cf. Figs. 2.4(F), 2.11 and section 2.5], implying a diverging time scale separation and stable coexistence in the thermodynamic limit.

## 2.3 Discussion

These observations from experiment and theory imply that polar waves and nematic lanes are both intrinsically stable structures, suggesting that the non-equilibrium steady state represents a dynamic equilibrium between different patterns, which - although they have conflicting polar and nematic symmetries - coexist in a dilute, disordered background. We attribute their coexistence to the weak interaction between the active particles, which determines macroscopic order not at the microscopic level but renders the symmetry of collective order itself to become an emergent property, which is dynamic in space and time. If this picture is valid, then an increase in the alignment strength at the binary level should eliminate the ambiguity in symmetry and prevent the emergence of coexistence. To test this hypothesis, we performed extensive numerical simulations by varying $\alpha$ and $\phi_p$ [Fig. 2.4(E)] and looking for multistability. Indeed, we find that as the total degree of alignment, i.e. both $\phi_n$ and $\phi_p$, is increased, the multistable region contracts and eventually vanishes completely. In this limit there appears to be a sharp transition between a polar and nematic phase, similar to previous findings in a Vicsek-type toy model [87]. We therefore conclude that the coexistence of patterns with mutual polar and nematic symmetries depends upon sufficiently weak alignment interactions between individual filaments. Furthermore, it seems to be crucial that the computational model includes arbitrary pairwise interactions and spatiotemporal correlations without relying on any ad hoc truncation. This allows for coarsening dynamics, where many different mesoscale filament configurations are explored until they take the form of either polar clusters or nematic lanes. These patterns become local attractors of the dynamics, such that

– despite their conflicting symmetries – they can exist in juxtaposition within the same system. This indicates that the celebrated Gibbs phase rule - stating that in thermal equilibrium, one-component systems a three-phase coexistence only occurs at a singular point in parameter space - is invalid in active systems. Overcoming this thermodynamic constraint may be an essential and simple prerequisite for biological systems to produce heterogeneous, multitasking structures out of a single set of constituents, like it is the case for the cellular actin network [30, 156] and migrating cell layers [146, 147].

## 2.4 Appendix: Experimental system

### 2.4.1 Assay preparation

G-actin solutions were prepared by dissolving lyophilized G-actin obtained from rabbit skeletal muscle [160, 161] in deionized water and dialyzing against fresh G-buffer ($2mM$ Tris pH 7.5, $0.2mM$ ATP, $0.2mM$ $CaCl_2$, $0.2mM$ DTT and 0.005% $NaN_3$) overnight at $4\,°C$. Polymerization of actin was initiated by adding one volume of tenfold concentrated F-buffer ($20mM$ Tris, $20mM$ $MgCl_2$, $2mM$ DTT and $1M$ KCl) to nine volumes of the G-actin sample. Heavy meromyosin (HMM) was prepared by dialyzing rabbit skeletal muscle against myosin buffer ($0.6M$ NaCl, $10mM$ $NaH_2PO_4$, $2mM$ DTT, $2mM$ $MgCl_2$, 0.05% $NaN_3$) at $4\,°C$ [162]. For fluorescence microscopy, fluorescently labelled filaments stabilized with Alexa Fluor 488 phalloidin (Invitrogen) were used. Flow chambers were prepared by fixing coverslips (Carl Roth, Germany) to microscope slides (Carl Roth, Germany) with parafilm. The coverslips were coated with a 0.1% nitrocellulose solution, which was made by diluting a 2% solution (Electron Microscopy Sciences, Hatfield, PA) in amylacetate (Roth), and were left to dry overnight, prior to constructing the flow chambers. The chamber is typically three orders of magnitude larger than the length of a single filament, to avoid boundary effects. Prior to experiments, HMM was diluted in assay buffer ($25mM$ imidazole hydrochloride pH 7.4, $25mM$ KCl, $4mM$ $MgCl_2$, $1mM$ EGTA and $1mM$ DTT), and actin was added to assay buffer that had been premixed with PEG 35,000 (Sigma) to yield a final PEG concentration of 0-3% (w/v). The flow chamber was briefly incubated with the HMM dilution and the surfaces were then passivated with BSA ($10mg/ml$ BSA (Sigma) dissolved in assay buffer), prior to addition of the actin solution. To initiate an experiment, $2mM$ ATP dissolved in assay buffer was injected into the flow chamber, together with a standard antioxidant buffer supplement (GOC, containing $2mg$ glucose oxidase (Sigma) and $0.5mg$ catalase (Fluka)) to prevent oxidation of the fluorophore. After all components had been combined, the flow chamber was sealed with vacuum grease (Bayer Silicones).

### 2.4.2 Assay concentrations

A list of all actin and PEG concentrations used for the figures and movies can be found in table 2.1. Unless stated otherwise, the HMM concentration was fixed at 0.1 $mg/ml$. Depending on the quality of the actin batch and the HMM motor proteins, filaments vary in length. Hence, critical densities in terms of monomeric actin concentrations vary between batches. Moreover, filament lengths appeared to be sensitive to PEG level, perhaps owing to enhanced filament rupture due to the increase in effective processivity. To obtain a reproducible, quantitative phase diagram from the patterns observed for different actin and PEG concentrations, we prepared a single actin batch (incubated at $10\mu M$ monomeric actin), with which we performed 39 experiments within $36h$, at final concentrations of between 0.8 and 10 $\mu M$ monomeric actin (the fraction of fluorescently labelled filaments was 1:25). For every experiment, the assay buffer was freshly prepared with one or other of seven different PEG premixes (0%, 0.5%, 1%, 1.5%, 2%, 2.5%, 3%). In Fig. 2.4(B) every actin concentration was normalized with respect to an estimated critical actin concentration of $1.75\mu M$ (at zero PEG) for this specific actin batch. At this critical concentration, the filament density was roughly 9.2 filaments $\mu m^{-2}$ and filament lengths were exponentially distributed with a mean in the range of $0.5 - 0.7\mu m$.

### 2.4.3 Image acquisition

A Leica DMI 6000B inverted microscope equipped with a 40x oil-immersion objective (NA: 1.25) was used to acquire data. Images were captured at a resolution 1344 x 1024 pixels with a charge-coupled device (CCD) camera (C4742-95, Hamamatsu) attached to a 0.35x or 1x camera mount. To track filament velocities, a TIRF microscope (Leica DMI 6000B, 100x oil-immersion objective (NA: 1.47), Andor iXon-Ultra-9369 camera with a resolution of 512 x 512 pixels) was used.

### 2.4.4 Experimental binary collision statistics

To study the binary collision statistics [20], the acquired images were first converted into binary images and filaments were then identified by skeletonization using a standard library "bwmorph" available in Matlab. The coordinates of the filament contour were extracted by using a cubic spline fit to obtain $\theta_1$, $\theta_2$ and $\theta'_1$, $\theta'_2$ to determine the incoming angle $\theta_{in}$ and outgoing angle $\theta_{out}$ [Fig. 2.5(A)]. Analysis of a collision begins once the images of two filaments intersect. In Fig. 2.5(A), the images that are framed by red boxes are representative of a detected collision event. The incoming angle $\theta_{in}$ is obtained 1 frame (0.13 sec) before the detected collision event, and the outgoing angle $\theta_{out}$ is taken 1 frame after the filaments cease to intersect. Here, only binary collisions are studied and all collisions involving more
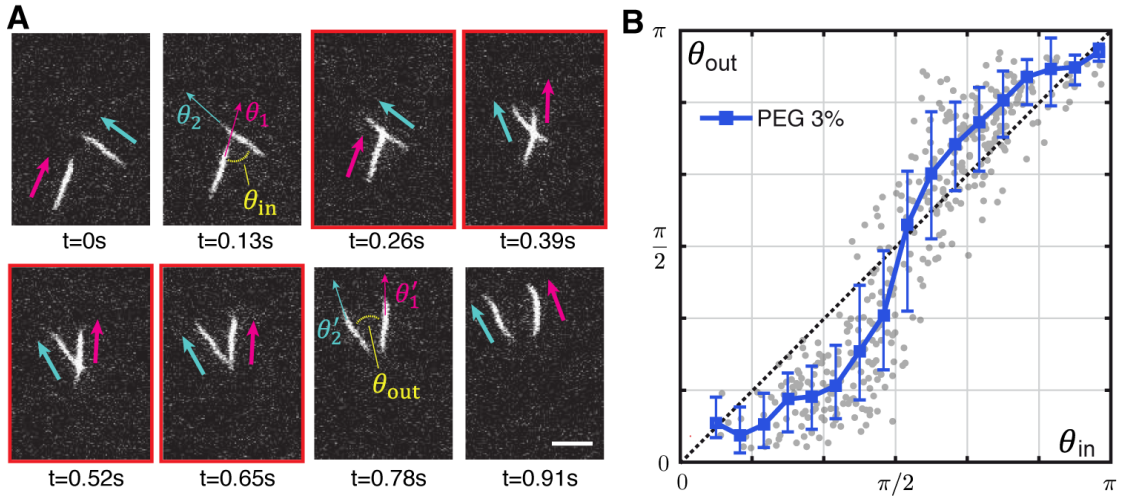
**Figure 2.5 Collision measurements.** (**A**) Illustration of collision angles during a binary collision. Scale bars: 2 $\mu m$. (**B**) Full binary collision statistics at a PEG concentration of 3%. Error bars, ± SD.

than 3 filaments were discarded. Fig. 2.5(B) shows all recorded collision events for a PEG concentration of 3%.

### 2.4.5 Processivity

To study the change in the filament-motor interaction as a function of the PEG concentration, the degree to which filaments were forced onto the HMM motor lawn as a result of the excluded-volume effect was evaluated by measuring the effective processivity. Processivity is a measure of the ability of a single motor to execute a power stroke continuously without releasing the filament. While HMM is non-processive, i.e. always releases the actin filament after the power stroke, an effective processivity at the single (actin) filament level can be assumed, since many motors act simultaneously along a filament and also the number of active motors should increase due to the filaments being pressed down onto the motor lawn by the PEG. The effective processivity was evaluated by monitoring the change in filament velocity as a function of changing the motor density; the absence of a change in velocity with a decrease in HMM density demonstrates maximal effective processivity, while decrease in velocity with decrease in HMM density indicates that the interaction is effectively non-processive in nature [163].

### 2.4.6 Velocity distribution and local order

Recording the nematic type of motion requires identification of single-filament motion, since opposing filament fluxes cancel each other out on larger length scales. For this reason, images were obtained by TIRF microscopy, which affords higher contrast and high temporal resolution (cycle time $\Delta t = 0.0853s$), to track the local motion of individual filaments between consecutive frames. We recorded a nematic lane at $5\mu M$ actin and 2% PEG concentration, and a polar cluster and a disordered region at $10\mu M$ actin and 1% PEG concentration [Figs. 2.6(A-C)]. We then segmented the images into 8 x 8 local bins and used the Kanade-Lucas-Tomasi feature-tracking algorithm in Mathematica 11.0.0.0, which is a robust estimator of the optical flow velocity, by maximizing the local intensity gradient correlation for each segment, in order to obtain a large number ($\sim O(105)$) of displacement vectors of filaments between consecutive image frames over an acquisition time of about a minute. From this we calculated smooth probability densities $P(v)$ of filament velocities [lower left panels of Figs. 2.6(A-C)], as well as the local polar and nematic order parameters $P = |\langle \exp(i\theta) \rangle_{\mathrm{ROI}}|$ and $N = |\langle \exp(2i\theta) \rangle_{\mathrm{ROI}}|$ at a given time in the region of interest (ROI), respectively, over the acquisition time [lower right panels of Figs. 2.6(A-C)]. To account for the shape of the lane structure, we only included bins that covered the lane [Fig. 2.6(A)]. Note that for the polar and nematic order parameters, the respective amplitudes are comparable to those from simulations. Apart from the case of a polar cluster [Fig. 2.6(B)], which is inherently not static within the fixed ROI, the order of a nematic lane [Fig. 2.6(A)] is stationary over an interval corresponding to filaments crossing the ROI about 2 times.

### 2.4.7 Autocorrelation function

Using an image sequence of a lane (Movie S2 in [159]), we tracked 39 individual filaments starting inside lanes by eye and extracted the orientations $\delta\theta(t) = \theta(t) - \theta(0)$ out of the recorded path at different times [Fig. 2.2(D), Fig. 2.6(D)]. From this the polar and nematic autocorrelation functions $\langle \cos[\delta\theta(t)] \rangle$ and $\langle \cos[2\delta\theta(t)] \rangle$ for different filaments [Fig. 2.6(E)] were obtained and averaged over every time point. As can be seen from the differences in decay times, polar order decays much faster than nematic order.

### 2.4.8 Additional observations

At high concentrations of PEG and low actin concentration, the nematic lanes evolved into a packed vortex-like arrangement of branches after long times (roughly 15 min after the beginning of the experiment), indicating the emergence of additional types of order in this parameter region [Fig. 2.10(D)]. For large concentrations of both
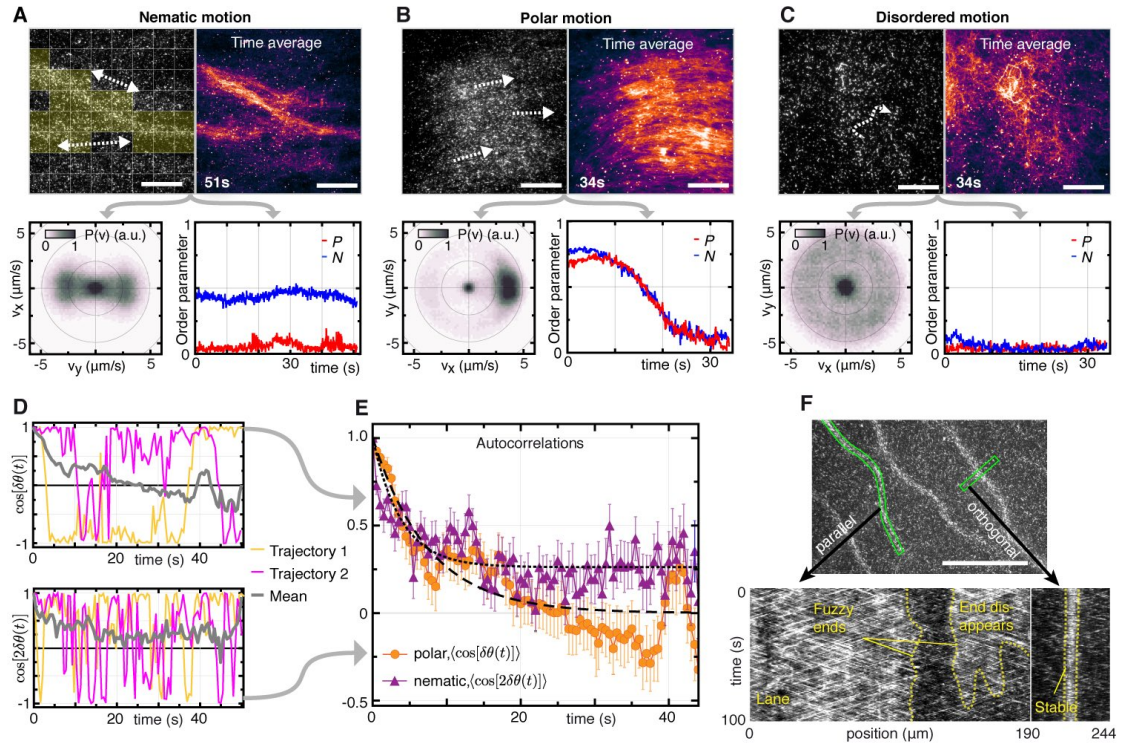
**Figure 2.6 Filament dynamics.** (**A-C**) Local dynamics of filaments within nematic lanes (**A**), polar clusters (**B**) and in disordered motion (**C**): Upper left panels are plain snapshots. In (**A**), the yellow area denotes the subgrid in which filaments were tracked. Upper right panels are time-averaged images over a time period indicated in the graphs to display the average motion of structures. Lower left and right panels depict two-dimensional probability densities $P(v)$ and evolution of corresponding polar (red line) and nematic (blue line) order parameters during acquisition time, respectively. (**D**) Time evolution of $\cos[\delta\theta(t)]$ and $\cos[2\delta\theta(t)]$ for two selected trajectories [yellow and pink traces in [Fig. 2.2(D)]. Reversal events are manifested by jumps in the amplitude from 1 to -1 or back. (**E**) Autocorrelation functions of filament orientation inside lanes ($n = 39$); dashed gray lines are fits to guide the eye. Error bars, ± SD. (**F**) Kymographs of lane structures, taken orthogonally to a lane (lower left panel) and parallel to, and past the end of a lane (lower right panel). Dashed yellow lines depict lane edges. Scale bars are 20 $\mu m$ in (**A-C**), 100 $\mu m$ in (**F**).

actin and PEG, we observed the occasional bulk formation of long actin bundles [Fig. 2.10(E)] which attach to the motor lawn already shortly after experiment initialization, indicating additional depletion forces in-plane of the motility assay and suggesting a possible bundling transition for PEG concentrations above 3%. Note that the presence of bundles did not affect the formation of nematic lanes.

| Experiment from | Actin ($\mu$M) | PEG (%) |
|---|---|---|
| Fig. 2.2A | 10.0 | 0.5 |
| Fig. 2.2B, Movie S1 | 5.0 | 3.0 |
| Fig. 2.2C, Fig. 2.6A | 5.0 | 2.0 |
| Fig. 2.2D, Fig. 2.6D,E, Movie S2 | 10.0 | 2.0 |
| Fig. 2.4D, Movie S8 | 5.0 | 2.0 |
| Fig. 2.6B | 10.0 | 1.0 |
| Fig. 2.6C | 10.0 | 1.0 |
| Fig. 2.6F | 4.0 | 2.0 |
| Fig. 2.10A-C, Movie S9 | 2.5 | 2.0 |
| Fig. 2.10D | 2.0 | 3.0 |
| Fig. 2.10E | 7.0 | 3.0 |
| Movie S3 | 5.0 | 2.0 |
| Movie S4 | 10.0 | 2.0 |

**Table 2.1** List of actin ($\mu$M) and PEG (w/v) concentrations used for figures and movies.

## 2.5 Appendix: Simulation system

### 2.5.1 Computational Model

Propelled actin filaments are modeled as discrete, slender chains of $N-1$ cylindrical segments of length $L$ and width $a$ ($L \gg a$), with the leading segment (tip) of each filament moving at a speed $v$, and the body of the filament following the tip. The direction $\theta_0$ in which a filament tip is moving changes upon interaction with other filaments, as well as through interaction with molecular motors. The latter is described by a Gaussian white-noise process with a path persistence length $L_p > L$. The body of the filament with index $n$ is pulled by its tip, parallel to its backbone. Hence, the motion of a cylinder segment with director $\boldsymbol{u}_i^{(n)}$ is given by $\boldsymbol{v}_i^{(n)} = K_s(\boldsymbol{u}_{i-1}^{(n)}+\boldsymbol{u}_i^{(n)})/2\,[|\boldsymbol{r}_i^{(n)}-\boldsymbol{r}_{i-1}^{(n)}|-L/(N-1)]$, where the index $i \in \{1, \ldots, N-1\}$ represents the contour position, and $K_s$ is a sufficiently strong spring constant to ensure cylinder length conservation. Note that the direction of propulsion of every position $\boldsymbol{r}_i^{(n)}$ is the average of its' neighboring cylinder orientations, to provide a smooth lateral motion. When the leading segment of a given filament $n$ collides with a segment of another filament $m$ at a relative segment orientation $\theta$, an alignment potential $U(\theta)$ acts on the tip's orientation; see figure 2.7(A). The alignment potential is present within the area occupied by a filament of length $L$ and width $a$, and acts on the tips of other filaments. To avoid artifacts such as surface roughness caused by discontinuous jumps and potential superpositions of bent filaments, cylinder potentials at inner bends are averaged, and at outer bends the cylinder gap is

filled with a circular potential segment. In this way, local features of this potential do not change significantly when the contour moves, and discretization effects are small. Figure 2.7(A) depicts the geometry of filaments. The equations of motion (with unitary friction) are then given by

$$\frac{\partial}{\partial t} r_0^{(n)} = v u_0^{(n)} = v(\cos\left[\theta_0^{(n)}\right], \sin\left[\theta_0^{(n)}\right])^T, \tag{2.1}$$

$$\frac{\partial}{\partial t} r_i^{(n)} = K_s \left(u_{i-1}^{(n)} + u_i^{(n)}\right)/2 \left(\left|r_i^{(n)} - r_{i-1}^{(n)}\right| - \frac{L}{N-1}\right), \quad \text{for} \tag{2.2}$$

$$\frac{\partial}{\partial t} \theta_0^{(n)} = -\frac{\delta H_0^{(n)}}{\delta \theta_0^{(n)}} + \sqrt{2v/L_p}\xi^{(n)}, \tag{2.3}$$

where $\xi^{(n)}$ is random white noise with zero mean and unit variance, and

$$H_0^{(n)} = \sum_m \sum_j U_{m,j}^{(n)} \tag{2.4}$$

is the total alignment potential acting onto the direction of a given tip of a filament; the sum runs over all overlapping filaments $m$ and all cylindrical segments $j$ of each of those filaments. For the alignment potential, we assume

$$U_{m,j}^{(n)} = C\left(\left|r_0^{(n)} - r_j^{(m)}\right|_{shDist}\right) \left[A_n\left(\theta_0^{(n)} - \theta_j^{(m)}(r_0^{(n)})\right) + A_p\left(\theta_0^{(n)} - \theta_j^{(m)}(r_0^{(n)})\right)\right],$$
$$A_p(\theta) = \frac{\varphi_p v}{a}cos[\theta], A_n(\theta) = \frac{\varphi_n v}{a}\cos[2\theta], \tag{2.5}$$

where $A_p$ and $A_n$ are the polar and nematic parts of the alignment potential, respectively (Fig. 2.7(B)). The cutoff function $C(x)$ is zero for $x > a$ and otherwise $(a - x)/a$. The argument of the cutoff function, $|...|_{shDist}$, is the shortest distance between the tip and the cylindrical segment with which it is interacting. The values of local orientations $\theta_j^{(m)}(r_0^{(n)})$ are determined by the direction tangent to the potential at contour position $j$ of filament $m$ and the relative tip position of $r_0^{(n)}$. The parameters $\varphi_p$, $\varphi_n$ give the scale of typical reorientations during a collision, as can be easily seen by rescaling time in units of the collision time, i.e. $t \to t\frac{a}{v}$. During a multiparticle simulation, these alignment potentials may gradually lead to a maximal overlap of all contours at their centerline. Adding a weak repulsion force with a small amplitude $s(s \ll v)$ which acts on tips and is proportional to $C(x)$ did not change the phenomenology, but avoided the unphysical and numerically very costly case of hundreds of filaments overlapping simultaneously.

### 2.5.2 Numerical implementation

For the time integration, we used an Euler scheme. To ensure maximal performance, the code was implemented in C++ and designed to operate on a parallelized architecture. Despite the sophisticated interaction geometry, which requires many machine operations per iteration, we were able to realize large simulation times for systems of many filaments, by exploiting the localized nature of filament interactions: for each filament tip, a Verlet [164] list was used to store all filaments which were located within a certain cutoff range. After a certain number of time steps a cell list algorithm [164] was used to update the Verlet lists. The cutoff distance was chosen such that no interaction occurring between consecutive updates could be overlooked. The cell algorithm used for the update of the Verlet lists divides the surface into squares of a sufficient size. Instead of calculating the distances to all other filaments in the whole system, only the distance to filaments in the same or in a neighboring cell must be checked. We further used OpenMP to parallelize the code. To further increase performance, we applied an additional averaging procedure by replacing the individual relative angles $\theta$ in the alignment potential with the mean value over all interaction partners of a respective tip. This allows for a better numerical convergence for larger temporal step sizes, while the properties of the system remain the same.

### 2.5.3 Simulation parameters

For the simulations in the paper, we fixed the following filament parameters (length units are given in filament lengths, i.e. $L = 1$): filament aspect ratio $L/a = 21$, persistence length $L_p = 31.75L$, velocity $v = 1$, and filaments were discretized into $N = 5$ segments. In these units, $t = L/v = 1$ corresponds to the time in which a filament travels a distance equal to its own length $L$. A fixed time increment of $\delta t = 3.17 \cdot 10^{-4}$ was sufficient to achieve minimal numerical errors. The range of interaction strengths $\phi_p$, $\phi_n$ was set between $2.1°$ and $12.9°$, which is comparable to the average amount of reorientation observed in the experiments (up to $14.6°$ for 3% PEG). The sensitivity of the onset and type of collective motion with respect to other parameters like persistence length and aspect ratio will be the subject of a subsequent study.

### 2.5.4 Computational binary collision statistics

Using a small system with two filaments and random initial conditions, the change in polymer orientation (measured from front to back) during a collision was recorded. A collision begins at the time when two filaments first touch, i.e. approach to within a distance smaller than a, and ends when the distance between them becomes

larger than $L/4$, or, when the filaments have nearly aligned, after propagating a cutoff distance $2L$. The resulting scatter plot of incoming and outgoing angles is then binned into intervals of different incoming angles and averaged to produce the binary collision curve displayed in Fig. 2.3(B). Fig. 2.7(C) shows the continuous variation of the average reorientation $\Delta = \langle\theta_{out}\rangle - \theta_{in}$ as a function of $\alpha$. Note that angular fluctuations $\sigma = \sqrt{Var[\theta_{out}]}$ for $L_p = 31.75L$ are of the same order as $|\Delta|$, similar as in the experiment [Fig. 2.1(D)]. Figs. 2.7(D,E) visualize the effect of noise during binary collisions.

### 2.5.5 Macroscopic states in simulations

In large-scale simulations ($L_{box} = 650.2L$, 544,000 filaments), stationarity was not reached within feasible simulation times, but we observed a subsequent coarsening dynamics of the emergent patterns (Movies S5-7 in [159]). We emphasize the striking similarity between the nematic lane network and the dynamics of its branches [Fig. 2.8(A), Movie S6 in [159]] and the patterns seen in our experiments. To visualize these simulations, the system was subdivided into a grid of 256 x 256 bins with well-defined local variables: Per bin, the local density $\rho$, polar order $p = |\langle\exp(i\theta)\rangle_{bin}|/\rho_0$, and nematic order $n = |\langle\exp(2i\theta)\rangle_{bin}|/\rho_0$ are calculated and normalized by the average density $\rho_0 = 544,000/L_{box}^2 = 1.29/L^2$.

For the smaller systems (box length $L_{box} = 81.3L$), stationarity was typically achieved by $t < 1,500$ [Fig. 2.8(B)] and the states were characterized by the value of the global order parameters $P$, $N$. The observed polar steady states appear to be very similar to those already reported in Refs. [84, 85, 127, 165], in spite of the conceptually different definitions of the underlying microscopic particles and their interactions that rely on idealized alignment rules. In the nematic steady state, the orientational autocorrelations resemble their experimental counterparts in exhibiting non-vanishing nematic correlations [Fig. 2.8(C)]. Similar to the polar case, the observed phase separation into a high-density nematic band and a low-density gas resembles the patterns observed in Refs. [86, 88, 165], despite different interaction schemes. Due to the periodic boundary conditions, horizontal/vertical orientations predominate [Fig. 2.3(E)], but diagonal states were also found [Fig. 2.8(D)]. We occasionally encountered the emergence of dual polar waves, which are locally polar and collide head-on, such that the global order is (almost) nematic. These states are predominantly located in the polar and multistable parameter regime, especially for large densities [roughly $\rho_0 > 1.5/L^2$, see Figs. 2.9(A-D)]. While they are established by smectic decay of a nematic lane [Fig. 2.8(D)], it is not clear whether these colliding waves represent a transient phase on the way to a purely polar state or a stable solution of their own. We did not observe these patterns in our experiments, but this can be explained by hydrodynamic effects that are present in the actin motility assay [82]: large polar actin clusters induce a flow field in the
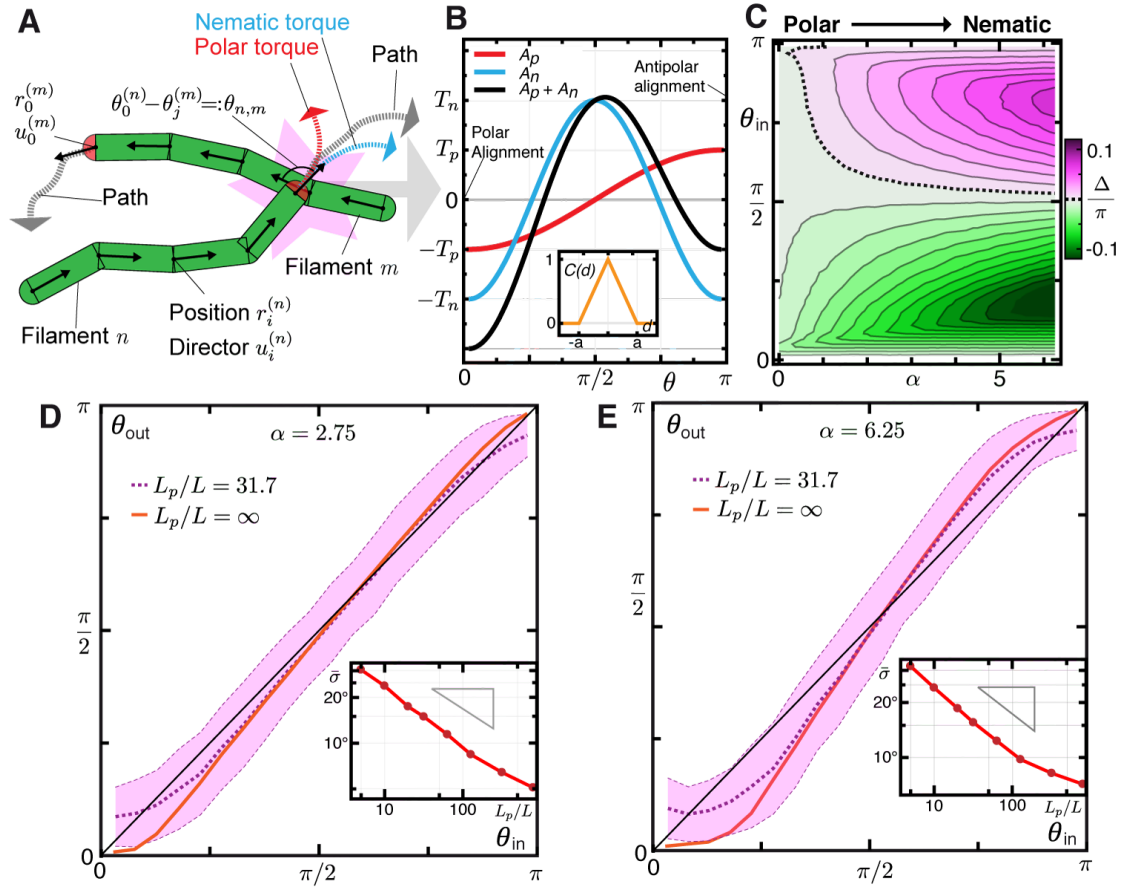
**Figure 2.7 Collisions in the simulation model.** (**A**) Illustration and annotation of the filament geometry. The collision occurs at the point marked by the pink region. (**B**) Nematic (blue line) and polar (red line) alignment potential and the mixed symmetry of their superposition (black line) plotted as a function of the relative orientation $\theta$. Inset: cutoff potential $C(d)$. (**C**) Average reorientation $\Delta = \langle\theta_{out}\rangle - \theta_{in}$ during binary collisions plotted as a function of the incoming angle $\theta_{in}$ and the relative alignment strength $\alpha$ ($L_p = \infty$) . (**D, E**) Binary collision statistics for $\alpha = 2.75$ (**D**) and $\alpha = 6.25$ (**E**) with different $L_p$ ($\phi_p = 2.1°$) The shaded area marks the regions within the standard deviation $\sigma$ for $L_p = 31.7L$. Inset: Dependence of the average standard deviation $\bar{\sigma} = \langle\sigma\rangle_{\theta_{in}}$ for different angles on $L_p$; the gray triangle corresponds to a scaling of $L_p^{-1/3}$.

surrounding fluid, which suppresses any opposed local filament motion of large amplitude (in contrast to low-amplitude nematic motion within lanes). For large polar alignment strengths $\phi_p$, polar states did not evolve into smooth wave profiles but persisted as a collection of erratically moving polar flocks [Fig. 2.8(E)]. In this regime, the multistable region with respect to nematic lanes becomes elusive, similar to the previously reported abrupt switch between polar and nematic symmetry
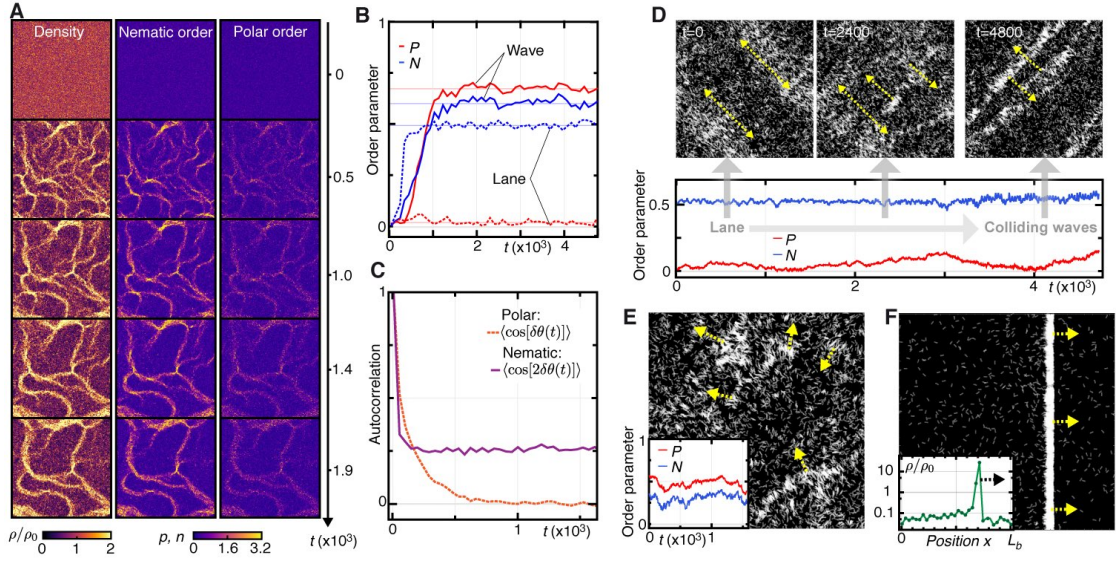
**Figure 2.8 Evolution of patterns in simulations.** (**A**) Dynamics of large nematic networks ($\phi_p = 2.1°$, $\alpha = 6.25$, $\rho_0 = 1.29/L^2$, $L_{box} = 650.2L$). The panels depict the evolution of the local density $\rho$ (left), nematic order $n$ (middle) and polar order $p$ (right). (**B**) Evolution of global order parameters $P$, $N$ in systems with waves [solid lines, from the simulation of Fig. 2.3(F), upper left panel] and lanes [dashed lines, from the simulation in Fig. 2.3(F), upper right panel]. (**C**) Autocorrelation of filament orientations within a lane [from the simulation in Fig. 2.3(F), upper right panel]. (**D**) Decay of a nematic lane (upper left panel) towards colliding waves (upper right panel) along the diagonal axis of the system ($\phi_p = 2.1°$, $\alpha = 4.5$, $\rho_0 = 1.51/L^2$). Note that the decay process does not involve large jumps in the global order parameters (lower panel). (**E**) Irregular polar cluster. Inset: evolution of its order parameters ($\phi_p = 5.0°$, $\alpha = 2$, $\rho_0 = 1.29/L^2$). (**F**) Very narrow and dense polar wave in a subcritical parameter region ($\phi_p = 3.6°$, $\alpha = 0$, $\rho_0 = 1.29/L^2$). Inset: density profile of the wave in x-direction. For (**B-F**), $L_{box} = 81.3L$.

in a Vicsek-like model with fully aligning interactions of stochastically switching symmetry [87]. For both large polar and nematic alignment strengths, filaments appear globally disordered but with some degree of local nematic order [upper right region of Fig. 2.4(E)], which appear similar to turbulent nematic states reported previously [166].

## 2.5.6 Hysteresis analysis

To quantify the multistable region, we used smaller system sizes in our simulations ($L_{box} = 81.3L$). We started our simulations in a strictly polar parameter regime ($\alpha = 0$, $\phi_p \neq 0$) and waited until the dynamics had become stationary ("waiting" time $\Delta t = 1,587.3$). We then incrementally increased $\alpha$ by a small amount $\Delta \alpha$ during
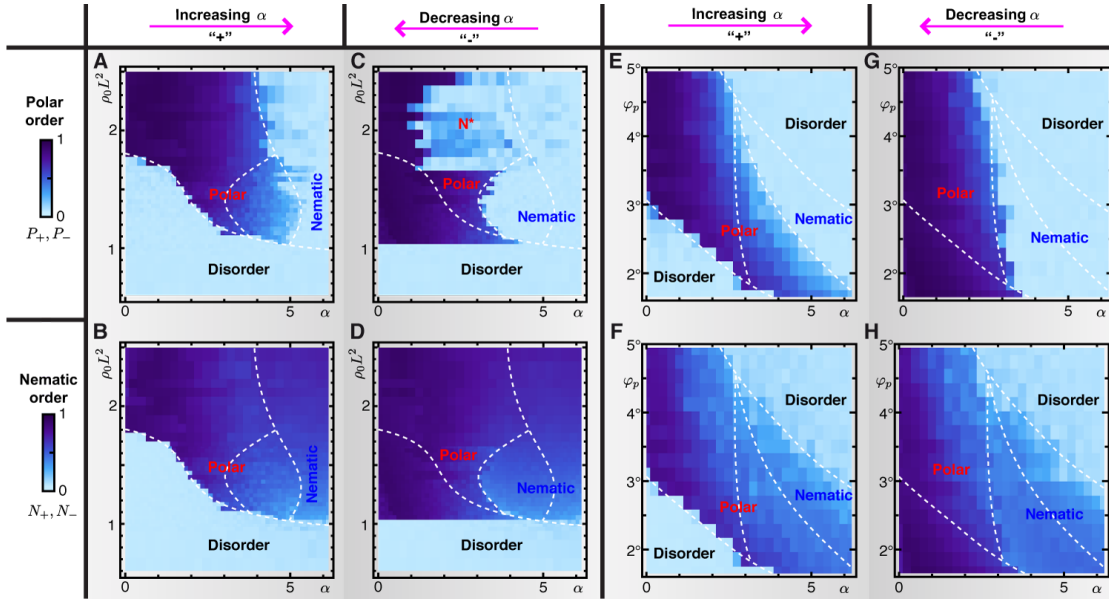
**Figure 2.9 Hysteresis analysis of global order parameters.** Global order parameters plotted as a function of the relative alignment strength $\alpha$ for (**A-D**) different filament densities $\rho_0$ (at $\phi_p = 2.1°$) and for (**E-H**) different polar alignment strengths $\phi_p$ (at $\rho_0 = 1.29/L^2$). The direction of increasing $\alpha$ is depicted in (**A, E**) ($P_+$) and (**B, F**) ($N_+$), the decreasing direction is given by (**C, G**) ($P_-$) and (**D, H**) ($N_-$). White dashed lines represent critical values between domains of different patterns to guide the eye. The region $N^*$ in (**C**) corresponds to states which were dominated by waves colliding head-on.

the simulation, measured $P_+$, $N_+$ ("+" for increasing direction), and reiterated the procedure until $\alpha = 6.25$ was reached. Then, we changed the direction and progressively reduced $\alpha$ while recording the values of $P_-$, $N_-$ to complete the hysteresis loop in $\alpha$. We obtained two-dimensional phase diagrams by repeating the hysteresis analysis for different filament densities $\rho_0$ and different polar alignment strengths $\phi_p$ [Figs. 2.4(A,E)]. Figs. 2.9(A,B,E,F) show the corresponding global order parameters in the "+" direction, Figs. 2.9(C,D,G,H) in the "-" direction, respectively. For Fig. 2.4(A), and for $\rho_0 < 1.67/L^2$ in Figs. 2.9(A-D), we used $\Delta\alpha = 0.175$; for all other data $\Delta\alpha = 0.25$. Note that the multistable parameter region depends only weakly on the system size: upon doubling $L_{box} = 162.5L$ the boundaries only shift slightly in parameter space [Fig. 2.11(A)].

As can be seen in Fig. 2.3(F) the transition from a nematic lane into a polar wave is rather discontinuous; a lane becomes completely destabilized by a randomly emerging polar flock. The transition from polar waves to nematic lanes is quite different: the global polar order amplitude seems to vanish smoothly, although spatial structures change from a wave (orthogonal to particle motion) into a lane (parallel to the particle motion). It should be noted that a single polar wave,
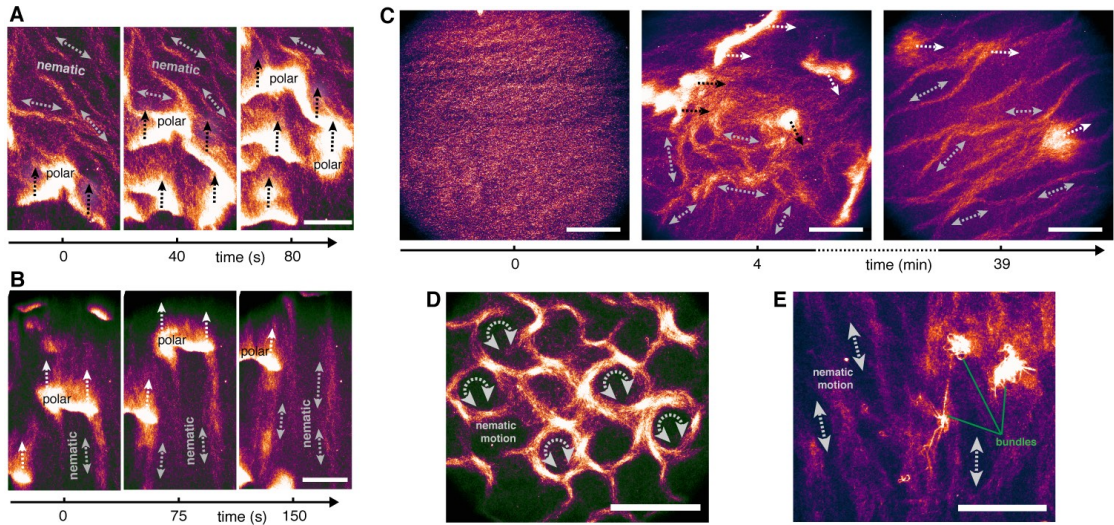
**Figure 2.10 Interplay and dynamics of macroscopic structures.** (**A**) Time evolution of polar clusters engulfing nematic lanes by running over them. (**B**) Time evolution of a polar cluster that leaves nematic lanes trailing from its "wing-tips". (**C**) Evolution of coexisting patterns during an experiment, visualized by snapshots at different times after ATP addition. Within a few minutes (roughly 2 min), both polar clusters and nematic lanes are fully developed (middle panel). At the end of the experiment, coexistence is still present (right panel). (**D**) Vortex-like mesh of nematic branches. (**E**) Lane network with occasional dynamic actin bundles. Scale bars are 100 $\mu m$ in (**A-C**), and 50 $\mu m$ in (**D, E**). Uni- and bi-directional arrows denote polar and nematic motion, respectively.

once formed, is very stable, even when $\alpha$ is decreased in the minus direction far below the onset of collective motion [see the lower left corners of Figs. 2.9(C,G)]; occupying almost all filaments, the wave profile becomes extremely dense and ordered [Fig. 2.8(F)], which represents a limiting case of the model assumptions (polar flocks do not stop to accumulate filaments for increasing density).

### 2.5.7  Time scale analysis of coexistence

To quantify and extrapolate the long-time behavior of coexisting polar and nematic structures in the simulations, we analyzed different time scales of pattern formation as a function of the (finite) system size. To this end, we tracked the evolution of the local order parameters, which are reliable indicators of the nature of the ordered state, and determined the fixation times $t_{fix}$ upon which a system adapted either a distinctly polar ordered or nematically ordered state, as a function of the system size $L_{box}$. The local order parameters are defined as follows: any system of $M$ filaments can be decomposed into a set of clusters of overlapping filaments, $\{c\}$. A cluster $c$ has the following properties: cluster

size $m_c$, cluster polar order $\pi_c = |\sum_{j=1}^{m_c} \exp(i\theta_j)|/m_c - \Delta(m_c)$ , cluster nematic order $\nu_c = |\sum_{j=1}^{m_c} \exp(2i\theta_j)|/m_c - \Delta(m_c)$, where $\Delta(l) = |\sum_{j=1}^{l} \exp(iU_j)|/l$, $\{U_j\} \in U(0, 2\pi)$ is the expected random order of a finite-size cluster. Hence, the local polar and nematic order $\langle \pi_c \rangle = \sum_{\{c\}} \pi_c m_c / M$, $\langle \nu_c \rangle = \sum_{\{c\}} \nu_c m_c / M$ are given by the mean cluster orders, taken over the whole cluster population. Note that with this definition, the local order parameters do not depend on the global orientation and arrangement of the whole system.

Figs. 2.11(D,E) show the evolution of local order parameters $\langle \pi_c \rangle$, $\langle \nu_c \rangle$ with corresponding snapshots of the underlying simulations, for different initial conditions but identical parameters. Note that an initial plateau value of $\langle \pi_c \rangle$, $\langle \nu_c \rangle$ is achieved extremely fast, within a time scale $t_0$ which we call the initial pattern formation time as it corresponds to the emergence of local, polar clusters. Before the system has reached a stationary state, which is either polar or nematic in nature, it exhibits coexisting structures of both types, which is reflected in the behavior of the local order parameters: when the system becomes fully polar [Fig. 2.11(D)], the local polar order $\langle \pi_c \rangle$ eventually approaches the local nematic order $\langle \nu_c \rangle$ , at the fixation time (or coexistence time) $t_{fix}$. When the system becomes fully nematic [Fig. 2.11(E)], the local polar order $\langle \pi_c \rangle$ drops to a value below its initial plateau value and saturates at a lower (but finite) level at $t_{fix}$. Figs. 2.4(F), 2.11(B,C) show the statistics of these time scales, which were obtained by fitting piecewise-linear functions or crossing times of $\langle \pi_c \rangle$, $\langle \nu_c \rangle$ at any simulation, and for two different sets of $\alpha$, $\phi_p$ in the multistable parameter region. Note that the linear dependence of $t_{fix}$ on $L_{box}$ has a very large amplitude ($t_{fix}/t_0 \approx 100$ for $L_{box} = 325.1L$), and that there are strong variations towards very large fixation times. Unexpectedly, neither $t_0$, nor $t_{fix}$ seem to not depend much on the overall strength of filament interaction (given the different parameter sets $\alpha$, $\phi_p$), and hence on the exact position in multistable parameter domain.
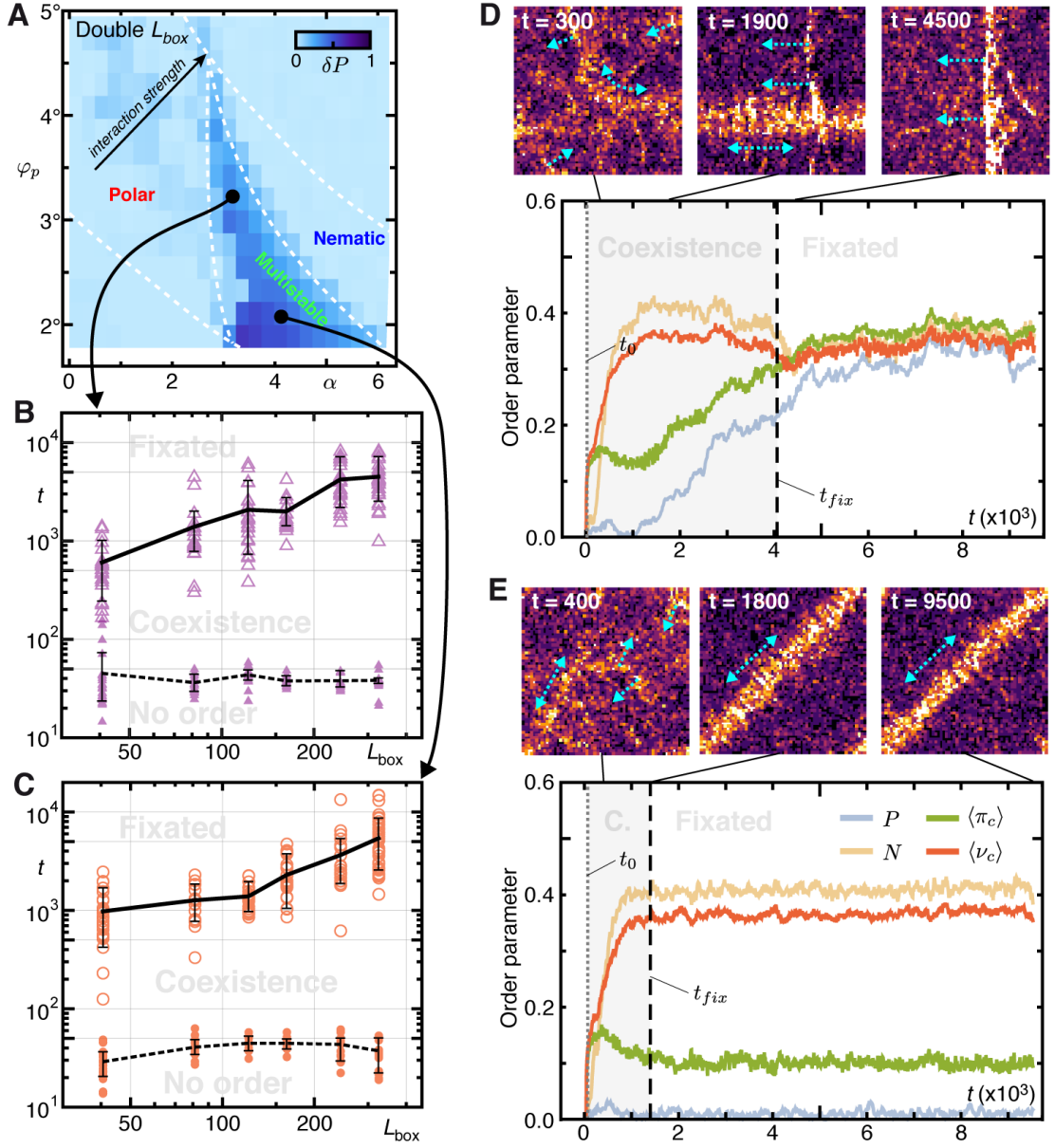
**Figure 2.11 System size dependence of dynamics observed in simulations.** (**A**) Multistable parameter region obtained by hysteresis analysis, with doubled system size $L_{box} = 162.5L$ as compared to Figs. 2.4(E), 2.9(E-H) with otherwise identical parameters. White dashed lines denote the approximate stability domain boundaries of half-sized systems which are already shown in Figs. 2.4(E), 2.9(E-H). (**B, C**) System size scaling analysis at (**B**) $\phi_p = 2.1°$, $\alpha = 4.17$ and (**C**) $\phi_p = 3.3°$, $\alpha = 3.13$. Open purple triangles and open orange circles denote individual $t_{fix}$ events, full symbols depict $t_0$, respectively. Black lines and arrow bars are average values and $15^{th}/85^{th}$ percentiles [as in Fig. 2.4(F)]. (**D, E**) Examples of time evolutions of local ($\langle\pi_c\rangle$: green line; $\langle\nu_c\rangle$: red line) and global ($P$: light blue line; $N$: light orange line) order parameters, fixating in either a polar wave (**D**) or a nematic lane (**E**). Vertical lines denote respective time scales upon which local order emerges ($t_0$, short-dashed line) and finally fixates at a distinct type of order ($t_{fix}$: long-dashed line). Note that panels (**D, E**) share identical parameters: $\phi_p = 2.1°$, $\alpha = 4.17$, $\rho_0 = 1.29/L^2$, $L_{box}, = 162.5L$.

# 3 Microphase separation in active filament systems is maintained by cyclic dynamics of cluster size and order

*The following chapter is based on research published in Phys. Rev. Research **3**, 013280 [2] (under a CC BY 4.0 licence) that I conducted together with Lorenz Huber and Erwin Frey and to which I, together with L.H., contributed as one of the shared first authors.*

The onset of polar flocking in active matter is discontinuous, akin to gas-liquid phase transitions, except that the steady state exhibits microphase separation into polar clusters. While these features have been observed in theoretical models and experiments, little is known about the underlying mesoscopic processes at the cluster level. Here we show that emergence and maintenance of polar order are governed by the interplay between the assembly and disassembly dynamics of clusters with varying size and degree of polar order. Using agent-based simulations of propelled filaments in a parameter regime relevant for actomyosin motility assays, we monitor the temporal evolution of cluster statistics and the transport processes of filaments between clusters. We find that, over a broad parameter range, the emergence of order is determined by nucleation and growth of polar clusters, where the nucleation threshold depends not only on the cluster size but also on its polar moment. Growth involves cluster self-replication, and polar order is established by cluster growth and fragmentation. Maintenance of the microphase-separated, polar-ordered state results from a cyclic dynamics in cluster size and order, driven by an interplay between cluster nucleation, coagulation, fragmentation and evaporation of single filaments. These findings are corroborated by a kinetic model for the cluster dynamics that includes these elementary cluster-level processes. It consistently reproduces the cluster statistics as well as the cyclic turnover from disordered to ordered clusters and back. Such cyclic kinetic processes could represent a general mechanism for the maintenance of order in active matter systems.

## 3.1 Introduction

Polar flocking in active matter marks the onset of collective particle motion and has been observed in many experiments, ranging from biopolymer systems [15,
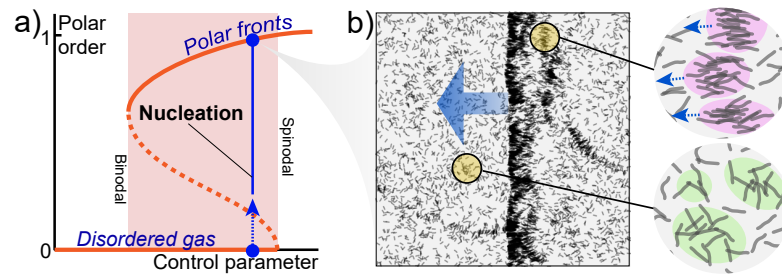
**Figure 3.1** a) Schematic of a typical bifurcation scenario for a flocking transition. Control parameters are, for example, particle density or interaction strength. Between binodal and spinodal, flocking is triggered by spontaneous nucleation events (blue line). (b) Illustration of clustering of active polymers in the polar, phase-separated state. Locally, both ordered (pink shading) and disordered (green shading) clusters are observed.

16, 19–21] to colloids [24, 167] and discs [28, 143, 168, 169], as well as in theoretical studies using hydrodynamic descriptions [5, 84, 89, 94, 98, 120, 123, 125, 155, 170–172] and particle based simulations [61, 63, 85, 96]. The associated nonequilibrium phase transition is in general discontinuous [84, 85, 96, 173] and exhibits a subcritical parameter regime of polar patterns [20, 61, 63, 98, 127, 174], as illustrated in Fig. 3.1(a). While some aspects of flocking are akin to phase separation in thermal equilibrium systems [62, 63], there are also marked differences. In particular, both agent-based simulations and experiments have shown that active filament systems exhibit *microphase separation* into dense polar-ordered regions and dilute disordered regions [15, 63, 69, 85]. How these steady-state patterns depend on the macroscopic control parameters (e.g. particle density, noise, or interaction strength) is well described at the level of hydrodynamic theories [63, 94, 98]. The basic fact that spontaneous nucleation of particle clusters is vital for the initial stages of flocking is also well established [85, 96, 132]. However, the mechanisms underlying the formation and maintenance of a macroscopically ordered phase, which shows microphase separation into polar ordered clusters and a disordered background, is still unclear.

In the present work, we show that an interplay between cluster assembly and disassembly governs the emergence of polar order and microphase separation. We find that particles self-organize into a heterogeneous population of clusters with a characteristic distribution of sizes and degree of polar order. By analyzing the temporal evolution of clusters using agent-based simulations of **w**eakly **a**ligning **s**elf-propelled **p**olymers (WASPs) [1], we show that polar order and microphase separation in the flocking state are maintained by a continuous exchange of mass between coexisting populations of ordered and disordered clusters. To rationalize the underlying mechanism, we introduce a kinetic model consisting of two distinct cluster species, disordered and polar ordered, and study the ensuing assembly-

disassembly dynamics. We find that the kinetic model shows the same cluster statistics, mass-exchange dynamics, and bifurcation scenario as the agent-based system, even though it contains no information on the spatial dynamics. This theory explains the presence of microphase separation in the ordered state in terms of cyclic probability currents in a phase space spanned by cluster size and order.

## 3.2 Results

### 3.2.1 Simulation setup and observables

We consider agent-based simulations of a system with $M$ polymer filaments of fixed length $L$ on a two-dimensional substrate with periodic boundary conditions; for details see Ref. [1] as well as Appendix 3.4.1 and 3.4.2. Motivated by experiments using *in vitro* assays of gliding polymers [15–21, 157], each filament is assumed to consist of a head that performs a persistent random walk with persistence length $L_p$ and constant speed $v$, and a tail that passively follows it. Interactions between filaments are assumed to be weak and dominated by aligning interactions [1, 20]: upon local contact with adjacent filament contours, a polar and a nematic torque proportional to $\varphi_p \cos\theta$ and $\varphi_n \cos 2\theta$, respectively ($\theta$ being the impact angle), are exerted on the filament head. These active filament systems were shown to reproduce local collision statistics and collective phenomena—polar and nematic patterns—on large scales ($M = \mathcal{O}(10^6)$) [1], with filament density $\rho$ and relative alignment strength $\alpha = \varphi_n/\varphi_p$ as experimentally motivated control parameters. Here, we focus on the formation of large polar fronts as illustrated in Fig. 3.1(b). In the flocking state, one observes that filaments are locally organized into clusters of different sizes and, on closer inspection, also of different degree of internal ordering [Fig. 3.1(b)]: filament clusters in a polar front are highly ordered flocks while clusters elsewhere are much less structured.

To investigate the role of clusters of different sizes and order in the emergence and maintenance of order in a system of WASPs, we monitor the size and degree of order of each filament cluster. We decompose the system of filaments, $\{f_j\}$ with $j \in \{1, 2, \ldots, M\}$, into a set of clusters $\{c_\alpha\}$: filaments are assumed to belong to a specific cluster $c_\alpha$ if they lie closer to filaments in that cluster than a cutoff distance $\gamma$ with $\gamma \ll L$, as described in more detail in Appendix 3.4.3. Every cluster can be assigned a *cluster size*, the number $k$ of filaments, and a *cluster polar order*, $p_k := \frac{1}{k} |\sum_{j=1}^{k} \exp(i\theta_j)|$. In the following it will turn out to be useful to also define the *polar moment of a cluster*, $S_k = k\, p_k$, which measures the effective number of ordered filaments within a cluster. Since even clusters made up of filaments with randomly chosen orientations have on average a nonzero polar order $\Delta_k = (7 + \frac{1}{k})/(8\sqrt{k}) + \mathcal{O}(k^{-5/2})$ [Appendix 3.4.3], we define the net polar order

of a cluster by $\pi_k := p_k - \Delta_k$. Hence, the global polar order of the clusters is given by an average of the net polar order $\pi_k$ weighted by the respective cluster size: $\Omega_p := \frac{1}{M} \sum_{\{c\}} \pi_k^{(c)} k^{(c)}$ (*cluster polar order parameter*). In addition to this system-level quantity, we also record the *full statistics of cluster size and order*, $\Psi(k, p)$. We choose a normalization such that the marginalized distribution $\psi(k) = \int_0^1 dp\, \Psi(k, p)$ satisfies $\sum_{k=1}^M k\, \psi(k) = 1$. This choice means that in a given realization (simulation run) $\psi(k) = n(k)/M$ where $n(k)$ is the number of clusters of size $k$; hence, $\phi(k) = k\, \psi(k)$ gives the fraction of filaments contained in all clusters of size $k$. In the following we will refer to $\psi(k)$ as the cluster-size distribution.

### 3.2.2 Polar order emerges through a hierarchical process

To begin with, we show representative simulation results for the agent-based system in order to illustrate the dynamic processes that lead to the emergence of polar order starting from random initial conditions (as specified in Appendix 3.4.2). If not stated otherwise, we fixed the parameters $\varphi_p = 0.036$ and $\rho = 1.51/L^2$; for a complete list of default parameters please refer to Appendix 3.4.1 and 3.4.2. Time is given in units of correlation time $L_p/v$ and length in units of filament length $L$.

Figure 3.2(a) depicts the time evolution of the cluster polar order parameter $\Omega_p$ for $\alpha = 2$, where the WASPs exhibit the same collision statistics as observed for actin filaments in the actomyosin motility assay slightly above the previously reported onset of flocking [1]; for an illustration of the associated dynamic processes please refer to Movie S1 [175]. We observe that generically within a relatively short time $t_0$ the system develops some but still rather weak polar order of the clusters with $\Omega_p \approx 0.08$. The system persists in this disordered state for an extended time period until at some time $t_d$ cluster polar order suddenly and significantly increases and then approaches a stationary plateau value $\Omega_p^* \approx 0.7$; this growth phase is well described by an exponential law with the growth time $\tau$ [Fig. 3.2(a)]. Visual inspection of the agent-based simulations suggests that the onset of polar order at $t_d$ is marked by the nucleation of a sufficiently large and polar-ordered cluster which triggers a cascade of cluster assembly and disassembly processes leading to rapid exponential increase in polar order; cf. Movie S1 [175].

These qualitative observations are supported and quantified by the measured statistics of cluster size and oder $\Psi(k, p)$. In the quasi-stationary, disordered regime ($t < t_d$) the distribution of cluster sizes, $\psi(k)$, shows an exponential tail [Fig. 3.2(b)], similar to that found in previous studies [101, 107, 112, 133, 134, 176–178]. Moreover, the full distribution of cluster size and order, $\Psi(k, p)$, is centered around $p \sim \Delta_k$, indicating that typical clusters are only marginally more ordered than randomly assembled clusters [Fig. 3.2(b,c)]. In contrast, in the stationary, polar-ordered state ($t > t_d$), the distribution of cluster size is no longer exponential but
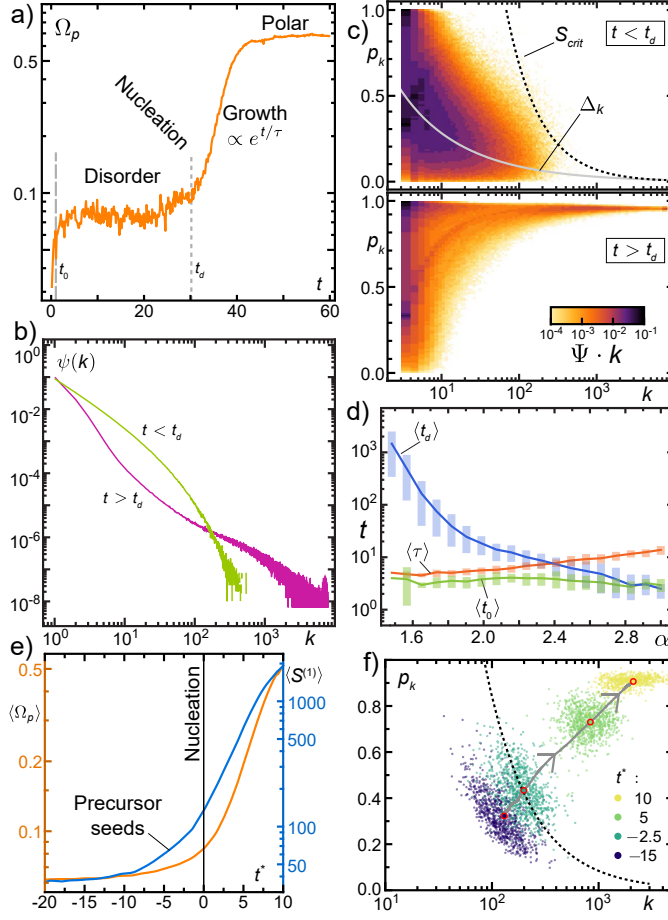
**Figure 3.2** a) Time evolution of the cluster polar order parameter $\Omega_p$. We use units where time is expressed in terms of the longest single-particle correlation time $\tau_p = L_p/v$, i.e. the time over which the filament trajectories are approximately straight. The initial time scale $t_0$ and the nucleation time $t_d$ are marked by long-dashed and short-dashed lines, respectively. b) Cluster size distribution, $\psi(k)$, in the disordered regime ($t < t_d$; green) and in the polar ordered steady state ($t > t_d$; purple). c) Heat plot (with color map shown in the graph) of the full statistics of cluster size and order, $k \cdot \Psi(k, p)$, plotted as a function of $k$ and $p$, in the disordered regime (upper panel) and in the polar ordered steady state (lower panel). The gray solid line depicts $\Delta_k$, and the dashed line indicates the estimated nucleation threshold $S_{\text{crit}} = p_c k \approx 66$ (see discussion later). d) Characteristic time scales $t_0$, $t_d$, and $\tau$ as a function of $\alpha$. Solid lines denote average values, and error bars represent the 15th, and 85th percentiles taken over 100 realizations for each $\alpha$. e) Time evolution of $\langle S^{(1)} \rangle$ (blue line) and $\langle \Omega_p \rangle$ (orange line), as a function of $t^* = t - t_d$, averaged over 892 independent realizations. f) Scatter plot for the size $k$ and order $p$ of the cluster corresponding to the largest cluster $S^{(1)}$ for 892 independent realizations. The probability clouds at different times $t^*$ are indicated in different colors in the graph. As time progresses the cloud of points follows the trajectory indicated by the gray solid line, which depicts the average path of $\langle S^{(1)} \rangle$ in $k$-$p$ space. The red open circles mark the average $\langle S^{(1)} \rangle$ at the indicated timepoints. The dashed line indicates $S_{\text{crit}} \approx 84$. In panels a-c we used $\alpha = 2$, and in panels e-f a value of $\alpha = 1.67$.

exhibits a broad tail [Fig. 3.2(b)], and from the full statistics we infer that typical clusters are highly ordered [Fig. 3.2(c)].

Our simulations show that the onset times $t_d$ of polar order are randomly distributed, suggesting that nucleation events are stochastic and require rare events that initiate the formation of clusters of sufficiently large size and order. Figure 3.2(d) shows the mean and the statistical variation of the characteristic time scales $t_0$, $t_d$, and $\tau$ in the parameter range $\alpha \in [1.5, 3.0]$; how these times are measured is detailed in Appendix 3.4.4. While the onset time $t_d$ of polar order increases strongly with decreasing $\alpha$, it remains finite even far below the previously reported onset of order at $\alpha \approx 1.8$ [1]. The onset times were found to be exponentially distributed with a coefficient of variation $\sqrt{\mathrm{Var}[t_d]}/\langle t_d \rangle \approx 1$, similar as in classical nucleation theory [179, 180]; for a detailed discussion of the observed variance in the onset time $t_d$ please refer to Appendix 3.4.4.3. With increasing $\alpha$, we find that the average onset time $\langle t_d \rangle$ decreases and eventually becomes comparable to the average values $\langle t_0 \rangle$ and $\langle \tau \rangle$, suggesting that the system instantly begins to develop polar order. For even larger $\alpha$, polar order emerges through a process akin to spinodal decomposition (see discussion below and Movie S2 [175], which shows the dynamics for $\alpha = 3$).

### 3.2.3 Nucleation barrier is determined by polar moment

To further characterize the processes underlying formation and growth of polar clusters we monitored the time evolution of all filament clusters and rank-ordered them according to the magnitude of their respective polar moments: $S^{(1)} \geq S^{(2)} \geq S^{(3)} \geq \ldots \geq S^{(n)}$. Figure 3.2(e) compares the time evolution of the cluster polar order parameter $\Omega_p$ and the largest polar moment $S^{(1)}$, averaged over 892 independent realizations and aligned in relation to the respective (stochastic) onset times $t_d$. The observation that growth of the largest cluster starts (on average) prior to the onset of polar order suggests that precursor seeds initiate cluster nucleation and growth. What then are their characteristic features?

The answer becomes evident upon inspection of the evolution of cluster size and polar order, shown in Fig. 3.2(f) as a scatter plot for different time points indicated in the graph; cf. Movie S3 [175]. Initially, before the onset time $t_d$, the probability cloud is widely extended in $k-p$ space and its center of mass hardly moves. As soon as the cloud crosses a line of constant polar moment [dashed hyperbolic curve in Fig. 3.2(f)], which occurs at a time that roughly coincides with the onset time $t_d$, we observe qualitatively different dynamics; we will quantify the precise location of this transition line below. The cloud then begins to contract and shows a clear trend toward large cluster sizes $k$ and higher polar order $p$, i.e. increasing polar moment $S$. From these observations we conclude that the polar moment $S$ is the key quantity which determines the nucleation threshold.
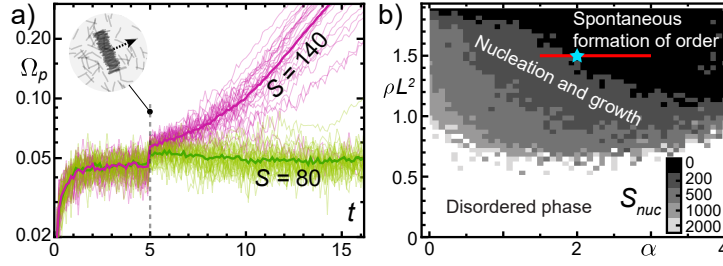
**Figure 3.3** a) Time evolution of cluster polar order parameter $\Omega_p$ for disordered systems ($\alpha = 1.25$) perturbed by the addition of (fully polar) ordered cluster of polar moment $S$ at time $t = 5$ (green: $S = 80$; pink: $S = 140$). Thin lines correspond to single realizations, thick curves to the corresponding mean over all realizations. b) Phase diagram as a function of $\alpha$ and $\rho$. The regions shown in different shades of gray indicate regimes where the final system is polar-ordered with $\Omega_p^* > 0.2$. The gray scale corresponds to different values that are proxies for $S_{\text{crit}}$, as explained in the main text. The red line indicates the parameters used in Fig. 3.2(d), and the blue star the parameters used in Fig. 3.2(a-c).

## 3.2.4 Nucleation and spontaneous emergence of polar order

In order to determine the parameter regimes where polar order emerges either through a nucleation and growth process or spontaneously, we performed simulations over a wide range of densities, $\rho$, and relative alignment strengths, $\alpha$. The black regime in Fig. 3.3(b) indicates the parameter range, within which we observed onset times for polar order below $t_d = 50$. We take this as a proxy for the regime where polar order builds up *spontaneously*, cf. Movie S2 [175]. On the other hand, to determine the nucleation and growth regime and the respective threshold value of the polar moment (critical nucleus 'size'), one would in principle need to monitor the time evolution of all clusters and wait for the spontaneous formation of a critical nucleus. While this is computationally feasible for parameter regimes where $t_d$ is reasonably small, it becomes practically impossible if $t_d$ is large, as is the case for small values of $\alpha$; c.f. Fig. 3.2(d). Therefore, we took a different approach and instead of waiting for a spontaneous nucleation event, we artificially inserted perfectly ordered ($p = 1$) clusters with different polar moments $S = k$ into a disordered system. While clusters with $S > S_{\text{crit}}$ trigger a transition of the whole system towards a globally ordered state, the system remains disordered for smaller clusters, cf. an exemplary case in Fig. 3.3(a). The different gray scales in Fig. 3.3(b) show parameter regimes where nucleation and growth occurred in our simulations after insertion of a cluster of certain discrete size $S_{\text{nuc}}$ as indicated in the graph. These values correspond to proxies of $S_{\text{crit}}$ in the respective parameter regimes; see Appendix 3.4.5.1 for a more detailed analysis of $S_{\text{crit}}$. For parameters where $t_d$ is small, we have explicitly checked that the critical value $S_{\text{crit}}$ obtained by artificially inserting a polar-ordered cluster and waiting for the spontaneous emergence of a

critical nucleus agree quantitatively [Appendix 3.4.5.2]. On a qualitative level, this becomes evident from Movie S3 [175]: The line given by $p(k) = S_{\text{crit}}/k$ defines a threshold curve in $k-p$ space, above which nucleation occurs, cf. also dashed curves in Fig. 3.2(f). Moreover, upon comparing the course of nucleation for artificially triggered and spontaneous nucleation events in $k-p$ space, we found that very rapidly the emerging statistics for the largest cluster $S^{(1)}$ become indistinguishable from each other; see Fig. 3.13 in Appendix 3.4.5.3.

In summary, the phase diagram in Fig. 3.3(b) exhibits two qualitatively distinct regimes. There is a regime where flocking is spontaneous akin to spinodal decomposition in liquid-gas systems, especially at high densities and large $\alpha$; cf. Movie S2 [175]. In addition, there is a broad range of parameters within which the transition to a polar ordered state proceeds by nucleation and growth. In contrast to liquid-gas systems, the critical nucleus is not only characterized by a large enough size but also by a sufficiently high polar order, such that $S_{\text{crit}} = k \cdot p$.

### 3.2.5 Coarsening and anti-coarsening

Next, we wanted to gain further insight into the processes leading from the formation of a critical nucleus to the assembly of (moving) polar clusters and ultimately the polar-ordered, non-equilibrium steady state. To this end, we artificially inserted seeds (fully ordered polar clusters) and observed their dynamics; for an illustration please refer to Fig. 3.4(a) and Movie S4 [175]. One observes that immediately after insertion the cluster begins to loose filaments. This loss is counteracted by a gain of filaments due to annexation of disordered clusters (with low polar order) that lie in its pathway of motion. Only when the size of the seed is large enough, as discussed in the previous section, this gain is sufficient to overcome the filament loss such that the cluster grows. These clusters, however, do not grow indefinitely, but eventually replicate by splitting up into several parts, which in turn grow individually; frequently they also merge again.

These qualitative observations can be quantified in terms of the rank-ordered polar moments, whose averages sampled over 30 realizations are shown for $S^{(1)}$ through $S^{(10)}$ in Fig. 3.4(b). After artificial insertion of a seed cluster (here of size $S_{\text{seed}} = 200$), this seed forms the cluster with the largest polar moment $S^{(1)}$ which then grows exponentially, while one after another clusters with the next largest polar moment follow suit. This sequential process corresponds to the continuous production of cluster fragments, which are created during splitting events and then grow by themselves. The seed cluster spins off daughter clusters, as can be read off from the decline in the number of filaments $I$ that originally formed the seed cluster and are still part of the largest cluster $S^{(1)}$, cf. $I(t^*)$ in Fig. 3.4(b).

To further investigate the dynamics of clusters and the filament exchange between them, we tracked the fate of particles that were part of a cluster at time $t$
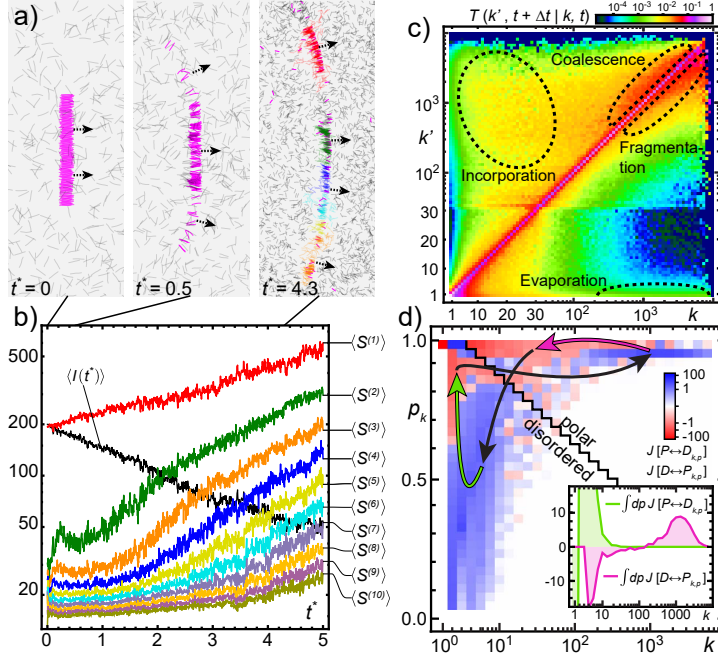
**Figure 3.4** a) Snapshots of a perfectly ordered cluster added to a disordered system, taken at different times $t^*$ after insertion (at $t^* = 0$). Filaments that are part of the original cluster are shown in magenta. After growing for some time, the cluster eventually splits up into several distinct parts that can then grow on their own (shown in different colors). b) Time evolution of the clusters with the ten largest polar moments $S^{(i)}$, after an artificial nucleation seed of size $S_{\text{seed}} = 200$ was placed into the systems at $t^* = 0$, averaged over 30 independent realizations. $I(t^*)$ specifies the temporal evolution of the amount of filaments which were originally part of the inserted cluster; cf. magenta filaments in panel a. c) Matrix of transition probabilities, $T(k', t + \Delta t | k, t)$, in color code as shown in the graph with $\Delta t = 0.0125$. As a guide to the eye, regions with dominant fragmentation or coalescence, incorporation or evaporation are encircled. d) Steady-state (in the polar-ordered phase) particle fluxes $J[D \leftrightarrow P_{k,p}]$ and $J[P \leftrightarrow D_{k,p}]$ between ordered ($P$) and disordered ($D$) clusters in $k{-}p$ space as obtained from numerical simulations of WASPs. The black zig-zag line depicts the chosen partition of $k{-}p$ space into a disordered ($D$) and a polar ($P$) compartment. The arrows indicate the overall tendency in the flow between clusters of different size and polar order. Inset: The fluxes $J[D \leftrightarrow P_{k,p}]$ and $J[P \leftrightarrow D_{k,p}]$ integrated over $p$ for comparison with Fig. 3.5(e). In all panels we used $\alpha = 1.67$.

and recorded their status after some time $\Delta t$. To this end, we define the transition probabilities $T(k', t + \Delta t | k, t)$ that quantify the likelihood that a filament which is part of a cluster of size $k$ at time $t$ will scatter into a cluster of size $k'$ at some later time $t + \Delta t$, normalized such that $\sum_{k'} T(k', t + \Delta t | k, t) = 1$; how $T$ is inferred from the simulation data is described in Appendix 3.4.7. For $\Delta t \to 0$, these transition probabilities become diagonal, $T(k', t | k, t) = \delta_{kk'}$, while for $\Delta t \to \infty$, as the

events become statistically independent, one obtains $T(k', \infty | k, t) = k' \psi(k')$ [cf. Fig. 3.15(a,d) in Appendix 3.5.3.1].

Figure 3.4(c) shows the matrix of these transition probabilities recorded for times $t$ in the stationary non-equilibrium steady state, and with the time increment chosen as $\Delta t = 0.0125$, a value corresponding to the time a filament takes to travel a distance comparable to its own contour length. This choice gives each filament sufficient time to escape from its previous cluster, but multi-scattering events are still unlikely. The precise value of this time increment is not important [see Appendix 3.4.7]. From Fig. 3.4(c) we infer that, while most clusters remain stable during this time increment (diagonal), especially large polar clusters either frequently *coalesce* or *fragment* into similarly sized clusters (bright off-diagonal matrix elements in the upper right of Fig. 3.4(c)), or *evaporate* very small clusters or single filaments (bottom right matrix elements in Fig. 3.4(c)). Clusters of smaller size, on the other hand, are frequently *incorporated* into clusters of larger size (upper left part of the matrix in Fig. 3.4(c)).

Next, because of the qualitatively very different behaviour of strongly ordered and disordered clusters, we classified them into two broad classes: disordered ($D$) and polar ($P$) population. For that classification, we chose a heuristic division line in $k-p$ space [zig-zag line in Fig. 3.4(d); cf. Appendix 3.4.6. This is chosen such that in the quasi-stationary disordered regime [Fig. 3.2(c), upper panel] most clusters would be classified as being disordered. We monitored the net filament fluxes between these two populations in steady state. Specifically, we measured how many filaments transition per unit time between disordered/ordered clusters (of all sizes and degree of order) and ordered/disordered clusters of a given size and order, $J[D \leftrightarrow P_{k,p}]$ and $J[P \leftrightarrow D_{k,p}]$, respectively [Fig. 3.4(d)]. These fluxes show that there is a cyclic flow of filaments between ordered and disordered clusters as indicated by the arrows in Fig. 3.4(d): While large, ordered clusters show a net gain from disordered clusters, small ordered clusters lose to disordered clusters (black arrows). Since we are in steady state, i.e. particle numbers for each species must remain constant on average, there must also be net intra-species currents: (i) fragmentation of larger into smaller polar clusters (magenta arrow), and (ii) enhanced ordering of disordered clusters (green arrow).

Taken together, the above analysis of the agent-based simulations suggests that the following processes govern the emergence and maintenance of the stationary non-equilibrium steady state: In the quasi-stationary, disordered state the system consists of mostly disordered clusters with a wide distribution of sizes $k$ [Fig. 3.2(b,c)]. Stochastically at time $t_d$, a critical nucleus (with polar moment of the order of $S_{crit}$) forms spontaneously, and subsequently grows exponentially by continuously incorporating more disordered clusters [Fig. 3.4(b,c)]. By eventually splitting up [Fig. 3.4(a-c)] due to orientational splay, polar clusters effectively self-replicate, which explains the exponential growth of the cluster polar order parameter $\Omega_p$ observed in Fig. 3.2(a). In the final nonequilibrium steady state, there is a balance
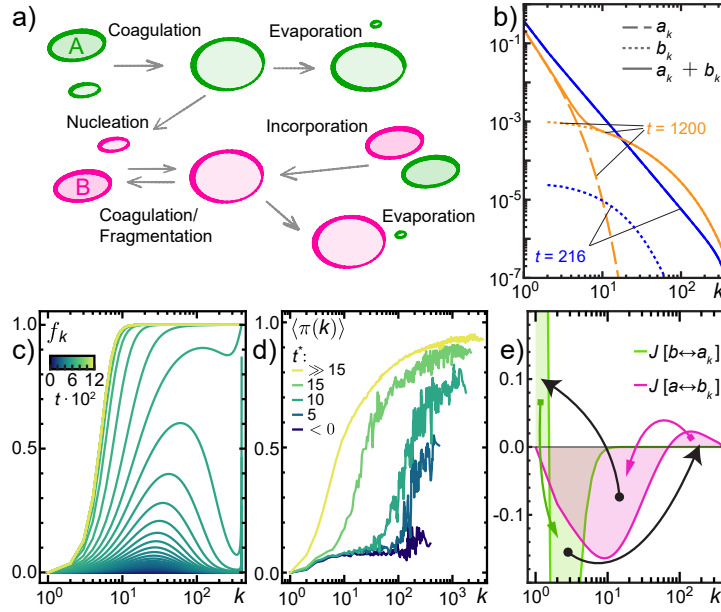
**Figure 3.5** a) Illustration of the two-species kinetic model with a disordered cluster type A (green) and an ordered type B (purple) and the various cluster assembly and disassembly processes. b) Time evolution of the cluster-size distributions, $a_k$ and $b_k$, of species A (long-dashed lines) and species B (short-dashed lines), respectively. The solid lines indicate the total distribution of cluster sizes, $n_k = a_k + b_k$, at two different times (blue at $t = 216$ and orange at $t = 1,200$). c) Time evolution of the relative fraction $f_k = b_k/n_k$. The color gradient depicts different times as quantified by the corresponding colour bar. d) Time evolution of the mean net cluster order $\langle\pi(k)\rangle_p$ during nucleation in the agent-based simulations. e) Steady-state particle fluxes $J[b \leftrightarrow a_k]$ and $J[a \leftrightarrow b_k]$ for both species as a function of cluster size $k$. Arrows: schematic depiction of inter-species (solid) and intra-species (solid colored) flux directions. For the data shown for the kinetic model we have used the parameters: $M = 400$, $A = 800$, $\nu = \beta_0 = \lambda_0 = 1$, $\mu_0 = 0.025$, $\sigma_{aa} = 1.6$, $\sigma_{ab} = 0.2$, $\sigma_{bb} = 1$ and $\omega_0 = 10^{-4}$. For the data shown in panel d) we used $\alpha = 1.67$.

between different cluster-level kinetic processes: Growth of polar-ordered clusters through coagulation of polar-ordered clusters and incorporation of disordered filaments is balanced by splitting (fragmentation) of clusters as well as evaporation of smaller filament clusters back into the 'pool' of disordered clusters [Fig. 3.4(a,c)]. These processes drive the cyclical interconversion of the different types of cluster species, as indicated by the arrows in Fig. 3.4(d).

## 3.2.6 Kinetic model for cluster assembly and disassembly

To determine whether these cluster assembly and disassembly processes constitute the essential mechanisms underlying the emergence and maintenance of the polar-

ordered non-equilibrium steady state, we introduce a simple kinetic model; cf. Fig. 3.5(a). It reduces the dynamics of the spatially extended system to a set of kinetic processes for two competing types of cluster species, a *disordered* type A and an *ordered* type B, with respective cluster size distributions $a_k = (\mathbf{a})_k$ and $b_k = (\mathbf{b})_k$, where $\mathbf{x} = (x_1, x_2, ..., x_M)$. The time evolution is assumed to be given by a set of coupled equations, $\partial_t \mathbf{a} = \mathbf{F}(\mathbf{a}, \mathbf{b})$ and $\partial_t \mathbf{b} = \mathbf{G}(\mathbf{a}, \mathbf{b})$ for the cluster size distributions, an approach frequently used to study coagulation and fragmentation dynamics in a broad class of systems [181–183]. The dynamics conserves the total number of particles, $\sum_{k=1}^{M} k \, (a_k + b_k) = 1$. Such kinetic models have successfully been used to describe the cluster statistics in a regime where polar order is absent [101, 133, 134]. Our kinetic model extends these studies to include a second species B representing polar ordered clusters, and thereby enables us to study the assembly and disassembly processes leading to the emergence of polar order.

The set of nonlinear functions $\mathbf{F}$ and $\mathbf{G}$ — for explicit forms see Appendix 3.5.1 — specify all the kinetic processes illustrated in Figure 3.5(a): (i) For the disordered species A, cluster assembly occurs by *coagulation* of smaller clusters of sizes $i$ and $j$ at a rate $\alpha_{ij} := \sigma_{aa} X_{aa}(i, j) \, v/A$. Here $v$ is the cluster velocity, $A$ the area of the whole system, and $X_{aa}(i, j)$ a term dependent on the cluster sizes which characterizes the likelihood of cluster collisions. Since disordered clusters are approximately spherical in shape such that their diameter scales as $\sqrt{i}$, we take $X_{aa}(i, j) = \sqrt{i} + \sqrt{j}$. The parameter $\sigma_{aa}$ is an amplitude measuring the strength of the coagulation process of disordered clusters; in short: *coagulation amplitude*. (ii) Likewise, for the ordered species B, there is a *coagulation* rate $\eta_{ij} := \sigma_{bb} X_{bb}(i, j) \, v/A$. The elongated shape of ordered clusters suggests geometric factors that scale with their linear extension, $X_{bb}(i, j) = i + j$. Similar as above, the parameter $\sigma_{bb}$ designates the *coagulation amplitude* for ordered clusters. (iii) Ordered clusters of linear extension $i$ can *incorporate* disordered ones of size $j$ at a rate $\gamma_{ij} := \sigma_{ab} X_{ab}(i, j) \, v/A$, and thereby form a larger ordered cluster. The geometric factor is now assumed to be $X_{ab}(i, j) = i$, and $\sigma_{ab}$ is called the *incorporation amplitude*. (iv) Cluster disassembly occurs via *split-up* (*fragmentation*) of ordered clusters at a constant rate $\mu_{ij} = \mu_0$, and *evaporation* of single disordered particles from cluster species A and B at rates $\beta_i := \beta_0 Y_a(i)$ and $\lambda_i := \lambda_0 Y_b(i)$, respectively. The geometric factors read $Y_a(i) = \sqrt{i}$ and $Y_b(i) = 1$, where the latter accounts for the observation that ordered waves evaporate particles mainly via its edges, i.e. there is no size dependence. (v) Finally, a disordered cluster may spontaneously *transform* into an ordered cluster, at a rate $\omega_i := \omega_0 Z(i)$ with $Z(i) = 1/(1 + e^{-(i-m_c-1)/v_c})$; this event effectively represents the *nucleation* of an ordered cluster. The sigmoidal shape accounts for the observation that nucleation only occurs above a certain threshold cluster size $m_c$. For specificity we choose $m_c = 100$ and $v_c = 10$ throughout our analysis. Variation of $m_c$ or $v_c$ results only in a shift in the onset of the transition to polar order, without any qualitative effects on the ordered state; cf. Appendix 3.5.1.

The kinetic model is not an exact representation of the kinetics observed in the agent-based model, but it emulates its core features. First, global polar order in the system of WASPs is analogous to the mass fraction of the ordered species $\phi_b = \sum_k k\, b_k$ in the kinetic model. Second, while the parameter $\alpha$ quantifies the (relative) strength of the alignment interaction responsible for flocking of WASPs, the corresponding analogs in the kinetic model are the amplitudes $\sigma_{ab}$ and $\sigma_{bb}$ that quantify the strength of processes leading to an increase in polar order $\phi_b$. In the following, we describe the influence of these parameters on the size distributions $a_k$ and $b_k$. For the coagulation amplitude $\sigma_{aa}$ of the disordered clusters we chose a fixed value of $\sigma_{aa} = 1.6$, such that — in the absence of an ordered species B — the size distribution $a_k$ resembles the previously observed exponentially truncated power law [101, 133, 134]; cf. Fig. 3.2(b). We integrated the set of kinetic equations to find the time evolution of the distribution of cluster sizes, $\{a_k(t), b_k(t)\}$, using a simple Euler scheme, and starting from initial conditions where all particles were in clusters of size $k = 1$: $a_1(0) = 1$. If not stated otherwise, we used the parameters specified in Fig. 3.5.

To begin with, we present the results for specific amplitudes: $\sigma_{ab} = 0.2$ and $\sigma_{bb} = 1$. In that case, the distribution of total cluster sizes, $n_k := a_k + b_k$, changes with time from an exponentially truncated power-law form [blue solid line in Fig. 3.5(b)] to a broad distribution with a distinct shoulder at intermediate $k$ [orange solid line in Fig. 3.5(b)], similar to the results obtained for a system of WASPs [Fig. 3.2(b)]. How polar order emerges is also quite comparable, as can be inferred from the time evolution of the fraction of ordered clusters, $f_k := b_k/n_k$, in the kinetic model [Fig. 3.5(c)] and the mean net cluster order, $\langle \pi(k) \rangle_p := \int_0^1 \mathrm{d}p\, \pi_k \Psi(k, p)$, in the agent-based simulations [Fig. 3.5(d)]. In both instances, ordered clusters begin to proliferate at intermediate sizes $k$, followed by a broadening of the distribution towards smaller as well as larger cluster sizes.

Next, as in the case of the agent-based model [cf. Fig. 3.4(c,d)], we wanted to learn how the various kinetic processes operating within species and between ordered and disordered clusters balance to maintain a stationary polar-ordered state, where $\partial_t a_k = 0 = \partial_t b_k$. For each species and each cluster size $k$, this requires a strict balance between inter-species and intra-species currents. Moreover, note that there is also a global balance such that the total number of particles remains constant. Figure 3.5(e) shows the net inter-species currents $J[a \leftrightarrow b_k]$ (magenta) and $J[b \leftrightarrow a_k]$ (green) for the ordered and disordered species, respectively; intra-species currents are simply the opposite, e.g. for the ordered species: $J[b \leftrightarrow b_k] = -J[a \leftrightarrow b_k]$. For the ordered clusters, $J[a \leftrightarrow b_k] < 0$ for a wide range of cluster sizes, indicating that there is an overall net loss of ordered clusters in favor of disordered clusters. A more detailed analysis shows that this is largely due to *evaporation* of single disordered particles [see Appendix 3.5.3]. At large cluster sizes, there is a net gain ($J[a \leftrightarrow b_k] > 0$) in the number of ordered clusters, which can be attributed to

the *incorporation* of disordered clusters by ordered clusters. The balance between intra-species and inter-species processes requires that there is a net flux from large to small ordered clusters, i.e. a surplus of cluster *fragmentations* relative to cluster *coagulation* events. This is phenomenologically similar to our findings in the agent-based simulations, cf. Fig. 3.4(d). There, we observed that large ordered clusters gain from disordered clusters, and small ordered clusters loose filaments to disordered clusters. This implies that there must be an intra-species current within ordered clusters, presumably also mediated by splitting of large into smaller ordered clusters. For the disordered clusters, we observe a net gain ($J[b \leftrightarrow a_k] > 0$) of single disordered particles, which is due to *evaporation* events from ordered clusters. On the other hand, there is a net loss ($J[b \leftrightarrow a_k] < 0$) of disordered clusters at intermediate cluster sizes, which is due to *incorporation* of disordered clusters into ordered clusters (and to smaller extent due to spontaneous transformation of disordered into ordered clusters). As the inter-species processes with ordered clusters create a surplus of single disordered particles, in steady state this must be balanced by a corresponding intra-species flux from small to large disordered clusters, which is facilitated by *coagulation* processes of disordered clusters.

In order to determine the phase diagram and the nature of the corresponding phase transitions, we studied how the emergence of polar order in the kinetic model depends on the strength of the various processes. We focused on the effects of *coagulation* of ordered clusters and the *incorporation* of disordered clusters into ordered clusters, varying the corresponding amplitudes $\sigma_{bb}$ and $\sigma_{ab}$, respectively. Figure 3.6(a) shows the time evolution of the mass fraction $\phi_b$ of the ordered B species for various values of the incorporation amplitude $\sigma_{ab}$. Like the cluster polar order parameter $\Omega_p$ [Fig. 3.2(a)] it exhibits a transient dwelling period before (exponentially fast) approaching the polar-ordered states. Interestingly, the duration of this dwelling time seems to be very sensitive to changes in the overall incorporation rate $\sigma_{ab}$ [Fig. 3.6(a)]. In addition, in accordance with our agent-based simulations [Fig. 3.3(b)] and as found in previous studies [20, 61, 63, 84, 85, 96, 98, 127, 173, 174], the order parameter $\phi_b$ shows a discontinuity and hysteresis as a function of a control parameter [Fig. 3.1(a)], here the incorporation amplitude $\sigma_{ab}$ [Fig. 3.6(b)]. Varying both $\sigma_{ab}$ and $\sigma_{bb}$, we obtain the bifurcation diagram (for the stationary state) shown in Fig. 3.6(c); please refer to Appendix 3.5.4 for a bifurcation diagram as a function of density $\rho_{kin}$ and $\sigma_{bb}$. The effects of coagulation of ordered clusters and incorporation of disordered clusters by ordered clusters on the emergence of polar order are quite distinct. While the amplitude of the incorporation processes ($\sigma_{ab}$) appears to regulate the transition from a disordered to a polar-ordered state, the amplitude of the coagulation processes of ordered clusters ($\sigma_{bb}$) affects the character of this phase transition. For small $\sigma_{bb}$ (weak propensity for coagulation of ordered clusters), the transition is continuous, and becomes discontinuous only above a
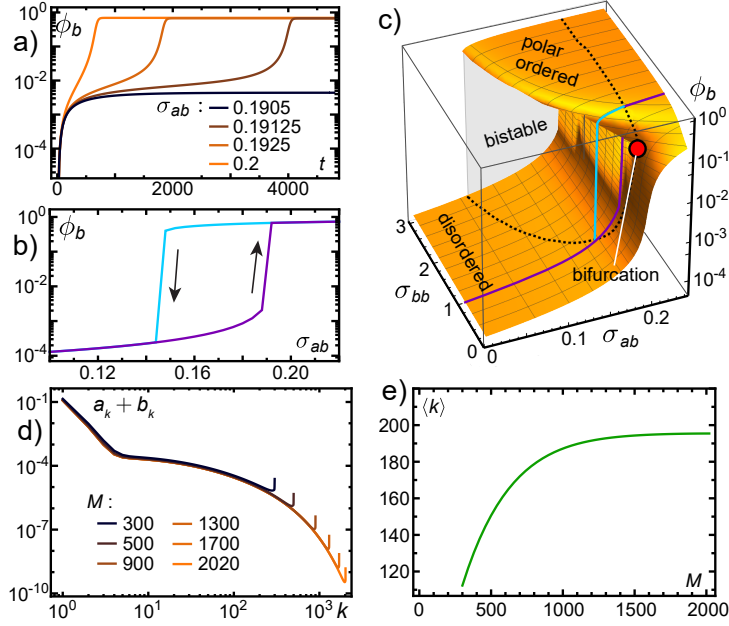
**Figure 3.6** a) Evolution of the mass fraction $\phi_b$, for different values of $\sigma_{ab}$ ($\sigma_{bb} = 1$). b) Hysteresis of the stationary mass fractions $\phi_b$ as a function of $\sigma_{ab}$. c) Bifurcation diagram of stationary mass fractions $\phi_b$ as a function of $\sigma_{ab}$ and $\sigma_{bb}$. The dashed lines mark the upper and lower boundaries of the bistable region, respectively. The coloured lines mark the position of the data shown in b). d) Stationary total cluster distribution $a_k + b_k$ as a function of the system size $M$. e) Stationary mean cluster size $\langle k \rangle$ as a function of the system size $M$. In panels d-e we used $\sigma_{aa} = 1.4$, $\sigma_{ab} = 0.2$, $\sigma_{bb} = 0.8$, $\mu_0 = 0.01$ and $\omega_0 = 10^{-5}$.

certain threshold value, with the ensuing bistable parameter regime broadening as $\sigma_{bb}$ increases further.

Finally, we checked whether the kinetic model also exhibits microphase separation, as observed in other models [15, 63, 69, 85]. To this end, we increased $M$ (adapting the area $A$ to keep the density constant) and recorded its influence upon the stationary total cluster distribution $n_k = a_k + b_k$, as well as the stationary mean cluster size $\langle k \rangle$ [Fig. 3.6(d,e)]. Notably, both become independent of system size above a certain value of $M$. We conclude that the polar phase of the kinetic model also exhibits arrested growth and hence microphase separation, like that observed in polar active systems [15, 63, 69, 85]. This contrasts with the single-species model of Peruani et al. [101, 133, 134] which exhibits a continuous order transition from a state with microscopic clusters towards a macrophase separated state.

## 3.3 Discussion

An intriguing phenomenon in polar active matter is not only the emergence of polar ordered clusters, but also the fact that the ordered state exhibits microphase separation into dense, polar-ordered clusters and a gas-like disordered filament reservoir. Here we asked how the kinetic processes of cluster assembly and disassembly might reveal the underlying mechanism. To answer this question we used a two-pronged approach based on agent-based simulations and a corresponding cluster-level kinetic theory. Our main conclusion is that microphase separation in polar active matter is a cyclic self-organizing process of particle clusters of different sizes and degrees of polar order.

Using agent-based simulations we monitored the kinetic processes at both the particle and the cluster level and thereby determined the time evolution of the cluster statistics in terms of cluster size and degree of polar order. Moreover, these simulations also allowed us to fully relate the mesoscopic cluster dynamics to the underlying microscopic dynamics of individual filaments. Taken together, this yielded the following key insights: First, we find two qualitatively distinct parameter regimes, one where polar order emerges spontaneously and another which requires the formation of a nucleus and its subsequent growth. Our simulations show that the nucleation barrier is not determined by either cluster size $k$ or cluster order $p_k$ alone, but by the polar moment $S_k = k \cdot p_k$. Second, once a critical nucleus has formed, an intricate dynamics of cluster assembly and disassembly processes is triggered that leads to microphase separation between high-density, polar-ordered clusters and a low-density, disordered background. It entails the growth of clusters by the incorporation of disordered filaments, the breakup of larger into smaller sub-clusters and their subsequent growth (cluster self-replication), coalescence of clusters and evaporation of filaments from ordered clusters into the disordered background. We have quantified these processes in terms of the probability currents between clusters of different size $k$ and degree of polar order $p$. This analysis suggests that the dynamics that maintains a non-equilibrium steady state is a cyclic dynamics in $(k, p)$ phase space.

These results suggested that the dynamics of the active filament system can be understood in terms of kinetic processes at the mesoscopic level of clusters, i.e. by considering the assembly and disassembly of clusters with different size and degree of order. To test this hypothesis we formulated a simple kinetic model that emulates the key processes identified in the agent-based simulations and analyzed the same or analogous observables. The kinetic model shows the same phenomenology as the agent-based simulations, including similar probability flows in phase space and the same topology of the bifurcation diagram. Most importantly, the kinetic model exhibits arrested growth and hence microphase separation. That opens a new perspective on this phenomenon: instead of focusing on a characterization of

the spatio-temporal patterns we identify the relevant kinetic processes that govern the probability flow in phase space.

We propose that the application of a similar methodology, namely the identification of key kinetic processes and their incorporation into a kinetic model, might be able to capture the essential dynamics of other collective phenomena in active systems, such as nematic laning [86, 88, 99], vortex formation [17, 128, 150] or coexisting types of order [1, 71, 129]. In particular, the flow in a properly defined phase space might reveal, as we show here, the mechanisms that underlie the emergence and maintenance of the corresponding non-equilibrium steady states.

## 3.4 Appendix: WASP simulations

In the following, we shortly discuss the implementation of the agent-based simulations of **w**eakly-**a**ligning **s**elf-propelled **p**olymers (WASP's). For a detailed description please refer to the Supplemental Material of Ref. [1].

### 3.4.1 WASP simulation model

We consider a system of $M$ polymer filaments, each with a fixed length $L$ and a width $d$. Individual polymers are modelled as discrete, slender chains consisting of $N - 1$ identical cylindrical segments connected by $N$ identical spherical joints; for an illustration see Fig. 3.7. In this way, each point along the polymer's contour has a well-defined, smooth surface and tangential direction, reducing artificial friction effects due to the discretization present in bead-spring-like representations [108].

The polymers perform a trailing motion on a planar surface: as the head of the polymer changes its direction the tail strictly follows the trajectory traced out by the head. This resembles the typical situation observed in actomyosin motility assays where in a planar geometry actin filaments are propelled along their contour by immobilized molecular motors and where motion orthogonal to the filament contour is suppressed [15, 20]. In these experimental setups, it is observed that the head of each polymer performs a persistent random walk (with persistence length $L_p$), and, in addition, changes its direction due to local alignment interactions when colliding with other polymers.

In order to model this dynamics, we describe each polymer $n$ by the positions $\mathbf{r}_j^{(n)}$ of its spherical joints $j$, where $n \in \{0, 1, \ldots, M - 1\}$ and $j \in \{0, 1, \ldots, N - 1\}$ (with the head of a polymer denoted by $j = 0$); for an illustration see Fig. 3.7. We assume that—given the direction $\mathbf{u}_0^{(n)}$ of a polymer's head—its equation of motion reads:

$$\partial_t \mathbf{r}_0^{(n)} = v\, \mathbf{u}_0^{(n)} - \mathbf{F}_{\text{rep}} = v \begin{pmatrix} \cos\theta_0^{(n)} \\ \sin\theta_0^{(n)} \end{pmatrix} - \mathbf{F}_{\text{rep}}. \tag{3.1}$$

Here $\theta_0^{(n)}$ denotes the $n^{\text{th}}$ polymer's orientation and $v$ the velocity of a free polymer. $\mathbf{F}_{\text{rep}}$ is a weak repulsive force (the exact definition of which we will give later in Eq. (3.7)) which only acts when the filament head overlaps with the head or tail of another polymer. The speed $v^{(n)}$ of filament $n$ is given by the absolute value of $\partial_t \mathbf{r}_0^{(n)}$.
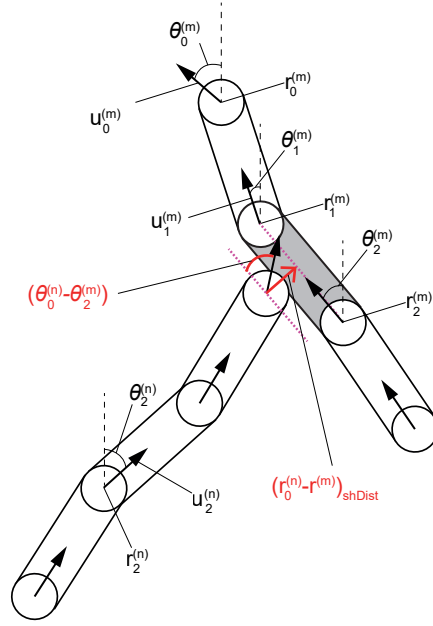
**Figure 3.7 Illustration of interactions in the filament model.** The head of a filament $n$ collides with the body (contour) of an adjacent filament $m$ between bead position $\mathbf{r}_1^{(m)}$ and $\mathbf{r}_2^{(m)}$. The *impact angle* between the two filaments is given by $\Delta\theta_{nm} := \theta_0^{(n)} - \theta_2^{(m)}$, where $\theta_0^{(n)}$ and $\theta_2^{(m)}$ denote the orientation of the head of the $n^{\text{th}}$ polymer and the orientation of the tangent to the body of the $m^{\text{th}}$ polymer where the collision happens. In the illustrated case the latter is given by the orientation of the $2^{\text{nd}}$ cylinder of the $m^{\text{th}}$ polymer (which in turn is given by the orientation of the normalized bond vector, $\mathbf{u}_2^{(m)} := (\mathbf{r}_1^{(m)} - \mathbf{r}_2^{(m)})/|\mathbf{r}_1^{(m)} - \mathbf{r}_2^{(m)}|$). If the collision happens at the head of the $m^{\text{th}}$ filament, $\theta_0^{(m)}$ is given by the orientation of its director $\mathbf{u}_0^{(m)}$. The distance vector (red arrow) $\Delta\mathbf{r}_{nm} = (\mathbf{r}_0^{(n)} - \mathbf{r}^{(m)})_{\text{shDist}}$ is the normal vector to the center-line of filament $m$ between $\mathbf{r}_1^{(m)}$ and $\mathbf{r}_2^{(m)}$, connecting to $\mathbf{r}_0^{(n)}$.

The equation of motion for the orientation $\theta_0^{(n)}$ of the $n^{\text{th}}$ polymer's head is given by

$$\partial_t \theta_0^{(n)} = -\frac{\delta H_0^{(n)}}{\delta \theta_0^{(n)}} + \sqrt{\frac{2\upsilon}{L_p}}\,\xi\,, \tag{3.2}$$

where the first term denotes the effect of other filaments on the orientation of filament $n$, and $\xi$ is an angular random white noise with zero mean and unit variance; the amplitude of the noise ensures that the value of the path persistence length of a free polymer is given by $L_p$. The effective potential $H_0^{(n)}$ acting on the director of filament $n$, is given by a sum $H_0^{(n)} = \sum_m U_m^{(n)}$ over the alignment potentials

$U_m^{(n)}$. These potentials describe the alignment interaction between filament $m$ and the head of filament $n$, and will depend on both the relative distance and the relative orientation of these filaments. To define these potentials we introduce the distance vector [Fig. 3.7]

$$\Delta \mathbf{r}_{nm} = \left( \mathbf{r}_0^{(n)} - \mathbf{r}^{(m)} \right)_{\text{shDist}}, \tag{3.3}$$

which denotes the vector connecting the head of polymer $n$ with that part of the body (contour) of an adjacent polymer $m$ that has the shortest possible distance to the head [red arrow in Fig. 3.7]. We signify the segment $j$ on filament $m$ that filament $n$ collides with as *collision segment*. The corresponding orientation of this collision segment is denoted by $\theta_j^{(m)}$ [Fig. 3.7]. With these definitions, we can now define the alignment potential as

$$U_m^{(n)} = C \left( |\Delta \mathbf{r}_{nm}| \right) \times \left( A_p \left( \Delta \theta_{nm} \right) + A_n \left( \Delta \theta_{nm} \right) \right), \tag{3.4}$$

where $\Delta \theta_{nm} = \theta_0^{(n)} - \theta_j^{(m)}$ denotes the impact angle of the collision of the head of polymer $n$ with the body of filament $m$. The first factor $C \left( |\Delta \mathbf{r}_{nm}| \right)$ accounts for the spatial dependence of the potential. For simplicity, we assume a potential that vanishes outside of an interaction radius $d$ and increases linearly for smaller distances:

$$C \left( |\Delta \mathbf{r}_{nm}| \right) = \begin{cases} 0 & \text{if } |\Delta \mathbf{r}_{nm}| > d \\ (d - |\Delta \mathbf{r}_{nm}|)/d & \text{else} \end{cases} . \tag{3.5}$$

The second factor is a sum of functions $A_{p/n}$ that describe the polar/nematic alignment-torques present during a collision. They are given by

$$A_p(\phi) = -\frac{\varphi_p v^{(n)}}{d} \cos \phi, \tag{3.6a}$$

$$A_n(\phi) = -\frac{\varphi_n v^{(n)}}{d} \cos 2\phi, \tag{3.6b}$$

with the amplitudes $\varphi_{p/n}$ characterizing the typical angular displacement in a single collision (see Supplemental Material of Ref. [1]). A variation of $\varphi_{p/n}$ allows to independently and continuously vary the preferences for polar or nematic alignment. As was shown in Ref. [1], the WASP simulation model shows the formation of both polar and nematic patterns, depending primarily on the relative alignment strength $\alpha = \varphi_n / \varphi_p$.

To prevent an unphysical aggregation of filaments—that can be triggered by the alignment torques when too many filaments overlap at the same location—we

added a very weak repulsion force $\mathbf{F}_{\text{rep}}$ to Eq. (3.1). It is given by

$$\mathbf{F}_{\text{rep}} = -s \sum_m C\left(|\Delta\mathbf{r}_{nm}|\right) \frac{\Delta\mathbf{r}_{nm}}{|\Delta\mathbf{r}_{nm}|} , \qquad (3.7)$$

where $s = 0.1$ denotes the small amplitude.

In actomyosin motility assays [1, 15, 16, 19, 20] one observes that the polymer tails follow the movement of their respective filament heads. In our agent-based model, we emulate this trailing motion as follows: First, in order to assure tangential motion, for a given filament $n$, each joint $\mathbf{r}_j^{(n)}$ in its tail ($j > 0$) is assumed to move in the direction of $\frac{1}{2}(\mathbf{u}_{j+1}^{(n)} + \mathbf{u}_j^{(n)})$, corresponding to the average of the segment's orientations adjacent to that joint [see Fig. 3.7]. Second, to also maintain an average length $b$ of the cylindrical segments between the bonds we assume a linear (Hookian) restoring force with spring coefficient $K_s$. Taken together, the equation of motion of a tail joint $j$ is defined as

$$\partial_t \mathbf{r}_j^{(n)} = K_s \left(\left|\mathbf{r}_j^{(n)} - \mathbf{r}_{j-1}^{(n)}\right| - b\right) \frac{1}{2}\left(\mathbf{u}_{j+1}^{(n)} + \mathbf{u}_j^{(n)}\right) . \qquad (3.8)$$

We chose $K_s = 200$ sufficiently large to keep the cylinder length close to its average value $b$.

In our simulations we observed that the performance of our algorithm significantly depended on the number of times the alignment torques, Eq. (3.6), were calculated. We, therefore, were searching for an averaging scheme that would reduce the computation of the alignment torques to at most once per filament per time step. The main idea put forward in Ref. [1]—and also shown there not to affect the system's dynamics—is to implement an averaging scheme as follows: One replaces the sum in $H_0^{(n)}$ by an averaged quantity $\tilde{H}_0^{(n)}$ defined as

$$\tilde{H}_0^{(n)} = A_p\left(\Delta\theta_p^{(n)}\right)|q_p| + \tilde{A}_n\left(\Delta\tilde{\theta}_n^{(n)}\right)|\Delta\tilde{e}_n| . \qquad (3.9)$$

The first term in Eq. (3.9) (polar interaction) is motivated as follows: Instead of calculating the polar torques, Eq. (3.6a), for each adjacent polymer $m$ and then summing over all these polymers with weights given by the repulsive linear potential $C(|\Delta\mathbf{r}_{nm}|)$, we determine the quantity

$$q_p = \sum_m C\left(|\Delta\mathbf{r}_{nm}|\right) \frac{v^{(m)}}{v} e^{i\theta_j^{(m)}} . \qquad (3.10)$$

It defines the average in the velocities of all the collision segments $j$ over all filaments $m$ weighted by the strength of the impact, $C\left(|\Delta\mathbf{r}_{nm}|\right)$, of filament $n$ with them. In

other words, this vector characterizes the weighted (by interaction strength) average of the velocities of the collision segments. We then use the orientation $\theta_p = \arg(q_p)$ of the average velocity to calculate the average exerted torque, $A_p\big(\Delta\theta_p^{(n)}\big)$ using the average polar impact angle defined as $\Delta\theta_p^{(n)} = \theta_0^{(n)} - \theta_p$. Note that the magnitude of $q_p$ measures the average strength of all the polar impacts on filament $n$. Here we have additionally introduced a velocity dependence ($v^{(m)}/v$ in Eq. (3.10)) to emulate that polar alignment in the motility assay is mainly caused by friction between filaments. With this, our agent based model can also be used in cases where filament velocities are broadly distributed. Since the filament velocity in the present study is constant and only very weakly influenced by $\mathbf{F}_{\mathrm{rep}}$, this velocity dependence can also be omitted without affecting the results.

The second term in Eq. (3.9) is motivated in a similar fashion as the first one: Instead of calculating Eq. (3.6b) for each adjacent polymer $m$, we define a weighted average direction of the connecting vector $\Delta\widetilde{\mathbf{e}}_n$

$$\Delta\widetilde{\mathbf{e}}_n := \sum_m C\left(|\Delta\mathbf{r}_{nm}|\right) \frac{\Delta\mathbf{r}_{nm}}{|\Delta\mathbf{r}_{nm}|} . \tag{3.11}$$

weighted, again, by the strength of the respective impact.

The overall magnitude of the repulsive potential to nematic alignment is given by the absolute value of $\Delta\widetilde{\mathbf{e}}_n$.

Similarly as for the polar case, we used the orientation $\tilde{\theta}_n$ of the vector $\Delta\widetilde{\mathbf{e}}_n$ to define an average nematic impact angle as $\Delta\tilde{\theta}_n^{(n)} = \theta_0^{(n)} - \tilde{\theta}_n$, which we used to compute the average nematic alignment torque in Eq. (3.9). Note that the nematic term in Eq. (3.9) reads

$$\tilde{A}_n(\theta) = \frac{\varphi_n v^{(n)}}{d} \cos 2\theta, \tag{3.12a}$$

since $\tilde{\theta}_n$ is derived from the normal vectors to the polymer contours (and not the tangential vectors, as it was done before).

### 3.4.2 WASP implementation and parameters

Algorithmically, we integrate the dynamics by a straightforward Euler algorithm with a time step of $2 \times 10^{-3}$, which was implemented in C++ using a heavily parallelized architecture in OpenMP [184]. Maximal performance of the simulation was achieved by employing a cell algorithm and Verlet lists [164] that exploit the fact that filament interactions are short-ranged. This implementation resulted in a practically linear scaling of simulation times with $M$ (the number of filaments in the

system). Throughout this work and if not stated otherwise, we fixed some of the model parameters to values similar to those used in Ref. [1]: filament aspect ratio $L/d = 21$, discretization $N = 5$, persistence length $L_p = 31.75L$, and velocity $v = 1$. The polar alignment strength was fixed to $\varphi_p = 0.036 \approx 2.1°$ to obtain collision statistics similar to those observed experimentally [20]. Moreover, we used a system consisting of $10^4$ filaments and a periodic simulation box of length $L_{\text{box}} = 81.3L$. Simulations were started with random initial conditions, i.e. filaments were placed at random positions and with random orientations in the simulation box. Time is measured in units of the correlation time $L_p/v$ and length measured in units of filament length $L$.

### 3.4.3 Cluster polar order and other order parameters

As described in the main text, we decomposed the assembly of polymers into clusters of close-by polymers. To that end, we define the distance between two polymers $n$ and $m$ as the length of the shortest one of the set of distance vectors $\mathbf{r}_j^{(n)} - \mathbf{r}_i^{(m)}$ between their nodes $j$ and $i$. We calculated all distances between adjacent polymers, and assigned polymers to the same cluster if their distance was smaller than the bond length $b$.

Next, to properly define the degree of polar order for each of these clusters, we defined the net polar order of a cluster (of size $k$) as $\pi_k := p_k - \Delta_k$, where $\Delta_k$ denotes the expected nonzero polar order of clusters where the orientation of each filament is chosen at random; the cluster polar order was defined as $p_k := \frac{1}{k}|\sum_{j=1}^{k} \exp(i\theta_j)|$. The quantity $\Delta_k$ is obtained by calculating the mean polar order $\Delta_k = \frac{1}{k}\langle|\sum_{j=1}^{k} e^{iO_j}|\rangle$ with the filaments' orientations $O_j$ uniformly distributed in the interval $[-\pi; \pi]$. Explicitly writing out the absolute value, $\Delta_k$ reads

$$\Delta_k = \frac{1}{k}\left\langle\left|\sum_{j=1}^{k} e^{iO_j}\right|\right\rangle = \frac{1}{k}\left\langle\left(\sum_{m,n=1}^{k} e^{i(O_m-O_n)}\right)^{1/2}\right\rangle. \tag{3.13}$$

By splitting up the double sums and introducing the shorthand notation $\delta_m^n = O_m - O_n$, this can be further rewritten as

$$\Delta_k = \frac{1}{k}\left\langle\left(\sum_{m=n}^{k} 1 + \sum_{m=1}^{k}\sum_{n=m+1}^{k} e^{i\delta_m^n} + \sum_{m=1}^{k}\sum_{n=1}^{m-1} e^{i\delta_m^n}\right)^{1/2}\right\rangle. \tag{3.14}$$

Evaluating the first sum and renaming the indices in the last sum, one obtains

$$\Delta_k = \frac{1}{k}\left\langle\left(k + \sum_{m=1}^{k}\sum_{n=m+1}^{k} e^{i\delta_m^n} + \sum_{m=1}^{k}\sum_{n=m+1}^{k} e^{-i\delta_m^n}\right)^{1/2}\right\rangle. \tag{3.15}$$

With the shorthand notation $\sum_{m=1}^{k}\sum_{n=m+1}^{k} =: \sum_{(m,n)}$ this can be written as

$$\Delta_k = \frac{1}{k}\left\langle\left(k + 2\sum_{(m,n)} \cos\delta_m^n\right)^{1/2}\right\rangle. \tag{3.16}$$

Finally, by expanding the square root in powers of $\cos\delta_m^n$ one finds

$$\Delta_k = \frac{1}{k}\left\langle\sqrt{k} + \frac{1}{\sqrt{k}}\sum_{(m,n)} \cos\delta_m^n - \frac{1}{2k^{3/2}}\sum_{(m,n)} \cos^2\delta_m^n\right.$$
$$\left. + \frac{1}{2k^{5/2}}\sum_{(m,n)} \cos^3\delta_m^n + \mathcal{O}(k^{-3/2})\right\rangle. \tag{3.17}$$

Since $\langle\cos^j\delta_m^n\rangle = 0$ for $j$ odd and $\langle\cos^2\delta_m^n\rangle = \frac{1}{2}$, this can be further simplified (note that, for $n \neq u$ or $m \neq v$, terms of the form $\langle\sum_{(u,v)}\sum_{(m,n)} \cos\delta_u^v \cos\delta_m^n\rangle$ can be factorized and thereby give no contribution in Eq. (3.17)). By evaluating the remaining sum, one obtains

$$\Delta_k = \frac{1}{\sqrt{k}}\left(1 - \frac{(k-1)}{8k}\right) + \mathcal{O}(k^{-5/2})$$
$$= \frac{1}{\sqrt{k}}\left(\frac{7}{8} + \frac{1}{8k}\right) + \mathcal{O}(k^{-5/2}). \tag{3.18}$$

In the main text, we defined the *cluster polar order parameter* as an average of the net order $\pi_k$ weighted by the respective cluster size $k$:

$$\Omega_p := \frac{1}{M}\sum_{\{c\}} \pi_k^{(c)} k^{(c)} \tag{3.19}$$

This has to be distinguished from the alternative definition of a global polar order parameter

$$\mathcal{P} = \frac{1}{M}\left|\sum_{j=0}^{M-1} e^{i\theta_0^{(j)}}\right|, \tag{3.20}$$
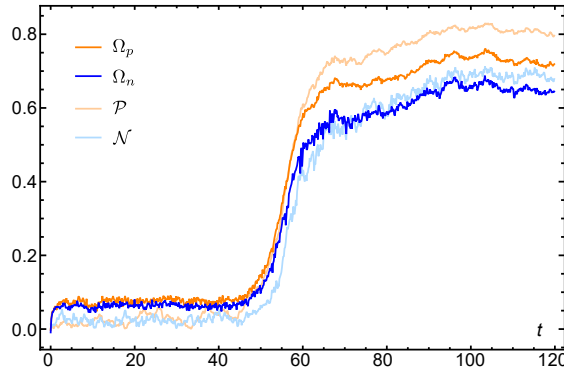
**Figure 3.8 Global order parameters:** Temporal evolution of the global *polar* order parameters $\Omega_p$ and $\mathcal{P}$, and the global *nematic* order parameters $\Omega_n$ and $\mathcal{N}$, as indicated in the graph. Parameters: $\alpha = 2$.

which is an average over all filament orientations independent of which clusters they belong to. The temporal evolution of both of these global order parameters, $\Omega_p$ and $\mathcal{P}$, is shown in Fig. 3.8. Although they are related quantities, there are clear differences:

(i) In the disordered phase, $\Omega_p$ still displays a nonzero value stemming from the small average polar order of the clusters present in the system. In contrast, $\mathcal{P}$ is almost zero in the disordered phase as it is averaged over all filaments in the system, whose orientations cancel out. (ii) In the ordered phase, however, $\Omega_p$ is smaller than $\mathcal{P}$ as single 'ordered' clusters are not contained in the sum for $\Omega_p$; note that $\pi(1) = 0$. Throughout this work we prefer to use $\Omega_p$, since it is more sensitive to polar structures which form in independent parts of a system, but whose orientations are not yet correlated. For example, two non-overlapping polar clusters of the same size and order, but opposite orientations, would yield $\mathcal{P} = 0$, whereas their presence would be detected with $\Omega_p$.

Similarly, one can define two distinct types of nematic order parameters, $\Omega_n$ and $\mathcal{N}$, by simply replacing every angle $\theta$ with $2\theta$ in the above definitions; see Fig. 3.8 for an example. However, since in our study we only investigate polar structures and in this case the nematic order parameter is slaved to the polar order, it is of little importance for our analysis.

### 3.4.4 Time scale analysis

#### 3.4.4.1 Measurement of $t_0$, $t_d$ and $\tau$

To obtain the initial time scale $t_0$, the dwell time $t_d$, and growth time $\tau$ from our data, we analysed the temporal evolution of the cluster polar order parameter $\Omega_p(t)$ (Fig. 3.8). To this end, we looked for a fit function $f(t)$ for $\Omega_p(t)$, which

should capture the main features of its temporal evolution: (i) fast rise towards the quasi-stationary, disordered regime (within a short time $t_0$), (ii) plateau until $t_d$, (iii) exponential growth starting at time $t_d$. In our analysis we decided to use the following piecewise defined function

$$f(t) = \begin{cases} a \left(1 - e^{-t/t_0}\right) & \text{for } t < t_d \\ a \left(1 - e^{-t_d/t_0}\right) e^{(t-t_d)/\tau} & \text{for } t > t_d. \end{cases} \tag{3.21}$$

Here $a$ is a fit parameter that quantifies the small, yet nonzero value of $\Omega_p$ during the quasi-stationary, disordered regime before nucleation. The fit was made up to the time point at which $\Omega_p(t) > 0.5$ for the first time, that is before $\Omega_p(t)$ started to saturate again.

### 3.4.4.2 System size dependence of $t_d$ and $\tau$

In the main text, we studied how the characteristic times $t_d$ and $\tau$ depend on the relative alignment strength $\alpha$ [Fig. 3.2(d)]. Here, we additionally investigate how these quantities depend on the system size; see Fig. 3.9(a). We find that the expected dwell time $\langle t_d \rangle$ scales inversely with the area of the system, $L_{\text{box}}^2$. This indicates that—for each given set of parameters—there is a constant probability per unit of area to nucleate a cluster large enough to trigger the exponential increase of order in the system. Hence, the formation of critical nuclei occurs independently in different parts of the system.

We further observe that the growth time $\tau$ is approximately independent of system size ($\tau \approx 4.5$), although $L_{\text{box}}$ is increased by more than a factor of 3. This is probably caused by the fact that on the one hand the mass of ordered clusters growths (after a critical nucleus has formed) exponentially with time, but that on the other hand the total filament mass of ordered clusters in an ordered system (i.e. the mass that has to be incorporated into the ordered clusters during the growth process) grows only approximately proportionally to the size of the system. It therefore takes only a very short time for the additional filaments (introduced by the increase in system size) to be incorporated into the ordered clusters. Hence, in order to observe a significant change of $\tau$, one would have to increase the number of filaments in the system (and thus $L_{\text{box}}$) by far more than a small factor; this however is beyond the numerically feasible limit.

### 3.4.4.3 Variance of the nucleation time

We also recorded the statistics of nucleation times $p(t_d)$ at one point in parameter space and for a small value of $\alpha$ (Fig. 3.9(b)). Similar as in classical nucleation theory [179, 180], it exhibits an exponential distribution of times. This is also
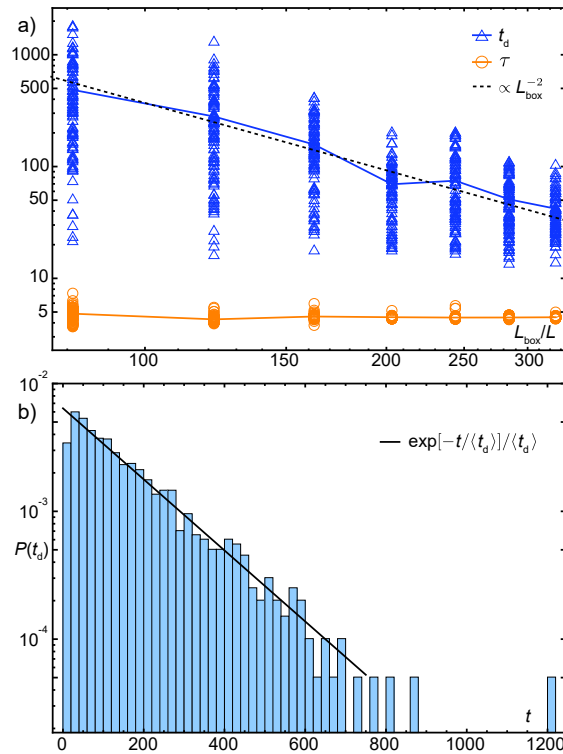
**Figure 3.9 System size dependence and distribution of waiting times.** (a) Waiting time $t_d$ and growth time $\tau$ as a function of the system size $L_{box}$ in units of the polymer length $L$. Solid lines denote average values (taken over $90 - 100$ independent simulations for each system size); data are shown as triangles and circles for $t_d$ and $\tau$, respectively. The black dashed line indicates a scaling law proportional to the area of the system. (b) Histogram of waiting times $t_d$ taken over an ensemble of 1000 simulations. The black solid line shows an exponential waiting time distribution $P(t_d)$ with mean $\langle t_d \rangle = 156$. Parameters: $\rho L^2 = 1.51$, $\alpha = 1.583$ for (a) and $\alpha = 1.67$, $L_{box} = 81.3L$ for (b).
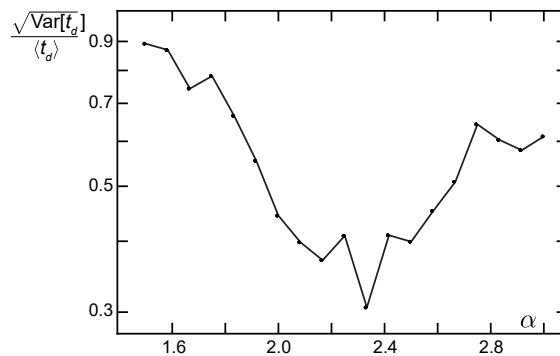


**Figure 3.10 Coefficient of variation** for the dwell time $t_d$, $CV = \sqrt{Var[t_d]}/\langle t_d \rangle$, as a function of $\alpha$. Parameters and data are identical to Fig. 3.2(d).

reflected in the coefficient of variation $CV = \sqrt{\text{Var}[t_d]}/\langle t_d \rangle \approx 1$, see Fig. 3.10. With increasing $\alpha$, however, we observe that the average dwell time $t_d$ shrinks until eventually the system instantly starts to develop polar order [cf. Fig. 3.2(d)].

This decrease of $t_d$ is accompanied by a decrease of the coefficient of variation [Fig. 3.10], indicating that the waiting times are no longer exponentially distributed. Since $t_d$ would always be zero in the limit of an instantaneous nucleation (and would also not fluctuate any more), this is in accordance with the above observation.

The subsequent increase of the coefficient of variation (after the minimum at $\alpha \approx 2.3$) is an artefact. It can be attributed to an increased error of the fit used to determine $t_d$; cf. Eq. (3.21). This increase in error is due to the fact that $\Omega_p$ no longer shows a clear plateau after reaching the metastable state but instead directly continues to grow exponentially towards macroscopic order.

### 3.4.5 Cluster stability analysis

#### 3.4.5.1 Critical polar moment

As discussed in the main text, we probed the stability of the disordered state by inserting perfectly ordered clusters of size $\tilde{k}$ (and hence polar moment $S = \tilde{k}$) into systems at time points where they were still in the metastable disordered state. Specifically, we chose the time point $t = 5 > t_0$, sufficiently later than the time when the systems had reached the metastable state. To keep the overall filament density constant, we extracted $\tilde{k}$ filaments at random and used them to construct the clusters with which we probed the system. To this end, we stacked these filaments in parallel, with a transversal distance $d$; see Fig. 3.4(a) for an illustration of such a cluster. We inserted the so formed cluster at a randomly chosen position and with random initial orientation.

We then monitored the temporal evolution of the cluster polar order parameter $\Omega_p$ until a given time point $t = 25$, which we chose such that it is much larger than $\tau$. Figure 3.11 shows a scatter plot of 30 realizations for each set of parameters as a function of $S$, for two different values of the relative alignment strength $\alpha$. As can be inferred from the statistical distribution of the observed cluster polar order parameters $\Omega_p$ (at times $t \gg \tau$), there is no hard threshold for the cluster size above which the system always develops polar order. Instead, the probability that insertion of the artificial nucleation seed leads to order formation increases gradually with $S$ over some finite width. We define the critical value $S_{\text{crit}}$ as that value of $S$ which leads to the emergence of polar order with probability $\frac{1}{2}$. To determine $S_{\text{crit}}$ from the recorded data, we fitted the averaged polar order parameter (which is proportional
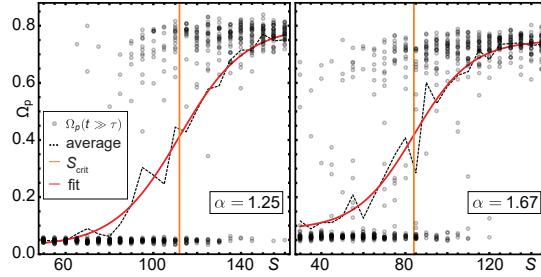
**Figure 3.11 Cluster stability analysis.** Scatter plots of the cluster polar order parameter $\Omega_p$ at $t = 25 \gg \tau$ (gray open circles) for different initial sizes $S$ of artificially inserted perfectly ordered clusters; for each set of parameters we conducted 30 independent simulations runs. The left and right panel show the results for relative alignment strengths $\alpha = 1.25$ and for $\alpha = 1.67$, respectively. The dashed black and solid red line indicate the average of the polar order parameter and a sigmodial fit, respectively. Vertical orange lines indicate the approximate values for the critical polar moment $S_{\mathrm{crit}}$.

to the nucleation probability) with a sigmoid function of the form

$$f(S) = a + \frac{b}{1 + e^{-(S - S_{\mathrm{crit}})/c}} \,, \tag{3.22}$$

where $a$, $b$ and $c$ are fitting parameters (Fig. 3.11).

As an alternative to inserting artificial clusters to study nucleation in regions of parameter space where $S_{\mathrm{crit}}$ is large, it may be worth considering in future studies an approach that facilitates the study of rare events through a strategy of cloning trajectories and/or modifying the underlying dynamics [185]. This would enable an investigation of spontaneous nucleation events even where $t_d$ is large. These methods have recently been applied to study other active matter systems [186–188].

### 3.4.5.2 Critical polar moment and spontaneous nucleation

We have tested whether the value of $S_{\mathrm{crit}}$—as obtained by insertion of artificial seeds—faithfully predicts the nucleation threshold for the spontaneous formation of polar order. To this end, we performed simulations in a parameter range where $t_d$ is small; see Fig. 3.12(a) for a single simulation run for $\alpha = 1.67$. As can be inferred from this figure, the cluster with the largest polar moment $S^{(1)}$ needs several 'attempts' before it finally succeeds in triggering the formation of polar order in the system. Given a threshold value $S_{\mathrm{crit}}$, one expects that each time $S^{(1)}$ exceeds this threshold it leads to polar order formation only with a certain success probability $p_{\mathrm{crit}}$. This implies that—sampling over many realization—the number of attempts $n_\times$ needed to trigger formation of polar order is given by a geometric
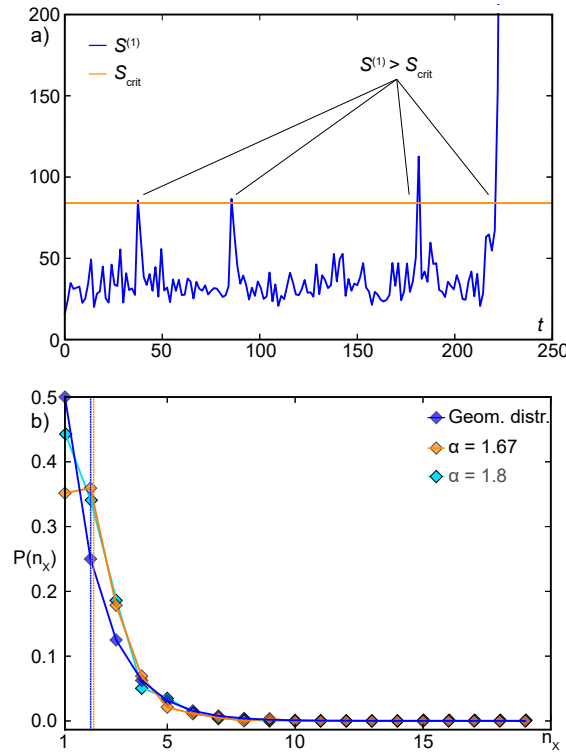
**Figure 3.12 Spontaneous formation of critical nucleation clusters. (a)** Temporal evolution of the largest polar moment $S^{(1)}$ in a single simulation run (blue solid line). The orange line represents the value of the critical polar moment $S_{\mathrm{crit}} \approx 84$ as obtained from Fig. 3.11 (right panel). Before the system eventually exhibits rapid formation of polar order, there are three instances where it crosses that line but is not successful in developing polar order. Parameters: $\alpha = 1.67$, $\Delta t = 1.5$. **(b)** Probability distribution $P(n_\times)$ of the number of times $n_\times$ the largest polar moment $S^{(1)}$ exceeds the threshold $S_{\mathrm{crit}}$ before it finally succeeds in forming polar order, obtained from the simulation data (orange and cyan line, for $\alpha = 1.67$ and $\alpha = 1.8$, respectively), in comparison with a geometric distribution (blue line) with parameter $p = 0.5$. The dashed vertical orange and cyan line represent the mean value of the simulation data ($\langle n_\times \rangle = 2.125$ and $\langle n_\times \rangle = 2.02$), for $\alpha = 1.67$ and $\alpha = 1.8$, respectively. The expectation value of the geometric distribution for $p = 0.5$ ($\mathbb{E}(n_\times) = 2$) is shown as a blue vertical line. Data were obtained in 892 simulation runs for each $\alpha$. For $\alpha = 1.8$ $S_{\mathrm{crit}} \approx 75$ was obtained with the same method as shown in Fig. 3.11 (data not shown).

distribution,

$$P(n_\times) = p_{\mathrm{crit}} \left( 1 - p_{\mathrm{crit}} \right)^{n_\times - 1} . \tag{3.23}$$

We define the critical cluster size such that if a cluster with a polar moment $S_{\mathrm{crit}}$ is formed randomly it should—on average—in half of the cases lead to the formation of polar order, i.e. the success probability should be $p_{\mathrm{crit}} = 0.5$.
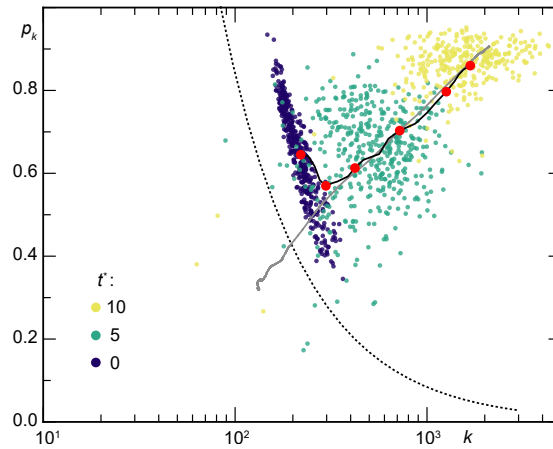
**Figure 3.13 Scatter plot for the size $k$ and order $p$ of the clusters with the largest polar moment $S^{(1)}$.** At time point $t^* = 0$, perfectly ordered clusters of size $k = 140$ are inserted into the system and their temporal evolution is monitored for 431 independent realizations. The ensuing probability clouds at different time points $t^*$ are indicated in the graph with different color. As time progresses the cloud moves on average along a trajectory indicated by the black solid line, which depicts the average path of $\langle S^{(1)} \rangle$ in $k$-$p$ space; for comparison the average path from Fig. 3.2(f) is shown in gray. The red circles mark the average $\langle S^{(1)} \rangle$ at equidistant timepoints ($\Delta t = 2$, starting at $t^* = 0$). The dashed line indicates $S_{\text{crit}} \approx 84$. Same parameters as for Fig. 3.2(f).

Indeed, our simulations show that the success probability closely resembles a geometric distribution [Fig. 3.12(b)]; for two values of $\alpha$ we sampled over 892 realizations with different random initial conditions and the same threshold value as found in the simulations using artificially inserted clusters. Moreover, the geometric distribution and the histogram obtained from our simulation data show the same mean value.

### 3.4.5.3 Course of nucleation in k-p space

As discussed in the main text and shown in Fig. 3.2(f) we monitored and sampled the temporal evolution of clusters with the largest polar moment $S^{(1)}$ in $k - p$ space for a sample size of 892 independent realizations. We tested whether our agent-based simulations take the same path towards polar order also if nucleation is triggered by insertion of an artificial nucleation seed, instead of waiting for a spontaneous nucleation and growth event to happen [Fig. 3.2(f))]. To this end, we inserted perfectly ordered clusters of size $k = 140$ into 431 different systems at a time point $t = 5$ where the system was still in a disordered state. As can be inferred from Fig. 3.13, the probability cloud of $S^{(1)}$ values rapidly becomes indistinguishable from the cloud shown in Fig. 3.2(f). Moreover, the center of mass follows, after
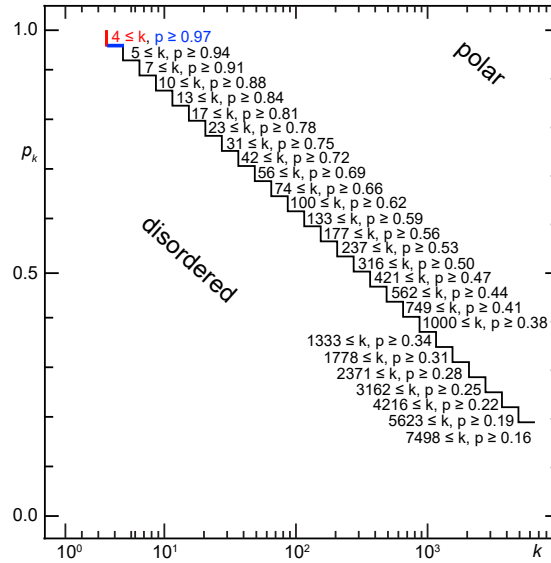
**Figure 3.14 Separation line between polar ordered and disordered regions.** Illustration of the heuristic choice for the Separation line between polar ordered and disordered regions shown in Fig. 3.4(d). The figure shows the numerical values for the positions of the "steps" of the heuristic division line. The value next to the $k$ ($p$) denotes the position of the left (lower) boundary of a step on the $k$-axis ($p$-axis). The first step and the corresponding numerical values are colored for illustration.

some initial transient, the same path as the center of mass of clusters in systems where these clusters spontaneously emerged. Note that the linear spread of the cloud at $t^* = 0$ is due to an overlap of the perfectly ordered seeds (placed into the system) with disordered clusters (already present in the system).

## 3.4.6 Steady-state flux of the flocking state

In order to obtain the steady state particle fluxes in cluster space shown in Fig. 3.4(d), we have investigated the exchange of filaments between different cluster size-order groups using agent-based simulations (WASP). Other than in the kinetic model, clusters in the agent-based simulations can have any degree of polar order $p_k$. Thus, for proper comparison, we ad hoc divided the phase space of cluster size and order (short: $k-p$–space) into two regions, a polar ordered and a disordered region; the corresponding heuristic separation line is shown in Fig. 3.4(d). All clusters above the dividing line are defined as polar for our analysis, and all clusters below as disordered. The line was chosen such that for a system in a disordered state, most cluster would be contained in the disordered region [cf. upper panel of Fig. 3.2(c) for an example of the statistics of cluster size and order in a disordered system]. The exact numerical definition of this division line is shown in Fig. 3.14.

To measure the particle currents, we initiated a set of simulations in a polar-ordered state and recorded—in short time intervals of $\Delta t$—for each filament $j$ the temporal evolution of the size $k(t,j)$ and polar order $p(t,j)$ of the cluster to which this filament $j$ belonged to. With that information at hand we were able to record for any given point $(k,p)$ in the polar-ordered (disordered) region the number $\Delta n_+(k,p)$ of filaments transferred to this point from any point of the disordered (polar-ordered) region. Likewise, $\Delta n_-(k,p)$ counts the number of filaments being transferred from this point $(k,p)$ towards any point in the disordered (polar-ordered) region. The particle currents $J[D \leftrightarrow P_{k,p}]$ ($J[P \leftrightarrow D_{k,p}]$) are then obtained as the difference of the counts $\Delta n_+(k,p)$ and $\Delta n_-(k,p)$ divided by the duration of the simulation. For data shown in Fig. 3.4(d), the simulations were performed in a steady polar-ordered state over a time period of $t = 50$, and we used $\Delta t = 0.0125$; averages were performed over 30 statistically independent realizations. Furthermore, we also determined $\int dp\, J[D \leftrightarrow P_{k,p}]$ and $\int dp\, J[P \leftrightarrow D_{k,p}]$ which measure the respective currents irrespective of the specific value of cluster polar order $p$ (inset of Fig. 3.4(d)).

The difference between the current into the disordered region in the agent based simulations ($\int dp\, J[P \leftrightarrow D_{k,p}]$) in the inset of Fig. 3.4(d)) and in the kinetic model ($J[b \leftrightarrow a_k]$ in Fig. 3.5(e)) is likely caused by two different factors. First, in our agent-based simulations, a classification of clusters into polar-ordered or disordered ones can only be done on grounds of heuristic criteria [cf. Fig. 3.4(d)]. For instance, this results in more cluster sizes to be only classified as disordered, when compared with the kinetic model [cf. "Kinetic model equations" in the Section "Kinetic nucleation model" below.]. Second, in the kinetic model only disordered clusters of size $k = 1$ can gain mass from polar-ordered clusters [cf. the section "Dynamical and steady-state properties" below], whereas in our agent-based simulations this happens also for disordered clusters larger than 1 [cf. Fig. 3.4(d)].

### 3.4.7 Transition probability

As described in the main text, we measured the transition probabilities that a filament which is in a cluster of size $k$ at time $t$ will be in a cluster of size $k'$ at a later time $t + \Delta t$.

To determine these transition probabilities, $T(k', t{+}\Delta t|k, t)$, we used an ensemble of simulations that each was initialized in an ordered state. During each simulation run we recorded—in time intervals of $\Delta t$ and for each filament $j$—the size $k(t,j)$ of the cluster to which the respective filament belonged to. We monitored for each filament all transition events from $k(t,j)$ to $k(t+\Delta t, j)$ and collected these data in a histogram matrix $\widetilde{T}^{M \times M}$ ($M$ is the number of filaments in the system). By normalizing
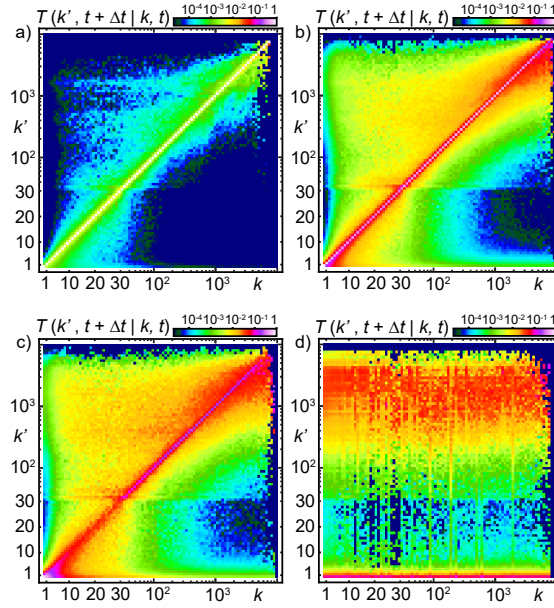
**Figure 3.15 Transition probabilities.** Matrix of transition probabilities, $T(k', t + \Delta t | k, t)$, in color code, for different values of the time increments $\Delta t$: a) $\Delta t = 0.000125$, b) $\Delta t = 0.00625$, c) $\Delta t = 0.025$, d) $\Delta t = 10.0$. In all panels we used $\alpha = 1.67$.

its columns we obtained an approximation for the transition probabilities:

$$T(k', t + \Delta t | k, t) \approx \frac{\widetilde{T}(k, k')}{\sum_{k'_0} \widetilde{T}(k, k'_0)} \,. \tag{3.24}$$

For the data shown in Fig. 3.4(c) ($\Delta t = 0.0125$) we averaged the results over five simulations, which each ran for a timespan of $T = 50$.

The time increment $\Delta t$ used in Fig. 3.4(c) is of the same order of magnitude as the time a filament needs to travel a distance comparable to its contour length ($L/v = 0.0315$). As discussed in the main text, the precise numerical value of this increment is not important. For comparison, Fig. 3.15(b-c) shows the matrix of transition probabilities for $\Delta t = 0.00625$ and $\Delta t = 0.025$, respectively. As can be inferred from this figure, they differ only on a quantitative level from Fig. 3.4(c). For the data shown in Fig. 3.15(b-c), we averaged the results over five simulations, which each ran for a timespan of $T = 50$. The data shown in Fig. 3.15 (a) and (d) ($\Delta t = 0.000125$ and $\Delta t = 10$) is interpreted and referenced in the discussion of the main text. We averaged the results for $\Delta t = 0.000125$ over five simulation runs, which each ran for $T = 50$. The results for $\Delta t = 10$ were averaged over 260 simulations which also ran for $T = 50$.
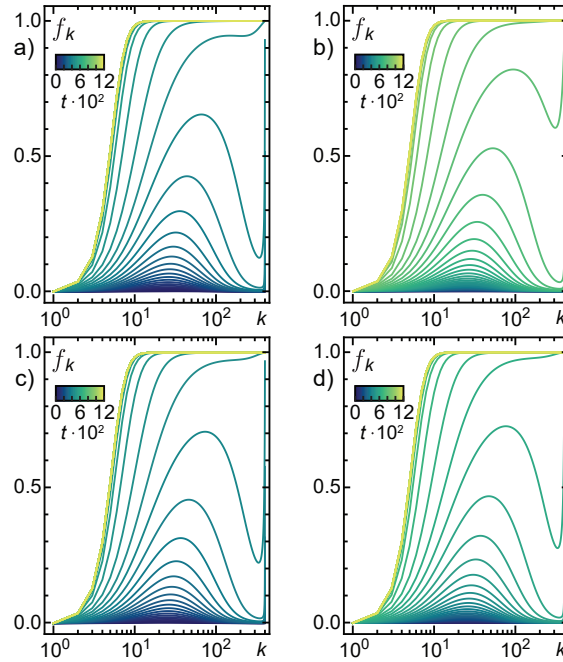
**Figure 3.16 Influence of** $m_c$ **and** $v_c$ **on** $f_k$**.** Time evolution of the relative fraction $f_k = b_k/n_k$ of ordered clusters, for different values of $m_c$ and $v_c$. The color gradient indicates different times as quantified by the corresponding color bar. (a) $m_c = 25$ and $v_c = 1$ (b) $m_c = 200$ and $v_c = 1$ (c) $m_c = 25$ and $v_c = 80$ (d) $m_c = 200$ and $v_c = 80$.

Note that the apparent discontinuity at $k' \approx 30$ is caused by changing from logarithmically arranged spacing of the binning for large cluster sizes to linear arranged spacing for small cluster sizes. This is necessary because clusters can only shrink or grow by integer values but a continuation of the logarithmic spacing would result in successive bin-distances becoming smaller than one.

## 3.5 Appendix: Kinetic nucleation model

### 3.5.1 Kinetic model equations

The temporal evolution of the distributions for the disordered species $a$ and the ordered species $b$ is given by:

$$\partial_t \mathbf{a} = \mathbf{F}(\mathbf{a}, \mathbf{b}) \,, \tag{3.25a}$$

$$\partial_t \mathbf{b} = \mathbf{G}(\mathbf{a}, \mathbf{b}) \,, \tag{3.25b}$$

where $\mathbf{F} = (F_1, F_2, ..., F_M)^T$ and $\mathbf{G} = (G_1, G_2, ..., G_M)^T$ are currents that include all possible reaction channels:

$$F_1 = 2\beta_2\, a_2 + \sum_{i=3}^{M} \beta_i\, a_i - \sum_{i=1}^{M-1} \alpha_{i,1}\, a_i a_1$$

$$+ \lambda\left(2b_2 + \sum_{i=3}^{M} b_i\right) - \sum_{i=2}^{M-1} \gamma_{i,1}\, b_i a_1\,, \tag{3.26a}$$

$$F_k = \beta_{k+1}\, a_{k+1} - \beta_k\, a_k + \frac{1}{2} \sum_{i=1}^{k-1} \alpha_{i,k-i}\, a_i a_{k-i}$$

$$- \sum_{i=1}^{M-k} \alpha_{i,k}\, a_i a_k - \sum_{i=2}^{M-k} \gamma_{i,k}\, b_i a_k - \omega_k\, a_k\,, \tag{3.26b}$$

and

$$G_1 = 0\,, \tag{3.27a}$$

$$G_k = \lambda\,(b_{k+1} - b_k) - \sum_{i=2}^{M-k} \eta_{i,k}\, b_i b_k \tag{3.27b}$$

$$+ \frac{1}{2} \sum_{i=2}^{k-2} \eta_{i,k-i}\, b_i b_{k-i} + \mu_0\left(\sum_{i=2}^{M-k} b_{i+k} - \frac{1}{2}\sum_{i=2}^{k-2} b_k\right)$$

$$+ \sum_{i=2}^{k-1} \gamma_{i,k-i}\, b_i a_{k-i} - \sum_{i=1}^{M-k} \gamma_{k,i}\, b_k a_i + \omega_k a_k\,,$$

with $k \in \{2, ..., M\}$. Note that by convention, all rates are equal to zero when the indices for species $a$ are less than 1 and larger than $M$, or less than 2 and larger than $M$ for the indices of species $b$. It can be straightforwardly checked that these currents conserve particle mass $\sum_{k=1}^{M} k\,(F_k + G_k) \equiv 0$. Please refer to the main text for the definitions and interpretations of the parameters $\beta_i$, $\alpha_{i,j}$, $\lambda_j$, $\gamma_{i,j}$, $\omega_j$, $\mu_0$ and $\eta_{i,j}$. Note that we have assumed that clusters of size 1 are always disordered, i.e. $b_1 = \partial_t b_1 = 0$. As mentioned in the main text, we fixed the parameters of the kinetic model to $M = 400$, $A = 800$, $\nu = \beta_0 = \lambda_0 = 1$, $\mu_0 = 0.025$, $\sigma_{aa} = 1.6$, $\sigma_{ab} = 0.2$, $\sigma_{bb} = 1$ and $\omega_0 = 10^{-4}$, if not stated otherwise.

As discussed by the authors of Ref [134], $\sigma_{aa}$, $\beta_0$ and their ratio determine the shape of the distribution $a_k$ in the absence of species $b$ and exhibits a critical transition from a unimodal to a bimodal distribution. For our system, we took
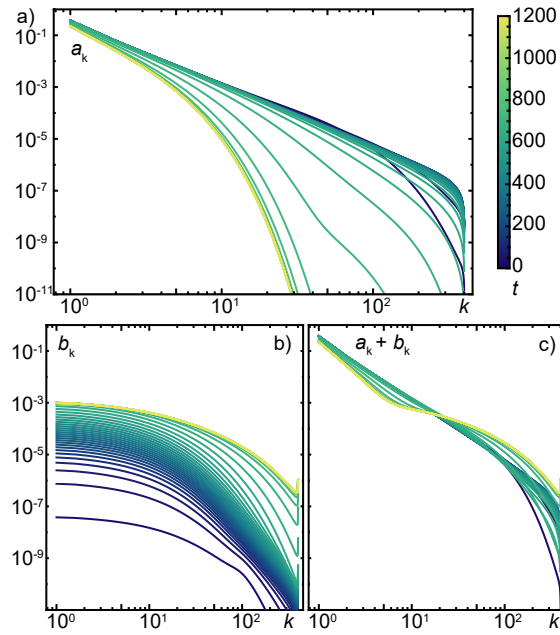
**Figure 3.17 Temporal evolution of the cluster distributions.** Temporal evolution from a disordered towards an ordered state of the single and combined cluster species distributions. The color gradient indicates different times as quantified by the corresponding color bar. (a) disordered species $a_k$, (b) ordered species $b_k$, and (c) sum of both $a_k + b_k$.

parameters such that they are always below this point to avoid structure formation in this domain.

As noted in the main text, we have investigated how the choice of $m_c$ and $v_c$ in the expression for the transformation rate from disordered to ordered clusters $(Z(i) = 1/(1 + e^{-(i-m_c-1)/v_c}))$, influence the transition to polar order and the ordered state itself. To this end we have performed the same kind of simulations as shown in Fig. 3.5(c) but with different values for $m_c$ and $v_c$. As can be seen in Fig. 3.16, only the course of the transition towards polar order changes slightly. The stationary state, however, is identical to the one shown in Fig. 3.5(c). This illustrates that the qualitative behaviour of the system is not sensitive to the exact choice of $m_c$ and $v_c$.

## 3.5.2 Kinetic model implementation

We integrated Eqs. (3.25a, 3.25b) using a straightforward Euler scheme in C++ with a time step of $3 \times 10^{-2}$, which we found—for system sizes $M \lesssim 1000$—to be numerically faster than an adaptive time-step $4^{\text{th}}$-order Runge-Kutta algorithm. It is furthermore simpler than implicit integration schemes, which we expect to be more stable for larger $M$.
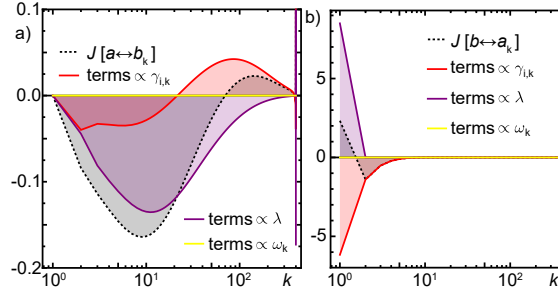
**Figure 3.18 Contributions to inter-species fluxes.** Stationary inter-species particle fluxes $J[a \leftrightarrow b_k]$ (a) and $J[b \leftrightarrow a_k]$ (b) and individual rate contributions as a function of cluster size $k$.

### 3.5.3 Dynamical and steady-state properties

#### 3.5.3.1 Evolution of the cluster distributions

Figure 3.17 shows the temporal evolution of the polar-ordered and disordered cluster distributions, $a_k$, $b_k$, for the parameters and data shown in Fig. 3.5 ($\sigma_{aa} = 1.6$, $\sigma_{ab} = 0.2$). One observes that up to intermediate times ($t \approx 800$) there is little change of the cluster distributions. Once there is a significant fraction of $b$-clusters the dynamics speeds up and their amount then increases strongly [cf. Fig. 3.17(b)]. This in turn leads to a substantial reduction of $a$-clusters [cf. Fig. 3.17(a)] and a corresponding change of the sum of both distributions [cf. Fig. 3.17(c)].

#### 3.5.3.2 Details of particle fluxes

The inter-species fluxes of the particle mass, $J[b \leftrightarrow a_k]$ and $J[a \leftrightarrow b_k]$, as depicted in the main text in Fig. 3.5(e), are obtained by setting all species-internal rates in Eq. (3.25a) and Eq. (3.25b) to zero. This leaves only inter-species contributions to $a_k$ (resulting in $J[b \leftrightarrow a_k]$) and inter-species contributions to $b_k$ (resulting in $J[a \leftrightarrow b_k]$), respectively. One obtains the following equations:

$$J[b \leftrightarrow a_1] = \lambda \left(2b_2 + \sum_{i=3}^{M} b_i\right) - \sum_{i=2}^{M-1} \gamma_{i,1} b_i a_1, \tag{3.28a}$$

$$J[b \leftrightarrow a_k] \overset{k \geq 1}{=} k \cdot \left(-\sum_{i=2}^{M-k} \gamma_{i,k} b_i a_k - \omega_k a_k\right), \tag{3.28b}$$
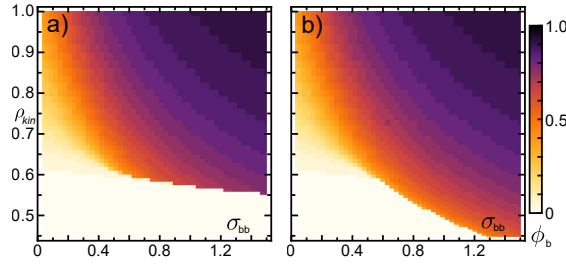
**Figure 3.19** $\rho_{\mathbf{kin}}$-$\sigma_{bb}$ **bifurcation diagram.** Density plot of the stationary mass fraction $\phi_b$ as a function of $\sigma_{bb}$ and the density $\rho_{\mathrm{kin}}$ with different initial conditions: (a) started with mainly $a$ clusters present ($a_k(t{=}0) = \delta_{1,k}$ and $b_k(t{=}0) = 0$), and (b) started with mainly $b$ clusters present (i.e. started in a state that is similar to the stationary state in Fig. 3.17). Parameters: $\sigma_{aa} = 1.8$, $\sigma_{ab} = 0.15$, $\omega_0 = 10^{-3}$.

and

$$J[a{\leftrightarrow}b_k] \overset{k>1}{=} k \cdot \left( \lambda (b_{k+1} - b_k) \right.$$

$$\left. + \sum_{i=2}^{k-1} \gamma_{i,k-i} b_i a_{k-i} - \sum_{i=1}^{M-k} \gamma_{k,i} b_k a_i + \omega_k a_k \right). \tag{3.29}$$

Figure 3.18 illustrates the contribution of the individual currents proportional to $\lambda$, $\gamma_{i,k}$, and $\omega_k$. This shows that species $a$ gains mass only by evaporation of single, disordered filaments from ordered clusters. In contrast, species $b$ gains cluster mass by coalescence of smaller ordered and disordered clusters (transferring mass to larger cluster sizes) and by transformation of disordered into ordered clusters.

### 3.5.4 Parameter space and hysteresis

Besides the interaction strength, the particle density is another relevant control parameter of active matter systems; e.g. in our agent-based simulations both control parameters influence the phase behaviour of the system [cf. Fig. 3.3(b)]. For that reason, we investigated whether the density plays a comparable role in the kinetic model. To this end, we determined a bifurcation diagram as a function of $\rho_{\mathrm{kin}} = M/A$ and $\sigma_{bb}$ (analogous to the bifurcation diagram of stationary mass fractions $\phi_b$ as a function of $\sigma_{ab}$ and $\sigma_{bb}$ [cf. Fig. 3.6(c)]).

Fig. 3.19(a)/(b) shows the disordered/ordered branch of the bifurcation (i.e. the stationary state of the simulations which were started in a disordered/ordered state). Here, too, there is a bistable region between the ordered and disordered state, and, for varying the density, a discontinuity and hysteresis occurs (as it is the case for varying $\sigma_{ab}$, see Fig. 3.6(b)). In addition to the 3D-representation
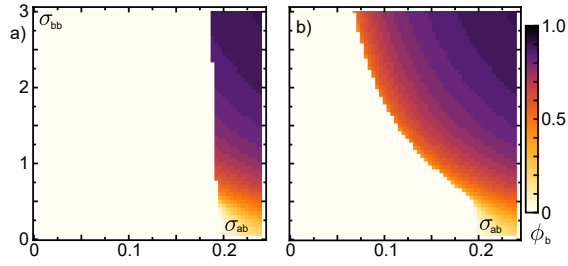
**Figure 3.20** $\sigma_{ab}$-$\sigma_{bb}$ **bifurcation diagram.** Density plot of the stationary mass fraction $\phi_b$ as a function of $\sigma_{ab}$ and $\sigma_{bb}$ with different initial conditions: (a) started with mainly $a$ clusters present ($a_k(t{=}0) = \delta_{1,k}$ and $b_k(t{=}0) = 0$), and (b) started with mainly $b$ clusters present (i.e. started in a state that is similar to the stationary state in Fig. 3.17). Parameters and data identical to Fig. 3.6(b,c).

of the $\sigma_{ab}$-$\sigma_{bb}$ bifurcation diagram in Fig. 3.6(c), and to facilitate a comparison with Fig. 3.19, Fig. 3.20 shows the disordered/ordered branches of that bifurcation separately.

# 4 Condensed topological defects and filamentous arc ejections in phase-separated weak active nematics

*The following chapter is based on research I conducted together with Ivan Maryshev and Erwin Frey and will soon be submitted to publication. I.M. and E.F. designed and performed hydrodynamic approach. T.K. and E.F. designed and performed simulations. All authors participated in interpreting the results.*

Historically, topological defects with charges ±1/2 have been considered a hallmark of homogeneous active nematics. Phase separated systems, in turn, have been known for the formation of dense, typically unstable nematic bands, but so far, half-integer defects have not been observed in them. In this paper, we use the agent-based model for weakly-aligning self-propelled filaments and, for the first time, demonstrate that phase-separated active nematics form $-1/2$ defects of a new kind. In contrast to the well-studied homogeneous case, these new defects coincide with density peaks, condense nematic fluxes, and coexist with bending bands. We also observe filamentous arc ejections - formations of lateral arcuate structures that separate from the band's bulk and move in a transverse direction. We show that the key control parameters defining the route from the topologically charged structures to stable bands are the initial density of particles and their path persistence length. We introduce a hydrodynamic theory qualitatively recapitulating all the main features of the agent-based model and use it to show that the emergence of the different topologically charged structures can be attributed to the same anisotropic active fluxes. Finally, we speculate about experimental verification of the provided model, its role in other phenomena, such as active foam, and potential applications.

## 4.1 Introduction

Active nematics are a broad class of active matter systems [5, 189–192] with the order invariant under director reflection. Dense spatially uniform active nematics have become a platform for studying pairs of half-integer topological defects with opposite charge – namely their formation, dynamics, and annihilation [18, 48–51, 146, 193–199]. Dilute or weakly interacting systems, on the other hand, exhibit

qualitatively quite different ordering behavior and dynamics [7]. One observes phase separation into nematic bands with an intriguing complex dynamics [1, 7, 86–88, 99, 129, 135, 151, 200], but so far without the emergence of half-integer topological defects.

Here we show that these two hitherto seemingly incompatible phenomena – phase separation and topological defects – can actually be closely linked in weakly interacting active nematics. In particular, we discover a new class of topological defects that exhibit particle mass condensation and active particle currents near their center. We show that these 'defect condensates' coexist with nematic bands and are mainly formed by collisions of triplets of nematic lanes. We also observe another topologically charged structure, filamentous arc ejections –elongated bow-like density domains that detach from the nematic band and travel in the direction perpendicular to its main axis– remotely resembling +1/2 defects behavior.

One of the principal experimental realizations of weak active nematics is the actomyosin motility assay [1, 15, 16, 19–21]. In this two-dimensional model system, hydrolysis of adenosine triphosphate (ATP) enables actin filaments to actively glide over a lawn of nonprocessive heavy meromyosin motor proteins [157], so that they perform a path-persistent random walk with relatively constant speed. A detailed experimental characterization of the binary collision statistics between the filaments has shown that they interact only weakly with each other and can slide over each other relatively easily [1, 20, 21].

To explore the phenomenolgy of such weak nematics, we use an agent-based model of "weakly-aligning self-propelled polymers" (WASP) which has been shown to faithfully reproduce the full behavior of actomyosin motility assays on all relevant length and timescales including the pattern formation processes and the topology of the phase diagram [1, 2]. This allows us to leverage these agent-based simulations as an *in-silico* experimental system to discover new phenomena. To gain access to the mechanisms underlying these phenomena, we, in addition, introduce a hydrodynamic theory, building on previously published models [124, 136].

Exploiting the respective strength of these two complementary theoretical approaches we investigate the dynamical and morphological properties of the obtained structures. We further provide an explanation for the occurrence of the defects, the arc ejections and the underlying flux. Moreover, we systematically explore the "phase space" of the occurrence of condensed topological defects and filamentous arc ejections and identify the control parameters defining the transition between the structures.
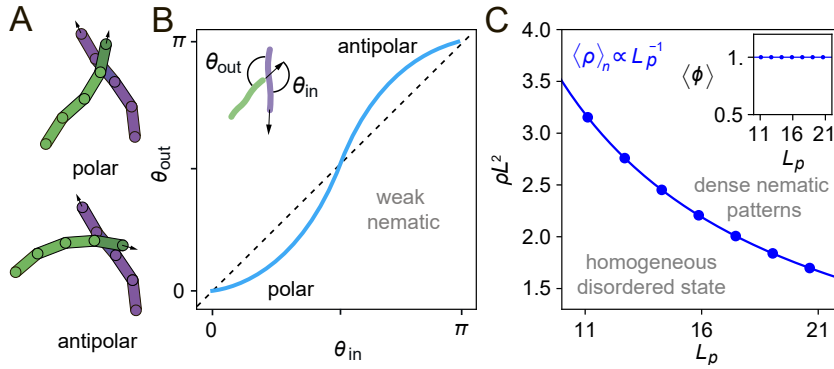
**Figure 4.1** Nematic interaction between filaments and onset of order. (*A*) Schematic depiction of two interacting polymers. Depending on the impact angle being smaller or larger $\frac{\pi}{2}$ filament directions are either aligned (*upper panel*) or anti-aligned (*lower panel*). (*B*) Illustration of the binary collision statistics corresponding to a weak nematic interaction between polymers, which is point-symmetric with respect to the neutral line around $\pi/2$ (*C*) Phase diagram of a weak active nematic with collision statistics shown in panel B. The blue line shows the density corresponding to isotropic-nematic transition $\langle \rho \rangle_n$ which is inversely proportional to the persistence length $\langle \rho \rangle_n \propto L_p^{-1}$. Please refer to section 4.5.2 for details on this transition line. *Inset*: The same graph as a function of $\langle \phi \rangle = \langle \rho \rangle / \langle \rho \rangle_n$ and $L_p$.

## 4.2 Results

### 4.2.1 Simulation setup

We use agent-based simulations that model the dynamics of weakly interacting self-propelled polymers (WASP) of fixed length $L$ on two-dimensional surfaces building on earlier work [1, 2]: please refer to section 4.5.1 for further details on the algorithm. Each filament consists of a tail pulled by a tip that moves forward on a trajectory corresponding to a persistent random walk with persistence length $L_p$. Upon collision of a filament tip with the contour of another polymer, a weak alignment torque is assumed to act that changes its direction of motion (Fig. 4.1A). Here we use a purely nematic alignment interaction (Fig. 4.1B) whose strength is set by $\alpha_n$.

Previous work on weak nematics has found phase transitions between disordered states, polar patterns, and nematic patterns [1, 2, 7, 71, 86–88, 99, 105, 124, 129, 135, 136, 151, 200, 201], as well as phases exhibiting a dynamic coexistence of ordered states with fluctuating nematic and polar symmetry [1, 2]. This rich phenomenology of spatiotemporal patterns emerges from tuning the degree of polar and nematic symmetry in binary collision statistics [1]. Here we are interested in systems that have a collision statistics with nematic symmetry (Fig. 4.1B), i.e., nematically ordered states of active matter. Figure 4.1C shows the phase diagram of

such a weak nematic as a function of the average filament density $\langle\rho\rangle L^2$ and path persistence length $L_p$. It exhibits an isotropic-nematic transition from a disordered homogeneous phase to a nematically ordered phase. The phase boundary $\langle\rho\rangle_n(L_p)$ approximately scales as $L_p^{-1}$; please refer to section 4.5.2 for further details on this transition. Thus, when the phase diagram is redrawn as a function of $L_p$ and the averaged normalized density $\langle\phi\rangle = \langle\rho\rangle/\langle\rho\rangle_n$, the phase boundary essentially becomes a horizontal line (inset of Fig. 4.1C).

### 4.2.2   Dense topological charged structures

As expected for nematically interacting systems, our simulations show isolated nematic lanes that exhibit strong bending fluctuations on large length and time scales caused by lateral instabilities [86, 88, 99, 124, 135, 136, 200].

Strikingly, in addition to these typical nematic lanes, our simulations also show distinct types of topologically charged structures. In particular, we observe three-armed filamentous structures containing a topological defect with charge $-1/2$ at their center; see examples shown in Fig. 4.2A. Mostly they are formed when three curved nematic lanes — with their convex sides facing each other — meet and condense into a topological defect with a high density core region (Fig. 4.2B). Unlike defects in non-compressible active nematics, these *condensed topological defects* (CTDs) do not have a directly corresponding positively charged pair. Rather, they are surrounded by an extended topologically charged region with a dispersed positive charge, as can be seen in Fig. 4.2A (lower right panel) depicting the topological charge density [136, 202]. Moreover, the simulations show that the active nematic flux is gradually compressed as the triple junction of the nematic lanes (defect core) is approached (Fig. 4.2A, top right panel). This leads to a reduction in lane width and a corresponding increase in density, which reaches a maximum just before the core. On the concave sides of the junction, density drops. These three-armed topological defects are dynamic structures that are constantly being dissolved and reassembled.

The second type of structure we observe is lateral arcuate filamentous arcs that separate from the bulk of a straight nematic band and eventually move in transverse direction. A time trace of such a *filamentous arc ejection* (FAE) is shown in Fig. 4.2C. These structures have similarities to $+1/2$ defects: they are "curved" and always move antiparallel to the curvature vector. Moreover, they are accompanied by a cloud of positive topological charge on their concave side, but do not exhibit a singularity.

Having discovered these collective topological structures in our *in-silico* experiments, we sought to explore how their emergence is affected by a change of parameters. However, since lateral instabilities of nematic bands required for the formation of CTDs occur only on very long time scales [7, 99], a systematic invest-
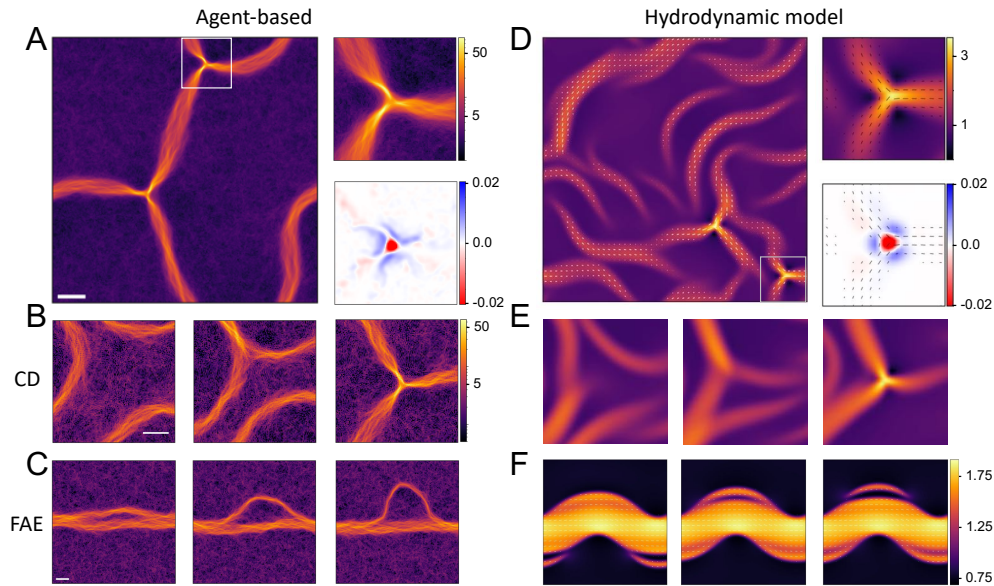
**Figure 4.2** Condensed defects and filamentous arc ejection. Left column (*A* to *C*) shows results for agent based simulations, right column (*D* to *F*) for the hydrodynamic model. (*A* and *D*, *left panels*) Spatial density distribution of a system simultaneously exhibiting two condensed defects. A magnified view of one defect (rectangular marked region) is shown in the *upper right panels* in (*A*) and (*D*). The *lower right panel* in (*A*) and (*D*) shows the topological charge density $q$ of the magnified region. In both cases a $-\frac{1}{2}$ defect is surrounded by positively charged regions of space. (*B* and *E*) Formation of a condensed defect. Three convex bands meet and self-focus into a dense structure in the center of which the topological charge that was previously on the outside of the bands is trapped. (*C* and *F*) A filamentous arc ejection at different time points of its evolution. LTR: Before formation of a partially separated arc, after arc formation and right before complete separation.

igation of a phase diagram in agent-based simulation is numerically prohibitively demanding. Therefore, we sought an alternative way to explore the spatiotemporal dynamics of the systems that would enable us to dissect and asses the processes underlying the formation of CTDs and FAEs. As discussed next, we achieved this by adopting a hydrodynamic approach that recapitulates all of the main features of our agent-based simulations.

### 4.2.3 Hydrodynamic model provides access to the phase diagram

Our hydrodynamic model (in short HM) is formulated in terms of two variables of space and time: the normalized density of filaments $\phi = \int P(\theta)\mathrm{d}\theta/\langle\rho\rangle_n$ and the traceless and symmetric order parameter describing their coarse-grained nematic

alignment $Q_{ij} = \langle n_i n_j - \delta_{ij}/2 \rangle = \int P(\theta)(n_i n_j - \delta_{ij}/2)\mathrm{d}\theta$. Where $\mathbf{n} = (n_x, n_y) = (\cos\theta, \sin\theta)$ denotes the unit vector of a particular filament, and $P(\theta)$ is the probability density function. The eigenvector associated with the larger eigenvalue of $Q$-tensor can be treated as an average orientation of polymers. Here and below the space and time dependencies are suppressed for brevity; $_i$ and $_j$ take the values of the Cartesian components; and $\delta_{ij}$ represents Kronecker delta. We also imply summation for repeating indices following the Einstein convention.

By analogy with passive *Model C* in Hohenberg-Halperin classification [203] we introduce two coupled evolution equations for conserved $\phi$ and tensorial $Q_{ij}$. Our hydrodynamic model contains the terms, which in general can be obtained via minimization of free energy functional, however some contributions imply nonintegrable dynamics and are motivated by the derived models for active nematics. Such terms in our *active Model C* drive the system out of equilibrium and are not determined by the gradient descent on any free energy landscape, however, the analogy with the passive case still can provide some intuition.

The mass-conserving equation for density [(4.1)] contains isotropic and anisotropic fluxes controlled by $\mu$ and $\chi$ respectively:

$$\partial_t \phi = \partial_i J_i^{\mathrm{iso}} + \partial_i J_i^{\mathrm{aniso}} = \Delta(\mu(\phi)\phi) + \partial_i \partial_j \left( \chi(\phi) Q_{ij} \right), \tag{4.1}$$

where $\Delta = \partial_i \partial_i$ denotes Laplace operator. Isotropic term plays the role of a chemical potential similar to typical *Model B* [203]. It contains motility-induced contribution to the effective diffusion, but also includes a quadratic part representing the steric repulsion due to excluded volume interactions [119, 204, 205]: $\mu = \lambda^2 + \mu_\phi \phi$. Parameter $\lambda$ is proportional to $L_p$, that is why below we use it as a proxy for persistence length, $\mu_\phi$ corresponds to $F$ in agent-based model. Second term in Eq. (4.1) (anisotropic flux) leads to the phase separation since it condenses density in the direction perpendicular axis of the orientational order. It also contains motility- and interaction-induced parts: $\chi = \lambda^2 + \chi_\phi \phi$.

Our evolution equation for the orientational order partly can be obtained from Landau-de Genne-like free energy functional [206], but it also includes density-induced interfacial torques:

$$\partial_t Q_{ij} = -\frac{1}{\gamma}\frac{\delta F_{LG}}{\delta Q_{ij}} + \text{interfacial torques} \tag{4.2}$$

$$= \left[ \left( (\phi - 1) - \beta Q^2 \right) Q_{ij} + \Delta(\kappa(\phi)Q_{ij}) \right]$$
$$+ \left[ \partial_i \partial_j (\omega(\phi)\phi) + \omega^a 2 \left( \partial_i \phi \partial_j \phi \right) \right]^{ts}, \tag{4.3}$$

where $[...]^{ts}$ indicates the symmetric and traceless part of the expression, $Q^2 = Q_{kl}Q_{kl}$, rotational viscosity $\gamma$ is set to unity, and

$$F_{LG} = \int d\mathbf{r} \left[ (1 - \phi + \frac{\beta}{2}Q^2)Q^2 + (\partial_p(\kappa Q_{qp}))^2 \right] / 2. \qquad (4.4)$$

The first expression in the (4.3) is responsible for standard isotropic-nematic transition. Analogues terms are characteristic of conventional *Model A* for tensors [203]. The linear term defines the distance from criticallity, whereas the saturating cubic term determines the equilibrium value of $Q_{ij}$ in a homogeneous nematic state. The term with Laplacian operator plays the role of elasticity, and again contains two contributions – one from motility of filaments, and the other one due to the interactions: $\kappa = \lambda^2/2 + \kappa_\phi\langle\phi\rangle$.

The last expression in (4.3), enclosed in square brackets, contains symmetric and traceless part of the interfacial torques. It enables the coupling between density gradients and nematic alignment occurring within inhomogeneous active systems.

The torque associated with $\omega$-term ($\partial_i\partial_j(...)$) rotates the director at the nematic – isotropic interface. It typically conflicts with $\chi$ related coupling term in Eq. (4.1) leading to chaotic behaviour of bands known as dry "active turbulence". $\omega = \lambda^2 + \omega_\phi\phi$, where $\lambda^2$ appears due to the self-propulsion, while the term proportional to $\phi$ occurs in derived models for the interacting particles.

Finally, the term bilinear in the density gradients ($\partial_i\phi\partial_j\phi$) is motivated by coarse-grained microscopic models for active filaments [124]. It can be considered as an effective liquid-crystalline "anchoring" to the density interface [136]. Since we expect anchoring to be tangential, the parameter $\omega^a$ is negative, implying that filaments tend to orient perpendicular to the density gradients. Or, in other words, tangential anchoring ensures the parallel orientation of filaments to the boundary of dense nematic band.

We want to stress that, unlike the majority of models, in our theory the coefficients $\mu$, $\chi$, $\kappa$ and $\omega$ are functions of density. They contain not only terms occurring due to self-propulsion [88, 89] but also the density dependant corrections due to the binary interactions usually ignored for non-phase-separating "strong" active nematics. We introduce $\mu_\phi$, $\chi_\phi$, $\kappa_\phi$, $\omega_\phi$ and $\omega^a$ phenomenologically and vary them arbitrarily.

Our model is capable of reproducing the results obtained in the agent-based simulation to a very high degree of fidelity. It exhibits CTDs and FAEs whose structure, topological charge, and formation process are very similar to the ones observed in WASP; cf. Fig. 4.2D-F.

### 4.2.4 From CTDs to FAEs and bands

Encouraged by the promising first results our hydrodynamic theory showed, we leveraged the relative ease of obtaining long-time behavior with it and generated a $(\lambda, \langle\phi\rangle)$ phase diagram (Fig.4.3A).

As can be seen, at low values of $\lambda$ and $\langle\phi\rangle$, CTD formation dominates, while in areas of high $\lambda$ and $\langle\phi\rangle$ stable nematic lanes emerge. Between these regions lies a band of parameters that cause the system to form mainly FAEs.

In order to check whether this relation determined in the hydrodynamic model also holds in our agent based simulations, we obtained the propensity to form CTDs in agent-based simulation along one-dimensional lines of the $(L_p, \langle\phi\rangle)$ phase space; one along a constant value of $\langle\phi\rangle$ and one along a constant value of $L_p$. As can be seen in Figs. 4.3C and D, the results for both agent based simulations and hydrodynamic model are in good agreement.

We further checked the frequency of FAEs in the agent based simulations as a function of $L_p$, again they qualitatively agree well with the results from the hydrodynamic model Fig. 4.3B and E. (Please refer to section 4.5.3 for further details on how this data was obtained).

Taken together, these results suggest that the simulations and the hydrodynamic model not only exhibit the same patterns, but that their occurrence also shows the same dependence on parameter changes.

It is further worth to note that in both approaches we observed that the formation of condensed defects and filamentous arc ejections is inextricably linked to the stability of the nematic lanes i.e. to their propensity to exhibit an undulating instability [7, 86, 99, 124, 135, 136, 200]. For low $L_p/\lambda$ and $\phi$, nematic bands are not stable and strong undulations occur (i.e. no spatial configuration of nematic lanes remains stationary, not even transiently). This coincidence with the parameter range in which the occurrence of CTDs is high (cf. Fig. 4.3A) can be well reconciled with the observation of the defect formation process, see Figs. 4.2B and E. The shorter the lanes are stable and the more the lanes are undulating, the more likely it is that multiple lanes will "collide" and form defects.

When $L_p$ resp. $\phi$ are increased further, bands remain unstable for a certain span of parameters, but, increasingly, some configurations–in particular only slightly curved system spanning configurations of single bands–become transiently stable. Often, elongated openings develop in these bands in their lateral regions, which develop into filamentous arcs (cf. Fig. 4.2C and F). As no surprise, the parameter regime where these transiently stable bands form, roughly coincides with the region where the formation of FAEs is dominant (cf. orange stars in Fig. 4.3A).

Increasing $L_p$ even further, leads to ever more stable bands that eventually stop to undergo undulation instabilities (for the investigated system size) and are completely straight, coinciding with the drop in observed FAE frequency.

The observed dependence of the undulating instability on the parameters (and the concomitant change in the phenomena) can be further understood by the following considerations. In case of an increased $L_p$ (or $\lambda$ in hydrodynamic model), the Frank constant grows [207], and the effective elasticity (or collective rigidity of filaments) starts to prevail over anisotropic density fluxes. Consequently, and as observed (Fig. 4.3A, C), the bending instability becomes weaker. In the hydrodynamic model we further observe that low elasticity favours CTD formation, while a large elastic constant $\kappa$ hinders the system to obtain topological distortions (not shown).

In case of an increased density $\phi$, a system spanning nematic band occupies a growing fraction of space i.e. bands become broader, while the bulk density remains mostly the same [cf. section 4.5.6]. Broader bands are less subject to a bending instability, thus the increase of $\langle \phi \rangle$ leads to a decay of defect formation (Fig. 4.3A, D). Interestingly, for very small densities, close to the criticality, both models exhibit a decay of the observed CTD number, presumably due to fewer mass being inside the ordered phase and hence not enough mass present to form several curved bands.

### 4.2.5 Detailed structure of CTDs and FAEs

To better understand the structure of the condensed defects, we studied the filament flows through them in detail. To this end, we tracked the motion of each filament as it passed through a condensed defect. This allows us to distinguish between flows from one particular arm of the defect to another particular arm, and to investigate whether there is a relationship between the lateral position of individual filaments and their eventual turning direction. As can be inferred from Fig. 4.4A-C and Movie 7, the flow in each defect arm is strongly compressed laterally. It then splits almost exactly at the centerline of the lane before entering the defect and undergoing a sharp change in direction. Only at a greater distance from the center of the defect do the flows begin to mix again (Fig. 4.4A-C). This shows that the overall topology often present at the birth of the defect (Fig. 4.2B and E), continues to survive in the flow structure of the fully formed CTD as three almost nonmixing nematic fluxes.

In addition, we investigated whether the velocity of the filaments is affected as they move through a CTD. As can be seen from Fig. 4.4E, their speed remains almost unchanged and only a slowdown in the per mil range is observed. One can see two insignificant velocity drops corresponding to regions with the maximal density of polymers. Interestingly, in the immediate vicinity of the core of the defect, the particle velocity briefly returns to the average value, corresponding to particles inside the nematic band.

Further, we studied the temporal evolution of filamentous arc ejections. The motion of a separating arc in WASP and hydrodynamic model, can be visualized using the kymograph of the density projection shown in Fig. 4.3B. As can be inferred from the bending of the lateral extrusions, the separation process of the arcs starts
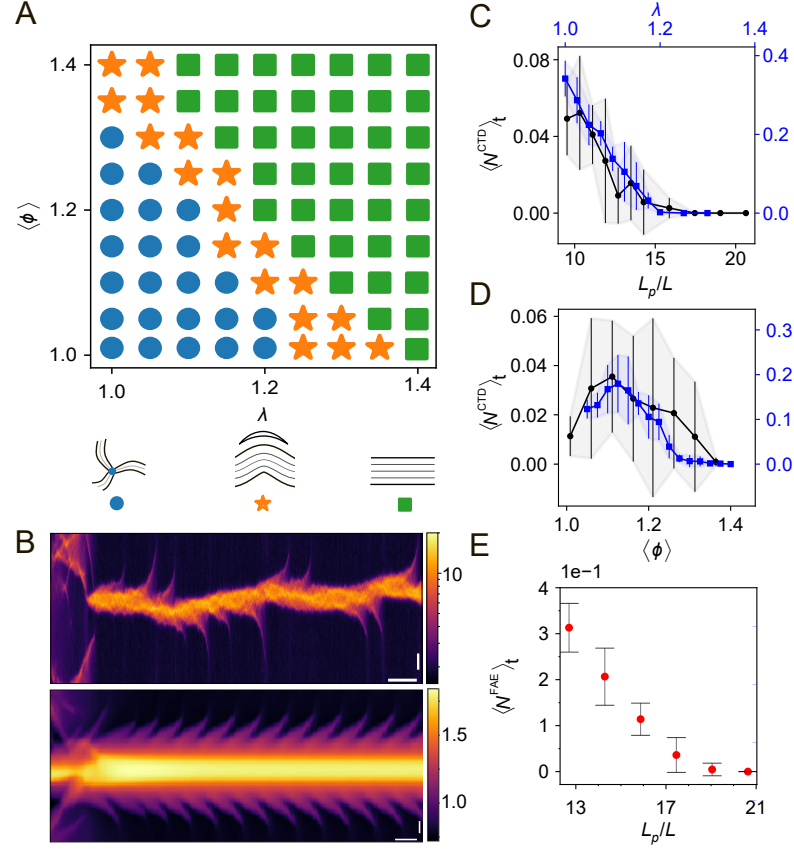
**Figure 4.3** Occurrence of condensed defects and filamentous arc ejections in dependence of parameters, in agent based simulations and hydrodynamic model. By increasing density and/or persistence length resp. lambda (in WASP resp. hydrodynamic model) the mainly occurring type of phenomena can be tuned from CTDs, to FAEs to straight lanes, in both agent based simulations and hydrodynamic model. (*A*) Phase diagram as a function of lambda and $\langle\phi\rangle$ in hydrodynamic model. The occurrence of CTDs is indicated by blue dots, of FAEs by orange stars and of straight lanes by green squares. (*B*) Illustration of a system exhibiting several filamentous arc ejections in sequence in agent based simulations (*B, upper panel*) and hydrodynamic model (*B, lower panel*). After formation of a straight lane, the density is projected along the axis of the lane. The resulting 1-D slices are stacked into the shown Kymograph. Each FAE can be recognized by an extrusion from the lane. The slight bending of these extrusions towards a more vertical shape is a signature of the accelerated motion of the ejection. (*C*) Mean number of CTDs present, in WASP resp. hydrodynamic model, as a function of $L_p$ resp. $\lambda$. (*D*) Mean number of CTDs present, in WASP resp. hydrodynamic model, as a function of $\langle\phi\rangle$. (*E*) Occurrence rate of FAEs, in WASP resp. hydrodynamic model, as a function of $L_p$ resp. $\lambda$.
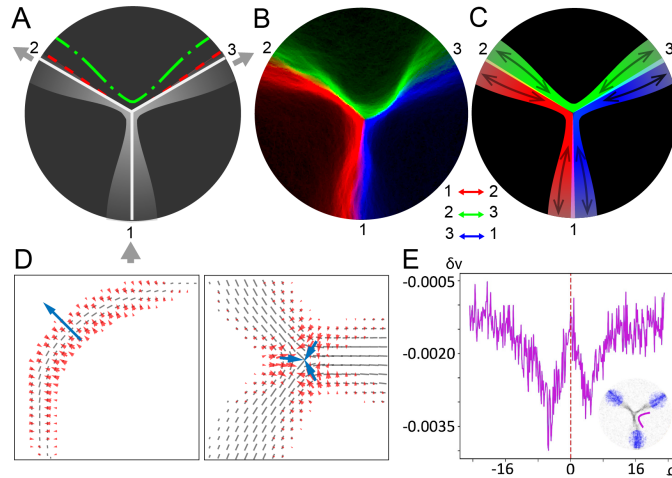
**Figure 4.4** Details of filament fluxes through a condensed defect in agent based simulations. (*A*) Schematic depiction of the filament flux density coming from one specific arm (source arm) and going into the two other arms (target arm) in grey scale. Shown for the flux from arm 1 and into arms 2 and 3 [cf. Movie 7]. Solid white lines depicts the center line of the arms. Green dash-dotted line indicates the boundary of the total flux in the arms. Red dashed line denotes the boundary of the flux into the target arms. From the observation that the red dashed line does not coincide with the center line but is slightly shifted, it can be inferred that the two currents into a source arm mix only in a small region near the center line. (*B*) Simulation data visualizing the information shown in (*A*). All filaments coming from one specific arm and going into another specific arm or vice versa are colored in the same color. E.g. all filaments coming from or going into arm 1 and going into or coming from arm 2 are colored in red. From the almost perfect separation of colors it can be inferred that filament fluxes from or into one lane are divided near the center line and diverted into the two other arms. The small mixing region of the different fluxes can be identified by the additive color mixing occurring when streams overlap (e.g. overlapping red and green fluxes lead to a yellow coloring of the flux-mixture). (*C*) Pictorial representation of the colored simulation data. (*D*) Plot of the anisotropic active flux $-\partial_j(\chi Q_{ij})$ in the hydrodynamic model. The flux leads to a propagation in the indicated direction of bended structures (left panel) and upconcentrates the density in a defect (right panel). (*E*) Average relative velocity change $\delta v$ of filaments as they pass through a CTD as a function of the distance to the defect core $d$ (see inset for an illustration of the path). Only an almost undetectable slowdown in the per mille range can be observed.

slowly and continues to accelerate until complete ejection and eventual dissolution of the arc.

Having characterized and established the existence of CTDs and FAEs in our agent based *in-silico* experimental system and having successfully introduced a hydrodynamic theory faithfully reproducing the results of the simulations as well as providing access to the phase space of the observed pattern, we asked: why are

these phenomena observed? What are the underlying mechanisms responsible for their formation?

To answer this question we leveraged the capability of the hydrodynamic model to provide access to single terms of its defining equations (Eqs. (4.1,4.3)). Doing this, it becomes apparent that both the formation of dense defects and the movement of arches have the same root cause, namely the anisotropic ("curvature-induced") density flux [5, 152, 189], described by $-\partial_j(\chi Q_{ij})$ in Eq. (4.1) in the hydrodynamic model. This can be understood by plotting $-\partial_j(\chi Q_{ij})$ in the region of a FAE and a CTD, see Fig. 4.4D left panel and right panel, respectively. As can be seen, on different sides of the bent arc the amplitudes of the fluxes are distinct. An effective "active force" acting on the concave side is greater than that one on the opposite side, which leads to the movement of the bent band (or arc) in the corresponding direction (Fig. 4.4D, left panel).

When tree lanes meet, the same curvature-dependent fluxes upconcentrate polymers in the core of the obtained defect (Fig. 4.4D, right panel). This condensation is eventually balanced by the isotropic part of (4.1) and particularly by steric repulsion of polymers. To test this hypothesis, we set the excluded volume force $F$ (see section 4.5.1) to zero in our agent based simulations. Observations in this case indicate that the formation of CTDs is reduced and that, if they are formed, the density begins to diverge, leading to subsequent destruction of the defects. Thus, we infer that formation of the dense defects are predominantly determined by interplay between two counteracting processes: isotropic and anisotropic density fluxes.

## 4.3 Discussion

From Fig. 4.4E it is clear that CTDs are not related to the phenomenon called motility–induced phase separation (MIPS) [74] – clusters formation associated with the slowdown of self-propelled particles due to steric interactions. In this context it is worth to note that the filamentous structure of WASP-filaments does not prevent the condensation of density near defects, while it was shown that MIPS is interrupted for anisotropically shaped aligning particles [208].

Unlike standard phase separation in "compressible" dry active matter [1, 7, 124, 129, 136, 200, 205], here we observe a hierarchy of condensation. Active agents firstly concentrate themselves in the bulk of nematic lanes, but subsequently can do a "next step" and reach even higher compressions around CTDs. This second phenomenon further differentiates itself since high density clusters are localised in very limited regions around the defects, making it a good candidate for a delivery mechanism in cases where a highly localized density peak of active particles is needed. Notably, unlike MIPS, this process produces a strong condensation without impeding particle velocity.

Linear (coming from advection) parts of coefficients in our HM (Eqs. (4.1,4.3)) are proportional to $L_p^2$, while density dependant corrections occurring due to the interactions are distinct. That leads to an additional degree of freedom and potentially explains the fact that the CTDs presented here have not yet been detected in models lacking density dependant corrections. It is further thinkable that the weak interactions, filamentous nature, semi-flexibility, -in comparison with standard variations of Viscek models- in our models further promote dense defect formation. However, we expect that CTDs can be still can found in such approaches, but probably in a smaller region of parameter space.

It is worth to mention that Eqs.(4.1, 4.3) are structurally similar to the active *Model C* originally derived for non-self-propelled particles [124, 136]. The only significant difference being that the thermal translational diffusion and the terms quadratic in $Q$ are neglected.

To conclude, we have provided a composite in silico approach combining agent based simulations and hydrodynamic theories to investigate pattern formation in phase separated nematic active matter systems. Two astounding features of nematic active matter (formation of topological defects and phase separated nematic patterns) previously considered as two separate phenomena, coexist and are related in the investigated system. We observed the formation of these novel topological defects, investigated them and underscore underlying mechanism of their formation. CTDs can condesate the nematic fluxes and potentially play the role of capacitors of negative topological charge: due to the lateral propagation of bent lanes in the direction of their convex side, these lanes collide and self-compress into a highly dense structure, thereby trapping the formally spread out negative charge.

Formation, mutual orientation and even decay of dense defects are distinct from the ones of standard disclinations observed in homogeneous ("incompressible") active matter. We often see that the axis of two near-by CTDs are connected by one streamline (Fig. 4.2A), whereas in incompressible active matter negative half-strength disclination usually points towards the +1/2 defect. If bending of all three arms has the same orientation (curvature of all either clockwise or anti-clockwise with respect to center) then the defects disappear via rotation. Whereas in homogeneous systems defect pairs of opposite charge annihilate each other. Finally, dense −1/2 topological defects concentrate the filaments, while other active systems on contrary, e.g. bacteria incorporated in liquid crystals [141] and cytoskeletal suspensions at the interfaces [209] exhibit density depletion in −1/2 disclinations.

A promising extension of the provided model is the investigation of active foam [136, 151]. In this state of active matter, receiving increasing attention recently, dense ordered bands form junctions and constitutes actively reforming cellular networks. For a small region of parameters, active foam can be realized in our HM model - CTDs occur more often, are connected and exist for longer times. We see no obstacles preventing formation of foams state in WASP, however rigorous

exploration of the full phase space is numerically very challenging and will be left to a future study.

## 4.4 Materials and methods

### 4.4.1 WASP simulation method

We now describe the agent-based simulations of **w**eakly-**a**ligning **s**elf-propelled **p**olymers (WASP's). Please also refer to section 4.5.1 and the Supplemental Materials of Refs. [1, 2] for more details.

In our systems we simulate $N$ filaments, each of length $L$. Orientational diffusion causes the tip of each filament to perform a persistent random walk. When colliding with another polymer, local interaction causes the tip to gradually align its direction. Attached to the polymer tips are tails that just follows the path that is outlined by the tip. This dynamics mimics the behavior of actin filaments in actomyosin motility assays [1, 2]. In these, polymers move in a snake-like fashion over a lawn of motor proteins and orthogonal motion to the contour is suppressed [15, 20]. Here we use purely nematic interactions between filaments which is primarily tuned by the nematic alignment amplitude $\alpha_n$ that allows for a continuous variation of the rate of alignment.

### 4.4.2 Parameters

If not stated otherwise, we used the following model parameters: discretization $N = 5$, filament aspect ratio $L/d = 21$, nematic alignment strength $\alpha_n = 0.126 \approx 7.2°$ and a periodic simulation box of length $L_{\text{box}} = 162.5L$. The velocity $v^{(n)}$ of each filament is randomly drawn from the interval $[0.75, 1.]v_0$. We started simulations with random initial conditions, i.e. randomly oriented filaments were placed at random positions in the simulation box. Time is measured in units of $L/v_0$.

### 4.4.3 Continuous theory

We numerically investigate equations Eqs.(4.1,4.3) under periodic boundary conditions by using finite differences of second order [210] on a $300 \times 300$ grid with the spatial resolution $\delta x = 0.5$. The time integration was performed via a second order predictor-corrector scheme with time step $dt = 10^{-2}$. We use the parameter values $\beta = 0.05$, $\kappa_\rho = 0.2$, $\omega^a = -0.5$, $\chi_\rho = 0.2$, $\mu_\rho = 1$, $\omega_\rho = 0$. Unless explicitly stated, we are initialize simulations from an isotropic uniform state with a small amount of noise. To make time and space dimensionless we rescale them by setting the rotational diffusion coefficient and $\mu_\rho$ equal to unity.

## 4.5  Appendix

### 4.5.1  WASP simulation method

In this section we will provide a brief summary of the agent based simulations. The focus will be on the aspects most relevant for the current study. For a detailed description of the WASP simulation method, please refer to the supplemental materials of Refs. [1, 2].

In the agent based simulations, we consider $M$ filaments moving in two dimensions. Each polymer $n$ consist of $N$ spherical joints $j$ which are located at a position $\mathbf{r}_j^{(n)}$ (with $j \in \{0, 1, \ldots, N-1\}$, where the filament tip is denoted by $j = 0$).

The direction of a polymer's tip is denoted by $\mathbf{u}_0^{(n)}$ and its motion is described by:

$$\partial_t \mathbf{r}_0^{(n)} = v^{(n)} \mathbf{u}_0^{(n)} - \mathbf{F}_{\mathrm{rep}} = v^{(n)} \begin{pmatrix} \cos \theta_0^{(n)} \\ \sin \theta_0^{(n)} \end{pmatrix} - \mathbf{F}_{\mathrm{rep}} \,. \tag{4.5}$$

Here $\mathbf{F}_{\mathrm{rep}}$ describes a weak repulsion force (see (4.11)) acting on a filament head while in contact with the contour of another polymer. $\theta_0^{(n)}$ denotes the orientation of a filament and $v^{(n)}$ its free speed. For this study, the speed of each polymer was chosen at random from a continuous uniform distribution in the interval $[0.75, 1]v_0$, where $v_0$ denotes the maximal velocity of a free filament. With this, we avoided the decay of nematic lanes towards colliding waves (see supplemental material of [1]).

The orientation of a polymer's head evolves in time according to

$$\partial_t \theta_0^{(n)} = -\frac{\delta \tilde{H}_0^{(n)}}{\delta \theta_0^{(n)}} + \sqrt{\frac{2 v^{(n)}}{L_p}} \xi \,, \tag{4.6}$$

where $\xi$ is random white noise with zero mean and unit variance. The prefactor before $\xi$ causes free polymers to travel on a trajectory that has a path persistence length of $L_p$. $\tilde{H}_0^{(n)}$ sets the, in this study purely nematic, torque caused by interactions with other filaments.

Before we come to a description of $\tilde{H}_0^{(n)}$, it will proof useful to introduce several other quantities. The first is the distance vector

$$\Delta \mathbf{r}_{nm} = \left( \mathbf{r}_0^{(n)} - \mathbf{r}^{(m)} \right)_{\mathrm{shDist}} \,. \tag{4.7}$$

This vector connects the tip of a filament $n$ with the position of an adjacent polymer's (denoted by $m$) contour that has the shortest possible distance. The local orientation of the contour of the adjacent polymer $m$ is given by $\theta_j^{(m)}$, which corresponds to the orientation of the filament segment $j$ of polymer $n$ to which $\Delta\mathbf{r}_{nm}$ connects.

Second, if a polymer is interacting with several filaments at a time, we define a weighted average direction of the connecting vectors:

$$\Delta\widetilde{\mathbf{e}}_n := \sum_m C\left(|\Delta\mathbf{r}_{nm}|\right) \frac{\Delta\mathbf{r}_{nm}}{|\Delta\mathbf{r}_{nm}|} \ . \tag{4.8}$$

Here $C\left(|\Delta\mathbf{r}_{nm}|\right)$ is a weighting factor accounting for the assumption that a more distant polymer contributes less to an interaction. It is given by

$$C\left(|\Delta\mathbf{r}_{nm}|\right) = \begin{cases} 0 & \text{if } |\Delta\mathbf{r}_{nm}| > d \\ (d - |\Delta\mathbf{r}_{nm}|)/d & \text{else} \end{cases}, \tag{4.9}$$

where $d$ defines the interaction radius.

Using the orientation of the averaged connecting vector $\tilde{\theta}_n$, we define an averaged nematic impact angle as $\Delta\tilde{\theta}_n^{(n)} = \theta_0^{(n)} - \tilde{\theta}_n$.

We now can define the alignment potential as

$$\tilde{H}_0^{(n)} := \frac{\alpha_n v_0}{d} \cos(2\Delta\tilde{\theta}_n^{(n)})|\Delta\widetilde{\mathbf{e}}_n|, \tag{4.10}$$

where the overall amplitude of the alignment is set by the absolute value of the weighted connecting vector, combined with the nematic alignment strength $\alpha_n$.

The repulsion force $\mathbf{F}_{\text{rep}}$ in (4.5) is given by

$$\mathbf{F}_{\text{rep}} = -s \sum_m C\left(|\Delta\mathbf{r}_{nm}|\right) \frac{\Delta\mathbf{r}_{nm}}{|\Delta\mathbf{r}_{nm}|} \ , \tag{4.11}$$

which is used to prevent unphysical aggregation of filaments. It is assumed to be weak with $s = 0.05$.

Filaments in actomyosin motility assays are observed to conduct a trailing motion, where the tail of a polymer follows the movement of the tip [1, 15, 16, 19, 20].

To emulate this behaviour, tail joints move according to

$$\partial_t \mathbf{r}_j^{(n)} = K_s \left(\left|\mathbf{r}_j^{(n)} - \mathbf{r}_{j-1}^{(n)}\right| - b\right) \frac{1}{2}\left(\mathbf{u}_{j+1}^{(n)} + \mathbf{u}_j^{(n)}\right) \ . \tag{4.12}$$

Here, the second part of the equation, $\frac{1}{2}\left(\mathbf{u}_{j+1}^{(n)} + \mathbf{u}_j^{(n)}\right)$, ensures the movement to be in the direction of the average of the segment's orientations that are adjacent to joint
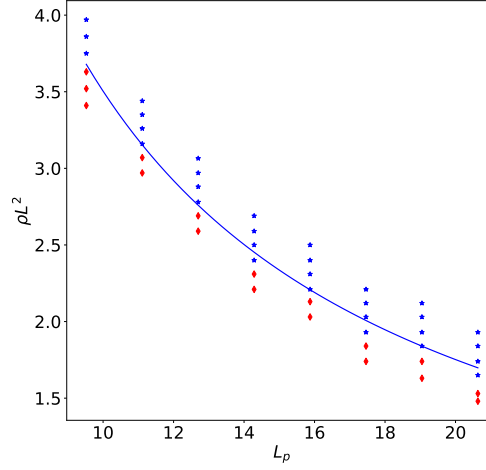
**Figure 4.5** Phase space of nematic order. Agent based simulations yielding nematic patterns are marked with blue stars. Simulations not exhibiting order are shown as red diamonds. A fit of the functional form $f_\rho(L_p) = a/L_p$, where $a$ is the free fit parameter, to the ordered datapoints with the lowest density is shown in solid blue.

$j$. The rest of (4.12) corresponds to a linear (Hookian) restoring force with spring coefficient $K_s = 200$ that ensures an average length $b$ of the cylindrical segments between bonds.

## 4.5.2  Onset of nematic patterns

To determine the density as a function of $L_p$ above which nematic patterns are formed, we conducted exploratory simulations in the phase space spanned by global filament density $\langle\rho\rangle L^2$ and the persistence length $L_p$, see Fig. 4.5.

After finding several density values for all examined $L_p$ that exhibited patterns after a certain simulation time of 15873, and several that did not, we fitted a function $f_\rho(L_p) = a/L_p$ (with $a$ as the free fit parameter) to the data points with the lowest density that still exhibited patterns [solid line in Fig. 4.5]. The functional dependence $\sim L_p^{-1}$ is motivated by results of the hydrodynamic model.

We take the course of $f_\rho(L_p)$ as an approximation to the density corresponding to the onset of nematic patterns, denoted by $\langle\rho\rangle_n$, at the respective $L_p$.

To further validate if this is a sufficient approximation, we ran ten independent simulations at a density corresponding to $\langle\rho\rangle_n$ and further ten at a density of 90% $\langle\rho\rangle_n$ for several different $L_p$ [cf. dots in Fig. 4.1C] for a time of 31746. All simulations at $\langle\rho\rangle_n$ formed ordered patterns, while none at 90% $\langle\rho\rangle_n$ did, affirming that $f_\rho(L_p)$ sufficiently approximates the position of the isotropic-nematic transition.

### 4.5.3 Defect detection

To algorithmically detect $-1/2$ defects, we made use of the fact that inside a defect core the topological charge density $q$, defined as [202]

$$q = \frac{1}{4\pi} \left( \partial_x Q_{xa} \partial_y Q_{ya} - \partial_x Q_{ya} \partial_y Q_{xa} \right), \tag{4.13}$$

has a very large negative value.

Hence, we define any contiguous region of space in which q falls below a certain threshold value $q_{\mathrm{thrs}}$ as one $-1/2$ defect.

To obtain $q$ in WASP simulations, we rasterized space onto a grid with a grid-spacing of $\Delta x$. We used the orientations $\theta_0^{(n)}$ of filament tips residing inside each gridpoint at a given time to calculate a local value of $q(\mathbf{r}, t)$. To suppress noise, we averaged the value of $q(\mathbf{r}, t)$ over a timespan of 15.87 in which 11 frames were recorded.

Additionally, to avoid missclassifying small and short lived density peaks that occur sporadically in the simulations as CTDs, we required the value of the charge density to be above $q_{\mathrm{thrs}}$ for at least two consecutive measurements of $q(\mathbf{r}, t)$ (which were taken in intervals of $\Delta t = 159$). For the simulations in this project, we used $\Delta x = 0.317L$ and ($q_{\mathrm{thrs}} = 0.032$). The total runtime of each simulation was 142857 from which we cutted an initial transient before starting the measurement, see section 4.5.7. For each value of $L_p/\langle \phi \rangle$ we averaged over ten independent simulations.

Note that the main purpose of the data from the agent-based simulations in Fig. 4.3C-E is to qualitatively confirm the trend observed in the hydrodynamic model. To quantify the data with a high degree of precision would require averaging over larger ensembles, which would be numerically prohibitively demanding given the very long time scales on which the observed phenomena occur.

Similarly, we define topological defects in our hydrodynamic model. In particular, the positions of $-1/2$ defects are defined as local minima of the function $q$ given by the Eq. 4.13.

### 4.5.4 Flux measurement through defects

In the main text, we studied the mass flow through a defect as well as the speed of particles during a CTD passage, see Fig. 4.4B and E, respectively. To that end, we needed detailed information about the position and speed of particles as they transition from one arm of a defect to another one.

For this, we leveraged the possibility offered by the agent based simulations to access the position of each individual filament at any point in time.

Starting from a simulation that had reached a state in which it exhibited defects, we partitioned the simulation box into several "filter-regions" (cf. Fig. 4.6 for an

illustration), which we each assigned a unique identifier $id$. At every subsequent iteration after the partitioning, we checked for every filament $i$ if its position coincided with one of the "filter-regions". If this was the case, filament $i$ was assigned the identifier of the region and the time of assignment $t_{\text{assign}}$ was saved. If filament $i$ already had a different identifier $id'$ assigned (and hence also a different $t'_{\text{assign}}$), this meant that it had traveled from another "filter-region" into the current region (without crossing a third region in the meantime). In such a case, we stored the pairs of tuples $(id', t'_{\text{assign}})$ and $(id, t_{\text{assign}})$, which allow (combined with with the also saved information of the position and speed of every filament at every iteration) to reconstruct the path filament $i$ has taken propagating from region $id'$ to $id$. Subsequently, we replaced the assigned identifier and assignment time of filament $i$ with that of the current region and the current time and continued the simulation. For the data in Fig. 4.4B and E, we placed filter regions above the three lanes that
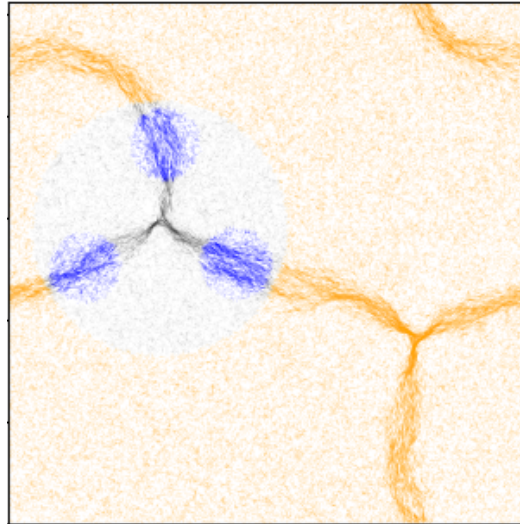


**Figure 4.6 Illustration of filter regions.** Plot of the 91217 filaments in a simulation exhibiting two condensed defects. Over each lane transitioning to the arms of one of the defects a round filter region is placed (areas in which the filaments are colored blue). Filaments far away from the defect (shown in orange) are pooled into one large filter region. All black colored filaments do not belong to any filter region. Parameters: $L_p = 11.1L$, simulation box size: $162.5L$.

transition into the three arms of a defect (cf. blue regions in Fig. 4.6), allowing to identify every filament propagating through these lanes. Additionally, all parts of the simulation box being further away from the defect core than a specific distance was incorporated into a single large filter region (cf. orange region in Fig. 4.6), allowing to identify filaments leaving the region of interest. Note that the black colored area does not pertain to any filter region.
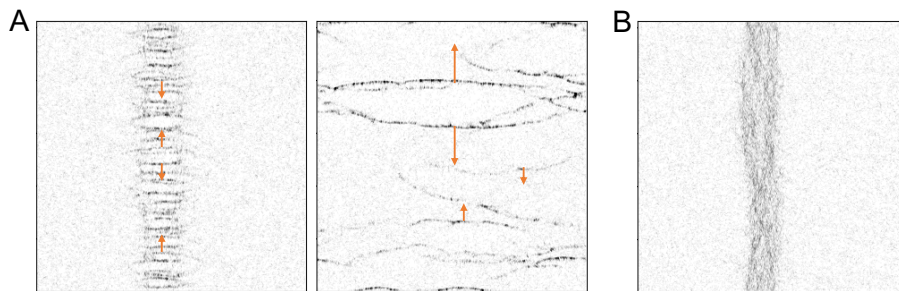
**Figure 4.7 Counterpropagating polar waves.** (*A*) Nematic lane in a simulation where all agents travel with the same speed and mutually align via nematic alignment torques only decays into counter-propagating locally polar waves. Orange arrows depict the direction of motion of some of the waves. (Right snapshot taken at a later point in time. Time difference between snapshots: 2397.) (*B*) Nematic lane in a simulation where the velocity of agents is drawn from a distribution; no decay occurs. Parameters: $L_p = 20.6L$ and $\langle \phi \rangle = 1.1$. In (*A*): $v^{(n)} = v_0 = \text{const.}$

Recording transition events in such a configuration for a time span sufficiently long enough that many particles can travel from one blue region to another blue region (cf. Fig. 4.6), but short enough such that bending undulations do not change the position of the individual lanes significantly, allows to record many trajectories of particles passing through a defect from all directions.

### 4.5.5 Filament velocity

In chapter 2 it was observed that in systems where interactions have a mixed symmetry, purely nematic patterns can decay into oppositely propagating polar waves while retaining their nematic order globally (cf. Fig. 2.8D). In the current work we are interested in the formation of nematic lanes only. Therefore, any decay of nematic lanes (that we found to also occur when alignment interactions were purely nematic, cf. Fig. 4.7) would be undesirable and we looked for a means to prevent it.

In chapter 3 it was found that formation and growth of polar structures can be described in terms of kinetic processes at the mesoscopic level. Hence, we speculated that changing the effective rates in a way that inhibits the growth of polar structures may be a successful approach that counteracts the formation of colliding polar waves, although, with the restriction, that such an approach may not inhibit the formation of nematic structures. When visually inspecting an ordered cluster over its growth and propagation process (see chapter 3), it becomes clear that these processes heavily rely on the coherence of the constituents of the clusters, i.e. in

order for a polar structure to form and be stable, particles must have a very similar velocity.

If single agents would not move with the same speed, an additional loss process should set in, caused by fast particles overtaking the mean velocity of the propagating wave and being lost towards the front, whereas individual particles, which are slow, are lost towards the back. At the same time, a spread in velocity should presumably not affect the stability of nematic lanes, as nematic structures do not rely on a coherence of density peaks along the direction of motion of particles. Indeed, we found that drawing the assigned speed of filaments from a distribution (cf. Section 4.5.1), successfully prevented any decay into locally polar structures, while not impeding the formation of nematic lanes (see Fig. 4.7).

To check whether particles that possess different free velocities behave differently on the level of macroscopic structures –for example by causing an effective sorting of particles into spatially separate populations, where only relatively fast/slow particles form part of patterns– we obtained $\langle v^{(n)} \rangle$, the local average of $v^{(n)}$, inside a simulation exhibiting nematic lanes and CTDs. Any local accumulation of fast/slow particles would lead to a different value of $\langle v^{(n)} \rangle$ when compared to the global average $\langle v^{(n)} \rangle_{\text{glob}}$.
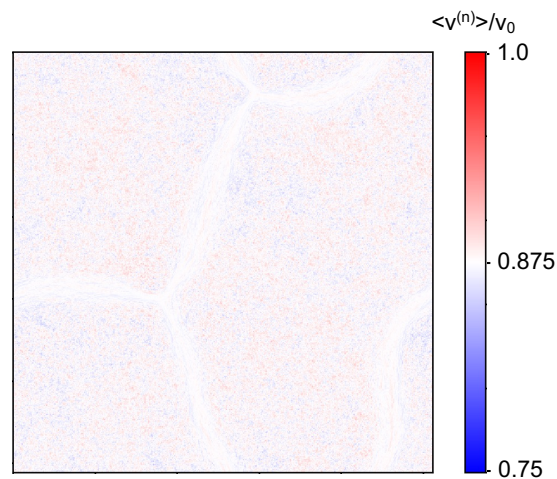


**Figure 4.8 Local averaged velocities.** Locally averaged $v^{(n)}$ of agents in a system exhibiting nematic patterns and CTDs. No deviation of the global average ($\langle v^{(n)} \rangle_{\text{glob}}/v_0 = 0.875$) occurs, up to random fluctuations. The position of the patterns is still slightly perceivable since fluctuations in the low density disordered background are less suppressed (due to the lower number of filaments over which is being averaged) compared with the high density nematic lanes. Same data as in Fig. 4.2A.

As can be inferred from Fig. 4.8, this system is well mixed (up to random fluctuations) with respect to filament velocities, suggesting that no particle, regardless of its velocity, occupies a special role inside patterns.

### 4.5.6  Width of nematic lanes

As discussed in the main text, we measured the width of nematic lanes in dependence of density $\langle \phi \rangle$ in both the agent based simulations and the hydrodynamic model. To this end, we started several simulations at different filament densities but at a fixed persistence length (resp. several realizations of the hydrodynamic model at different $\langle \phi \rangle$ and fixed $\lambda$). After these systems had reached a configuration in which they exhibited a single straight lane, we measured the width of the band and the average density $\langle \phi \rangle_{\text{bg}}$ in the disordered background.
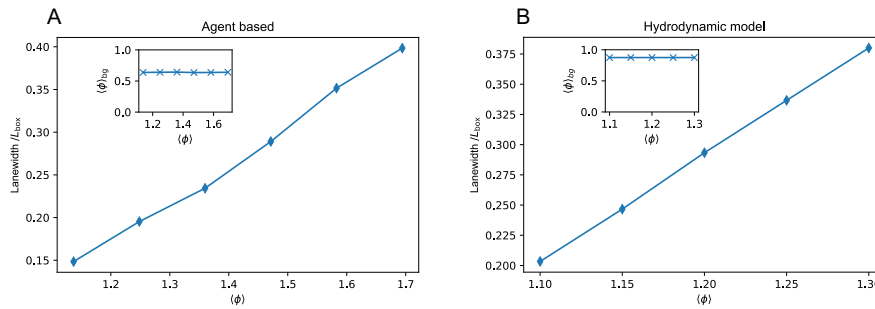


**Figure 4.9 Width of nematic lanes.** (*A*) shows results for agents based simulations and (*B*) for the hydrodynamic model. The width of stable nematic lanes grows with an increase of the global density $\langle \phi \rangle$ while the background density $\langle \phi \rangle_{\text{bg}}$ stays constant (inset). Parameters: $L_p = 20.6L$ for (A)

As shown in Fig. 4.9, the thickness of the lanes grows linearly with density in both the agent-based simulations and hydrodynamic model, while the density of the disordered background remains constant.

### 4.5.7  Pattern dynamics

Figure 4.10 illustrates in a pictorial way the behaviour of the systems over the course of the parameter sweeps discussed in the main text. Whereas deep in the low-stability regime (cf. Fig. 4.10 A) nematic bands are always unstable and potentially CTDs are formed, deep in the high-stability regime a single, stable and straight nematic band forms.
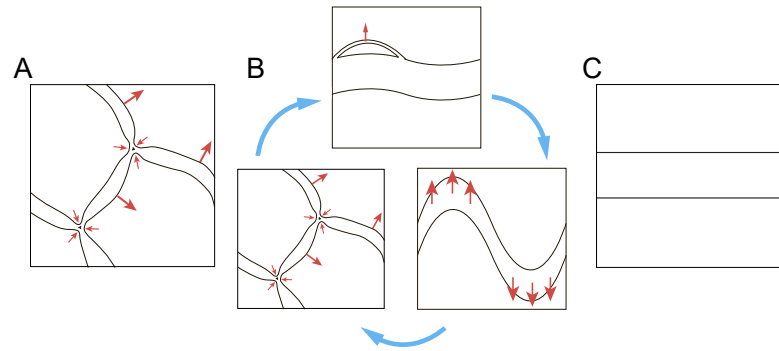
**Figure 4.10 Pictorial illustration of lane behaviour at different levels of stability.** (*A*)
Systems in parameter regimes of low $L_p/\lambda$ resp. $\langle\phi\rangle$ exhibit unstable nematic lanes with
a high level of activity. Red arrows indicate the direction in which the anisotropic fluxes
drive the lanes. Stochastically CTDs can be formed. (*B*) At intermediate values of $L_p/\lambda$
resp. $\langle\phi\rangle$ system-spanning bands form. At their lateral sides FAE can eject (upper panel).
These bands are meta-stable only and stochastically decay (lower right panel) causing the
system to enter a phase of high activity (lower left panel). Eventually, by chance, a new
system spanning band forms and the circle starts a new. (*C*) With increasing values of $L_p/\lambda$
resp. $\langle\phi\rangle$, decay events of system-spanning bands occur less frequently until they eventually
become stable. In parallel, the rate of FAE formation drops.

Between these extremes lies a parameter range in which the systems cycle
through qualitatively different states.

The first of these states is identical to the one observed deep in the low-stability re-
gime. Long curved lanes are unstable and dynamically evolve (Fig. 4.10B, lower left
panel). While in this state, a system spanning band can form by chance (Fig. 4.10B,
upper panel) transitioning the system to the other possible state. The formed band is
meta-stable and often slightly curved. From its side filamentous arcs are ejected with
some rate. Stochastically decay events occur during which this bands gets destroyed
(Fig. 4.10B, lower right panel) transitioning the system back to the dynamically
unstable state (Fig. 4.10B, lower left panel).

It is worth to note that agent based simulations started with random initial
conditions very frequently begin to form patterns in a dynamically evolving state
(also for parameters in the high-stability regime).

We measured the duration of this initial transient and found that in $\gg$ 90% of
the cases it's shorter than a time of 70000 (data not shown). We discarded this
initial timespan in the measurements of the CTD rate (cf. section 4.5.3) to rule out
any influence of the initial transient on the results.

### 4.5.8 FAE rate measurement

As described in the main text, we measured the formation rate of FAEs at different parameter regimes in the agent based simulation and the hydrodynamic model (Fig. 4.3). For this we logged the formation of every FAE in the investigated systems. We have found that the most reliable method for detecting FAEs is simple manual inspection of simulation videos. To obtain the formation rate, we divided the total number of FAEs found by the total time the individual runs were exhibiting meta-stable system-spanning lanes (cf. Fig. 4.10B).

For every investigated $L_p$ in the agent based simulations, we averaged over ten independent simulations, which each ran for a time of 142857.

### 4.5.9 Hydrodynamic model

To provide the motivation of our hydrodynamic model we start form the Boltzmann-like equation for the probability distribution function $P(\mathbf{r}, \theta, t)$:

$$\partial_t P(\theta) = - L_p \partial_i (n_i P(\theta)) + \partial_\phi^2 P(\theta) + \text{Interactions.} \tag{4.14}$$

where $\mathbf{n} = (\cos\theta, \sin\theta)$ is director vector of particular polymer, $L_p = v/D$ is path persistence length of filaments, and time is normalised by the diffusion coefficient. Note, that we consider only rotational diffusion and neglect transnational one. Here and below the space and time dependencies are suppressed for brevity.

We define the particle density, the polarity and nematic Q-tensor as the first three moments of the probability distribution function:

$$\rho = \int_0^{2\pi} d\theta P, \qquad p_i = \int_0^{2\pi} d\theta n_i P, \qquad Q_{ij} = \int_0^{2\pi} d\theta \left(2 n_i n_j - \delta_{ij}\right) P. \tag{4.15}$$

where $_i$ and $_j$ take the values of the Cartesian components; and $\delta_{ij}$ represents Kronecker delta. According to their definitions, $\rho$, $p_i$, and $Q_{ij}$ can be expressed via Fourier harmonics as follows:

$$\rho = 2\pi P_0, \tag{4.16}$$
$$p_i = \pi \left((P_1 + P_{-1}), i(P_1 - P_{-1})\right), \tag{4.17}$$
$$Q_{ij} = \pi \left((P_2 + P_{-2}), i(P_2 - P_{-2})\right). \tag{4.18}$$

By introducing the projection onto $m_{th}$ harmonics of $P$:

$$\overline{(\ldots)}^m = \frac{1}{2\pi} \int_0^{2\pi} e^{-im\theta} (\ldots) d\theta, \tag{4.19}$$

we can obtain the following contributions from the advective and diffusive parts of (4.14) to the evolution equations of $P_m$:

$$\partial_t P_m = -m^2 P_m - \overline{L_p \partial_i (n_i P(\mathbf{r}, \theta))}^m$$

$$= -m^2 P_m - L_p \frac{1}{2} \left[ \partial_x \sum_k P_k (\delta_{k,m-1} + \delta_{k,m+1}) + \partial_y \sum_k P_k (\delta_{k,m-1} - \delta_{k,m+1})/i \right]. \tag{4.20}$$

Being translated to the variables it reads:

$$\partial_t \rho = -L_p \partial_i p_i,$$

$$\partial_t p_i = -p_i - \frac{L_p}{2} \partial_i \rho + \frac{L_p}{2} \partial_j Q_{ij},$$

$$\partial_t Q_{ij} = -4Q_{ij} - \frac{L_p}{2} [\partial_i p_j + \partial_j p_i - \delta_{ij} \partial_k p_k]. \tag{4.21}$$

Note, that we imply summation for repeating indices following the Einstein convention.

After the time rescaling, adiabatic elimination of polarity $p_i$, and the introduction of parameter $\lambda = L_p/(2\sqrt{2})$, one obtains a simpler set of equations:

$$\partial_t \rho = \lambda^2 \Delta \rho + \lambda^2 \partial_i \partial_j Q_{ij},$$

$$\partial_t Q_{ij} = -Q_{ij} + \frac{\lambda^2}{2} \Delta Q_{ij} + \frac{\lambda^2}{2} (2\partial_i \partial_j \rho)^{st}. \tag{4.22}$$

where $\Delta = \partial_i \partial_i$ denotes Laplace operator, and $(\ldots)^{st}$ indicates the symmetric and traceless part of the expression.

Inspired by Refs.[124, 136] we also introduce the following terms to describe the nematic interactions of the polymers:

$$\partial_t \rho = \cdots + \tilde{\mu} \Delta \rho^2 + \tilde{\chi} \partial_i \partial_j (\rho Q_{ij}),$$

$$\partial_t Q_{ij} = \cdots + \tilde{\alpha} \rho Q_{ij} - \tilde{\gamma} Q^2 Q_{ij} + \tilde{\kappa} \Delta (\rho Q_{ij}) + \tilde{\omega} (2\partial_i \partial_j \rho^2)^{st} + \tilde{\omega}^a (2\partial_i \rho \partial_j \rho)^{st}. \tag{4.23}$$

Finally, to obtain the equations of motion presented in the main text we simply combine (4.22) and (4.23) and re-normalize density by the critical one $\phi = \rho/\rho_{cr}$.

# 5 Polar flow of gliding microtubules steered by passive nematic defects

*The following chapter is based on research I conducted together with Alfredo Sciortino, Lukas Neumann, Ivan Maryshev, Erwin Frey and Andreas R. Bausch and will soon be submitted to publication. A.R.B. and A.S. designed experiments. A.S. and L.N. carried out experiments. I.M., T.K., A.S. and E.F. designed and performed simulations and the heuristic approach.*

## 5.1 Introduction

The macroscopic properties of materials can surprisingly depend on microscopic impurities they contain. For instance, defects in the crystalline order of materials can lead to unexpected transport properties and are at the base of semiconductor physics [211, 212]. The art of controlling defects to manipulate materials is thus a fundamental one, and it is starting to find applications in the field of soft matter [213]. Active materials, whose building blocks are microscopic components able to turn energy into motion, are similarly often characterized in terms of the presence of defects and their dynamics [5, 32, 197, 214]. In this case, the scale of the defects is not only the same as that of the building blocks of the material itself but also the same scale at which energy is injected in the system. For example, in the case of elongated active particles, defects in their relative alignment have been identified in a plethora of different contexts [215] and have been found to play a role in the cytoskeleton self-organization [49, 216–219], in cells' motion [147, 220–222] and in development [223]. One promising way to control active matter thus is by controlling the system's boundary condition or topology in order to control defects [49, 224–227]. In all of these cases however, defects are themselves part of the active system and thereby move or spontaneously form and destroy. Only little control of their position, number and dynamics is possible. A different strategy is to embed the active system into a passive medium, taking advantage of our ability to control traditional materials. Passive material properties and their defects have indeed been shown to influence the emergence of collective structures [218, 228–230]. In particular, confining swimming bacteria in a passive liquid crystal has shed light on the interplay between active matter and passive defects, showing that defects

can be used shape pattern formation [103, 142] or accumulate particles in space [141]. Thus, nematic defects can induce distortions in a passive material that end up shaping the behavior of the active system they contain in a non-trivial way [231]. However, most of these results lack microscopic resolution and are strongly affected by long range hydrodynamic interactions that might hide the microscopic behavior. In addition, to understand the potential of passive nematic materials to control active systems, microscopic resolution of the interactions between the two is needed. Here we steer the pattern formation process of an active system by the presence of a passive liquid crystal. This is achieved by coupling a two-dimensional microtubule gliding assay to a self-assembled actin nematic. Gliding filaments quickly assemble into ordered, polar structures that would not emerge in the absence of the actin layer. We are then able to observe with high resolution their emergence and to pinpoint nematic distortions originating from defects as their source. Specifically, -1/2 defects act by inducing long-range distortions in the material that affect the active flow. Instead and more strikingly, the conformation of +1/2 defects is found to be a fundamental funneling and polarity sorting element. Overall, this leads to the emergence of polar active flow, despite the nematic symmetry of the passive layer. We find that the formation of patterns and their shape are purely a consequence of the shape of the nematic field and its defects, that impose a structure on an otherwise disordered system. It is indeed the precise positioning in space of microscopic point defects which organizes the active fluid flow on a mesoscopic scale, an observation we can rationalize by simulations, which fully recapture the experimental results.

## 5.2 Formation of active polar lanes in passive nematic layer

The experimental setup consists of binding streptavidin-functionalized kinesin motors on a supported lipid bilayer (SLB) containing 1.25 % biotinylated lipids. Successively, the desired concentration of short ($\approx 2\mu m$), GMP-CPP stabilized microtubules (MTs) is incubated for 2 minutes and washed, before the final addition of 1µM short phalloidin-stabilized actin filaments together with a 0.25 % methylcellulose as a depletant and 2mM ATP as chemical fuel (see Methods). In this conditions, the actin filaments quickly (5-15 minutes) form a 2-dimensional nematic layer [232], featuring both +1/2 and -1/2 nematic defects (Fig. 5.1B, insets). Defects are spontaneously assembled due to quenching of the filaments on the SLB. Because of the planar geometry, we observe on average a total topological charge of 0 and hence defects of opposite charge form in pairs. The SLB both acts as a cushion for the sedimentation of actin filaments but also enforces steric interactions between gliding filaments and passive ones [219, 233]. Hence microtubules are forced to glide inside this nematic material and to locally align with actin filaments (Fig. 5.1A). After the
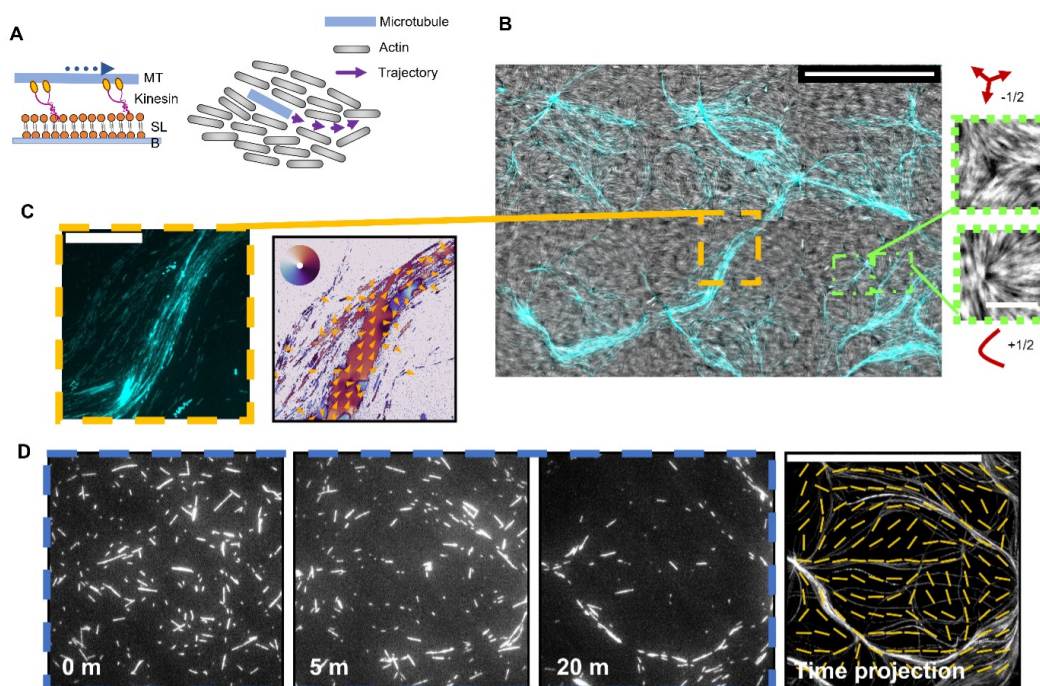
**Figure 5.1 Description of the system and formation of polar lane** A) Schematic of the system. Kinesin motors are bound to a SLB and propel short, stabilized microtubules. A passive actin nematic is sedimented on top. B) The nematic quickly assembles and features topological defects of half-charge. Microtubules glide into it. Over time, the system evolves into dense polar lanes spanning the whole sample. Scale bar is 100 $\mu$m. C) Lanes are found to be locally polar, with microtubules mostly gliding in the same direction as shown by the mean mass flow. Scale bar is 50$\mu$m. D) An initial isotropic distribution of microtubules evolves into lanes as the nematic sediments. The last picture on the right shows a time projection of the last 10 minutes with an overlay of the final actin nematic director field, showing how eventually formed lanes move along the nematic director field.

actin nematic is stabilized, at a MT surface concentration of $\sigma = 0.08$MTs/$\mu$m$^2$, we observe that over the course of 20 minutes the microtubules, initially isotropic in space, aggregate in thick streams, much longer than the individual filaments, that span the whole sample (Fig. 5.1B and D) and, strikingly, are composed of filaments locally all moving in the same direction (Fig. 5.1C). The microtubule streams appear to locally follow the local orientation of the actin nematic (Fig. 5.1D, right, Movie 1). Notably, in the absence of actin microtubules at a similar surface concentration do not form stable polar patterns, simply moving in straight lines with a persistence length of $\sim 100$µm and a speed of $\sim 200 - 300$nm/s (Movie 3) and only transiently aligning upon collision. Additionally, by varying the MC concentration such that actin sediments without forming a stable nematic no formation of ordered structures
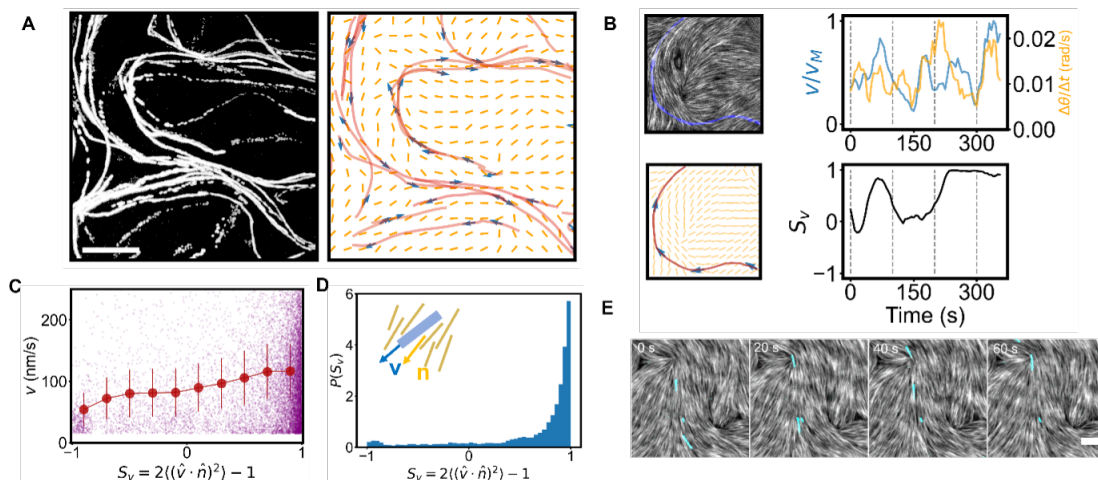
**Figure 5.2 Microscopic behavior of microtubules gliding in a passive actin nematic and effect of distortions** A) Individual microtubules glide into the nematic following its director. Their trajectory projected over time (total: 7 minutes) is shown on the left, selected tracked trajectories on the right together with the underlying nematic field B) By tracking individual gliding filaments, we can confirm that microtubules cross regions of different local order and that misalignment with the nematic leads to a re-orientation and a drop in speed. C) The microtubules' speed has a slight dependency on the local alignment with the nematic $S_v$, resulting in slower speed at low alignment. D) On average however, microtubules are mostly aligned, with $S_v \approx 1$. E) Different microtubules (two in this case) end up gliding along the same trajectories. Scale bars are 5 μm.

is observed, indicating that the nematic background is necessary for these effects to arise (Movie 3).

## 5.3  Passive nematic field align active microtubules

We analyzed the behavior of the system at low microtubules' density ($\sigma = 0.003$ MTs/μm$^2$) using TIRF microscopy, thus being able to both follow the trajectory of individual microtubules (Fig. 5.2A) and to extract the local nematic orientation $\boldsymbol{n}(\boldsymbol{r})$ of the actin filaments at any point $\boldsymbol{r}$ of the image (see Methods). We perform single-particle tracking (conditions are: 1 μM Actin, 0.03MTs/μm$^2$) to extract both the speed and orientation $\boldsymbol{v}$ of microtubules. MTs are found to glide mostly in the direction set by the nematic material and thus with a position-dependent velocity $\boldsymbol{v} = v_0\boldsymbol{n}$, with a mean speed of $v_0 \approx 100$nm/s (Movie 1). We compute the order parameter $S_v = 2(\boldsymbol{v} \cdot \boldsymbol{n}/|\boldsymbol{v}|)^2 - 1$, which measures the alignment between gliding microtubules and the passive actin nematic and is expected to be 1 if the filaments are aligned with the nematic field and lower otherwise. The distribution of $S_v$ is

found to be strongly peaked at $S_\nu \approx 1$ (Fig. 5.2D) indicating strong alignment between the microtubules and the nematic director.

We measure a dependence of the filament's speed on their local alignment with the nematic, with microtubules poorly oriented moving slower (Fig. 5.2C). Fig. 5.2B shows an example of a microtubules' trajectory. It shows periods of high and low speed, dependent on the local alignment with the nematic. As the MT enters an area in which it is misaligned with the nematic director, it slows down and progressively realigns. This shows that microtubules are able to reorient to resolve local misalignments and escape obstacles, i.e., there is an effective torque due to their misalignment that reorients them. Hence microtubules in general align with the nematic director and follow its distortions.

Over time, individual microtubules, even at such low density, end up gliding along the same main paths and mostly moving in the same direction (Fig. 5.2D). This indicates that the nematic alignment field selects trajectories on which most of the microtubules are directed. In a perfectly aligned nematic this would not be possible due to the absence of distortions present. As in this system distortions in the nematic director field always originate from defects and then propagate at longer distances, we set out to determine their microscopic effect on the active system.

## 5.4 Distortions and Defects in the passive nematic steer the active fluid

We then monitor the behavior of the filaments in the presence of different distortions in the nematic, in particular on splay (high values of $(\nabla \cdot \mathbf{n})^2$), bend (high values of $\mathbf{n} x \nabla x \mathbf{n}$) and close to nematic defects' cores. We observe the system both at low ($\sigma = 0.003 \text{MTs}/\mu\text{m}^2$) and higher MT density ($\sigma = 0.06 - 0.08 \text{MTs}/\mu\text{m}^2$) to extract information about both the individual and the average behavior of microtubules. As expected, since MTs are forced to follow the nematic orientation, splay is the source for convergence (divergence) of the microtubules flow, leading to an increase (decrease) of the density (Fig. 5.3A, top). Since $v = \pm v_0 \mathbf{n}$ then clearly the splay of the velocity field is given by $\nabla \cdot \mathbf{v} = \pm v_0 \nabla \cdot \mathbf{n}$ thus being proportional to that of the nematic director field. Splay additionally leads to different streams merging. In the case of pure bend, instead, filaments just glide along the deformation, but no change is density is present (Fig. 5.3B, bottom). We then turned to the behavior close to defects' cores. In the presence of -1/2 defects (Fig. 5.2B), individual filaments simply turn around its core following the alignment of the nematic field and only rarely cross it. Hence, they only modify the microtubules' flow by bending their direction with three-fold symmetry due to the bend deformations they induce in their proximity (Fig. 5.3B top,C) Conversely and more strikingly, when gliding filaments hit a +1/2 nematic defect, where no alignment is defined, they abruptly
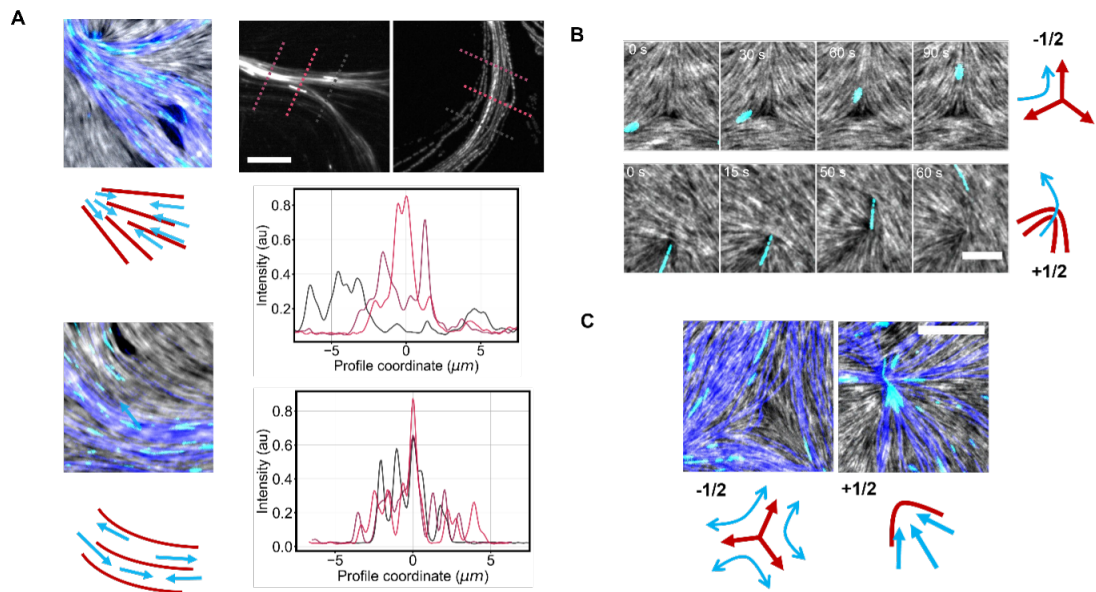
**Figure 5.3 Behavior at distortions in the nematic** A) In the presence of splay and bend distortions, the microtubules' flow is affected. Splay changes the concentration of filaments, as shown by the intensity profile along the stream, whereas bend only their orientation. B) At -1/2 defects (top), microtubules are simply redirected and usually do not reach the core. At +1/2 defects (bottom), where no director is defined, microtubules get directed towards the defect's core and then are ejected in the nematic again, where they re-align. C) Collectively, filaments at defects behave like individual ones do, bending at negative 1/2 defects and getting converged at positive ones.

reorient themselves. Indeed, microtubules are funneled directly to the defect's core by the defect's induced local splay and get stuck in it, until able to realign with the local field to escape the defect (Fig. 5.3B, bottom). After microtubules are ejected, the actin nematic, while deforming when microtubules at high concentration glide through it, gradually recovers its initial conformation over time. However, in the present case, the defects are passive and stable in time and space and the active particles do not simply get trapped but are able to escape it by realigning. The behavior is seen to be the same at all observed densities (Fig. 5.3C), showing how +1/2 defects converge and then deviate the average MT flow.

## 5.5   Defects-based formation of streams

We determine that positive-defect based funneling of microtubules is the main mechanism of pattern formation. Zooming in from the beginning of the experiment on the position at which a +1/2 defect will eventually form, it becomes clear that

the initially disordered filaments are funneled, as soon as the nematic forms, into ordered structures by the defect itself (Fig. 5.4A). Not only does the splay-dominated part of the defect accumulate the microtubules toward its core, but due to their conformation, defects can only be accessed by microtubules on one side, so that they always and only exert a converging effect on the microtubules' density. Thus +1/2 defects allow to break the spatial symmetry. Additionally, if the nematic field right after the defect's core is oriented at a skewed angle with the defect's axis, all the ejected microtubules will preferentially turn in one direction, choosing the one that minimizes their rotation (Fig. 5.4B, Movie 6). Positive +1/2 defects then are the source of net polarity in the system, as they select a main direction. This results in macroscopic polar streams (Fig. 5.3B, left). After the streams are formed, the shape of the polar patterns are still tightly bound to the position and conformations of defects present in the nematic. Trajectories of microtubules indeed follow defect-induced distortions of the passive nematic (Fig. 5.4B-D). Plotting the position and orientation of the topological defects on top of the MTs' flow, it becomes clear how they are having an effect in shaping the trajectories as the trajectories deform around defects (Fig. 5.4C). Microtubules are deviated by distortions in the nematic field and in addition they are funneled by +1/2 defects forming polar streams. After they are formed, streams rarely cross +1/2 defects anymore but are surrounded by them. This indicates that previously +1/2 defects have played a role in channeling the MT flow on the final trajectories and setting their final polarity. We verify that streams are polar by computing the mean flow along the lanes in different positions of the sample, showing domains of polar orientation (Fig. 5.4C, right). We find that multiple defects arranged in specific conformations further steer the polar flow. For instance, conformations containing both a positive and a negative defect can give rise to channeling of microtubules (Fig. 5.4D, bottom inset). The formation of closed loops in the MTs' trajectories is another feature of this system (Fig. 5.4D, top inset,E). All observed loops have in common to be composed of N negative defects and N+2 positive ones, as the total charge inside a loop has to equal +1 by the definition of charge itself (Movie 7). As loops consist in microtubules following the nematic field and ending up in the original position with the same orientation, they are indeed only permitted if the nematic field allows a smooth, closed path, to which n is tangential, enclosing a total topological charge of +1. While this constraint is topological in origin, the precise shape of the loop is instead given by the particular shape of the defects, in- and outside the loop, and their distortions (Fig. 5.3E), as the microtubules still glide along the nematic director around the defects.

Overall, these results indicate that defects play a two-fold role in shaping the microtubules flow: on the one hand, they produce deformations of the nematic field that affect the microtubules' flow even at a distance from the defect's core. On the other hand, +1/2 defects and their surroundings play a more direct role by both funneling microtubules but also selecting one out of two possible directions.
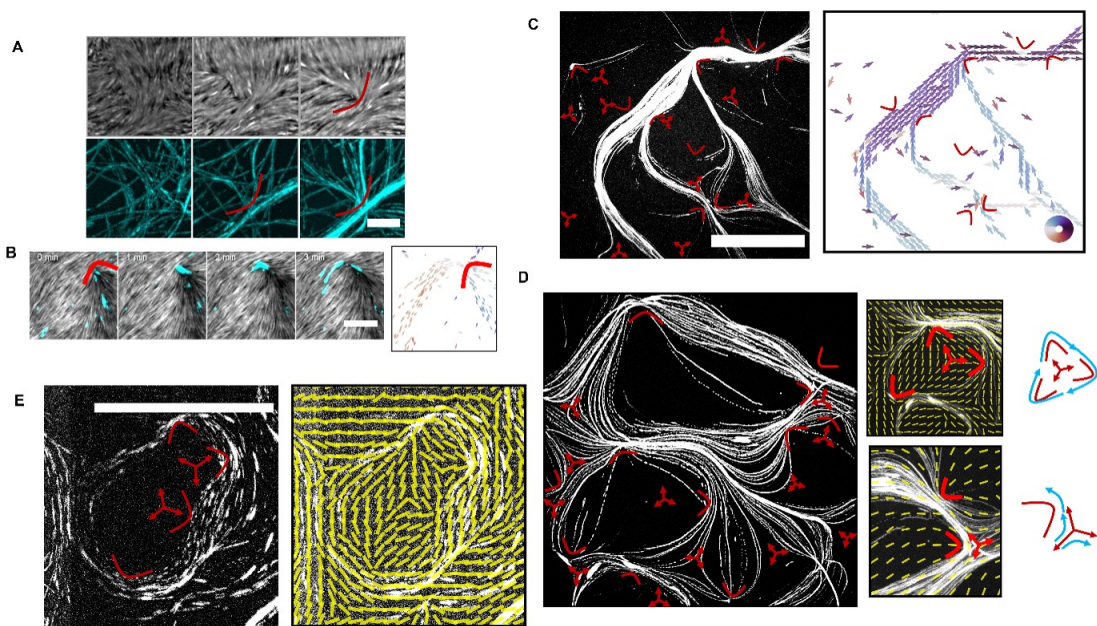
**Figure 5.4 Formation of polar streams and role of defects** A) Positive defects play a role in the formation of lanes as the initially isotropic distribution is funneled by defects into lanes (close ups from the same sample as in Fig. 5.1D). B) Positive defects not only converge the flow but also break the orientational symmetry by ejecting microtubules preferentially in one direction. C) This turns eventually into the formation of strongly polar lanes, as shown by the average flux of microtubules. While the shape is given by deformations in the actin nematic induced by defects, streams tend to be surrounded by positive defects that funnel microtubules into them. D) The microtubules' flow assembles into streams and follow defect-induced deformations of the nematic field. Defects' position and orientations are marked in red. Close ups reveal how defects configurations can shape the microtubules' flow, including channeling of the flow in specific directions or formation of closed loops. E) Loops are polar and thus must enclose a total charge of +1, given by N negative and N+2 positive defects. The specific shape of the loop is due to the shape of the nematic field which is influenced by defects inside and outside the loop.

## 5.6  Simulations and streams prediction

The formation of polar lanes and their morphology are seemingly only due to the shape of the nematic field, and in particular to the presence of defects, coupled to the fact that microtubules are self-propelled. To rationalize this observation, we extract the field $n(r)$ from microscopy images (see SI) and use agent-based simulations to predict the path the microtubules will follow. Additionally, we develop a heuristic approach able to predict which trajectories are going to be amplified based entirely on the conformation of the nematic field and its positive defects. Both approaches

and the results are summarized in Fig. 5.5A. First, we implemented an agent-based simulation mimicking the behavior of microtubules interacting with a nematic field. For that, we initially use $N$ non interacting point-like particles that move persistently in direction $\boldsymbol{u} = (\cos(\theta), \sin(\theta))$, with a constant speed $v$. Particles receive an aligning torque by a nematic background field $\boldsymbol{n} = (\cos(\phi), \sin(\phi))$. We assume the equations of motion, for a given particle $i$, to be

$$\frac{\mathrm{d}\boldsymbol{r}^i}{\mathrm{d}t} = v\boldsymbol{u}^i, \tag{5.1}$$

$$\frac{\mathrm{d}\theta^i}{\mathrm{d}t} = A\sin\left(2[\phi(\mathbf{r}^i) - \theta^i]\right) + \sqrt{\frac{2v}{L_p}}\xi, \tag{5.2}$$

where $\xi$ is random white noise and the pre-factor ensures a path persistence length $L_p$ (parameters and details are given in SI). The parameter $A$ is an alignment rate that represents the strength of the coupling between the active particles and the nematic field.

To test the influence of alignment with the nematic background field, we conducted parameter sweeps over $A$, i.e. varying the strength of the coupling between particles and the nematic field. Remarkably, as $A$ is increased above a nonzero value, the system rapidly forms lanes that very closely those observed in the experiments, see Fig. 5.5A(center), B. These lanes are polar and show the same structure and local orientation as the experiments (Fig. 5.5E). After reaching a threshold of about $A \sim 0.01\mathrm{rad/s}$, a further increase in alignment strength does not change the observed overall topology of the lanes and the systems continues to resemble the experimentally observed patterns (Fig. 5.5C).

By further performing simulations on randomly-generated nematic fields (see SI) several conformations observed in experiments (including loops enclosing a total charge of $+1$) are observed, suggesting our observation is a general property of defect-containing nematic materials.

Thus agent-based simulations confirm that the structure and polarity of the observed patterns are purely due to the presence of a nematic field that fixes the local orientation, but not the direction, of particles in space. The fact that simulations, despite the simplicity of the model featuring shape-less, point-like particles, still closely mimic the experimental results, suggests that the observed structure formation is a general process for self-propelled agents, and does not depend on the microscopic details of how microtubules move. The only necessary assumptions are that particles must move persistently and, to some degree, align with the nematic field. This is further confirmed by the fact that main trajectories are amplified even at low MT density and that simulations including interaction

show the same structures too (see SI), suggesting that interaction between filaments is not a relevant parameter to predict the patterns.

Emerging patterns are thus more of a consequence of the conformation of the field $n$ rather than of the microscopic dynamics. The observation that the only points at which microtubules are strongly funneled and deviated are $+1/2$ defects indicates that positive defects and their surroundings are the fundamental elements of the pattern formation process. They indeed mediate polar sorting by ejecting microtubules preferentially in one direction and the fact that they choose preferentially one direction is due to distortions in the nematic right after the defect's core.

We then develop a polar streamline heuristic prediction approach based only on the characteristics of the nematic field in the vicinity of positive defects, in turn summarized by the nematic tensor $Q$ and its derivatives. It consists in identifying a) starting points for trajectories right after defects; b) the preferred direction of such trajectories based on the characteristics of the field $n$ (see SI for a full description).

First, we identify the positions $r^{+1/2}$ of positive defects. Due to the continuous self-propulsion of the microtubules we expect that the position of the streamline starting point will be shifted with respect to the defects' core along the defect's axis and end up in position $r^{\text{seed}} = r^{+1/2} + d p^{+1/2}$, where $p^{+1/2}$ is the defect's axis computed from the divergence of $Q$ and $d \approx 2.5\mu\text{m}$ (approximately one microtubule length) is a phenomenological parameter summarizing the mean distance travelled by a MT before realigning. We expect the best value of $d$ in general to be dependent on the particles' speed and shape, that modulate the effectiveness of alignment. The position $r^{\text{seed}}$ will then act as a seed for the streamlines.

As a last step, to choose the direction of the streamlines, one can, again from the divergence of the tensor Q, also obtain a polarity field $p = \nabla \cdot Q / |\nabla \cdot Q|$ able to predict what direction MTs will follow after they cross a $+1/2$ defect. This divergence indeed contains information about both splay and bend distortions and encodes the main direction they enhance and is then tightly connected to the mechanical properties of the passive nematic [231, 234, 235]. Microtubules leaving a defect will feel such distortion and orient accordingly. From then on, filaments will just follow the nematic streamlines of the field n in the predicted direction. We thus impose that particles perfectly align with the nematic field in the seeding position $n(r^{\text{seed}})$ and define the preferred direction of motion as $\text{sign}\left(-n(r^{\text{seed}}) \cdot (p^{\text{seed}})\right) n(r^{\text{seed}})$ i.e., as the direction minimizing the scalar product between $n(r^{\text{seed}})$ and the divergence of $Q$ in the seeding position. This corresponds to the fact that particles preferentially follow distortions in a direction that minimizes the change in their direction. Streamlines are then evolved from the seeding position in the chosen direction until they reach another $+1/2$ defect or one of the edges. The approach is sketched in Fig. 5.5F, right side.
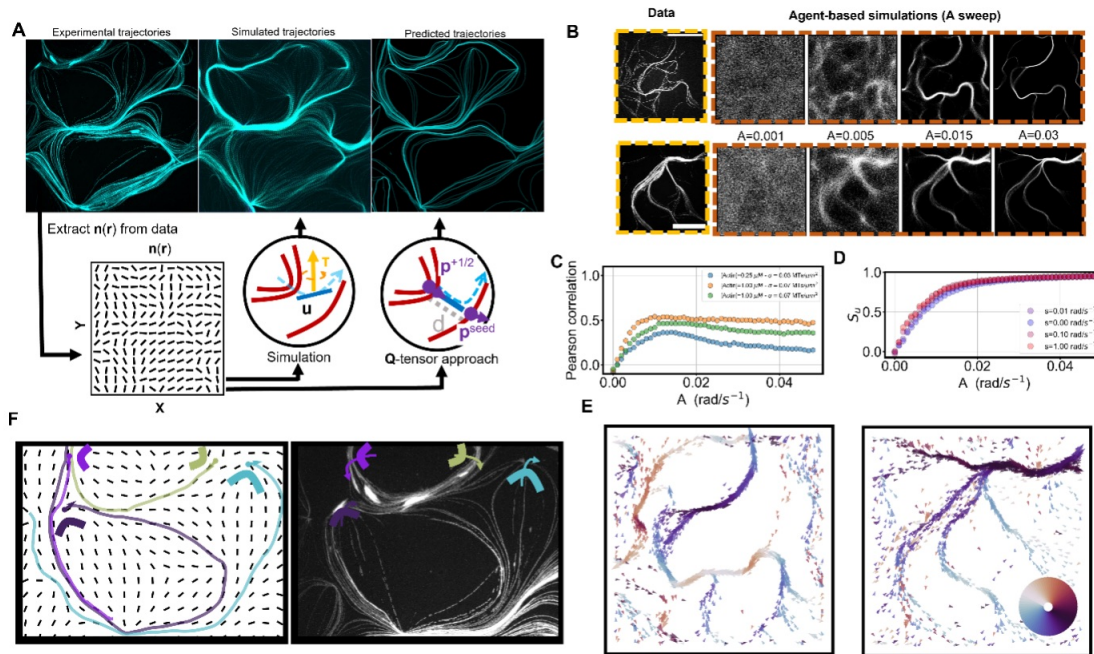
**Figure 5.5 Simulations and heuristic arguments describe the experimental results well** A) The experimental trajectories (top left) can be very well reproduced by different approaches that start from the knowledge of only the nematic field. We can extract the nematic field $n$, which in turn can be used as input for agent-based simulations (top center) and a $Q$-tensor based heuristic approach predicting streams (top right). Both approaches are schematized on the bottom. Starting from the nematic field and a minimal set of rules, we can thus reproduce the experimental trajectories. B) Both at low and high density, simulations recover experimental trajectories. Simulations rely on a local torque acting on the agents to align them with the field and allows to vary parameter such as alignment strength, interaction, etc. C) As the alignment rate is increased to $A \approx 0.01$ simulations start showing very good agreement with experimental trajectories, as quantified by the Pearson correlation coefficient between experimental and simulated images. D) Regardless of the particle-particle interaction parameter B, simulated particles all align with the nematic field with the same efficiency, as quantified by the parameter $S_u$ E) Simulations also precisely recover the polar flow of experiments (to be compared with Fig. 5.4C) indicating that the information about the polarity is encoded in the field. F) To further confirm it, the $Q$-tensor approach instead focuses on the role of $+1/2$ defects. Defects are identified in the nematic field and the morphology of their surrounding is used to identify the streamlines they generate by converging the MTs' flow. To each defect corresponds a color-coded streamline (left) to be compared with experimental data (right). Only selected defects are shown. This proves that $+1/2$ defects directly play a role in shaping the flow.

This defect-based streams prediction again is able to predict, starting uniquely from the experimentally extracted nematic field *n* the trajectories of MTs (Fig. 5.5A,F). Additionally, however, it only uses information about the position and conformation of +1/2 defects, underlining their role in shaping the flow's directionality. Differently from simulations, only trajectories starting right after a +1/2 defect are allowed and yet experimental results are still confirmed, indicating that trajectories indeed are funneled +1/2 defects. By simply knowing how defects are arranged in space one can predict the formation of polar lanes. Both approaches confirm that it is the field n that shapes the final patterns and that +1/2 defects are in this case the fundamental polarity-sorting configurations.

Simulations suggest that the only relevant parameter is the coupling between the nematic field and the particles' orientation. The results is true for both high-density and low-density experiments, suggesting that the formation of main paths is a characteristic of the nematic field itself. This latter statement is confirmed by the *Q* tensor approach, which in addition underlines the role of +1/2 nematic defects in sorting the polarity, while the following evolution of the system is solely dependent on MTs staying aligned with the actin nematic.

## 5.7  Conclusion and discussion

We have shown that a passive nematic material containing defects can influence the motion of active filaments and lead to the formation of polar structures on a mesoscopic scale. Differently from recent results combining actin and microtubules [234, 236] we separate the active component (microtubules) and the passive one (actin). While formation of patterns induced by the presence of a nematic material has already been observed in bacterial systems [142], in this case we are presented with a purely 2D system which we can observe with high resolution to understand the microscopic dynamics. In the presence of self-propulsion, passive defects lead to the selection of specific oriented trajectories. Specifically, we confirm that the emergence of ordered flow is due uniquely to the presence of defects and to their conformation. A similar funneling of active particles accumulating in +1/2 defects had already been observed in the case of bacteria [141] and was shown to cause the formation of polar structures in the case of gliding filaments [219]. We extend these results and find that the information about the morphology and direction of the polar streams is embedded in the passive nematic only and its conformation, i.e., it is a general property which does not depend on fine details of the active system.

As gliding microtubules do not produce substantial flow and since the nematic is stable over time, this system falls into the dry active matter category [7, 124]. The absence of hydrodynamic interactions enhances the stability of the forming patterns and allows defects to be fixed in space. Hence, as the positioning and orientation

of defects govern the polar streams, they somewhat act as lenses would for light beams, by focusing and re-directioning the flow. Similar to an optical path, the arrangement of defects guide pattern formation. This suggests general strategies to drive the flow of dry active matter which do not require macroscopic patterning of the whole surface, as done instead for instance in [142], as only the position and orientation of individual nematic defects needs to be controlled. Coupled with our ability to control liquid crystals, we can envision the formation of mixed systems in which a passive nematic material is controlled in order to direct active patterns, similarly to how a microfluidic setup controls liquid flow [237]. This would lead to a more targeted and energetically efficient manipulation of nematic materials in order to tune macroscopic active flow.

A final straightforward outlook would be to extend this discussion in different topologies, taking advantage of constraints on the alignment fixing the total charge and the defects morphology to obtain diverse patterns. This would prove that many of the observed active behavior under confinement, including breaking of the chirality symmetry in non-dry systems, are due to fundamental properties of nematic configurations [225, 238, 239]. Additionally, as filament-like structures are ubiquitous in nature, with the most prominent example being the cell's cytoskeleton, we expect this sort of mechanism suggests strategies that biological system might already be using to direct matter's flow in one direction, using local nematic. For example, nematic structures are fundamental in processes such as the development of the organism hydra [223], the formation of bacterial biofilms and many more biologically-related processes [192, 215, 240].

## 5.8 Appendix

### 5.8.1 Simulation

In our agent-based model, we consider spherical self-propelled particles of diameter $\delta = 1$ μ$m$. The particles move with velocity $v = 0.1$μ$m/s$ in the plane and their positions can be described as:

$$\frac{\mathrm{d}\boldsymbol{r}^i}{\mathrm{d}t} = v\boldsymbol{u}^i, \tag{5.3}$$

where $\boldsymbol{u}^i = (\cos(\theta^i), \sin(\theta^i))$ is the orientation of particle $i$.

The individual particle has a nematic alignment with an external field $\boldsymbol{n}(\boldsymbol{r}) = (\cos(\phi(\boldsymbol{r})), \sin(\phi(\boldsymbol{r})))$, with the alignment rates $A$, and with neighbors within the interaction radius $\delta = 1$ μ$m$, with the alignment rate $S$:

$$\frac{\mathrm{d}\theta^i}{\mathrm{d}t} = A\sin(2[\phi(\mathbf{r}^i) - \theta^i]) + S\sum_{j\neq i, r_{ij} < \delta}\sin\left(2[\theta^j - \theta^i]\right) + \sqrt{\frac{2v}{L_p}}\xi. \tag{5.4}$$

where $\xi$ is random white noise with zero mean and unit variance with a pre-fractor ensuring a path persistence length of $L_p = 100$ μ$m$.

If not stated otherwise, the simulation was configured as follows: The nematic background fields had a resolution of $2008 \times 2008$, with a pixel edge-length of $64.5nm$. The density of particles was set to be $0.029/$μ$m^2$. Simulations were initiated with random initial conditions (i.e. particles initially placed at random positions and with a random orientation). To cut off initial transients, we let the simulation proceed for $2000s$ before starting to obtain measures. These were subsequently recorded in 800 frames, equally spaced over a time-window of $8000s$.

Measures in the experiments were taken with a microscopic field of view much smaller than the whole experimental system, hence the nematic field on opposing sides as well as particles exiting resp. entering the observed area of the system are not correlated (see e.g. Fig. 5.2A). To account for this fact in the simulations, we used "grand canonical" boundary conditions when simulating an experimentally obtained field. Here, when particles cross a boundary, they are put at a random position along one randomly chosen side of the simulation box with a randomly chosen orientation. Otherwise we used periodic boundaries.

### 5.8.2 Heuristics

To address the formation of polar streams, we consider the behavior of particles on a two-dimensional square periodic domain of the size $L$ with synthetically generated nematic fields containing simple configurations of topological defects. We firstly con-
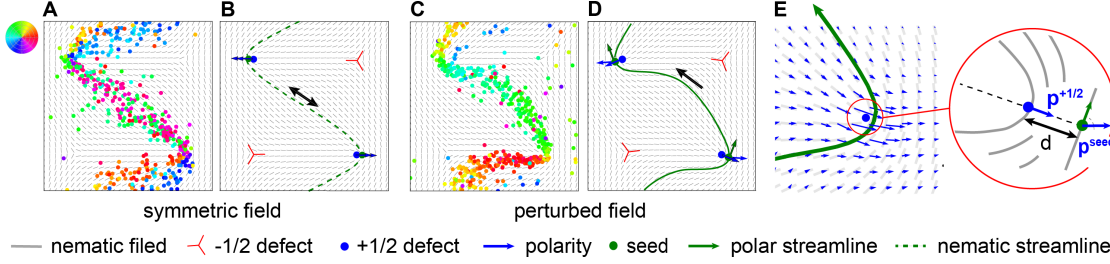
**Figure 5.6** Panels (**A,C**) show the results of agent-based simulations for symmetric (**A**) and disturbed (**C**) nematic textures. (**B**) and (**D**) illustrate the heuristic predictions for (**A**) and (**C**), respectively. (**E**) depicts the heuristic rule. Red tripods are for $-1/2$ defects, bold blue dots corresponds to $+1/2$ defects, green lines represents the streams of particles, blue arrows show the divergence of nematic field.

sider two pairs of symmetrically located $\pm 1/2$ defects, and introduce the following director field: $\mathbf{n} = (\cos(\phi), \sin(\phi))$, where $\phi = \sum_i k_i \tan^{-1}((y - y_i^0)/(x - x_i^0)) + \phi_0$.

Here $k_i$ and $(x_i^0, y_i^0)$ define topological charge and the core's position of the $i_{th}$ defect, and $\phi_0$ is initial angle. Particularly,

$$k_1 = -1/2, (x_1^0, y_1^0) = (-l, l) + (x_c, y_c), \tag{5.5}$$

$$k_2 = 1/2, (x_2^0, y_2^0) = (l, -l) + (x_c, y_c), \tag{5.6}$$

$$k_3 = 1/2, (x_3^0, y_3^0) = (-l, l) + (x_c, y_c), \tag{5.7}$$

$$k_4 = -1/2, (x_4^0, y_4^0) = (-l, -l) + (x_c, y_c), \tag{5.8}$$

where the $(x_c, y_c) = (L/2, L/2)$ is the center of the domain, and $l \approx L/4$.

Running the simulations on the introduced director field, we observe that particles form nematic lane, which passes in the vicinity of positive topological defects, perpendicular to their axis (Fig.5.6A). That goes in line with the fact that topological defects correspond to the maximal distortion of the nematic field: splay deformation leads to the convergence of the nematic streamlines in $+1/2$ disclinations (and divergence in $-1/2$ ones) [141]. Thus, positively charged defects play the role of natural attractors, although the lane is shifted from the defect core by a small distance along the defect's axis.

However, if one introduces small perturbation $\mathbf{n}_\delta = (0, \cos(2\pi x/L))$, particles moving in a distorted field $\mathbf{n}_d = (\mathbf{n} + \mathbf{n}_\delta)/|(\mathbf{n} + \mathbf{n}_\delta)|$ form the polar stream (Fig.5.6C). It illustrates that deviation of the field around the defect from a perfectly symmetric one can lead to a symmetry breaking.

Armed with this knowledge, we can formulate our heuristic rule predicting polar streamlines' location. It consists of (i) identifying a starting point of the potential

stream and (ii) determination of its direction. We first identify the positions $r_i^{+1/2}$ of positive defects as local maxima of the topological charge density $q$ [136, 202] defined as:

$$q = \frac{1}{4\pi} \left( \partial_x Q_{xi} \partial_y Q_{yi} - \partial_x Q_{yi} \partial_y Q_{xi} \right), \tag{5.9}$$

where $Q_{ij}$ - tracelesss and symmetric tensor describing an average alignment of filaments disregarding their orientation. $Q_{ij} = \langle n_j n_j - \delta_{ij}/2 \rangle$ with $\delta_{ij}$ denoting Kronecker delta.

From the symmetry grounds, the only source of the polarity coming from the actin layer is the divergence of the nematic field. We define the local actin-induced polarity (or just "polarity" hereafter) as $p_i = -\partial_j Q_{ij}/|\partial_j Q_{ij}|$. Accordingly, the axis of $+1/2$ defect can be defined as averaged $p_i$ at the defect core: $a_i = p_i^{+1/2}$ [241]. Due to the continuing self-propulsion of the particles, we expect that position of the streamline starting point (seed) is shifted in respect to the defect core: $r_i^{+1/2} + \mathrm{d}\, a_i$ where d is a small phenomenological parameter depending on the allingment strength $A$. It can be explained both by the particles overshooting and curvature-induced flux [152, 189]. Finally, preferred direction of motion can be defined as $n_i \mathrm{sign}(-n_k \partial_j Q_{kj})$ at the stream line's starting point. As one can see, if topological defect is perfectly symmetric actin-induced polarity is normal to the local director ($n_k \partial_j Q_{kj} = 0$), consequently no symmetry breaking can be observed and the stream remains nematic. However, the symmetry breaks down when director field departs from the ideal profile. Any imperfections (e.g. inherent "twist" [242], or the influence of adjacent defect [241, 243]) can result in polar streams.

Our heuristic rule is pictorially illustrated in Fig. 5.6E; blue arrows correspond to the polarity field ($p_i$), grey segments are for the nematic alignment. When a particle moves from left to right being funneled by wedge-shape form of $+1/2$ defect, it reaches defect core region (green dot) and overshoots by distance d keep moving along the defect axis ($p_i^{+1/2}$). At this point (blue dot), the fate of particle is determined by the projection of local polarity ($p_i^{seed}$) on the nematic director. A smaller angle between polarity and $\pm n_i$ corresponds to a higher probability for particles to turn to the corresponding direction (green arrow). The introduced heuristics being applied to two mentioned director fields (Fig. 5.6 A, C) reproduce the localization of particles and their orientation with a high level of fidelity (Fig. 5.6 B, D, respectively).

It is worth mentioning, that divergence of Q-tensor contains both splay and bend deformations: $\partial_j Q_{ij} \propto n_i \partial_j n_j + (n_j \partial_j) n_i$. Splay deformation itself can concentrate particles and lead to the formation of the polar streams [142] (see the results for $\mathbf{n} = (\cos(\pi y/L), -\sin(\pi y/L))$ in Fig. 5.7A). Bend deformation, on contrary, can lead to the nematic stream (not shown). However, in the real passive nematics,

these two types of distortion are typically localized around the defects, which is often energetically beneficial.

Finally, to verify the existence of polar streams in the randomly oriented but realistic defects we generate artificial nematic patterns by integrating the equation for relaxational dynamics of passive nematics. Particularly we use the simplest form of Landau-de Genne's free energy $F$ with one-elastic-constant approximation:

$$\partial_t Q_{ij} = -\frac{1}{\gamma}\frac{\delta F}{\delta Q_{ij}} = [\alpha - \beta Q_{kl}Q_{kl}]\, Q_{ij} + \kappa \Delta Q_{ij}, \qquad (5.10)$$

where $\gamma$ is rotational viscosity. Elasticity $\kappa$ is Frank constant $K$ (normalized by $\gamma$), $\alpha$ and $\beta$ are standard Ginzburg-Landau coefficients. We stop the time evolution of the field before the system reaches an equilibrium homogeneous state and use the output as the pre-imposed director field for our agent-based simulation. In this case, particles also form polar streams "touching" the $+1/2$ defects. Remarkably, for some configurations of defects we even observe the polar rings discussed in the main text (Fig. 5.7B).
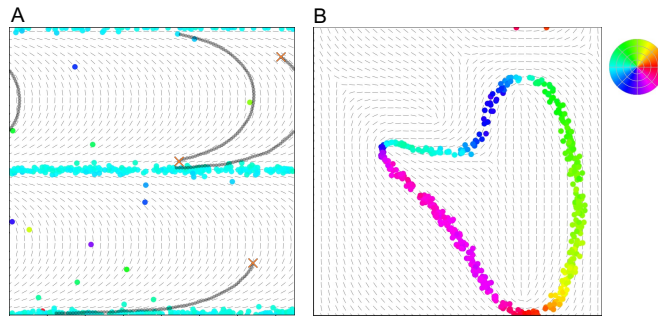


**Figure 5.7** Polar lanes in agent-based simulations. **(A)** After agents have been randomly placed in an artificial nematic field with very strong splay; they immediately concentrate into polarly moving lanes. To visualize individual agents, we trace the trajectories of three particles (with their starting position indicated by red crosses). **(B)** Agents form a dense polar ring around three $+1/2$ defects c.f. Fig. 5.3C. ($\kappa = 0.1$, $\alpha = 0.4$, $\beta = 0.05$, field resolution of $150 \times 150$, $A = 0.8$ and $L_p = 100nm$) (Directional color-code for both panels on the upper right.)

# 6 Conclusion and outlook

In this thesis we had a strong focus on the investigation of patterns, order and interactions in active matter systems. To this end we mainly applied numerical models and simulations.

In chapter 2, we developed a novel agent-based algorithm for the numerical simulation of the actin motility assay and combined large-scale simulations with experiments. Consistently they showed that polar and nematic patterns are not strictly distinct phenomena, but indeed can coexist in active systems. This finding implies that other than commonly assumed, the symmetry of macroscopic patterns in active matter is not uniquely set by the symmetry of microscopic interactions.

Several aspects of the coexistence between nematic and polar patterns we described in chapter 2 have since been observed by others. Interestingly, this was done both in agent-based simulations [71], where the authors used a different agent-based simulation than ours and observed metastability between nematic and polar patterns, and in kinetic Boltzmann resp. hydrodynamic approaches [129]. This indeed suggests that the three-phase coexistence does not depend on specific details of our simulations or the motility assay, but could be a more general feature of a wide range of active matter systems. To me, an open and worth pursuing question in this context is what prerequisites the microscopic constituents in agent-based systems that are dominated by alignment interactions (i.e. without significant steric exclusion as present in e.g. Ref. [71]) really have to fulfil in order for a coexistence of nematic and polar structures to be possible. In chapter 2 an interaction with a slight polar bias was necessary to facilitate a coexistence. Yet, we already saw some hints in this thesis that a polar bias may be entirely unnecessary to produce structures that are, at least locally, polar; see discussion about colliding waves produced by agents that align purely nematic in section 4.5.5 (it is worth to note that in Ref. [129] similar decays of nematic lanes were found). This could be a hint that even in agent based models in the limit of pure nematic alignment that exhibit phase separation into nematic lanes –yet are microscopically composed of polar moving particles with a constant speed– nematic structures are generally prone to such a decay in certain parameter regimes. If true, this would imply that nematic and polar structures are much more intertwined than it was long believed and that the commonly assumed phase separation scenario for nematic systems [7] is more complex than thought.

As just discussed, it seems that the three phase coexistence does not depend on specific details of our model. We nevertheless believe, on an arguably more

subjective and rather intuition-based level, that the investigation of the impact of some specific details in active matter systems could potentially be more fruitful than it may first appear. One example is the speed of particles. In order to suppress the above-mentioned decay of nematic lanes into colliding waves, we had to introduce a distribution of velocities instead of employing, as it is commonly done, the same for every agent (see again section 4.5.5). Does a broad distribution of agents speed maybe have other interesting consequences? It could, e.g., even lead to phenomena like a "phase separation" into different structures respectively composed of sub-populations of particles with different speeds.

Further, a close look at the details of collisions between agents in our simulation, cf. chapters 2 and 3 as well as Fig. 1.5, reveals that interactions are mostly non-reciprocal; a filament does not "feel" another one that is interacting with its tail (only when two filament heads overlap they mutually align). This is different than in most other models and could potentially have relevant consequences. It is not ruled out to be a factor in the formation of the defects we observed in chapter 4 or it may lead to a stabilization of polar waves and therefore be a factor in the relative ease with which we can observe the coexistence of polar and nematic patterns.

Besides their coexistence, we also in-depth investigated single types of patterns in active systems. In chapter 3 in particular we concentrated on the formation process of polar ordered structures and how they are maintained. By employing our simulation method we identified and investigated the mesoscopic processes on the level of particle clusters that drive the formation and maintenance of microphase separated polar patterns. We used these processes as a basis for the construction of a novel kinetic model, which showed the same cluster statistics, mass-exchange dynamics, and bifurcation scenario as the agent-based system, even though it contains no information on the spatial dynamics. This suggests that the presence of microphase separation in the ordered state, and potentially also other types of ordered patterns in different systems, can be understood by analyzing the flow in a properly defined phase space. A concrete next step could be to investigate how nematic structures form. How does the pattern formation proceeds on the level of microscopic constituents in this case? It may also start from mesoscopic nematic clusters analogous to the polar case. If so, there might be an interplay between polar and nematic clusters on the mesoscopic level whose investigation could also contribute to the understanding of interplay and coexistence of these patterns on larger length scales.

In addition to polar ordered structures, we further focused on the investigation of nematic patterns in chapter 4. More specifically, we discovered in our simulation that in the nematic phase-separated state, previously unreported $-1/2$ defects can form in triple junctions of lanes which are associated with a marked increase in

density, as well as filamentous arcs which are remotely reminiscent of +1/2 defects. We combined our agent-based analysis with a hydrodynamic model that exhibits the same phenomenology and topologically charged structures. That way we characterized how the occurrence of these structures depends on parameters and found that they are both closely linked with the lateral instabilities of nematic lanes. Our analysis implies that phase separation and topological defects – two hitherto seemingly incompatible phenomena – can actually be closely linked in weakly interacting active nematics. While it is as of yet unclear whether the emergence of these defects can also be observed in other nematic models that exhibit phase separation, we see at least no obvious reason why this should not be possible. So maybe even the seemingly well-explored phase-separated states with only one type of pattern still hold surprises that have been unnoticed so far.

Besides patterns and order that form self-organized due to particle-particle interactions only, we also investigated in chapter 5 how active matter systems can be externally controlled. More precisely, we focused on how polar patterns form in a microtubules gliding assay that is coupled to a passive actin nematics. We developed an agent-based model and a heuristic approach that consistently reproduced the experimental results, thereby showing that alignment to the nematic background is sufficient to obtain the observed polar streams. We identified +1/2 defects and their orientation to be the defining factors for the formation and guidance of polar patterns. Our results highlight the potential of controlling active particles via coupling to a passive background. In particular, a targeted positioning and orientation of defects could open up a general pathway to control the flow of active particles.

All this being said, we want to close with a broader (and subjective) statement. The starting point of this thesis was an experimental observation that we found hard to reconcile with the existing theoretical results at that time. Without this "cue from reality", many of the findings of this thesis, especially the ones presented in chapter 2, would not have been made yet (most certainly not by us, at least). Together with the rather uncommon experience of conducting experiments, although being a theoretical physicist (for which we feel very lucky), makes us prone to believe that close collaboration between experiment and theory was and is the best way forward. Many of the design choices we made for our simulation were inspired by closely examining the experiments and by a subsequent attempt to build the key defining characteristics into a model that is as simple as possible but not too simplistic. We think that most likely a similar feedback-loop between well-controlled experiments and well-controlled simulations (resp. theory) will be crucial in uncovering the most interesting findings that are still to be made in active matter.

# Bibliography

[1] L. Huber, R. Suzuki, T. Krüger, E. Frey and A. R. Bausch. Emergence of coexisting ordered states in active matter systems. *Science* **361**(6399), 255–258, 2018. DOI: 10.1126/science. aao5434. (Cit. on pp. v, vii, 1, 3, 10, 11, 21, 46–48, 50, 61, 62, 64, 65, 67, 86, 87, 96, 99–101).

[2] L. Huber, T. Krüger and E. Frey. Microphase separation in active filament systems maintained by cyclic dynamics of cluster size and order. *Phys. Rev. Research* **3**, 013280, 2021. DOI: 10.1103/PhysRevResearch.3.013280. (Cit. on pp. v, vii, 45, 86, 87, 99, 100).

[3] S. Ramaswamy. The Mechanics and Statistics of Active Matter. *Annual Review of Condensed Matter Physics* **1**(1), 323–345, 2010. DOI: 10.1146/annurev-conmatphys-070909-104101. (Cit. on pp. 1, 2, 4, 6).

[4] T. Vicsek and A. Zafeiris. Collective motion. *Physics Reports* **517**(3-4), 71–140, 2012. DOI: 10.1016/j.physrep.2012.03.004. (Cit. on pp. 1, 2, 4, 8, 10).

[5] M. C. Marchetti, J. F. Joanny, S. Ramaswamy, T. B. Liverpool, J. Prost, M. Rao and R. A. Simha. Hydrodynamics of Soft Active Matter. *Reviews of Modern Physics* **85**(3), 1143–1189, 2013. DOI: 10.1103/RevModPhys.85.1143. (Cit. on pp. 1–4, 8, 10, 14, 46, 85, 96, 111).

[6] C. Bechinger, R. Di Leonardo, H. Löwen, C. Reichhardt, G. Volpe and G. Volpe. Active Particles in Complex and Crowded Environments. *Reviews of Modern Physics* **88**(4), 045006, 2016. DOI: 10.1103/RevModPhys.88.045006. (Cit. on pp. 1, 2).

[7] H. Chaté. Dry Aligning Dilute Active Matter. *Annual Review of Condensed Matter Physics* **11**(1), 189–212, 2020. DOI: 10.1146/annurev-conmatphys-031119-050752. (Cit. on pp. 1–4, 6, 8–10, 14, 16, 86–88, 92, 96, 122, 129).

[8] M. Das, C. F. Schmidt and M. Murrell. Introduction to Active Matter. *Soft Matter* **16**(31), 7185–7190, 2020. DOI: 10.1039/D0SM90137G. (Cit. on pp. 1, 2).

[9] G. Gompper *et al.* The 2020 Motile Active Matter Roadmap. *Journal of Physics: Condensed Matter* **32**(19), 193001, 2020. DOI: 10.1088/1361-648X/ab6348. (Cit. on pp. 1, 2, 4).

[10] A. Czirók, E. Ben-Jacob, I. Cohen and T. Vicsek. Formation of complex bacterial colonies via self-generated vortices. *Physical Review E* **54**(2), 1791–1801, 1996. DOI: 10.1103/PhysRevE. 54.1791. (Cit. on p. 1).

[11] C. Dombrowski, L. Cisneros, S. Chatkaew, R. E. Goldstein and J. O. Kessler. Self-Concentration and Large-Scale Coherence in Bacterial Dynamics. *Physical Review Letters* **93**(9), 098103, 2004. DOI: 10.1103/PhysRevLett.93.098103. (Cit. on p. 1).

[12] L. H. Cisneros, R. Cortez, C. Dombrowski, R. E. Goldstein and J. O. Kessler. Fluid dynamics of self-propelled microorganisms, from individuals to concentrated populations. *Experiments in Fluids* **43**(5), 737–753, 2007. DOI: 10.1007/s00348-007-0387-y. (Cit. on p. 1).

[13] A. Sokolov, I. S. Aranson, J. O. Kessler and R. E. Goldstein. Concentration Dependence of the Collective Dynamics of Swimming Bacteria. *Physical Review Letters* **98**(15), 158102, 2007. DOI: 10.1103/PhysRevLett.98.158102. (Cit. on p. 1).

[14]  A. Sokolov, R. E. Goldstein, F. I. Feldchtein and I. S. Aranson. Enhanced mixing and spatial instability in concentrated bacterial suspensions. *Physical Review E* **80**(3), 031903, 2009. DOI: 10.1103/PhysRevE.80.031903. (Cit. on p. 1).

[15]  V. Schaller, C. Weber, C. Semmrich, E. Frey and A. R. Bausch. Polar Patterns of Driven Filaments. *Nature* **467**(7311), 73–77, 2010. DOI: 10.1038/nature09312. (Cit. on pp. 1, 3, 9, 14, 21, 22, 45–47, 59, 62, 65, 86, 99, 101).

[16]  T. Butt, T. Mufti, A. Humayun, P. B. Rosenthal, S. Khan, S. Khan and J. E. Molloy. Myosin Motors Drive Long Range Alignment of Actin Filaments. *Journal of Biological Chemistry* **285**(7), 4964–4974, 2010. DOI: 10.1074/jbc.M109.044792. (Cit. on pp. 1, 3, 9, 21, 22, 45, 47, 65, 86, 101).

[17]  Y. Sumino, K. H. Nagai, Y. Shitaka, D. Tanaka, K. Yoshikawa, H. Chaté and K. Oiwa. Large-Scale Vortex Lattice Emerging from Collectively Moving Microtubules. *Nature* **483**(7390), 448–452, 2012. DOI: 10.1038/nature10874. (Cit. on pp. 1, 21, 22, 47, 61).

[18]  T. Sanchez, D. T. N. Chen, S. J. DeCamp, M. Heymann and Z. Dogic. Spontaneous Motion in Hierarchically Assembled Active Matter. *Nature* **491**(7424), 431–434, 2012. DOI: 10.1038/nature11591. (Cit. on pp. 1, 16, 47, 85).

[19]  S. Hussain, J. E. Molloy and S. M. Khan. Spatiotemporal Dynamics of Actomyosin Networks. *Biophysical Journal* **105**(6), 1456–1465, 2013. DOI: 10.1016/j.bpj.2013.08.001. (Cit. on pp. 1, 3, 9, 22, 45, 47, 65, 86, 101).

[20]  R. Suzuki, C. A. Weber, E. Frey and A. R. Bausch. Polar Pattern Formation in Driven Filament Systems Requires Non-Binary Particle Collisions. *Nature Physics* **11**(10), 839–843, 2015. DOI: 10.1038/nphys3423. (Cit. on pp. 1, 3, 9, 10, 22, 23, 31, 46, 47, 58, 62, 65, 67, 86, 99, 101).

[21]  R. Suzuki and A. R. Bausch. The Emergence and Transient Behaviour of Collective Motion in Active Filament Systems. *Nature Communications* **8**(1), 41, 2017. DOI: 10.1038/s41467-017-00035-3. (Cit. on pp. 1, 3, 9, 46, 47, 86).

[22]  I. Theurkauff, C. Cottin-Bizonne, J. Palacci, C. Ybert and L. Bocquet. Dynamic Clustering in Active Colloidal Suspensions with Chemical Signaling. *Physical Review Letters* **108**(26), 2012. DOI: 10.1103/PhysRevLett.108.268303. (Cit. on pp. 1, 21).

[23]  J. Palacci, S. Sacanna, A. P. Steinberg, D. J. Pine and P. M. Chaikin. Living Crystals of Light-Activated Colloidal Surfers. *Science* **339**(6122), 936–940, 2013. DOI: 10.1126/science.1230020. (Cit. on pp. 1, 21).

[24]  A. Bricard, J.-B. Caussin, N. Desreumaux, O. Dauchot and D. Bartolo. Emergence of Macroscopic Directed Motion in Populations of Motile Colloids. *Nature* **503**(7474), 95–98, 2013. DOI: 10.1038/nature12673. (Cit. on pp. 1, 2, 21, 22, 46).

[25]  V. Narayan, S. Ramaswamy and N. Menon. Long-Lived Giant Number Fluctuations in a Swarming Granular Nematic. *Science* **317**(5834), 105–108, 2007. DOI: 10.1126/science.1140414. (Cit. on pp. 1, 3, 7).

[26]  I. S. Aranson, D. Volfson and L. S. Tsimring. Swirling motion in a system of vibrated elongated particles. *Physical Review E* **75**(5), 051301, 2007. DOI: 10.1103/PhysRevE.75.051301. (Cit. on pp. 1, 3).

[27]  A. Kudrolli, G. Lumay, D. Volfson and L. S. Tsimring. Swarming and Swirling in Self-Propelled Polar Granular Rods. *Physical Review Letters* **100**(5), 2008. DOI: 10.1103/PhysRevLett.100.058001. (Cit. on pp. 1, 3, 7).

[28]   J. Deseigne, S. Léonard, O. Dauchot and H. Chaté. Vibrated Polar Disks: Spontaneous Motion, Binary Collisions, and Collective Dynamics. *Soft Matter* **8**(20), 5629, 2012. DOI: 10.1039/c2sm25186h. (Cit. on pp. 1, 3, 46).

[29]   N. Kumar, H. Soni, S. Ramaswamy and A. K. Sood. Flocking at a distance in active granular matter. *Nature Communications* **5**(1), 4688, 2014. DOI: 10.1038/ncomms5688. (Cit. on p. 1).

[30]   L. Blanchoin, R. Boujemaa-Paterski, C. Sykes and J. Plastino. Actin Dynamics, Architecture, and Mechanics in Cell Motility. *Physiological Reviews* **94**(1), 235–263, 2014. DOI: 10.1152/physrev.00018.2013. (Cit. on pp. 1, 22, 30).

[31]   M. J. Shelley. The Dynamics of Microtubule/Motor-Protein Assemblies in Biology and Physics. *Annual Review of Fluid Mechanics* **48**(1), 487–506, 2016. DOI: 10.1146/annurev-fluid-010814-013639. (Cit. on p. 1).

[32]   D. Needleman and Z. Dogic. Active matter at the interface between materials science and cell biology. *Nature Reviews Materials* **2**(9), 17048, 2017. DOI: 10.1038/natrevmats.2017.48. (Cit. on pp. 1, 111).

[33]   S. Banerjee, M. L. Gardel and U. S. Schwarz. The Actin Cytoskeleton as an Active Adaptive Material. *Annual Review of Condensed Matter Physics* **11**(1), 421–439, 2020. DOI: 10.1146/annurev-conmatphys-031218-013231. (Cit. on p. 1).

[34]   I. D. Couzin and N. R. Franks. Self-Organized Lane Formation and Optimized Traffic Flow in Army Ants. *Proceedings of the Royal Society of London. Series B: Biological Sciences* **270**(1511), 139–146, 2003. DOI: 10.1098/rspb.2002.2210. (Cit. on pp. 1, 24).

[35]   J. Buhl, D. J. T. Sumpter, I. D. Couzin, J. J. Hale, E. Despland, E. R. Miller and S. J. Simpson. From Disorder to Order in Marching Locusts. *Science* **312**(5778), 1402–1406, 2006. DOI: 10.1126/science.1125142. (Cit. on p. 1).

[36]   A. Attanasi *et al.* Collective Behaviour without Collective Order in Wild Swarms of Midges. *PLoS Computational Biology* **10**(7), e1003697, 2014. DOI: 10.1371/journal.pcbi.1003697. (Cit. on p. 1).

[37]   F. Heppner. *Three-dimensional structure and dynamics of bird flocks*. Ed. by J. K. Parrish and W. M. Hamner. Cambridge University Press, 1997. Pp. 68–89. DOI: 10.1017/CBO9780511601156.005. (Cit. on p. 1).

[38]   M. Ballerini *et al.* Interaction Ruling Animal Collective Behavior Depends on Topological Rather than Metric Distance: Evidence from a Field Study. *Proceedings of the National Academy of Sciences* **105**(4), 1232–1237, 2008. DOI: 10.1073/pnas.0711437105. (Cit. on pp. 1, 3).

[39]   I. L. Bajec and F. H. Heppner. Organized flight in birds. *Animal Behaviour* **78**(4), 777–789, 2009. DOI: 10.1016/j.anbehav.2009.07.007. (Cit. on p. 1).

[40]   Y. Hayakawa. Spatiotemporal dynamics of skeins of wild geese. *EPL (Europhysics Letters)* **89**(4), 48004, 2010. DOI: 10.1209/0295-5075/89/48004. (Cit. on p. 1).

[41]   A. Attanasi *et al.* Information transfer and behavioural inertia in starling flocks. *Nature Physics* **10**(9), 691–696, 2014. DOI: 10.1038/nphys3035. (Cit. on p. 1).

[42]   J. K. Parrish, S. V. Viscido and D. Grünbaum. Self-Organized Fish Schools: An Examination of Emergent Properties. *The Biological Bulletin* **202**(3), 296–305, 2002. DOI: 10.2307/1543482. (Cit. on p. 1).

[43]  C. K. Hemelrijk and H. Kunz. Density distribution and size sorting in fish schools: an individual-based model. *Behavioral Ecology* **16**(1), 178–187, 2005. DOI: 10.1093/beheco/arh149. (Cit. on p. 1).

[44]  C. Becco, N. Vandewalle, J. Delcourt and P. Poncin. Experimental evidences of a structural and dynamical transition in fish school. *Physica A: Statistical Mechanics and its Applications* **367**, 487–493, 2006. DOI: 10.1016/j.physa.2005.11.041. (Cit. on p. 1).

[45]  A. J. W. Ward, D. J. T. Sumpter, I. D. Couzin, P. J. B. Hart and J. Krause. Quorum decision-making facilitates information transfer in fish shoals. *Proceedings of the National Academy of Sciences* **105**(19), 6948–6953, 2008. DOI: 10.1073/pnas.0710344105. (Cit. on p. 1).

[46]  M. Moussaïd, D. Helbing and G. Theraulaz. How simple rules determine pedestrian behavior and crowd disasters. *Proceedings of the National Academy of Sciences* **108**(17), 6884–6888, 2011. DOI: 10.1073/pnas.1016507108. (Cit. on p. 1).

[47]  J. L. Silverberg, M. Bierbaum, J. P. Sethna and I. Cohen. Collective Motion of Humans in Mosh and Circle Pits at Heavy Metal Concerts. *Physical Review Letters* **110**(22), 228701, 2013. DOI: 10.1103/PhysRevLett.110.228701. (Cit. on p. 1).

[48]  L. Giomi, M. J. Bowick, X. Ma and M. C. Marchetti. Defect Annihilation and Proliferation in Active Nematics. *Physical Review Letters* **110**(22), 228101, 2013. DOI: 10.1103/PhysRevLett.110.228101. (Cit. on pp. 1, 3, 16, 85).

[49]  F. C. Keber, E. Loiseau, T. Sanchez, S. J. DeCamp, L. Giomi, M. J. Bowick, M. C. Marchetti, Z. Dogic and A. R. Bausch. Topology and Dynamics of Active Nematic Vesicles. *Science* **345**(6201), 1135–1139, 2014. DOI: 10.1126/science.1254784. (Cit. on pp. 1, 3, 16, 85, 111).

[50]  S. J. DeCamp, G. S. Redner, A. Baskaran, M. F. Hagan and Z. Dogic. Orientational order of motile defects in active nematics. *Nature Materials* **14**(11), 1110–1115, 2015. DOI: 10.1038/nmat4387. (Cit. on pp. 1, 3, 16, 85).

[51]  G. A. Vliegenthart, A. Ravichandran, M. Ripoll, T. Auth and G. Gompper. Filamentous Active Matter: Band Formation, Bending, Buckling, and Defects. *Science Advances* **6**(30), eaaw9975, 2020. DOI: 10.1126/sciadv.aaw9975. (Cit. on pp. 1, 16, 85).

[52]  E. Lauga and T. R. Powers. The hydrodynamics of swimming microorganisms. *Reports on Progress in Physics* **72**(9), 096601, 2009. DOI: 10.1088/0034-4885/72/9/096601. (Cit. on p. 2).

[53]  M. T. Downton and H. Stark. Simulation of a model microswimmer. *Journal of Physics: Condensed Matter* **21**(20), 204101, 2009. DOI: 10.1088/0953-8984/21/20/204101. (Cit. on p. 2).

[54]  J. Elgeti, R. G. Winkler and G. Gompper. Physics of Microswimmers—Single Particle Motion and Collective Behavior: A Review. *Reports on Progress in Physics* **78**(5), 056601, 2015. DOI: 10.1088/0034-4885/78/5/056601. (Cit. on p. 2).

[55]  E. Lauga. Bacterial Hydrodynamics. *Annual Review of Fluid Mechanics* **48**(1), 105–130, 2016. DOI: 10.1146/annurev-fluid-122414-034606. (Cit. on p. 2).

[56]  R. G. Winkler and G. Gompper. *Hydrodynamics in Motile Active Matter*. Ed. by W. Andreoni and S. Yip. Springer International Publishing, Cham, 2020. Pp. 1471–1491. DOI: 10.1007/978-3-319-44677-6_35. (Cit. on p. 2).

[57] W. F. Paxton, K. C. Kistler, C. C. Olmeda, A. Sen, S. K. St. Angelo, Y. Cao, T. E. Mallouk, P. E. Lammert and V. H. Crespi. Catalytic Nanomotors: Autonomous Movement of Striped Nanorods. *Journal of the American Chemical Society* **126**(41), 13424–13431, 2004. DOI: 10.1021/ja047697z. (Cit. on p. 2).

[58] J. Palacci, B. Abécassis, C. Cottin-Bizonne, C. Ybert and L. Bocquet. Colloidal Motility and Pattern Formation under Rectified Diffusiophoresis. *Physical Review Letters* **104**(13), 138302, 2010. DOI: 10.1103/PhysRevLett.104.138302. (Cit. on p. 2).

[59] L. Giomi, M. J. Bowick, P. Mishra, R. Sknepnek and M. Cristina Marchetti. Defect dynamics in active nematics. *Philosophical Transactions of the Royal Society A: Mathematical, Physical and Engineering Sciences* **372**(2029), 20130365, 2014. DOI: 10.1098/rsta.2013.0365. (Cit. on p. 3).

[60] S. P. Thampi, R. Golestanian and J. M. Yeomans. Instabilities and topological defects in active nematics. *EPL (Europhysics Letters)* **105**(1), 18001, 2014. DOI: 10.1209/0295-5075/105/18001. (Cit. on p. 3).

[61] A. P. Solon and J. Tailleur. Revisiting the Flocking Transition Using Active Spins. *Phys. Rev. Lett.* **111**, 078101, 2013. DOI: 10.1103/PhysRevLett.111.078101. (Cit. on pp. 3, 14, 46, 58).

[62] A. P. Solon and J. Tailleur. Flocking with Discrete Symmetry: The Two-Dimensional Active Ising Model. *Physical Review E* **92**(4), 042119, 2015. DOI: 10.1103/PhysRevE.92.042119. (Cit. on pp. 3, 14, 46).

[63] A. P. Solon, H. Chaté and J. Tailleur. From Phase to Microphase Separation in Flocking Models: The Essential Role of Nonequilibrium Fluctuations. *Phys. Rev. Lett.* **114**, 068101, 2015. DOI: 10.1103/PhysRevLett.114.068101. (Cit. on pp. 3, 6, 14, 46, 58, 59).

[64] Y. Fily and M. C. Marchetti. Athermal Phase Separation of Self-Propelled Particles with No Alignment. *Physical Review Letters* **108**(23), 235702, 2012. DOI: 10.1103/PhysRevLett.108.235702. (Cit. on p. 3).

[65] G. S. Redner, M. F. Hagan and A. Baskaran. Structure and Dynamics of a Phase-Separating Active Colloidal Fluid. *Physical Review Letters* **110**(5), 055701, 2013. DOI: 10.1103/PhysRevLett.110.055701. (Cit. on p. 3).

[66] I. Buttinoni, J. Bialké, F. Kümmel, H. Löwen, C. Bechinger and T. Speck. Dynamical Clustering and Phase Separation in Suspensions of Self-Propelled Colloidal Particles. *Physical Review Letters* **110**(23), 238301, 2013. DOI: 10.1103/PhysRevLett.110.238301. (Cit. on p. 3).

[67] S. Paliwal, J. Rodenburg, R. van Roij and M. Dijkstra. Chemical potential in active systems: predicting phase equilibrium from bulk equations of state? *New Journal of Physics* **20**(1), 015003, 2018. DOI: 10.1088/1367-2630/aa9b4d. (Cit. on p. 3).

[68] P. Digregorio, D. Levis, A. Suma, L. F. Cugliandolo, G. Gonnella and I. Pagonabarraga. Full Phase Diagram of Active Brownian Disks: From Melting to Motility-Induced Phase Separation. *Physical Review Letters* **121**(9), 098003, 2018. DOI: 10.1103/PhysRevLett.121.098003. (Cit. on p. 3).

[69] X.-q. Shi and H. Chaté. Self-Propelled Rods: Linking Alignment-Dominated and Repulsion-Dominated Active Matter. 2018. arXiv: 1807.00294. (Cit. on pp. 3, 6, 14, 46, 59).

[70] R. van Damme, J. Rodenburg, R. van Roij and M. Dijkstra. Interparticle torques suppress motility-induced phase separation for rodlike particles. *The Journal of Chemical Physics* **150**(16), 164501, 2019. DOI: 10.1063/1.5086733. (Cit. on p. 3).

[71]   R. Großmann, I. S. Aranson and F. Peruani. A Particle-Field Approach Bridges Phase Separation and Collective Motion in Active Matter. *Nat Commun* **11**(1), 5365, 2020. DOI: 10.1038/s41467-020-18978-5. (Cit. on pp. 3, 7, 13, 61, 87, 129).

[72]   A. Jayaram, A. Fischer and T. Speck. From scalar to polar active matter: Connecting simulations with mean-field theory. *Physical Review E* **101**(2), 022602, 2020. DOI: 10.1103/PhysRevE.101.022602. (Cit. on p. 3).

[73]   R. Wittkowski, A. Tiribocchi, J. Stenhammar, R. J. Allen, D. Marenduzzo and M. E. Cates. Scalar $\varphi^4$ field theory for active-particle phase separation. *Nature Communications* **5**(1), 4351, 2014. DOI: 10.1038/ncomms5351. (Cit. on p. 3).

[74]   M. E. Cates and J. Tailleur. Motility-Induced Phase Separation. *Annual Review of Condensed Matter Physics* **6**(1), 219–244, 2015. DOI: 10.1146/annurev-conmatphys-031214-014710. (Cit. on pp. 3, 96).

[75]   T. Speck, A. M. Menzel, J. Bialké and H. Löwen. Dynamical Mean-Field Theory and Weakly Non-Linear Analysis for the Phase Separation of Active Brownian Particles. *The Journal of Chemical Physics* **142**(22), 224109, 2015. DOI: 10.1063/1.4922324. (Cit. on p. 3).

[76]   A. P. Solon, J. Stenhammar, M. E. Cates, Y. Kafri and J. Tailleur. Generalized Thermodynamics of Phase Equilibria in Scalar Active Matter. *Physical Review E* **97**(2), 020602, 2018. DOI: 10.1103/PhysRevE.97.020602. (Cit. on p. 3).

[77]   F. Ginelli and H. Chaté. Relevance of Metric-Free Interactions in Flocking Phenomena. *Physical Review Letters* **105**(16) Publisher: American Physical Society, 168103, 2010. DOI: 10.1103/PhysRevLett.105.168103. (Cit. on p. 3).

[78]   A. Peshkov, S. Ngo, E. Bertin, H. Chaté and F. Ginelli. Continuous Theory of Active Matter Systems with Metric-Free Interactions. *Physical Review Letters* **109**(9), 2012. DOI: 10.1103/PhysRevLett.109.098101. (Cit. on p. 3).

[79]   Y.-L. Chou, R. Wolfe and T. Ihle. Kinetic theory for systems of self-propelled particles with metric-free interactions. *Physical Review E* **86**(2) Publisher: American Physical Society, 021120, 2012. DOI: 10.1103/PhysRevE.86.021120. (Cit. on p. 3).

[80]   D. Martin, H. Chaté, C. Nardini, A. Solon, J. Tailleur and F. Van Wijland. Fluctuation-Induced Phase Separation in Metric and Topological Models of Collective Motion. *Physical Review Letters* **126**(14), 148001, 2021. DOI: 10.1103/PhysRevLett.126.148001. (Cit. on p. 3).

[81]   P. Rahmani, F. Peruani and P. Romanczuk. Topological flocking models in spatially heterogeneous environments. *Communications Physics* **4**(1), 2021. DOI: 10.1038/s42005-021-00708-y. (Cit. on pp. 3, 17).

[82]   V. Schaller, C. Weber, E. Frey and A. R. Bausch. Polar Pattern Formation: Hydrodynamic Coupling of Driven Filaments. *Soft Matter* **7**(7), 3213, 2011. DOI: 10.1039/c0sm01063d. (Cit. on pp. 3, 38).

[83]   J. Toner and Y. Tu. Long-Range Order in a Two-Dimensional Dynamical XY Model: How Birds Fly Together. *Physical Review Letters* **75**(23), 4326–4329, 1995. DOI: 10.1103/PhysRevLett.75.4326. (Cit. on pp. 4, 8, 10).

[84]   E. Bertin, M. Droz and G. Grégoire. Boltzmann and hydrodynamic description for self-propelled particles. *Phys. Rev. E* **74**, 022101, 2006. DOI: 10.1103/PhysRevE.74.022101. (Cit. on pp. 4, 9, 10, 14, 22, 38, 46, 58).

[85] H. Chaté, F. Ginelli, G. Grégoire and F. Raynaud. Collective motion of self-propelled particles interacting without cohesion. *Phys. Rev. E* **77**, 046113, 2008. DOI: 10.1103/PhysRevE.77.046113. (Cit. on pp. 4, 6, 10, 14, 38, 46, 58, 59).

[86] F. Ginelli, F. Peruani, M. Bär and H. Chaté. Large-Scale Collective Properties of Self-Propelled Rods. *Phys. Rev. Lett.* **104**, 184502, 2010. DOI: 10.1103/PhysRevLett.104.184502. (Cit. on pp. 4, 6–8, 10, 16, 22, 38, 61, 86–88, 92).

[87] S. Ngo, F. Ginelli and H. Chaté. Competing Ferromagnetic and Nematic Alignment in Self-Propelled Polar Particles. *Physical Review E* **86**(5), 2012. DOI: 10.1103/PhysRevE.86.050101. (Cit. on pp. 4, 6, 8, 10, 16, 22, 29, 40, 86, 87).

[88] A. Peshkov, I. S. Aranson, E. Bertin, H. Chaté and F. Ginelli. Nonlinear Field Equations for Aligning Self-Propelled Rods. *Phys. Rev. Lett.* **109**, 268701, 2012. DOI: 10.1103/PhysRevLett.109.268701. (Cit. on pp. 4, 8–10, 16, 38, 61, 86–88, 91).

[89] A. Peshkov, E. Bertin, F. Ginelli and H. Chaté. Boltzmann-Ginzburg-Landau Approach for Continuous Descriptions of Generic Vicsek-like Models. *The European Physical Journal Special Topics* **223**(7), 1315–1344, 2014. DOI: 10.1140/epjst/e2014-02193-y. (Cit. on pp. 4, 9, 10, 46, 91).

[90] B. Mahault, X.-c. Jiang, E. Bertin, Y.-q. Ma, A. Patelli, X.-q. Shi and H. Chaté. Self-Propelled Particles with Velocity Reversals and Ferromagnetic Alignment: Active Matter Class with Second-Order Transition to Quasi-Long-Range Polar Order. *Physical Review Letters* **120**(25), 2018. DOI: 10.1103/PhysRevLett.120.258002. (Cit. on pp. 4, 10).

[91] T. Vicsek, A. Czirók, E. Ben-Jacob, I. Cohen and O. Shochet. Novel Type of Phase Transition in a System of Self-Driven Particles. *Physical Review Letters* **75**(6), 1226–1229, 1995. DOI: 10.1103/PhysRevLett.75.1226. (Cit. on pp. 4, 6, 22).

[92] C. W. Reynolds. Flocks, Herds and Schools: A Distributed Behavioral Model. *SIGGRAPH Comput. Graph.* **21**(4), 25–34, 1987. DOI: 10.1145/37402.37406. (Cit. on p. 4).

[93] I. Aoki. A Simulation Study on the Schooling Mechanism in Fish. *Bulletin of the Japanese Society of Scientific Fisheries* **48**(8), 1081–1088, 1982. DOI: 10.2331/suisan.48.1081. (Cit. on p. 4).

[94] A. P. Solon, J.-B. Caussin, D. Bartolo, H. Chaté and J. Tailleur. Pattern formation in flocking models: A hydrodynamic description. *Phys. Rev. E* **92**, 062111, 2015. DOI: 10.1103/PhysRevE.92.062111. (Cit. on pp. 4, 6, 14, 46).

[95] O. Chepizhko, D. Saintillan and F. Peruani. Revisiting the emergence of order in active matter. *Soft Matter* **17**(11), 3113–3120, 2021. DOI: 10.1039/D0SM01220C. (Cit. on p. 4).

[96] G. Grégoire and H. Chaté. Onset of Collective and Cohesive Motion. *Phys. Rev. Lett.* **92**, 025702, 2004. DOI: 10.1103/PhysRevLett.92.025702. (Cit. on pp. 6, 14, 22, 46, 58).

[97] M. Nagy, I. Daruka and T. Vicsek. New aspects of the continuous phase transition in the scalar noise model (SNM) of collective motion. *Physica A: Statistical Mechanics and its Applications* **373**, 445–454, 2007. DOI: 10.1016/j.physa.2006.05.035. (Cit. on p. 6).

[98] J.-B. Caussin, A. Solon, A. Peshkov, H. Chaté, T. Dauxois, J. Tailleur, V. Vitelli and D. Bartolo. Emergent Spatial Structures in Flocking Models: A Dynamical System Insight. *Physical Review Letters* **112**(14), 148102, 2014. DOI: 10.1103/PhysRevLett.112.148102. (Cit. on pp. 6, 14, 46, 58).

[99]    S. Ngo, A. Peshkov, I. S. Aranson, E. Bertin, F. Ginelli and H. Chaté. Large-Scale Chaos
        and Fluctuations in Active Nematics. *Phys. Rev. Lett.* **113**, 038302, 2014. DOI: 10.1103/
        PhysRevLett.113.038302. (Cit. on pp. 6, 8, 10, 16, 22, 27, 61, 86–88, 92).

[100]   L.-b. Cai, H. Chaté, Y.-q. Ma and X.-q. Shi. Dynamical subclasses of dry active nematics.
        *Physical Review E* **99**(1), 010601, 2019. DOI: 10.1103/PhysRevE.99.010601. (Cit. on pp. 6,
        8, 16).

[101]   F. Peruani, A. Deutsch and M. Bär. Nonequilibrium clustering of self-propelled rods. *Phys.
        Rev. E* **74**, 030904, 2006. DOI: 10.1103/PhysRevE.74.030904. (Cit. on pp. 7, 8, 12, 15, 48,
        56, 57, 59).

[102]   F. Thüroff, C. A. Weber and E. Frey. Critical Assessment of the Boltzmann Approach to
        Active Systems. *Physical Review Letters* **111**(19), 190601, 2013. DOI: 10.1103/PhysRevLett.
        111.190601. (Cit. on pp. 7, 9).

[103]   S. Zhou, A. Sokolov, O. D. Lavrentovich and I. S. Aranson. Living liquid crystals. *Proceedings of
        the National Academy of Sciences* **111**(4), 1265–1270, 2014. DOI: 10.1073/pnas.1321926111.
        (Cit. on pp. 7, 112).

[104]   S. Thutupalli, M. Sun, F. Bunyak, K. Palaniappan and J. W. Shaevitz. Directional reversals
        enable *Myxococcus xanthus* cells to produce collective one-dimensional streams during
        fruiting-body formation. *Journal of The Royal Society Interface* **12**(109), 20150049, 2015.
        DOI: 10.1098/rsif.2015.0049. (Cit. on p. 7).

[105]   D. Nishiguchi, K. H. Nagai, H. Chaté and M. Sano. Long-Range Nematic Order and Anomalous
        Fluctuations in Suspensions of Swimming Filamentous Bacteria. *Physical Review E* **95**(2),
        2017. DOI: 10.1103/PhysRevE.95.020601. (Cit. on pp. 7, 8, 22, 87).

[106]   S. Tanida, K. Furuta, K. Nishikawa, T. Hiraiwa, H. Kojima, K. Oiwa and M. Sano. Gliding
        filament system giving both global orientational order and clusters in collective motion.
        *Physical Review E* **101**(3), 032607, 2020. DOI: 10.1103/PhysRevE.101.032607. (Cit. on
        p. 7).

[107]   Y. Yang, V. Marceau and G. Gompper. Swarm behavior of self-propelled rods and swimming
        flagella. *Phys. Rev. E* **82**, 031904, 2010. DOI: 10.1103/PhysRevE.82.031904. (Cit. on pp. 8,
        12, 48).

[108]   M. Abkenar, K. Marx, T. Auth and G. Gompper. Collective Behavior of Penetrable Self-
        Propelled Rods in Two Dimensions. *Physical Review E* **88**(6), 062314, 2013. DOI: 10.1103/
        PhysRevE.88.062314. (Cit. on pp. 8, 12, 62).

[109]   H.-S. Kuan, R. Blackwell, L. E. Hough, M. A. Glaser and M. D. Betterton. Hysteresis, Reen-
        trance, and Glassy Dynamics in Systems of Self-Propelled Rods. *Physical Review E* **92**(6),
        060501, 2015. DOI: 10.1103/PhysRevE.92.060501. (Cit. on pp. 8, 12).

[110]   S. Weitz, A. Deutsch and F. Peruani. Self-Propelled Rods Exhibit a Phase-Separated State
        Characterized by the Presence of Active Stresses and the Ejection of Polar Clusters. *Physical
        Review E* **92**(1), 012322, 2015. DOI: 10.1103/PhysRevE.92.012322. (Cit. on pp. 8, 12).

[111]   R. E. Isele-Holder, J. Elgeti and G. Gompper. Self-Propelled Worm-like Filaments: Spontan-
        eous Spiral Formation, Structure, and Dynamics. *Soft Matter* **11**(36), 7181–7190, 2015.
        DOI: 10.1039/C5SM01683E. (Cit. on p. 8).

[112]   Ö. Duman, R. E. Isele-Holder, J. Elgeti and G. Gompper. Collective dynamics of self-propelled
        semiflexible filaments. *Soft Matter* **14**(22), 4483–4494, 2018. DOI: 10.1039/C8SM00282G.
        (Cit. on pp. 8, 12, 48).

[113] J. M. Moore, T. N. Thompson, M. A. Glaser and M. D. Betterton. Collective motion of driven semiflexible filaments tuned by soft repulsion and stiffness. *Soft Matter* **16**(41), 9436–9442, 2020. DOI: 10.1039/D0SM01036G. (Cit. on pp. 8, 12).

[114] M. R. Shaebani, A. Wysocki, R. G. Winkler, G. Gompper and H. Rieger. Computational models for active matter. *Nature Reviews Physics* **2**(4), 181–199, 2020. DOI: 10.1038/s42254-020-0152-1. (Cit. on p. 8).

[115] J. Toner and Y. Tu. Flocks, Herds, and Schools: A Quantitative Theory of Flocking. *Physical Review E* **58**(4), 4828–4858, 1998. DOI: 10.1103/PhysRevE.58.4828. (Cit. on pp. 8, 22).

[116] P. Degond and S. Motsch. Continuum limit of self-driven particles with orientation interaction. *Mathematical Models and Methods in Applied Sciences* **18**(supp01), 1193–1215, 2008. DOI: 10.1142/S0218202508003005. (Cit. on p. 9).

[117] A. Baskaran and M. C. Marchetti. Enhanced Diffusion and Ordering of Self-Propelled Rods. *Physical Review Letters* **101**(26), 2008. DOI: 10.1103/PhysRevLett.101.268101. (Cit. on p. 9).

[118] A. Baskaran and M. C. Marchetti. Hydrodynamics of Self-Propelled Hard Rods. *Physical Review E* **77**(1), 011920, 2008. DOI: 10.1103/PhysRevE.77.011920. (Cit. on pp. 9, 22).

[119] A. Baskaran and M. Cristina Marchetti. Nonequilibrium Statistical Mechanics of Self-Propelled Hard Rods. *Journal of Statistical Mechanics: Theory and Experiment* **2010**(04), P04019, 2010. DOI: 10.1088/1742-5468/2010/04/P04019. (Cit. on pp. 9, 90).

[120] F. D. C. Farrell, M. C. Marchetti, D. Marenduzzo and J. Tailleur. Pattern Formation in Self-Propelled Particles with Density-Dependent Motility. *Phys. Rev. Lett.* **108**, 248101, 2012. DOI: 10.1103/PhysRevLett.108.248101. (Cit. on pp. 9, 46).

[121] P. Romanczuk and L. Schimansky-Geier. Mean-field theory of collective motion due to velocity alignment. *Ecological Complexity* **10**, 83–92, 2012. DOI: 10.1016/j.ecocom.2011.07.008. (Cit. on p. 9).

[122] R. Großmann, L. Schimansky-Geier and P. Romanczuk. Active Brownian particles with velocity-alignment and active fluctuations. *New Journal of Physics* **14**(7), 073033, 2012. DOI: 10.1088/1367-2630/14/7/073033. (Cit. on p. 9).

[123] R. Großmann, L. Schimansky-Geier and P. Romanczuk. Self-Propelled Particles with Selective Attraction–Repulsion Interaction: From Microscopic Dynamics to Coarse-Grained Theories. *New Journal of Physics* **15**(8), 085014, 2013. DOI: 10.1088/1367-2630/15/8/085014. (Cit. on pp. 9, 46).

[124] I. Maryshev, A. B. Goryachev, D. Marenduzzo and A. Morozov. Dry active turbulence in a model for microtubule–motor mixtures. *Soft Matter* **15**(30), 6038–6043, 2019. DOI: 10.1039/C9SM00558G. (Cit. on pp. 9, 16, 17, 86–88, 91, 92, 96, 97, 110, 122).

[125] E. Bertin, M. Droz and G. Grégoire. Hydrodynamic equations for self-propelled particles: microscopic derivation and stability analysis. *Journal of Physics A: Mathematical and Theoretical* **42**(44), 445001, 2009. DOI: 10.1088/1751-8113/42/44/445001. (Cit. on pp. 9, 46).

[126] E. Bertin, A. Baskaran, H. Chaté and M. C. Marchetti. Comparison between Smoluchowski and Boltzmann Approaches for Self-Propelled Rods. *Physical Review E* **92**(4), 2015. DOI: 10.1103/PhysRevE.92.042141. (Cit. on p. 9).

[127]   F. Thüroff, C. A. Weber and E. Frey. Numerical Treatment of the Boltzmann Equation for Self-Propelled Particle Systems. *Physical Review X* **4**(4), 041030, 2014. DOI: 10.1103/PhysRevX.4.041030. (Cit. on pp. 9, 38, 46, 58).

[128]   J. Denk, L. Huber, E. Reithmann and E. Frey. Active Curved Polymers Form Vortex Patterns on Membranes. *Physical Review Letters* **116**(17), 178301, 2016. DOI: 10.1103/PhysRevLett.116.178301. (Cit. on pp. 9, 22, 61).

[129]   J. Denk and E. Frey. Pattern-Induced Local Symmetry Breaking in Active-Matter Systems. *Proc Natl Acad Sci USA* **117**(50), 31623–31630, 2020. DOI: 10.1073/pnas.2010302117. (Cit. on pp. 9, 13, 61, 86, 87, 96, 129).

[130]   R. E. Isele-Holder, J. Elgeti and G. Gompper. Self-Propelled Worm-like Filaments: Spontaneous Spiral Formation, Structure, and Dynamics. *Soft Matter* **11**(36), 7181–7190, 2015. DOI: 10.1039/C5SM01683E. (Cit. on p. 12).

[131]   M. Bär, R. Großmann, S. Heidenreich and F. Peruani. Self-Propelled Rods: Insights and Perspectives for Active Matter. *Annual Review of Condensed Matter Physics* **11**(1), null, 2020. DOI: 10.1146/annurev-conmatphys-031119-050611. (Cit. on p. 14).

[132]   C. A. Weber, V. Schaller, A. R. Bausch and E. Frey. Nucleation-induced transition to collective motion in active systems. *Phys. Rev. E* **86**, 030901, 2012. DOI: 10.1103/PhysRevE.86.030901. (Cit. on pp. 14, 46).

[133]   F. Peruani, L. Schimansky-Geier and M. Bär. Cluster Dynamics and Cluster Size Distributions in Systems of Self-Propelled Particles. *The European Physical Journal Special Topics* **191**(1), 173–185, 2010. DOI: 10.1140/epjst/e2010-01349-1. (Cit. on pp. 15, 48, 56, 57, 59).

[134]   F. Peruani and M. Bär. A Kinetic Model and Scaling Properties of Non-Equilibrium Clustering of Self-Propelled Particles. *New Journal of Physics* **15**(6), 065009, 2013. DOI: 10.1088/1367-2630/15/6/065009. (Cit. on pp. 15, 48, 56, 57, 59, 80).

[135]   R. Großmann, F. Peruani and M. Bär. Mesoscale Pattern Formation of Self-Propelled Rods with Velocity Reversal. *Physical Review E* **94**(5), 050602, 2016. DOI: 10.1103/PhysRevE.94.050602. (Cit. on pp. 16, 86–88, 92).

[136]   I. Maryshev, A. Morozov, A. B. Goryachev and D. Marenduzzo. Pattern formation in active model C with anchoring: bands, aster networks, and foams. *Soft Matter* **16**(38), 8775–8781, 2020. DOI: 10.1039/d0sm00927j. (Cit. on pp. 16, 17, 86–88, 91, 92, 96, 97, 110, 126).

[137]   H. H. Wensink and H. Löwen. Aggregation of self-propelled colloidal rods near confining walls. *Physical Review E* **78**(3), 031409, 2008. DOI: 10.1103/PhysRevE.78.031409. (Cit. on p. 17).

[138]   P. Galajda, J. Keymer, P. Chaikin and R. Austin. A Wall of Funnels Concentrates Swimming Bacteria. *Journal of Bacteriology* **189**(23), 8704–8707, 2007. DOI: 10.1128/JB.01033-07. (Cit. on p. 17).

[139]   A. Kaiser, H. H. Wensink and H. Löwen. How to Capture Active Particles. *Physical Review Letters* **108**(26), 268307, 2012. DOI: 10.1103/PhysRevLett.108.268307. (Cit. on p. 17).

[140]   C. Peng, T. Turiv, Y. Guo, Q.-H. Wei and O. D. Lavrentovich. Command of active matter by topological defects and patterns. *Science* **354**(6314), 882–885, 2016. DOI: 10.1126/science.aah6936. (Cit. on p. 17).

[141]   M. M. Genkin, A. Sokolov, O. D. Lavrentovich and I. S. Aranson. Topological Defects in a Living Nematic Ensnare Swimming Bacteria. *Physical Review X* **7**(1), 011029, 2017. DOI: 10.1103/PhysRevX.7.011029. (Cit. on pp. 17, 97, 112, 122, 125).

[142]  T. Turiv *et al.* Polar jets of swimming bacteria condensed by a patterned liquid crystal. *Nature Physics* **16**(4), 481–487, 2020. DOI: 10.1038/s41567-020-0793-0. (Cit. on pp. 17, 112, 122, 123, 126).

[143]  J. Deseigne, O. Dauchot and H. Chaté. Collective Motion of Vibrated Polar Disks. *Physical Review Letters* **105**(9), 098001, 2010. DOI: 10.1103/PhysRevLett.105.098001. (Cit. on pp. 21, 22, 46).

[144]  I. Buttinoni, J. Bialké, F. Kümmel, H. Löwen, C. Bechinger and T. Speck. Dynamical Clustering and Phase Separation in Suspensions of Self-Propelled Colloidal Particles. *Phys. Rev. Lett.* **110**, 238301, 2013. DOI: 10.1103/PhysRevLett.110.238301. (Cit. on p. 21).

[145]  D. Inoue, B. Mahmot, A. M. R. Kabir, T. I. Farhana, K. Tokuraku, K. Sada, A. Konagaya and A. Kakugo. Depletion Force Induced Collective Motion of Microtubules Driven by Kinesin. *Nanoscale* **7**(43), 18054–18061, 2015. DOI: 10.1039/C5NR02213D. (Cit. on pp. 21, 22, 24).

[146]  K. Kawaguchi, R. Kageyama and M. Sano. Topological Defects Control Collective Dynamics in Neural Progenitor Cell Cultures. *Nature* **545**(7654), 327–331, 2017. DOI: 10.1038/nature22321. (Cit. on pp. 21, 30, 85).

[147]  T. B. Saw, A. Doostmohammadi, V. Nier, L. Kocgozlu, S. Thampi, Y. Toyama, P. Marcq, C. T. Lim, J. M. Yeomans and B. Ladoux. Topological Defects in Epithelia Govern Cell Death and Extrusion. *Nature* **544**(7649), 212–216, 2017. DOI: 10.1038/nature21718. (Cit. on pp. 21, 30, 111).

[148]  J. Tailleur and M. E. Cates. Statistical Mechanics of Interacting Run-and-Tumble Bacteria. *Phys. Rev. Lett.* **100**, 218103, 2008. DOI: 10.1103/PhysRevLett.100.218103. (Cit. on p. 21).

[149]  Y. Fily and M. C. Marchetti. Athermal Phase Separation of Self-Propelled Particles with No Alignment. *Phys. Rev. Lett.* **108**, 235702, 2012. DOI: 10.1103/PhysRevLett.108.235702. (Cit. on p. 21).

[150]  M. Loose and T. J. Mitchison. The Bacterial Cell Division Proteins FtsA and FtsZ Self-Organize into Dynamic Cytoskeletal Patterns. *Nature Cell Biology* **16**(1), 38–46, 2014. DOI: 10.1038/ncb2885. (Cit. on pp. 22, 61).

[151]  K. H. Nagai, Y. Sumino, R. Montagne, I. S. Aranson and H. Chaté. Collective Motion of Self-Propelled Particles with Memory. *Physical Review Letters* **114**(16), 2015. DOI: 10.1103/PhysRevLett.114.168001. (Cit. on pp. 22, 27, 86, 87, 97).

[152]  R. Aditi Simha and S. Ramaswamy. Hydrodynamic Fluctuations and Instabilities in Ordered Suspensions of Self-Propelled Particles. *Phys. Rev. Lett.* **89**, 058101, 2002. DOI: 10.1103/PhysRevLett.89.058101. (Cit. on pp. 22, 96, 126).

[153]  T. B. Liverpool and M. C. Marchetti. Instabilities of Isotropic Solutions of Active Polar Filaments. *Physical Review Letters* **90**(13), 2003. DOI: 10.1103/PhysRevLett.90.138102. (Cit. on p. 22).

[154]  K. Kruse, J. F. Joanny, F. Jülicher, J. Prost and K. Sekimoto. Asters, Vortices, and Rotating Spirals in Active Gels of Polar Filaments. *Phys. Rev. Lett.* **92**, 078101, 2004. DOI: 10.1103/PhysRevLett.92.078101. (Cit. on p. 22).

[155]  S. Mishra, A. Baskaran and M. C. Marchetti. Fluctuations and pattern formation in self-propelled particles. *Phys. Rev. E* **81**, 061916, 2010. DOI: 10.1103/PhysRevE.81.061916. (Cit. on pp. 22, 46).

[156]   D. A. Fletcher and P. L. Geissler. Active Biological Materials. *Annual Review of Physical Chemistry* **60**(1) PMID: 18999991, 469–486, 2009. DOI: 10.1146/annurev.physchem.040808.090304. eprint: https://doi.org/10.1146/annurev.physchem.040808.090304. (Cit. on pp. 22, 30).

[157]   M. P. Sheetz, R. Chasan and J. A. Spudich. ATP-Dependent Movement of Myosin in Vitro: Characterization of a Quantitative Assay. *The Journal of Cell Biology* **99**(5), 1867–1871, 1984. (Cit. on pp. 22, 47, 86).

[158]   T. Yanagida, M. Nakase, K. Nishiyama and F. Oosawa. Direct Observation of Motion of Single F-Actin Filaments in the Presence of Myosin. *Nature* **307**(5946), 58–60, 1984. DOI: 10.1038/307058a0. (Cit. on p. 22).

[159]   *Online Supplemental Material for "Emergence of coexisting ordered states in active matter systems" at https://www.science.org/doi/10.1126/science.aao5434.* (Cit. on pp. 24, 25, 27, 29, 33, 38).

[160]   S. MacLean-Fletcher and T. D. Pollard. Identification of a factor in conventional muscle actin preparations which inhibits actin filament self-association. *Biochemical and Biophysical Research Communications* **96**(1), 18–27, 1980. DOI: https://doi.org/10.1016/0006-291X(80)91175-4. (Cit. on p. 30).

[161]   J. A. Spudich and S. Watt. The Regulation of Rabbit Skeletal Muscle Contraction. I. Biochemical Studies of the Interaction of the Tropomyosin-Troponin Complex with Actin and the Proteolytic Fragments of Myosin. *The Journal of Biological Chemistry* **246**(15), 4866–4871, 1971. (Cit. on p. 30).

[162]   S. J. Kron, Y. Y. Toyoshima, T. Q. Uyeda and J. A. Spudich. [33] Assays for Actin Sliding Movement over Myosin-Coated Surfaces. en. *Methods in Enzymology*. Vol. 196. Elsevier, 1991, pp. 399–416. DOI: 10.1016/0076-6879(91)96035-P. (Cit. on p. 30).

[163]   J. Howard. *Mechanics of Motor Proteins and the Cytoskeleton*. Sinauer Associates, Publishers, Sunderland, Mass, 2001. (Cit. on p. 32).

[164]   D.-B. Wang, F.-B. Hsiao, C.-H. Chuang and Y.-C. Lee. Algorithm Optimization in Molecular Dynamics Simulation. *Computer Physics Communications* **177**(7), 551–559, 2007. DOI: 10.1016/j.cpc.2007.05.009. (Cit. on pp. 37, 66).

[165]   F. Peruani, F. Ginelli, M. Bär and H. Chaté. Polar vs. Apolar Alignment in Systems of Polar Self-Propelled Particles. *Journal of Physics: Conference Series* **297**, 012014, 2011. DOI: 10.1088/1742-6596/297/1/012014. (Cit. on p. 38).

[166]   H. H. Wensink, J. Dunkel, S. Heidenreich, K. Drescher, R. E. Goldstein, H. Löwen and J. M. Yeomans. Meso-Scale Turbulence in Living Fluids. *Proceedings of the National Academy of Sciences* **109**(36), 14308–14313, 2012. DOI: 10.1073/pnas.1202032109. (Cit. on p. 40).

[167]   A. Kaiser, A. Snezhko and I. S. Aranson. Flocking Ferromagnetic Colloids. *Science Advances* **3**(2), e1601469, 2017. DOI: 10.1126/sciadv.1601469. (Cit. on p. 46).

[168]   C. A. Weber, T. Hanke, J. Deseigne, S. Léonard, O. Dauchot, E. Frey and H. Chaté. Long-Range Ordering of Vibrated Polar Disks. *Physical Review Letters* **110**(20), 208001, 2013. DOI: 10.1103/PhysRevLett.110.208001. (Cit. on p. 46).

[169]   K.-D. N. T. Lam, M. Schindler and O. Dauchot. Self-Propelled Hard Disks: Implicit Alignment and Transition to Collective Motion. *New Journal of Physics* **17**(11), 113056, 2015. DOI: 10.1088/1367-2630/17/11/113056. (Cit. on p. 46).

[170] T. Ihle. Kinetic theory of flocking: Derivation of hydrodynamic equations. *Phys. Rev. E* **83**, 030901(R), 2011. DOI: 10.1103/PhysRevE.83.030901. (Cit. on p. 46).

[171] A. Gopinath, M. F. Hagan, M. C. Marchetti and A. Baskaran. Dynamical self-regulation in self-propelled particle flows. *Phys. Rev. E* **85**, 061903, 2012. DOI: 10.1103/PhysRevE.85.061903. (Cit. on p. 46).

[172] T. Ihle. Invasion-wave-induced first-order phase transition in systems of active particles. *Phys. Rev. E* **88**, 040303(R), 2013. DOI: 10.1103/PhysRevE.88.040303. (Cit. on p. 46).

[173] G. Grégoire, H. Chaté and Y. Tu. Moving and Staying Together without a Leader. *Physica D: Nonlinear Phenomena* **181**(3-4), 157–170, 2003. DOI: 10.1016/S0167-2789(03)00102-7. (Cit. on pp. 46, 58).

[174] A. Morin and D. Bartolo. Flowing Active Liquids in a Pipe: Hysteretic Response of Polar Flocks to External Fields. *Phys. Rev. X* **8**, 021037, 2018. DOI: 10.1103/PhysRevX.8.021037. (Cit. on pp. 46, 58).

[175] *Online Supplemental Material for "Microphase separation in active filament systems is maintained by cyclic dynamics of cluster size and order" at http://link.aps.org/supplemental/10.1103/PhysRevResearch.3.013280.* (Cit. on pp. 48, 50–52).

[176] C. Huepe and M. Aldana. Intermittency and Clustering in a System of Self-Driven Particles. *Phys. Rev. Lett.* **92**, 168701, 2004. DOI: 10.1103/PhysRevLett.92.168701. (Cit. on p. 48).

[177] H. P. Zhang, A. Be'er, E. L. Florin and H. L. Swinney. Collective Motion and Density Fluctuations in Bacterial Colonies. *Proceedings of the National Academy of Sciences* **107**(31), 13626–13630, 2010. DOI: 10.1073/pnas.1001651107. (Cit. on p. 48).

[178] Y. Fily, S. Henkes and M. C. Marchetti. Freezing and Phase Separation of Self-Propelled Disks. *Soft Matter* **10**(13), 2132–2140, 2014. DOI: 10.1039/C3SM52469H. (Cit. on p. 48).

[179] R. P. Sear. Nucleation: theory and applications to protein solutions and colloidal suspensions. *Journal of Physics: Condensed Matter* **19**(3), 033101, 2007. DOI: 10.1088/0953-8984/19/3/033101. (Cit. on pp. 50, 70).

[180] V. I. Kalikmanov. *Nucleation theory*. Lecture notes in physics v. 860. Springer, Dordrecht ; London, 2013. 316 pp. (Cit. on pp. 50, 70).

[181] M. v. Smoluchowski. Versuch Einer Mathematischen Theorie Der Koagulationskinetik Kolloider Lösungen. *Zeitschrift für Physikalische Chemie* **92U**(1), 129–168, 1918. DOI: https://doi.org/10.1515/zpch-1918-9209. (Cit. on p. 56).

[182] S. Chandrasekhar. Stochastic Problems in Physics and Astronomy. *Reviews of Modern Physics* **15**(1), 1–89, 1943. DOI: 10.1103/RevModPhys.15.1. (Cit. on p. 56).

[183] P. L. Krapivsky, S. Redner and E. Ben-Naim. *A Kinetic View of Statistical Physics*. Cambridge University Press, Cambridge; New York, 2010. (Cit. on p. 56).

[184] L. Dagum and R. Menon. OpenMP: an industry standard API for shared-memory programming. *Computational Science & Engineering, IEEE* **5**(1), 46–55, 1998. DOI: 10.1109/99.660313. (Cit. on p. 66).

[185] T. Nemoto, F. Bouchet, R. L. Jack and V. Lecomte. Population-dynamics method with a multicanonical feedback control. *Phys. Rev. E* **93**, 062123, 2016. DOI: 10.1103/PhysRevE.93.062123. (Cit. on p. 73).

[186] S. Whitelam, K. Klymko and D. Mandal. Phase Separation and Large Deviations of Lattice Active Matter. *The Journal of Chemical Physics* **148**(15), 154902, 2018. DOI: 10.1063/1.5023403. (Cit. on p. 73).

[187] T. GrandPre and D. T. Limmer. Current fluctuations of interacting active Brownian particles. *Phys. Rev. E* **98**, 060601, 2018. DOI: 10.1103/PhysRevE.98.060601. (Cit. on p. 73).

[188] T. Nemoto, É. Fodor, M. E. Cates, R. L. Jack and J. Tailleur. Optimizing active work: Dynamical phase transitions, collective motion, and jamming. *Phys. Rev. E* **99**, 022605, 2019. DOI: 10.1103/PhysRevE.99.022605. (Cit. on p. 73).

[189] S. Ramaswamy, R. A. Simha and J. Toner. Active nematics on a substrate: Giant number fluctuations and long-time tails. *Europhysics Letters (EPL)* **62**(2), 196–202, 2003. DOI: 10.1209/epl/i2003-00346-7. (Cit. on pp. 85, 96, 126).

[190] D. Marenduzzo, E. Orlandini and J. M. Yeomans. Hydrodynamics and Rheology of Active Liquid Crystals: A Numerical Investigation. *Physical Review Letters* **98**(11), 118102, 2007. DOI: 10.1103/PhysRevLett.98.118102. (Cit. on p. 85).

[191] D. Marenduzzo, E. Orlandini, M. E. Cates and J. M. Yeomans. Steady-State Hydrodynamic Instabilities of Active Liquid Crystals: Hybrid Lattice Boltzmann Simulations. *Physical Review E* **76**(3), 031921, 2007. DOI: 10.1103/PhysRevE.76.031921. (Cit. on p. 85).

[192] A. Doostmohammadi, J. Ignés-Mullol, J. M. Yeomans and F. Sagués. Active nematics. *Nature Communications* **9**(1), 3246, 2018. DOI: 10.1038/s41467-018-05666-8. (Cit. on pp. 85, 123).

[193] L. Giomi, M. J. Bowick, P. Mishra, R. Sknepnek and M. Cristina Marchetti. Defect dynamics in active nematics. *Philosophical Transactions of the Royal Society A: Mathematical, Physical and Engineering Sciences* **372**(2029), 20130365, 2014. (Cit. on p. 85).

[194] E. Putzig, G. S. Redner, A. Baskaran and A. Baskaran. Instabilities, Defects, and Defect Ordering in an Overdamped Active Nematic. *Soft Matter* **12**(17), 3854–3859, 2016. DOI: 10.1039/C6SM00268D. (Cit. on p. 85).

[195] N. Kumar, R. Zhang, J. J. de Pablo and M. L. Gardel. Tunable Structure and Dynamics of Active Liquid Crystals. *Science Advances* **4**(10), eaat7779, 2018. DOI: 10.1126/sciadv.aat7779. (Cit. on p. 85).

[196] S. Shankar, S. Ramaswamy, M. C. Marchetti and M. J. Bowick. Defect Unbinding in Active Nematics. *Physical Review Letters* **121**(10), 108002, 2018. DOI: 10.1103/PhysRevLett.121.108002. (Cit. on p. 85).

[197] S. Shankar and M. C. Marchetti. Hydrodynamics of Active Defects: From Order to Chaos to Defect Ordering. *Physical Review X* **9**(4), 041047, 2019. DOI: 10.1103/PhysRevX.9.041047. (Cit. on pp. 85, 111).

[198] S. Shankar, A. Souslov, M. J. Bowick, M. C. Marchetti and V. Vitelli. Topological Active Matter. 2020. arXiv: 2010.00364. (Cit. on p. 85).

[199] Z. Zhou, C. Joshi, R. Liu, M. M. Norton, L. Lemma, Z. Dogic, M. F. Hagan, S. Fraden and P. Hong. Machine Learning Forecasting of Active Nematics. *Soft Matter* **17**, 10.1039.D0SM01316A, 2020. DOI: 10.1039/D0SM01316A. (Cit. on p. 85).

[200] L.-B. Cai, H. Chaté, Y.-Q. Ma and X.-Q. Shi. Dynamical subclasses of dry active nematics. *Phys. Rev. E* **99**, 010601, 2019. (Cit. on pp. 86–88, 92, 96).

[201] B. Mahault and H. Chaté. Long-Range Nematic Order in Two-Dimensional Active Matter. *Physical Review Letters* **127**(4), 048003, 2021. DOI: 10.1103/PhysRevLett.127.048003. (Cit. on p. 87).

[202] M. L. Blow, S. P. Thampi and J. M. Yeomans. Biphasic, Lyotropic, Active Nematics. *Physical Review Letters* **113**(24), 248303, 2014. DOI: 10.1103/PhysRevLett.113.248303. (Cit. on pp. 88, 103, 126).

[203] P. C. Hohenberg and B. I. Halperin. Theory of dynamic critical phenomena. *Reviews of Modern Physics* **49**(3), 435–479, 1977. DOI: 10.1103/RevModPhys.49.435. (Cit. on pp. 90, 91).

[204] A. Ahmadi, M. C. Marchetti and T. B. Liverpool. Hydrodynamics of isotropic and liquid crystalline active polymer solutions. *Physical Review E* **74**(6), 061913, 2006. DOI: 10.1103/PhysRevE.74.061913. (Cit. on p. 90).

[205] I. Maryshev, D. Marenduzzo, A. B. Goryachev and A. Morozov. Kinetic theory of pattern formation in mixtures of microtubules and molecular motors. *Phys. Rev. E* **97**(2), 22412, 2018. DOI: 10.1103/PhysRevE.97.022412. (Cit. on pp. 90, 96).

[206] P.-G. De Gennes and J. Prost. *The physics of liquid crystals*. 83. Oxford university press, 1993. (Cit. on p. 90).

[207] T. Sato and A. Teramoto. On the Frank Elastic Constants of Lyotropic Polymer Liquid Crystals. *Macromolecules* **29**(11), 4107–4114, 1996. DOI: 10.1021/ma950986a. (Cit. on p. 93).

[208] M. N. van der Linden, L. C. Alexander, D. G. A. L. Aarts and O. Dauchot. Interrupted Motility Induced Phase Separation in Aligning Active Colloids. *Physical Review Letters* **123**(9), 098001, 2019. DOI: 10.1103/PhysRevLett.123.098001. (Cit. on p. 96).

[209] P. Guillamat, J. Ignés-Mullol and F. Sagués. Control of Active Liquid Crystals with a Magnetic Field. *Proceedings of the National Academy of Sciences* **113**(20), 5498–5502, 2016. DOI: 10.1073/pnas.1600339113. (Cit. on p. 97).

[210] M. Abramowitz and I. A. Stegun. *Handbook of Mathematical Functions with Formulas, Graphs, and Mathematical Tables*. Dover, New York, 1964. (Cit. on p. 99).

[211] J. Spitaler and S. K. Estreicher. Perspectives on the Theory of Defects. *Frontiers in Materials* **5**, 70, 2018. DOI: 10.3389/fmats.2018.00070. (Cit. on p. 111).

[212] .Defects and Their Effects on Materials Properties. en. *Structure-Property Relations in Nonferrous Metals*. John Wiley & Sons, Inc., Hoboken, NJ, USA, Aug. 2005, pp. 18–27. DOI: 10.1002/0471708542.ch2. (Cit. on p. 111).

[213] A. Jangizehi, F. Schmid, P. Besenius, K. Kremer and S. Seiffert. Defects and defect engineering in Soft Matter. *Soft Matter* **16**(48), 10809–10859, 2020. DOI: 10.1039/D0SM01371D. (Cit. on p. 111).

[214] A. Majumdar, M. C. Marchetti and E. G. Virga. Perspectives in active liquid crystals. *Philosophical Transactions of the Royal Society A: Mathematical, Physical and Engineering Sciences* **372**(2029), 20130373, 2014. DOI: 10.1098/rsta.2013.0373. (Cit. on p. 111).

[215] M.-A. Fardin and B. Ladoux. Living proof of effective defects. *Nature Physics* **17**(2), 172–173, 2021. DOI: 10.1038/s41567-020-01084-0. (Cit. on pp. 111, 123).

[216] V. Schaller, C. A. Weber, B. Hammerich, E. Frey and A. R. Bausch. Frozen Steady States in Active Systems. *Proceedings of the National Academy of Sciences* **108**(48), 19183–19188, 2011. DOI: 10.1073/pnas.1107540108. (Cit. on p. 111).

[217] V. Schaller and A. R. Bausch. Topological Defects and Density Fluctuations in Collectively Moving Systems. *Proceedings of the National Academy of Sciences* **110**(12), 4488–4493, 2013. DOI: 10.1073/pnas.1215368110. (Cit. on p. 111).

[218]   G. Duclos *et al.* Topological structure and dynamics of three-dimensional active nematics. *Science* **367**(6482), 1120–1124, 2020. DOI: 10.1126/science.aaz4547. (Cit. on p. 111).

[219]   A. Sciortino and A. R. Bausch. Pattern formation and polarity sorting of driven actin filaments on lipid membranes. *Proceedings of the National Academy of Sciences* **118**(6), e2017047118, 2021. DOI: 10.1073/pnas.2017047118. (Cit. on pp. 111, 112, 122).

[220]   T. B. Saw, W. Xi, B. Ladoux and C. T. Lim. Biological Tissues as Active Nematic Liquid Crystals. *Advanced Materials* **30**(47), 1802579, 2018. DOI: 10.1002/adma.201802579. (Cit. on p. 111).

[221]   A. Doostmohammadi and B. Ladoux. Physics of liquid crystals in cell biology. *Trends in Cell Biology*, S0962892421002014, 2021. DOI: 10.1016/j.tcb.2021.09.012. (Cit. on p. 111).

[222]   D. Dell'Arciprete, M. L. Blow, A. T. Brown, F. D. C. Farrell, J. S. Lintuvuori, A. F. McVey, D. Marenduzzo and W. C. K. Poon. A growing bacterial colony in two dimensions as an active nematic. *Nature Communications* **9**(1), 4190, 2018. DOI: 10.1038/s41467-018-06370-3. (Cit. on p. 111).

[223]   Y. Maroudas-Sacks, L. Garion, L. Shani-Zerbib, A. Livshits, E. Braun and K. Keren. Topological defects in the nematic order of actin fibres as organization centres of Hydra morphogenesis. *Nature Physics* **17**(2), 251–259, 2021. DOI: 10.1038/s41567-020-01083-1. (Cit. on pp. 111, 123).

[224]   H. Wioland, F. G. Woodhouse, J. Dunkel, J. O. Kessler and R. E. Goldstein. Confinement Stabilizes a Bacterial Suspension into a Spiral Vortex. *Physical Review Letters* **110**(26), 268102, 2013. DOI: 10.1103/PhysRevLett.110.268102. (Cit. on p. 111).

[225]   J. Hardoüin, R. Hughes, A. Doostmohammadi, J. Laurent, T. Lopez-Leon, J. M. Yeomans, J. Ignés-Mullol and F. Sagués. Reconfigurable flows and defect landscape of confined active nematics. *Communications Physics* **2**(1), 121, 2019. DOI: 10.1038/s42005-019-0221-x. (Cit. on pp. 111, 123).

[226]   K. Thijssen, D. A. Khaladj, S. A. Aghvami, M. A. Gharbi, S. Fraden, J. M. Yeomans, L. S. Hirst and T. N. Shendruk. Submersed micropatterned structures control active nematic flow, topology, and concentration. *Proceedings of the National Academy of Sciences* **118**(38), e2106038118, 2021. DOI: 10.1073/pnas.2106038118. (Cit. on p. 111).

[227]   M. M. Norton, A. Baskaran, A. Opathalage, B. Langeslay, S. Fraden, A. Baskaran and M. F. Hagan. Insensitivity of active nematic liquid crystal dynamics to topological constraints. *Physical Review E* **97**(1), 012702, 2018. DOI: 10.1103/PhysRevE.97.012702. (Cit. on p. 111).

[228]   A. Martínez-Calvo, C. Trenado-Yuste and S. S. Datta. Active transport in complex environments. 2021. arXiv: 2108.07011. (Cit. on p. 111).

[229]   T. Bhattacharjee and S. S. Datta. Bacterial hopping and trapping in porous media. *Nature Communications* **10**(1), 2075, 2019. DOI: 10.1038/s41467-019-10115-1. (Cit. on p. 111).

[230]   A. E. Patteson, A. Gopinath, M. Goulian and P. E. Arratia. Running and tumbling with E. coli in polymeric solutions. *Scientific Reports* **5**(1), 15761, 2015. DOI: 10.1038/srep15761. (Cit. on p. 111).

[231]   A. Maitra, P. Srivastava, M. C. Marchetti, J. S. Lintuvuori, S. Ramaswamy and M. Lenz. A nonequilibrium force can stabilize 2D active nematics. *Proceedings of the National Academy of Sciences* **115**(27), 6934–6939, 2018. DOI: 10.1073/pnas.1720607115. (Cit. on pp. 112, 120).

[232] M. P. Murrell and M. L. Gardel. F-actin buckling coordinates contractility and severing in a biomimetic actomyosin cortex. *Proceedings of the National Academy of Sciences of the United States of America* **109**(51), 20820–20825, 2012. DOI: 10.1073/pnas.1214753109. (Cit. on p. 112).

[233] R. Grover, J. Fischer, F. W. Schwarz, W. J. Walter, P. Schwille and S. Diez. Transport efficiency of membrane-anchored kinesin-1 motors depends on motor density and diffusivity. *Proceedings of the National Academy of Sciences* **113**(46), E7185–E7193, 2016. DOI: 10.1073/pnas.1611398113. (Cit. on p. 112).

[234] R. Zhang, N. Kumar, J. L. Ross, M. L. Gardel and J. J. de Pablo. Interplay of structure, elasticity, and dynamics in actin-based nematic materials. *Proceedings of the National Academy of Sciences* **115**(2), E124–E133, 2018. DOI: 10.1073/pnas.1713832115. (Cit. on pp. 120, 122).

[235] A. Maitra and R. Voituriez. Enhanced Orientational Ordering Induced by an Active yet Isotropic Bath. *Physical Review Letters* **124**(4), 048003, 2020. DOI: 10.1103/PhysRevLett.124.048003. (Cit. on p. 120).

[236] L. Farhadi, C. Fermino Do Rosario, E. P. Debold, A. Baskaran and J. L. Ross. Active Self-Organization of Actin-Microtubule Composite Self-Propelled Rods. *Frontiers in Physics* **6**, 75, 2018. DOI: 10.3389/fphy.2018.00075. (Cit. on p. 122).

[237] R. Zhang *et al.* Structuring Stress for Active Materials Control. 2019. arXiv: 1912.01630. (Cit. on p. 123).

[238] T. Gao, M. D. Betterton, A.-S. Jhang and M. J. Shelley. Analytical structure, dynamics, and coarse graining of a kinetic model of an active fluid. *Physical Review Fluids* **2**(9), 093302, 2017. DOI: 10.1103/PhysRevFluids.2.093302. (Cit. on p. 123).

[239] T. N. Shendruk, A. Doostmohammadi, K. Thijssen and J. M. Yeomans. Dancing disclinations in confined active nematics. *Soft Matter* **13**(21), 3853–3862, 2017. DOI: 10.1039/C6SM02310J. (Cit. on p. 123).

[240] Q. Zhang, J. Li, J. Nijjer, H. Lu, M. Kothari, R. Alert, T. Cohen and J. Yan. Morphogenesis and cell ordering in confined bacterial biofilms. *Proceedings of the National Academy of Sciences* **118**(31), e2107107118, 2021. DOI: 10.1073/pnas.2107107118. (Cit. on p. 123).

[241] A. J. Vromans and L. Giomi. Orientational properties of nematic disclinations. *Soft Matter* **12**(30), 6490–6495, 2016. DOI: 10.1039/C6SM01146B. (Cit. on p. 126).

[242] D. J. G. Pearce and K. Kruse. Properties of twisted topological defects in 2D nematic liquid crystals. *Soft Matter* **17**(31), 7408–7417, 2021. DOI: 10.1039/D1SM00825K. (Cit. on p. 126).

[243] X. Tang and J. V. Selinger. Theory of defect motion in 2D passive and active nematic liquid crystals. *Soft Matter* **15**(4), 587–601, 2019. DOI: 10.1039/C8SM01901K. (Cit. on p. 126).

# Acknowledgements